MINISTÉRIO DA CIÊNCIA, TECNOLOGIA, INOVAÇÕES E COMUNICAÇÕES
INSTITUTO NACIONAL DE PESQUISAS ESPACIAIS

sid.inpe.br/mtc-m21b/2017/08.10.22.44-TDI

IMPROVED STAR IDENTIFICATION ALGORITHMS AND TECHNIQUES FOR MONOCHROME AND COLOR STAR TRACKERS

Márcio Afonso Arimura Fialho

Doctorate Thesis in Engineering and Space Technologies Graduate Studies, major area Engineering and Management of Space Systems, guided by Drs. Leonel Fernando Perondi, and Daniele Mortari, approved in August 17, 2017.

URL of the original document:
<http://urlib.net/8JMKD3MGP3W34P/3PE49N5>

INPE
São José dos Campos
2017

PUBLISHED BY:

Instituto Nacional de Pesquisas Espaciais - INPE
Gabinete do Diretor (GB)
Serviço de Informação e Documentação (SID)
Caixa Postal 515 - CEP 12.245-970
São José dos Campos - SP - Brasil
Tel.:(012) 3208-6923/6921
E-mail: pubtc@inpe.br

MINISTÉRIO DA CIÊNCIA, TECNOLOGIA, INOVAÇÕES E COMUNICAÇÕES
INSTITUTO NACIONAL DE PESQUISAS ESPACIAIS

sid.inpe.br/mtc-m21b/2017/08.10.22.44-TDI

IMPROVED STAR IDENTIFICATION ALGORITHMS AND TECHNIQUES FOR MONOCHROME AND COLOR STAR TRACKERS

Márcio Afonso Arimura Fialho

Doctorate Thesis in Engineering and Space Technologies Graduate Studies, major area Engineering and Management of Space Systems, guided by Drs. Leonel Fernando Perondi, and Daniele Mortari, approved in August 17, 2017.

URL of the original document:
<http://urlib.net/8JMKD3MGP3W34P/3PE49N5>

INPE
São José dos Campos
2017

Cataloging in Publication Data

Fialho, Márcio Afonso Arimura.

F441i Improved star identification algorithms and techniques for monochrome and color star trackers / Márcio Afonso Arimura Fialho. – São José dos Campos : INPE, 2017.

xxxii + 226 p. ; (sid.inpe.br/mtc-m21b/2017/08.10.22.44-TDI)

Thesis (Doctorate in Engineering and Space Technologies Graduate Studies, major area Engineering and Management of Space Systems) – Instituto Nacional de Pesquisas Espaciais, São José dos Campos, 2017.

Guiding : Drs. Leonel Fernando Perondi, and Daniele Mortari.

1. Star trackers. 2. Star identification algorithms. 3. Image processing. 4. Photometric systems. 5. Fundamental limits. I.Title.

CDU 621.376.5:524.3

Aluno (a): *Márcio Afonso Arimura Fialho*

Título: "IMPROVED STAR IDENTIFICATION ALGORITHMS AND TECHNIQUES FOR MONOCHROME AND COLOR STAR TRACKERS".

Aprovado (a) pela Banca Examinadora em cumprimento ao requisito exigido para obtenção do Título de *Doutor(a)* em

Engenharia e Tecnologia Espaciais/Eng. Gerenc. de Sistemas Espaciais

Dr. Walter Abrahão dos Santos

Presidente / INPE / São José dos Campos - SP

Dr. Leonel Fernando Perondi

Orientador(a) / INPE / São José dos Campos - SP

Dr. Daniele Mortari

Orientador(a) / TAMU / Estados Unidos - USA

Dr. Ronan Arraes Jardim Chagas

Membro da Banca / INPE / São José dos Campos - SP

Dr. Antonio Gil Vicente de Brum

Convidado(a) / UFABC / Santo André - SP

Dr. Josiel Urbaninho de Arruda

Convidado(a) / ITA / São José dos Campos - SP

Este trabalho foi aprovado por:

( ) maioria simples

(X) unanimidade

São José dos Campos, 17 de agosto de 2017

To my parents Jorge and Glória, for all their love and support, and for Tatiana, my sister, for her friendship.

This thesis is dedicated to all those who guided me in my life, illuminating my paths.

ACKNOWLEDGMENTS

I would like to thank my advisors: Dr. Daniele Mortari for hosting me during 2016 and for being a great professor and human being, and Dr. Leonel Perondi for also being a great professor, a very kind man and my advisor at INPE. I also say thanks for all friends and colleagues I had during this journey, for their encouragement and friendship, especially for my parents, Jorge and Glória, and my sister, Tatiana. Without their effort and patience, I would not be here.

I also want to thank CNPq and AEB for the scholarship grant 207308/2015-2. Without their financial support, it would be much more difficult to complete this doctorate thesis.

Finally, I want to say thanks for God, for giving me life and strength to complete this journey.

ABSTRACT

Modern fixed head star trackers are among the most accurate attitude sensors available for spacecraft use. Their principle of operation is basically to take pictures of the celestial sphere and identify stars present on these images, using the identified stars as references for attitude determination. This process encompasses tasks such as image pre-processing, image segmentation, centroiding, star identification and attitude determination from vector observations. In the task of stellar identification, this work investigates how brightness information (magnitudes) and color information (when available) can be used to improve the reliability and speed in star identification. Incorporating magnitude and color information checks in an state-of-the-art star-ID algorithm resulted in a reduction in the misidentification rate by more than two orders of magnitude. Many other improvements were proposed and implemented in this state-of-the-art star identification algorithm. Other contributions of this work are in the use of color indexes (common in Astronomy, but new to the area) to represent color information in star trackers, with advantages over the previous representation used in the literature, and a methodology to evaluate the suitability of different color indexes in stellar identification. An investigation on existing technologies for color star tracking is performed, with image sensors based on stacked pixels showing good potential for future application. This work also presents a simple image pre-processing technique capable of removing column bias in CMOS image sensor, developed for star trackers with limited memory and low computational power. An estimate of the theoretical lower bounds of attitude knowledge achieved by star trackers is derived. This lower bound represents, in a certain way, a fundamental limit to the accuracy attainable by star trackers that depends only on the stellar distribution in our stellar neighborhood, star tracker dimensions and the length of the temporal window used for observations; thus, being completely independent on star tracker technology employed. The usefulness of this estimate is that it provides a benchmark for comparing different star tracker designs. This estimate is computed using data from the Hipparcos, Tycho and 2MASS star catalogs. To the best knowledge of the author, the computation of this lower bound is a novel contribution to this research field.

keywords: star trackers. star identification algorithms. image processing. photometric systems. fundamental limits. computer simulations.

TÉCNICAS E ALGORITMOS DE IDENTIFICAÇÃO DE ESTRELAS APRIMORADOS PARA SENSORES DE ESTRELAS COLORIDOS E MONOCROMÁTICOS

RESUMO

Sensores de estrelas de cabeça-fixa modernos estão entre os sensores de atitude mais precisos disponíveis para uso em veículos espaciais. Seu princípio básico de operação consiste em adquirir imagens do céu e identificar as estrelas presentes nestas imagens, usando as estrelas identificadas como referências de atitude. Este processo engloba tarefas como pré-processamento de imagens, segmentação de imagens, cálculo de centroides, identificação de estrelas e determinação de atitude a partir de versores observados. Na tarefa de identificação de estrelas, este trabalho investiga como as informações de brilho (magnitudes) e cor (quando disponível) podem ser aproveitadas para melhorar a confiabilidade e a velocidade do processo de identificação de estrelas. Ao se incorporar verificações de magnitude e cor em um algoritmo de identificação de estrelas estado da arte, obteve-se uma redução na taxa de identificações incorretas maior que duas ordens de grandeza. Várias outras melhorias foram propostas e implementadas neste algoritmo de identificação de estrelas. Outras contribuições deste trabalho estão no uso de índices de cor (comum em astronomia, mas novo neste campo) na representação de cor em sensores de estrelas, com vantagens em relação à representação anteriormente usada na literatura, e no desenvolvimento de uma metodologia para avaliar a adequação de diferentes índices de cor no processo de identificação de estrelas. Uma investigação sobre tecnologias para imageamento a cores voltada para sensores de estrelas é realizada, na qual se verificou que sensores de imagem baseados em pixels empilhados apresentam potencial para aplicações futuras. Este trabalho também apresenta um algoritmo de pré-processamento de imagens simples para remoção da não uniformidade de coluna em sensores CMOS, desenvolvido para sensores de estrelas com pouca memória e baixo poder computacional. Uma estimativa do limite teórico para a precisão de sensores de estrelas é apresentada. Este limite representa, de certa forma, um limite fundamental para a precisão de sensores de estrelas que depende apenas da distribuição de estrelas na nossa vizinhança estelar, das dimensões físicas do sensor de estrelas e da duração da janela de tempo usada para observação das estrelas, sendo, portanto, completamente independente da tecnologia empregada. A utilidade desta estimativa é que ela provê uma referência ao qual se podem comparar diferentes sensores de estrelas. Esta estimativa foi calculada usando dados dos catálogos de estrelas Hipparcos, Tycho e 2MASS. Até onde o autor tenha conhecimento, o cálculo desta estimativa é uma contribuição original para esta área de pesquisa.

palavras-chave: sensores de estrelas. algoritmos de identificação de estrelas. processamento de imagens. sistemas fotométricos. limites fundamentais. simulações em computador.

LIST OF FIGURES

Page

LIST OF TABLES

Page

TERMS AND ACRONYMS

3T = three transistor

A/D = analog to digital

ADC = analog to digital converter

ADU = analog-digital unit = size of a quantization step of an ADC

AOCS = attitude and orbit control subsystem.

APS = active pixel sensor

AU = astronomical unit = mean distance from Earth to the Sun.

B = blue

CDS = correlated double sampling

CMOS = complementary metal oxide semiconductor

CPU = central processing unit

DBR = distributed Bragg reflector

DEA = *Divisão de Eletrônica Aeroespacial* = Aerospace Electronics Division (a division of INPE)

DPS = digital pixel sensor

ECI = Earth Centered Inertial

EPS = Enhanced Pattern Shifting algorithm

ESA = European Space Agency

ESO = European Southern Observatory

FOV = Field of View

FPN = fixed pattern noise

HRF = Hipparcos Reference Frame

HST = Hubble Space Telescope

I = Infrared

IAU = International Astronomical Union.

IBM = International Business Machines Corporation

ICRF = International Celestial Reference Frame

ICRS = International Celestial Reference System.

ID = identification

INPE = *Instituto Nacional de Pesquisas Espaciais* = Brazilian National Institute for Space Research

IRF = inertial reference frame

MOSFET = metal-oxide-semiconductor field-effect transistor

MS = Microsoft

NASA = National Aeronautics and Space Administration

NEA = Noise Equivalent Angle

NRRF = spacecraft non-rotating reference frame

PC = personal computer

PRNU = photo response non-uniformity

PS = Pattern Shifting algorithm

PSF = point spread function

PTASE = *Programa de Testes de Algoritmos para Sensores de Estrelas* = Test Program for Algorithms used in Star Sensors

PV = Photovoltaic

RAM = random access memory

RC circuit = resistor capacitor circuit

rms = root mean square

SEE = single event effect

SNR = signal to noise ratio

STR = star tracker

STRF = star tracker reference frame

STScI = Space Telescope Science Institute

TID = total ionizing dose

UV = ultraviolet

V = visual

WFC3 = Wide Field Camera 3 (an instrument of the Hubble Space Telescope)

LIST OF SYMBOLS

Latin:

a_{ij}	signal gain for pixel located at (*i*, *j*)
b	blue magnitude in custom photometric system
b_{ij}	bias for pixel (*i*, *j*)
B	brightness of a cluster of pixels or detected star
B	Johnson's blue magnitude
B_{ref}	reference brightness
C	capacitance
C	attitude matrix
C	black-body dilution factor
c	speed of light in vacuum
c_{ij}	dark current for pixel (*i*, *j*)
D	aperture diameter
e	base of natural logarithms = Euler's number ≈ 2.71828
e^-	electron
$\mathrm{E}\{\}$	expected value
f	frequency
f_{ij}	number of photons incident on pixel (*i*, *j*)
$\mathbf{F}$	Fisher information matrix
g	green magnitude in custom photometric system
G	constant for the lower bound on attitude error in the Solar System vicinity.
h	Planck constant
I	Johnson-Cousins near infrared magnitude
I_{dark}	dark current
k	Boltzmann constant ≈ $1.38065 \cdot 10^{-23}$ J/K
m_i	instrumental magnitude
m_v	visual magnitude = magnitude at band V.

m_{obs}	observed magnitude
m_x	apparent magnitude in spectral band x.
$M_{e,\lambda}(T,\lambda)$	spectral exitance of a black-body.
n	number of detected/observed stars
n	number of photons reaching a detector
n	number of thermally generated electron-hole pairs
$\bar{n}$	mean or expected number of photons striking a pixel
N	number of cataloged stars
N	number of photons detected
P_n	Probability of exactly *n* occurrences in a Poisson distribution.
$\mathbf{P}_{\vartheta\vartheta}$	attitude covariance matrix
q_e	elementary charge ≈ $1.6022 \cdot 10^{-19}$ C
r	red magnitude in custom photometric system
$\boldsymbol{R}$	unit vector representing a star in the star catalog
R_{ij}	response of pixel located at row *i* and column *j*
$R_X(\lambda)$	response function for spectral band *X*.
T	absolute temperature
t	time interval or exposure/integration time
v	velocity
V	Johnson's visual magnitude
V_{rms}	root mean square voltage

Greek:

α	right ascension
δ	declination
δ	variation or difference
ε	tolerance used in angular separations (lengths of star pairs)
η	quantum efficiency
θ	rotation angle

θ	length of star pair = angular separation between stars in that pair
θ	angle between the observer velocity vector and light source position.
$\bar{\vartheta}_{rms,min}$	lower bound on attitude error.
ι	parameter of Poisson distribution.
λ	wavelength
Λ	color ratio
ν	frequency
ξ	a very small number
π	constant pi = ratio between the perimeter of a circle and its diameter.
σ	standard deviation parameter or an estimate of the standard deviation parameter.
$\varphi_{BB,X}$	black-body flux at spectral band *X.*

Other:

°	degree sign = π /180 radians.
′	one arc-minute = 1/60 degree = π/10800 radians.
″	one arc-second = 1/3600 degree = π/648000 radians.
♈	vernal equinox

TABLE OF CONTENTS

Page

1 INTRODUCTION

For most space missions, in addition to precisely control spacecraft orbit or trajectory, it is also of utmost importance to properly control spacecraft orientation, also known in the field as attitude. This is especially true for missions with stringent pointing requirements, such as Earth observing spacecraft and space telescopes. For example, for Earth observing spacecraft, it is important that its remote sensing cameras be pointed towards Earth's center (nadir direction). In order to accomplish this, the spacecraft employs a variety of attitude sensors to determine its orientation in space. This work focuses on one type of attitude sensor: star trackers, and on the algorithms they use. A brief description of modern star trackers is given in Chapter 2.

1.1 Objectives / Purposes

With technological advancements and the need to reduce costs of space missions, there exists a trend to reduce size, mass, and power consumption of future spacecraft, while at the same time increasing spacecraft autonomy and on-board processing (WERTZ; LARSON, 1999). One way to achieve the desired capability and reliability in small spacecraft is to perform redundancy via instrument reconfiguration instead of duplicating the same hardware, in other words, use the same hardware for different purposes. For example, instead of carrying a backup star tracker powered off, a spacecraft could reconfigure one of its general-purpose cameras as a star tracker in the event one of its primary star tracker fails, by loading the appropriate software into that camera. Given that a multifunctional camera which is also capable of being used as a star tracker may be equipped with a color image sensor to satisfy the requirements of its other uses (a Navcam or scientific camera, for example), this work investigates the benefits that color information can bring to star identification reliability.

Another goal is to improve robustness and speed of a state-of-the-art star identification algorithm. This work presents many improvements to the Pyramid

star identification algorithm (MORTARI, 2001; MORTARI et al., 2004), also exemplifying how the use of additional information such as magnitude and color information can improve the robustness of stellar identification.

The development of techniques that can improve the performance of a star tracker, particularly, in older designs with limited memory and computational power, was also pursued.

Finally, a study about the ultimate limits imposed by the laws of Physics and stellar distribution in our stellar neighborhood is performed, in order to derive an approximate lower bound on attitude accuracy, that cannot be overcome with technological advancements.

1.2 Motivation / Utility

Considering that star trackers are used in virtually any mission with stringent pointing requirements (errors smaller than one arc-minute = 290 μrad) and there is a trend that these requirements will become even tighter for future missions, any development in the direction of improving the robustness of stellar identification, improving accuracy of centroids, and improving attitude determination in star trackers will be of great help.

As missions with more stringent pointing requirements are becoming more common, star trackers should become more widely used. For example, many future space missions to be developed by INPE, such as remote sensing satellites and scientific spacecraft, will have payloads with stringent pointing requirements, making the use of star trackers for attitude control a necessity. Yet, on the other end of the spectrum, there are nanosatellites and picosatellites, such as cubesats, which are becoming increasingly more common. These small systems cannot afford to have multiple redundant equipment, due to mass, power and space constraints. In these small systems, a key concept to achieve the required functionality and reliability is to have flexibility in its instruments. This can be achieved, for example, with the use of multifunctional cameras, capable of

working as a science camera, as a navigation camera, as a star tracker, as a horizon sensor, etc., just with a change in its software or operating mode. The reuse of the same hardware for a different purpose is not an entirely new concept. There are many examples of cameras normally used as star trackers that have been used for other purposes, such as the Clementine mission, where one of its star trackers was used as a scientific camera (KORDAS et al., 1995) and the navigation cameras (NAVCAM) of the Rosetta spacecraft (NASA, 2017).

The motivation for studying star identification algorithms that are capable of making use of color information comes from the fact that a multifunctional camera that is capable of working as a star tracker may provide color information due to other reasons, and this could be used to improve star identification. For some tasks, such as target recognition or optical navigation, color information is very important, being sometimes the only way to confidently discriminate an object (POLLOCK, T., 2016, personal communication). Considering that the same hardware can be used for multiple purposes, it is advantageous to use algorithms that are capable of making use of this extra information, given that any additional information gathered about observed stars may be helpful in confirming the identity of these stars, thus reducing the risk of misidentifications.

1.3 Contributions

The main contributions of this work to the field are:

- improvements in one of the state of the art star-identification algorithm, both in terms of robustness (reliability in star identification) and speed;
- use of magnitude and color indexes as additional verification methods in the aforementioned star identification algorithm;
- derivation of an estimate for the theoretical lower bound on attitude accuracy that can be achieved by star trackers in our stellar neighborhood, that is independent of star tracker technology;

- development of a technique to estimate the image sensor bias and column amplifier bias without having to sample all pixels in an image, which makes it suitable for embedded hardware with limited memory and computational power.

1.4 Thesis structure

Chapter 2 provides an overview of star trackers, giving a general explanation on how these attitude sensors are able to derive attitude information from raw images captured from the sky. It also introduces the basic concepts and terminology used in the field. Chapter 3 presents a discussion on how magnitude and color information can be helpful in increasing the reliability of stellar identification, especially in the cases where few stars are observed. This chapter also presents a discussion about the trade-offs that commonly have to be made with existing technologies to enable color determination, and some considerations whether they are worthful or not. It concludes with an analysis of a night sky test, performed with a camera using the new concept of stacked pixels for stellar identification, with promising results. Chapter 4 describes the simulation environment which was used for the Monte Carlo simulations performed in the following chapter. Chapter 5 introduces the many improvements made to the Pyramid star identification algorithm. Chapter 6 presents improvements in image processing algorithms with the purpose of improving centroiding accuracy and star detection. Chapter 7 introduces an original theoretical study that determines an estimate for the lower bound of attitude accuracy achievable in the vicinity of the Solar System. The results of this study provide a benchmark in which to compare different star tracker designs. Chapter 8 summarizes the main contributions of this work, proposing ideas for future works and pointing out areas that need more in-depth research.

2 BASIC CONCEPTS

This chapter gives a brief introduction to concepts and terminology used in the field. These concepts are briefly discussed here to provide to the reader a background on the subjects developed in this thesis.

A modern star tracker (STR) is basically a computerized camera that uses stars as references for attitude determination. In essence, the task of a STR is to determine or provide information that allows the determination of the relation between a reference frame that rotates with it with a reference frame that does not rotate (as defined in Section 2.5.2). This relation is nothing more than the STR attitude. Since the STR is rigidly mounted on the spacecraft, once the STR attitude is known, the spacecraft attitude can be easily computed.

In the following sections, an introduction to the many types of star sensors is provided, followed by a brief description of the typical modes of operation of a fixed head STRs, a detailed explanation of the process of attitude determination from observed stars in fixed head STRs and a brief description of the star identification techniques used. This chapter concludes with a brief description of the reference frames typically used in STRs.

2.1 Classification of star trackers

Star trackers are currently the most accurate attitude sensors generally available for spacecraft use, being able to provide absolute attitude measurements with errors smaller than few arc-seconds (few tens of microradians) (LIEBE, 2002). Nowadays, most star trackers are fixed head autonomous star trackers, capable of delivering three-axis attitude measurements at rates typically between 0.5 Hz and 10 Hz (LIEBE, 2002; ENRIGHT et al., 2010; MARKLEY; CRASSIDIS, 2014). These modern attitude sensors are basically computerized solid-state cameras, with a pattern recognition software that attempts to match the stars it observes with an on-board catalog of stars.

According to the classification given by Fallon III (1978), star trackers belong to a larger class of attitude sensors known as *star sensors*. In his scheme, star sensors are grouped into three large classes, according to its physical structure and operation: *star scanners*, *gimbaled star trackers* and *fixed head star trackers*. *Star scanners* include the simplest star sensors. Usually they consist of a "V" shaped slit and one or more detectors. They use the spacecraft rotation to acquire attitude information, as the star light passes through its slit. *Gimbaled star trackers* use mechanical gimbals to track a bright star, reading its position from the encoders in the gimbals. *Fixed head star trackers* have their optical head rigidly mounted on the spacecraft, scanning their field of view electronically. In this group, we encounter the most complex designs. Since modern fixed head star trackers are capable of observing many stars simultaneously, they are also known as *star cameras*. Like star scanners, and in contrast to gimbaled star trackers, they have no moving parts. Early models of fixed head star trackers were based on image dissector tubes or vidicons. Nowadays most fixed head star trackers are based on solid state image sensors, such as CCD image sensors and CMOS APS image sensors.

Another classification can be done regarding the field of view (FOV) and STR accuracy, where they can be classified in two large classes: coarse star sensors having wide FOV and fine pointing star sensors having narrow FOV (LIEBE, 1995). Modern STRs with wide fields of view (typically in the range of 8° × 8° to 25° × 25°) can determine the direction of their optics boresight axis with an uncertainty typically between 1" and 10" (1σ). Star trackers with narrow field of view (typically less than 3° × 3°) and accuracies better than one arc-second are less common. These ultra-fine star sensors are typically used in missions with very stringent pointing requirements, such as space telescopes.

A third classification is based on autonomy. An autonomous star sensor is capable of determining its own attitude without the aid of any external information or processing. In other words, they are capable of determining their attitude even when the spacecraft is in a *lost in space* situation, when no attitude estimate

exists. On the other hand, a non-autonomous star sensor is not able to find an attitude solution if a previous attitude estimate does not exist, or does not have the software routines needed to identify stars and determine attitude, relying on external processing. With technology advancements, most star trackers being used in modern spacecraft are autonomous star sensors.

This work focuses exclusively on fixed head autonomous star trackers with solid state detectors, having a wide FOV and accuracy in the determination range of 1” to 10” (1σ), as this is the most used type in three-axis stabilized spacecraft.

With many types of star sensors presented by Fallon III becoming obsolete and the market being dominated by fixed head star trackers (MARKLEY; CRASSIDIS, 2014), the distinction between the terms *star tracker*, *star sensor* and *star camera* seems to have lost its importance. Therefore, these terms will be used as synonyms in this work.

2.2 Modes of operation of a star tracker

A fixed head star tracker presents many modes of operation. Typically, the following modes are found (FIALHO, 2007; FIALHO; PERONDI; MORTARI, 2016):

- start-up/basic Initialization mode;
- a stand-by mode;
- Autonomous Attitude Determination mode:
    - Attitude Acquisition,
    - Attitude Tracking
- imaging mode;
- diagnostic modes;
- configuration modes.

The start-up/initialization modes include the basic tasks that are performed once a star tracker is powered up, or after a processor reset. In the stand-by mode the

star sensor sits idle, waiting for commands sent from an external source (e.g., commands sent by the AOCS computer). The *Autonomous Attitude Determination* mode is the mode where the star tracker works as a star tracker. This can be subdivided into *Attitude Acquisition* and *Attitude Tracking* sub-modes. The *Attitude Acquisition* sub-mode is entered when the star sensor is in a lost-in-space condition (when no a priori attitude knowledge exists) or when only a poor attitude estimate exists. In the “Attitude Tracking” sub-mode, the star tracker has a good knowledge of its angular velocity and previous attitude state, so it can predict where stars will be in the next frame. Thus, in “Attitude Tracking”, the star tracker needs to read only pixels inside small rectangular windows placed around the expected positions of stars in the next image frame, reducing by two or three orders of magnitude the number of pixels that must be processed, which makes this mode extremely fast. The transition between the “Attitude Acquisition” and “Attitude Tracking” sub-modes is discussed in detail in the work of Brum *et al.* (2013). The present work discusses only the algorithms used in the “Attitude Acquisition” sub-mode.

It's very common for a modern star tracker to include an imaging mode, where a raw image is captured and made available for download. This mode is useful for checking the health of the imaging element in a star tracker. It can also be used when the star sensor is used as a general-purpose camera or as a scientific imaging camera.

Besides the modes previously discussed, a star tracker typically includes maintenance modes, such as in-orbit test modes, software update mode, diagnostic modes, etc. Sometimes with the proper software, a star tracker can also operate in other functions, such as a scientific camera (KORDAS et al., 1995), a space awareness camera, a space navigation camera (NASA, 1997) or even as a horizon sensor operating in the optical regime (e.g., using the atmospheric luminescence to detect the Earth’s limb at night).

2.3 Attitude acquisition in a fixed head star tracker

In modern, fixed head star trackers, attitude acquisition usually proceeds as depicted in Figure 2.1 (FIALHO, 2007), which may be phrased as follows:

Figure 2.1 - Attitude determination from a star field image

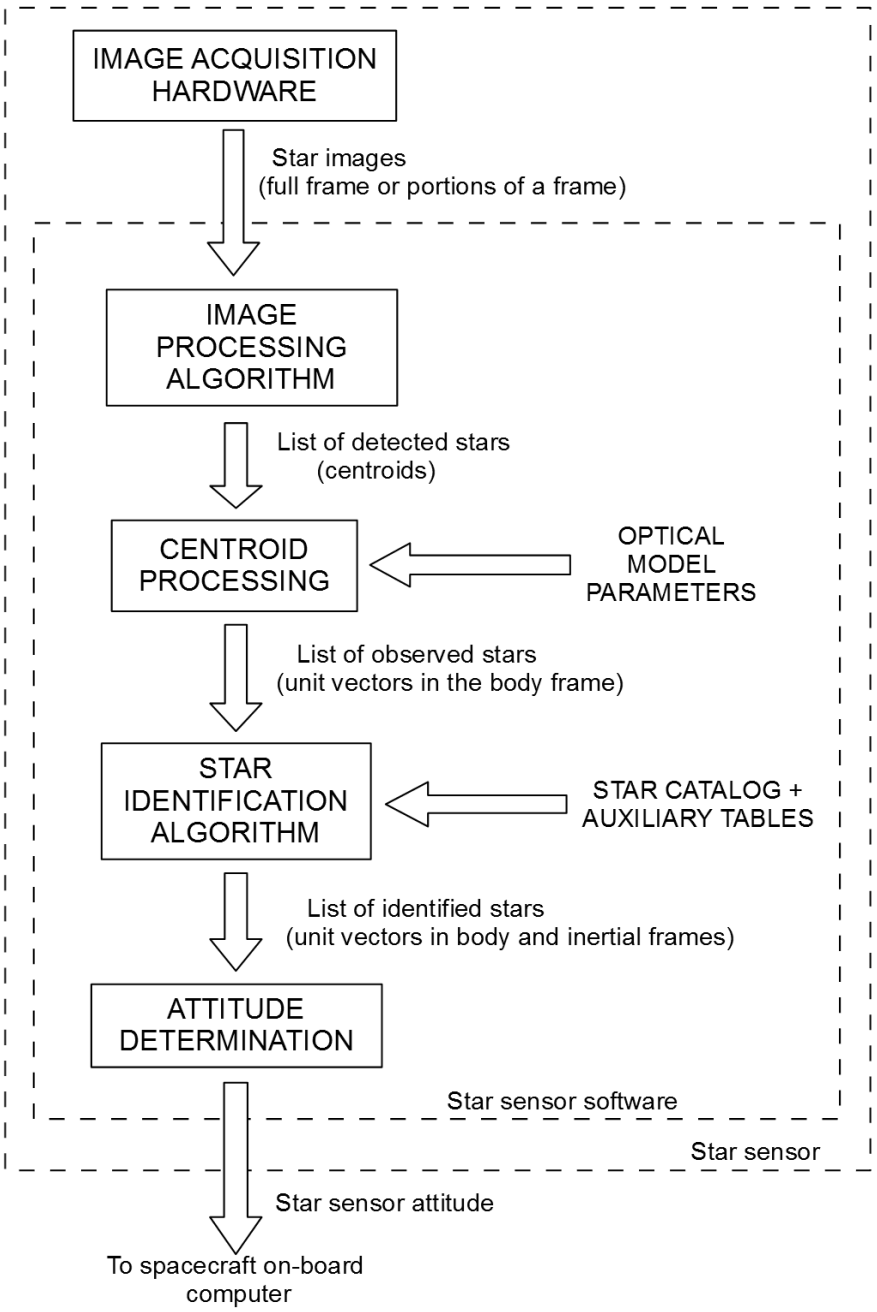

Source: Drawn by the author.

a) the hardware acquires an image;

b) an image processing algorithm extracts stars from this image, generating a list of centroids;

c) by taking into account optics parameters (focal length, pixel pitch, aperture and distortions introduced by the optics) this list of centroids is converted to a list of observed stars, whose coordinates are given in the star tracker reference frame (STRF);

d) a star-ID algorithm attempts to associate every star in the list of observed stars with a star in the on-board star catalog, generating a list of identified stars. The main goal of this process (stellar identification) is to discover the coordinates of observed stars in a non-rotating reference frame (NRRF) used in the working copy of the star catalog (see Section 2.5.2);

e) this list of identified stars is supplied to an attitude determination algorithm. By comparing the coordinates in the STRF with coordinates in the NRRF for each star in this list, this algorithm is capable of finding a relation between these two reference frames. This relation is nothing more than the star tracker attitude.

The star tracker attitude is usually the final output. This information is provided to the spacecraft attitude determination and control subsystem's computer, responsible for merging this measurement with measurements from other attitude sensors when computing the spacecraft attitude.

In many star sensors, the coordinates of both observed stars and cataloged stars are complemented with brightness information (stellar magnitudes), as this information is helpful in confirming the identity of stars, and in sorting the observed stars, so those stars that have the least probability of being false stars (usually the brightest stars) are used first. Also, many star-ID algorithms employ stellar magnitudes as a rough filter when selecting candidate stars from the star

catalog. When magnitude information is used, the pixel values belonging to the observed stars are also utilized to compute their observed instrumental magnitudes, usually at step c) - Centroid Processing.

2.4 Star identification

As stated in the previous section, the goal of star identification is to discover the coordinates of observed stars in a reference frame used for attitude determination (the reference frame used in the working copy of the star catalog, as explained in Section 2.5.2). To do so, the star-ID algorithms attempt to associate each observed star with a star in the star catalog, using one method or a combination of different methods. The outcome of the star identification process can be (CARVALHO, 2001):

a) correct identification: the observed star is correctly associated with the catalog star that corresponds to it;

b) ambiguous identification: there are many potential matches with stars in the catalog;

c) no identification: no star from the star catalog matches within measurement tolerances the observed star – this can happen if the observed star is a false star or a star absent in the star catalog;

d) incorrect identification (misidentification): the observed star is incorrectly assigned to a single catalog star that does not correspond to it.

In case of an ambiguous identification, the star-ID algorithm might attempt to solve the ambiguity by performing additional tests to improve the correct identification rate. However, if the ambiguity cannot be easily solved, or if the ambiguity resolution has a relatively large probability of misidentification, it is preferable to reject the identification than to risk returning an incorrect identification. As pointed out by Carvalho (2001), in real star trackers, there's no way to differentiate between a correct star identification from a misidentification,

since the true star identities are unknown. This is especially important during the attitude acquisition phase, when the STR has no attitude knowledge. Therefore, in a real application, a misidentification can have much more severe consequences than no identification (CARVALHO, 2001; MORTARI et al., 2004). A misidentification can lead to a significantly incorrect attitude estimate being returned by the star tracker. An incorrect attitude provided to the spacecraft's attitude and orbit control subsystem (AOCS), if not properly filtered, can cause the spacecraft to reorient itself in space in an incorrect way, with potentially catastrophic consequences, including mission loss. On the other hand, if the star tracker does not provide an attitude solution, the AOCS can rely on the information gathered from other attitude sensors or propagate attitude from previous measurements, provided these attitude measurement dropouts are infrequent. A typical specification for a star tracker would be: availability > 99% and incorrect attitude determination probability < 10^{-6} (DEA – Divisão de Eletrônica Aeroespacial, 2005, personal communication), where an incorrect attitude means an attitude with errors large enough to degrade or put a mission at risk. In summary, a good star identification algorithm should have a high success rate and a very low misidentification rate.

Many methods do exist for stellar identification. One of the first attempts to classify star identification methods was performed by Gottlieb (1978), with more recent classifications performed by Carvalho (2001), Spratling and Mortari (2009), Brätt (2013) and Zhang (2017).

2.5 Reference frames

For the process of star identification and attitude determination alone, only two reference frames would be needed: a reference frame that rotates with the star tracker and another reference frame with axes fixed in inertial space, serving as a reference for attitude determination. However, due to the effects of stellar aberration (explained in Section B.1.1 in the appendices) and stellar parallax, it is often necessary to define an intermediate reference frame between the inertial

reference frame used in the star catalog and the other reference frame that rotates with the star tracker. For a spacecraft orbiting Earth, stellar aberration can result in an attitude determination error up to 28 arc-seconds if it is not properly treated (ALBUQUERQUE; FIALHO, 2005). The effect of stellar parallax is much smaller and needs to be corrected only for high accuracy star trackers or for missions to the Outer Solar System and beyond, being discussed in Section B.1.2. Therefore, this section provides a brief description of these reference frames. A more comprehensive treatment of how the effects of stellar aberration and stellar parallax can be corrected or compensated is provided by Shuster (2003).

2.5.1 Master catalog inertial reference frame (IRF)

This reference frame is an inertial reference frame adopted by the master star catalog stored on-board in the star trackers simulated in this work.

Since the master star catalogs used in our work were derived from the Hipparcos star catalog (ESA, 1997), the inertial reference frame adopted here is the same as the one used in this star catalog, known as HRF (Hipparcos Reference Frame). This reference frame has its origin at the center of mass of the Solar System with its fundamental axes defined in a way to be backwards compatible with the old equatorial coordinate system used by astronomers using the equinox and poles of J2000.0 (Section A.2.1 in the appendices). Nevertheless, its defining axes are defined by a set of extragalactic sources and distant stars, being completely decoupled from the complex movements performed by the Earth. The HRF along other practical realizations of the ICRS (International Celestial Reference System) are currently the reference frames that best approach a truly inertial reference frame in spacecraft work. These reference frames are in essence the “J2000 reference frame” used by the Astronautical community. Figure 2.2 illustrates the inertial reference frame used in this work. Sections A.2 and A.2.2 in the appendices give a more detailed explanation of the HRF, ICRS and their historical background.

To better illustrate how the **x**, **y** and **z** axes of the HRF are defined, Figure 2.2 also shows the Earth on its orbit around the Sun, marking the approximate positions of the Earth during the solstices and equinoxes of the year 2000. In this figure, the Sun is at the center, practically coincident with the origin of the HRF. The Earth is on the background, just behind the Sun. The **x** axis is approximately aligned with the vernal equinox of the year 2000 (the straight line starting from Earth and going in the direction of the Sun during the spring equinox of March 2000), in the image, pointing towards the reader. The **z** axis points approximately to the north pole of the celestial sphere, and **y** is defined in such a manner that **x**, **y**, **z** define a right-handed coordinate system. For a definition of the astronomical terms see Appendix A.

Figure 2.2 – inertial reference frame used in this work (see text for explanations).

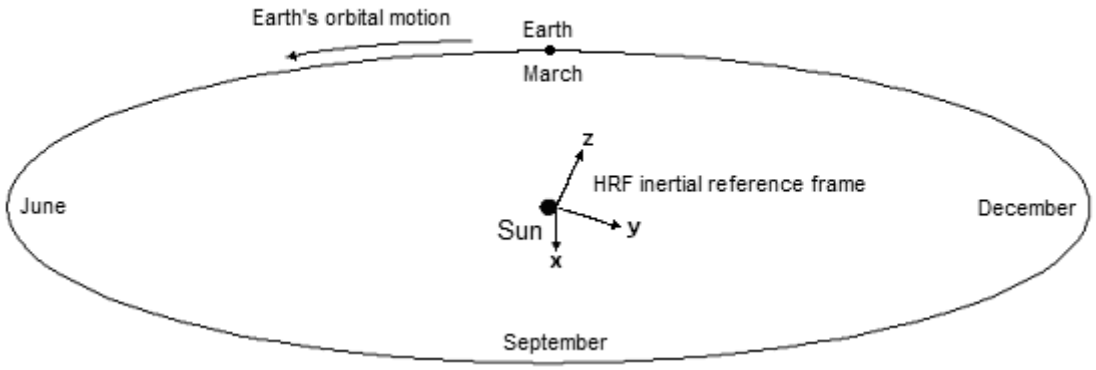

Source: adapted from Fialho (2007).

From the theoretical point of view, the HRF and any other reference frame defined at the barycenter of the Solar System is not truly inertial, due to the small gravitational acceleration of the Solar System as a whole caused by nearby stars, by the center and the remaining of our galaxy and to a lesser degree by extragalactic bodies. By this reason, the HRF is more appropriately defined as a “quasi-inertial” reference frame. However, the accelerations from these sources are so small that they may be ignored even for accurate work (FIALHO, 2007).

2.5.2 Spacecraft non-rotating reference frame (NRRF)

This reference frame has its origin in any point inside the spacecraft or inside the star tracker, but the directions of its defining axes remain fixed in space and parallel to the defining axes of the inertial reference frame used in the master star catalog. It is against this reference frame that the star tracker attitude is computed. For accurate attitude determination, coordinates of stellar vectors from the star catalog used in the process of star identification should be represented in this reference frame. These coordinates can be obtained from the master star catalog after including the effects of stellar aberration and (depending on the accuracy required) stellar parallax. Explanation of these phenomena and how to include their effects is given in Appendix B, sections B.1.1 and B.1.2.

An accurate method to compensate the effects of stellar aberration and parallax is to create a working copy of the star catalog including these effects at regular intervals. In particular, the effects of stellar aberration can be included by distorting star catalog coordinates using the approximate Equation (B.1), as described in Section B.1.1 of the appendices. The star coordinates in this working copy of the star catalog will be in an inertial frame that is a good approximation to the spacecraft NRRF. Table B.1 shows the magnitude of the residual aberration error versus the star catalog update interval.

The exact location of the origin of this reference frame inside the spacecraft has no practical importance in attitude determination. The distances to the stars are so vast in comparison to the dimensions of even the largest spacecraft, and differences in the velocity vector among different parts in the spacecraft (e.g., due to spacecraft rotation) are so small in comparison to the speed of light, that the spacecraft as a whole can be considered as a point, unless measurements in the micro-arc-second range are being made, where the differential stellar aberration effect among different parts of the spacecraft might become important.

2.5.3 Star tracker reference frame (STRF)

The star tracker reference frame, also known as the body reference frame, is attached to the star tracker optical head, being usually defined by the image sensor's matrix and optical axis. Figure 2.3 illustrates the STR reference frame.

Figure 2.3 – STR reference frame

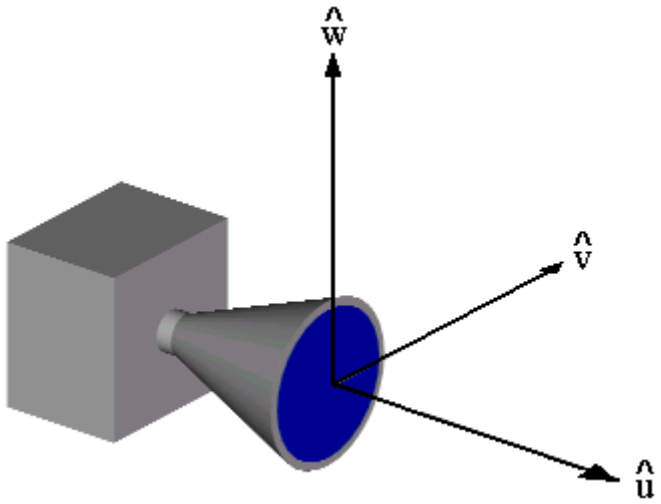

Source: Fialho (2007).

As previously stated, the star tracker attitude is simply the relation between this reference frame with the NRRF defined in the previous section.

2.6 Minimum number of observed stars for autonomous attitude determination

When only one star is observed, it is not possible to determine the STR attitude, even when its identity is already known (e.g., from previous identifications in tracking mode), since the minimum number of vector observations needed for attitude determination is two, and these need to be non-collinear. It is easy to understand the reason for that. With only one identified star (only one reference vector for attitude determination), the spacecraft could rotate around the line that joins the spacecraft to that star without changing its position on the STR FOV.

Thus, there are infinitely different attitudes providing exactly the same scene for the STR. The same situation happens when there are only two vector observations and these are collinear.

To determine attitude from vector observations, where each vector coordinates are known both in the body frame and in an inertial reference frame, the absolute minimum number of vectors needed is two and these vectors must be non-collinear. However, with only two observed stars it is not possible to determine their identity in a *lost in space* situation based solely on their position (McVITTIE, 2013), since a rotation of 180 degrees around an axis that passes through the center of the line joining these stars will give the same image. With the inclusion of additional information about the stars, such as magnitude or color index, identification with only two stars become possible in theory. Nevertheless, for the typical measurement tolerances of modern star trackers, there exist multiple potential matches from the star catalog to the observed pair of stars, even when using additional information such as stellar magnitudes and color indexes to aid star identification, which makes identification based solely on two stars in a lost-in-space scenario extremely unreliable. Therefore, most star-ID algorithms used in the attitude acquisition mode require at least three stars in the STR field of view to attempt identification.

3 USE OF MAGNITUDE AND COLOR INFORMATION FOR STAR TRACKERS

3.1 Introduction

When an attitude estimate is available, from a previous identification or from another attitude sensor, it can be used to filter the number of candidate stars from the catalog by selecting only those cataloged stars which are expected to be close or within the star tracker FOV (or FOVs for a multiple head STR). By reducing the size of the search space, this procedure reduces the dangers of misidentifications. However, this is not possible when no attitude estimate is available, i.e., when the spacecraft is in a *lost in space* condition. In that case, the star tracker faces the difficult task of finding the correct match among thousand stars from the star catalog. In this scenario, any information about the stars being identified made available to the star-ID algorithm can be helpful in reducing the probability of a misidentification happening.

The primary information about stars that is typically used in star identification algorithms is their geometric configuration, since this is in almost every case the most accurate information available for star identification – unit vectors representing stars are typically available with uncertainties in the order of few arcseconds (few tenths of microradians). Besides unit vectors, observed star brightness information is also usually available, typically being represented by a magnitude in the star tracker natural magnitude scale (for a definition of the magnitude scale used in Astronomy, the reader is referred to Appendix C in this work). Magnitude information is much less accurate than positional information, precluding its use as the sole mean of star identification (magnitude measurements typically have uncertainties in the range 0.05 to 0.5 magnitudes, which means that many stars will have the same magnitude within measurement tolerance). Nevertheless, it can be used to filter candidate stars, speeding up stellar identification; and to confirm the identity of stars, reducing the probability of a misidentification. Most star trackers (or cameras that can be used as star

trackers) are monochromatic (color insensitive). However, if the hardware can capture color information, this could be exploited to improve stellar identification speed and reliability.

This chapter starts with a description of the reasons to use magnitude and color information (when available) in stellar identification, followed by a discussion among different hardware classes that could be used for color sensitive star sensors. Some parts of this chapter have been derived from a conference paper presented by the author (FIALHO; MORTARI; PERONDI, 2016).

3.2 Benefits of magnitude use

The number of stars brighter than a certain magnitude follows, to a good approximation, a power law (LIEBE, 2002; RAO, BHAT, ALEX, 2005). Using data from the Hipparcos catalog (after merging stars that are closer than 0.05° into a single equivalent star) and visual magnitudes, the following relation was fitted by Fialho (2007, p. 95):

$$N = a \cdot 10^{b \cdot m_v} \tag{3.1}$$

where:

N = number of stars with magnitude lower (brighter) than m_v, after merging stars closer than 0.05° into a single equivalent star.

m_v = magnitude in the Johnson's V (visual) band given in the Hipparcos star catalog;

with $a = 5.520546$ and $b = 0.49386$.

If magnitude information is available, it can be used to filter the candidate stars from the star catalog, as shown in Figure 3.1. Let m_{obs} be the observed star magnitude and *tol_mag* the magnitude tolerance used. A simple magnitude filter would accept all stars within magnitude range [m_{obs} – *tol_mag*, m_{obs} + *tol_mag*] and reject all stars outside that range. The blue curve shown in this figure presents the relation between star position in a star catalog (horizontal axis)

versus stellar magnitude (vertical axis), after sorting this star catalog by magnitude (brightest stars first). Detailed explanation of how this catalog was prepared will be given in Section 4.2.

Figure 3.1 – Use of magnitude filtering to reduce number of candidate stars

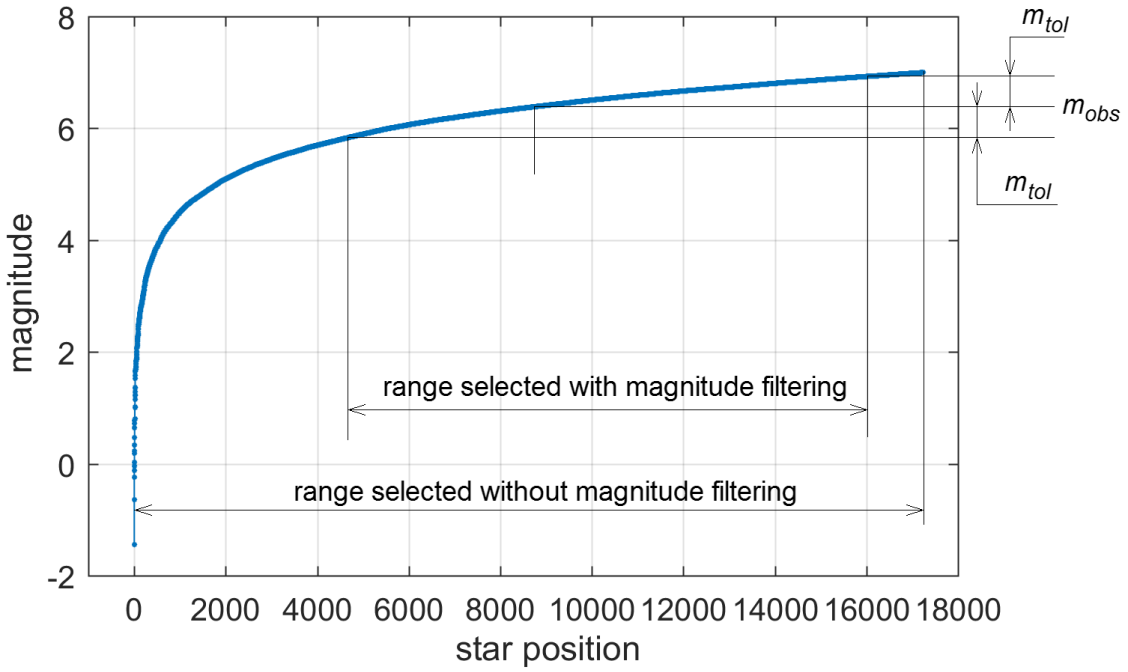

m_{obs} = observed magnitude
m_{obs} = 6.39

m_{tol} = magnitude tolerance
m_{tol} = 0.55

Source: Drawn by the author.

The worst situation where this magnitude filter is least effective happens when $m_{obs} = m_{max} - tol\_mag$, being m_{max} the limiting magnitude in the star catalog. For this scenario, the ratio between the number of stars after filtering ($N_{mf,wc}$) and before (N), is given by:

$$\frac{N_{mf,wc}}{N} = 1 - 10^{-2 \cdot b \cdot tol\_mag} \tag{3.2}$$

Here the wc subscript is used to indicate values in the worst-case situation.

Table 3.1 presents the ratio between stars after magnitude filtering and before. Values shown have been computed for the worst case using Equation (3.2). As

can be seen, the magnitude filter with a magnitude tolerance of ± 2.0 is very ineffective, since almost all the stars are retained, except if the observed star has a low magnitude, i.e., it is a bright star. The filtering becomes more effective when the tolerance is tightened. However, if the tolerance is too tight, the candidate star that really corresponds to the observed star has a higher probability of being filtered out, increasing the failure rate in star identification. Another potential issue with very tight tolerances is the intrinsic variability in brightness of some stars. Therefore, the optimal value to be used for the magnitude tolerance depends on how well the star tracker is able to measure accurately stellar magnitudes and also on the intrinsic variability in the brightness of some stars, being this a subject for future investigations.

Table 3.1 – Ratio between the number of candidate stars after and before filtering by magnitude, versus magnitude tolerance used, computed using Equation (3.2)

magnitude tolerance (*tol_mag*)	fraction of stars retained after filtering	magnitude tolerance (*tol_mag*)	fraction of stars retained after filtering
0.02	≤ 4.5%	0.3	≤ 49.5%
0.05	≤ 10.7%	0.5	≤ 67.9%
0.1	≤ 20.3%	1.0	≤ 89.7%
0.2	≤ 36.5%	2.0	≤ 98.9%

Source: Created by the author.

By reducing the number of candidate stars, magnitude filtering has the potential of decreasing the time spent in star identification. Another benefit is the reduction in the frequency of incorrect matches between observed stars and cataloged stars, reducing the probability that an incorrect attitude will be provided by the star tracker, even though it might increase the probability that no matching cataloged star will be found (identification failure).

3.3 Potential benefits and drawbacks of color information use

In the same way as magnitude information can improve star identification robustness by limiting the number of catalog stars that can match an observed star, so does color information. Besides this obvious advantage, a camera equipped with a color sensitive image sensor has the following advantages over monochrome cameras (FIALHO; MORTARI; PERONDI, 2016):

- for star trackers with refractive optics, color information makes it possible to measure and better compensate chromatic aberration in the optics;
- for refractive optics, there is the possibility to detect optics aging due to ionizing radiation, usually manifested as a reddening in the optics elements;
- additional information available to discriminate observed targets (stars, planets, moons, satellites, debris) when used as a navigation camera;
- possibility to perform multiband photometry in targets of scientific interest.

Despite all these potential advantages, to date, there is little scientific literature on using color information to increase the robustness of stellar identification process. This can be in part explained by the difficulties in obtaining a reliable and compact hardware with good performance for star tracking capable of color discrimination with existing technologies.

The main disadvantage of a color STR versus a monochrome STR is the added system complexity (both in hardware and in software) needed to acquire and correctly interpret color information. Another important aspect is if a color STR will be able to compute centroids with the same accuracy of a traditional monochrome STR. If the centroid accuracy of a color STR is much worse than that of a monochrome STR, the gains obtained by filtering stars with color information are lost by the need of increasing the positional tolerances in the star-ID algorithm and decreased accuracy of the estimated attitude.

Another challenge to algorithms using magnitude and color index for stellar identification is the existence of variable stars, stars whose brightness and color varies in a periodic or irregular fashion. Fortunately, it seems that for most stars the variation in their output and temperature is very small or negligible, as can be inferred from the small size of catalogs of variable stars (SAMUS et al., 2017) in comparison to all-sky surveys containing hundreds of millions or even billions of stars. Nevertheless, a more detailed study in this subject should be performed in the future, so that the impact of variable stars in the star-ID speed and success rate can be assessed, especially for tight tolerances (tighter than ± 0.05 mag.).

3.4 Technologies for color imaging in space

3.4.1 Image sensors with color filter array (CFA)

Most consumer cameras use image sensors with a color filter pattern over the pixel array, each pixel with a different spectral filter deposited over it, in a repeating pattern, as shown in Figure 3.2 (FIALHO; MORTARI; PERONDI, 2016). This technology has also found applications in space, such as the Mars Science Laboratory rover (GHAEMI, 2009), more popularly known as Curiosity rover.

Figure 3.2 – A color filter array scheme commonly used for color discrimination in color image sensors.

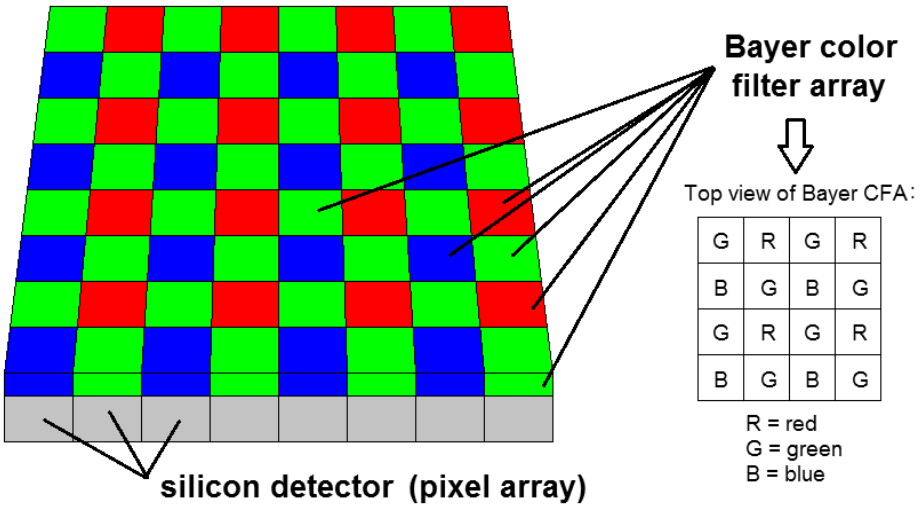

Source: Drawn by the author.

However, this kind of technology has many drawbacks for star trackers:

a) *photon flux reduction*: Each color filter absorbs a significant portion of the incoming light. This presents a problem for star trackers, as a reduction in the photon flux will increase the minimum exposure time required for assuring that a minimum number of stars needed for stellar identification will be detected for any spacecraft attitude, especially in regions with few bright stars, like the galactic poles. This increase in the minimum exposure time causes a decrease in the update rate and in the maximum acceptable angular velocity of the star tracker. As a matter of fact, most star sensor optics have apertures as wide as practical in order to collect as much light as possible. Even so, the minimum exposure time required for star detection (in the order of tens to hundreds of milliseconds) is the bottleneck of many star trackers, as is the case with the star tracker being developed in our group (FIALHO; PERONDI; MORTARI, 2016);

b) *difficulties for centroid computation*: Each pixel of the image having a different spectral response from its neighbors makes it more challenging to compute star centroids accurately. In order to overcome these difficulties, the star spot size must increase, usually by increasing the defocusing, so that more pixels are covered. This has the effect of degrading signal to noise ratio, as there will be more pixels contributing to noise (in comparison to a monochrome image sensor with a smaller star spot size). This leads to a degradation of the centroid accuracy;

c) *color filters may degrade*: color filters deposited over the image sensor may be subject to degradation caused by exposure to ionizing radiation present in space.

3.4.2 Use of dichroic prisms and multiple monochrome image sensors

Another approach for multispectral imaging consists in the use of dichroic prisms or interference mirrors for spectral separation and multiple monochrome image

sensors. This alternative has been explored by McVittie in his PhD thesis (2013) for a three-spectral band star tracker. A sketch of an optical setup based on this concept can be seen in Figure 3.3.

Figure 3.3 – A setup with three monochrome image sensors and a trichroic prism assembly for spectral separation. A detailed explanation of this trichroic prism assembly principle of operation is given in an European patent (VARINTELLIGENT LIMITED, 1999).

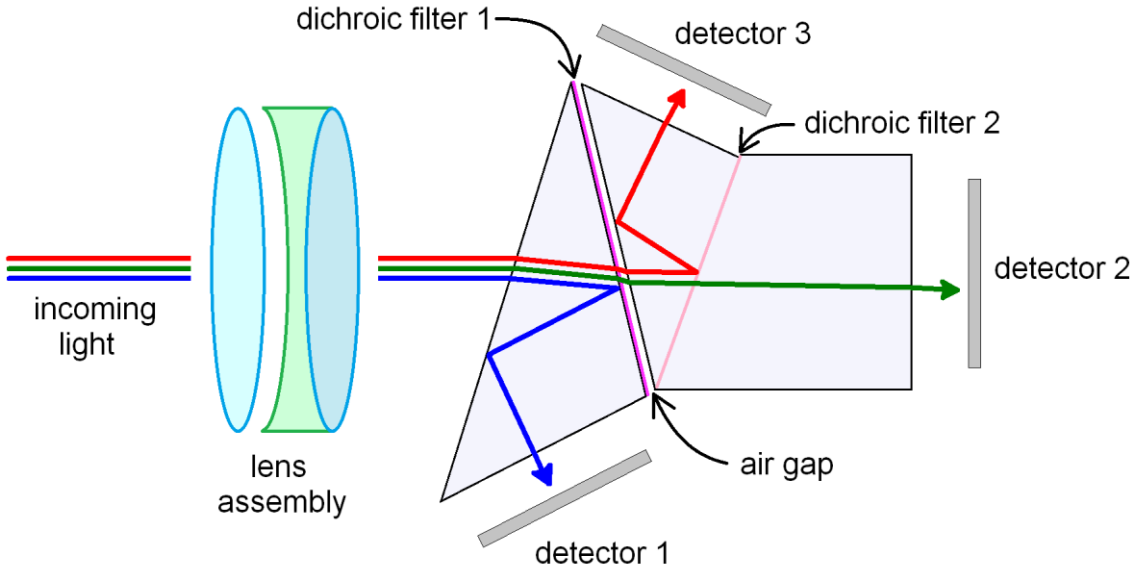

Source: Drawn by the author.

Advantages of this setup include excellent noise performance (if image sensors with low readout noise are used) and low attenuation of incoming optical radiation. However, the need to triplicate the focal plane and associated electronics, plus the issue of precisely aligning the image sensors so that corresponding pixels in different image sensors receive light from the same object, makes this solution less desirable for star trackers.

3.4.3 Use of a filter wheel with a monochrome camera

A commonly used method in space probes for multispectral imaging is to use a filter wheel in front of a monochrome camera (PORCO et al., 2004; ROBINSON; MALARET; WHITE, 2003; SMITH et al., 1997). This approach has the advantage

that custom spectral bands can be designed by redesigning the filter without having to redesign the image sensor. It is much easier to design and manufacture a custom filter than to design an image sensor with custom spectral bands. Unfortunately, this solution has many drawbacks for star trackers, which makes it unfeasible for star trackers and navigation cameras. An example of a filter wheel is shown in Figure 3.4.

Figure 3.4 – Filter wheel of the HST WFC3 camera.

Source: STScI ([2015?]).

Following is a list of the most important issues of using a filter wheel in a STR:

a) only one spectral band can be imaged at a time: this introduces several hurdles in calibration, especially if we consider that the spacecraft can be rotating;
b) spectral filters need to reject a portion of incoming light in order to narrow down the incoming light flux to the prescribed spectral band. This worsens the problem of minimum exposure time required to detect stars (current bottleneck of most star trackers);
c) a filter wheel involves moving mechanical parts. Mechanical parts are one of the greatest reliability concerns in spacecraft.

3.4.4 Remote sensing cameras

Multispectral (few wavelengths) and hyperspectral (up to thousands of wavelengths) cameras for space application, such as remote sensing cameras, do exist, however these cameras are generally not suitable to be used as star trackers. Besides being usually heavy and bulky, most of the traditional remote sensing cameras work more like scanners, projecting part of the scene onto a few detectors (*whiskbroom* configuration) or onto a linear image sensor (*pushbroom* configuration) (WERTZ; LARSON, 1999) that is rapidly read out by the electronics. These whiskbroom and pushbroom cameras depend on the orbital motion of the spacecraft coupled with accurate spacecraft rotation to scan the ground and form an image. A fixed head star tracker, on the contrary, needs to image simultaneously many stars, to avoid distortions introduced by the spacecraft rotation, even when it is rotating slowly. Thus, fixed head STRs typically employ matrix image sensors. In addition to that, there are huge differences in the exposure time required to image scenes on the ground and to image stars. Nevertheless, with current technology, it is not inconceivable to design a space camera that can work as a remote sensing camera, as a horizon sensor, as a navigation camera and as a star tracker, given that there exist matrix image sensors (both CCDs and CMOS) containing millions of pixels with exposure time electronically adjustable in the large range needed for remote sensing (less than a millisecond) and stellar imaging (tens to hundreds of milliseconds). This makes the use of color information more interesting for stellar identification, since color information required by the other functions of this multifunctional camera will be available anyway.

3.5 Image sensors with stacked photodiodes

In a previous work we explored the idea of using an image sensor with stacked pixels for color sensitive star trackers (FIALHO; MORTARI; PERONDI, 2016). Albeit this technology has been available for more than a decade (MERRIL, 2003; GILBLOM et al., 2003) we have not found any research article suggesting the

use of this technology in star sensors preceding our work. In this section, a discussion about this technology is provided. The basic idea behind this technology is to use the image sensor's material as a spectral filter, as can be seen in Figure 3.5.

Figure 3.5 – Example of an image sensor with a) two stacked pixels and with b) three stacked pixels.

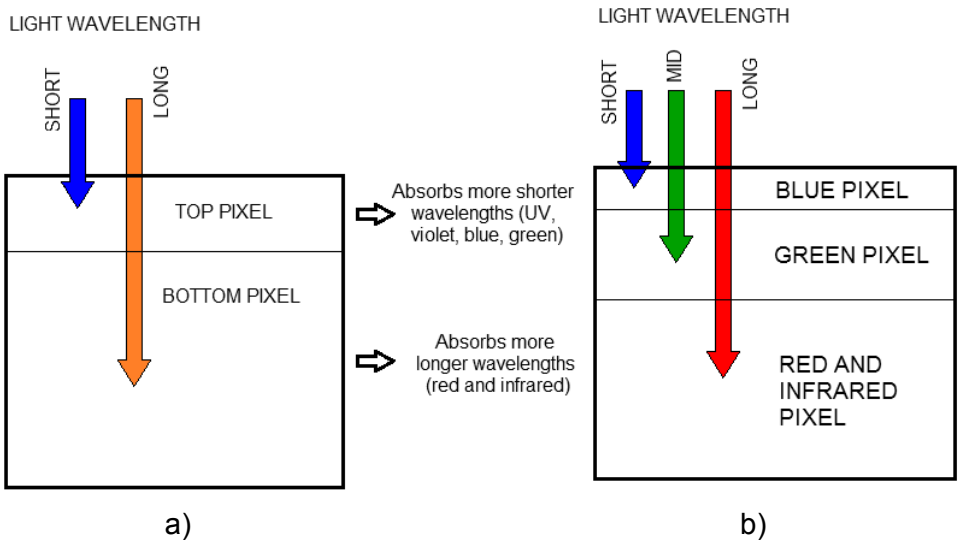

Source: Drawn by the author. Used previously in (FIALHO; MORTARI; PERONDI, 2016).

The main advantage of this approach in comparison to competing technologies is the possibility of getting multispectral data with minimum light attenuation using a compact hardware, while at the same time avoiding centroiding issues that arise when adjacent pixels in the image plane have different spectral responses.

Since microelectronics techniques are more advanced for silicon, it is very likely that the first star tracker or navigation camera employing this idea will have its spectral bands dictated by silicon absorption spectrum and pixel thickness, as can be seen in Figure 3.5. However, this idea could also be used with other materials, if another suitable material is found. Figure 3.6 presents the photon penetration depth in silicon. Note that lower energy photons (longer wavelengths) penetrate deeper into silicon. Figure 3.9 (on page 40) presents the spectral

response for each pixel layer, plus the combined responses, in an image sensor with three stacked pixel layers.

Figure 3.6 – Silicon spectral absorptivity (GREEN, 2008).

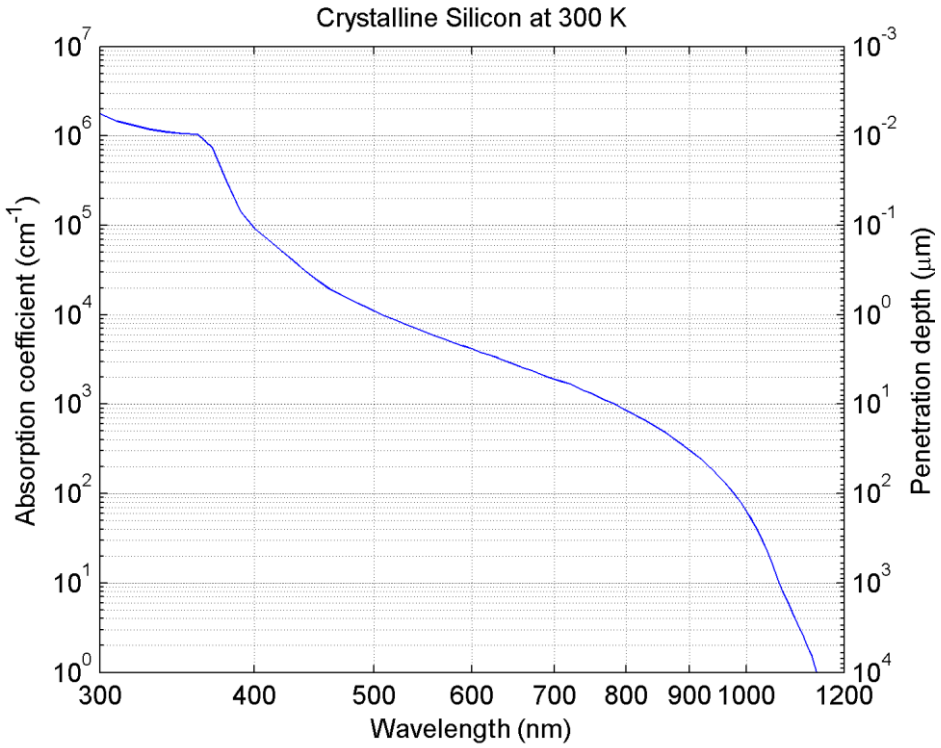

Source: Drawn by the author. Used previously in (FIALHO; MORTARI; PERONDI, 2016).

3.5.1 First generation

The first generation of image sensors employing this technology, commercially known as Foveon X3 technology (MERRIL, 2003; GILBLOM et al., 2003) contains three layers of pixels, providing measurements in three spectral bands. However, it has the drawback that it employs the simpler 3T pixel architecture (HOLST; LOMHEIM, 2011), that does not permit to perform a true CDS (correlated double sampling) to remove pixel kTC reset noise (as briefly explained in Section B.2.1), making it a noisy image sensor in low light conditions. An explanation of the CDS technique can be found in Holst and Lomheim (2011).

3.5.2 Second generation and possible improvements

A possible solution for the low light performance of the first generation of stacked pixel architecture comes from a patent filed by Mansoorian et al. (2015). This patent proposes the use of two (or more) silicon wafers bonded together. This approach enables the use of a pinned photodiode pixel architecture, enabling a significant reduction in sensor noise, possibly bringing low light performance to the same level of conventional monochrome image sensors. An excellent review of the pinned photodiode structure, explaining why it provides better low light performance is given by Fossum and Hondongwa (2014).

Another possible improvement for the stacked pixel concept comes from the incorporation of a distributed Bragg reflector (DBR), as proposed by Angazira and Fossum (2015). This is shown in Figure 3.7. The DBR improves spectral separation between spectral bands, leading to better color discrimination between targets, benefiting stellar identification in star trackers.

Figure 3.7 – A sketch of an image sensor with two layers of stacked pixels (two silicon wafers bonded together) using a DBR stack for improved spectral band separation.

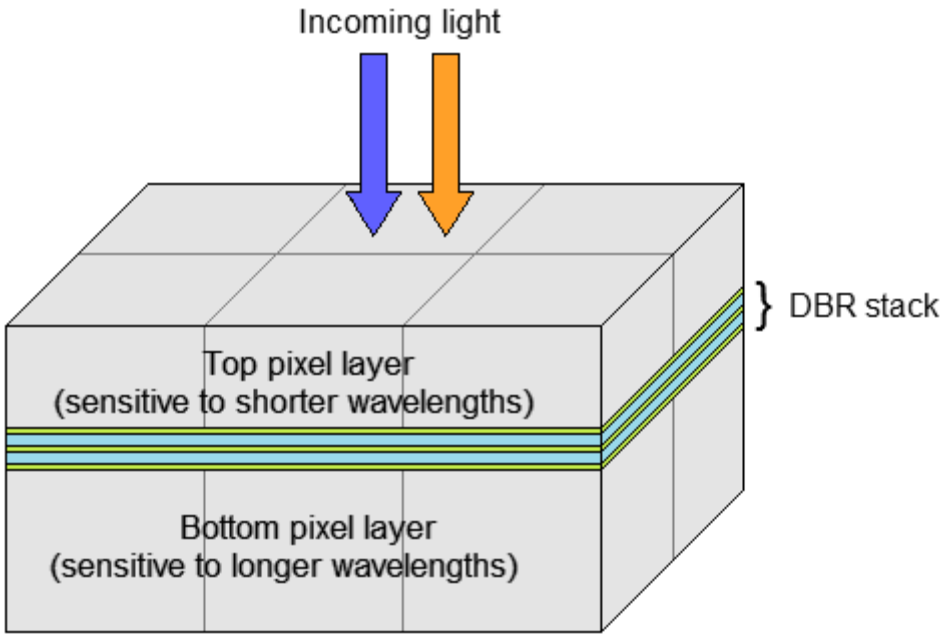

Source: Drawn by the author. Used previously in (FIALHO; MORTARI; PERONDI, 2016).

3.6 Experimental work

3.6.1 Camera selection

Knowing the limitations of the first generation of stacked pixel sensors, and the development of second generation stacked pixel sensors (MANSOORIAN et al., 2015; ANZAGIRA; FOSSUM, 2015), the author of this thesis contacted groups working with this new technology with the purpose of obtaining a prototype camera using a second-generation image sensor with stacked pixels. However, at the time this search was performed, many of these developments were still in a conceptual phase or pre-prototyping stage. Hence, a camera employing a stacked image sensor from the first generation was selected for experimental work instead. The selected camera was a Condor Foveon industrial camera (QUEST INNOVATIONS, [2015?]) employing the F13 image sensor (FOVEON, 2006). This section presents results of preliminary work performed with this camera. Due to delays in the selection and procurement phases, a more extensive experimental work could not be performed. Figure 3.8 presents a photo of the camera used in the experimental work.

Figure 3.8 – The Condor Foveon camera used in the experimental work.

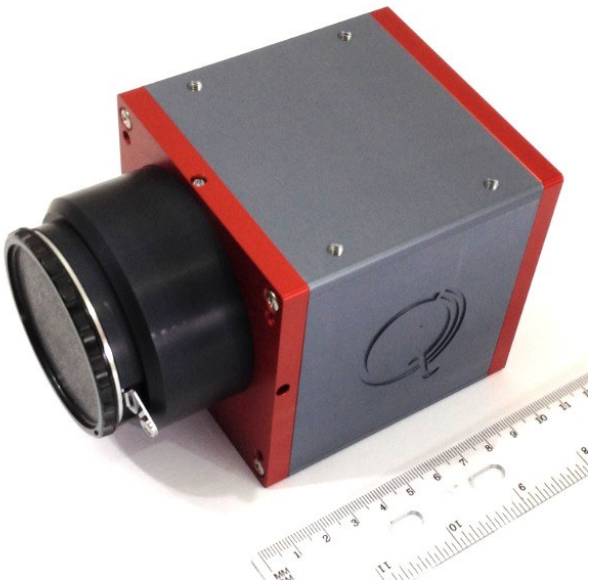

Source: Photo taken by the author.

3.6.2 Night sky tests

Using the Foveon camera, some images were captured during a night test, and a preliminary data analysis was performed with these images. Table 3.2 presents the specifications of the system and some of the settings used in the test.

Table 3.2 – Technical details of the setup used in the night tests

Parameter / Feature	Value / Description
Camera	Quest C1-RGB-FV-CL
Image sensor	Foveon X3 F13
Imager resolution	2652 x 1768 x 3
Pixel size	7.8µm x 7.8µm
Optics used	Nikkon 35mm f/1.4
exposure time selected	400 ms
Bit depth setting used	12 bits per pixel per each RGB channel

Source: Created by the author.

From the hundreds of images acquired during that night, eight images of the constellation Cygnus were selected for analysis. These images were captured using an exposure time (integration time) of 400 ms and the optics set at its widest opening (f# = 1.4). The focus used was the best that could be found visually.

A series of about 200 dark frames was acquired on the same night using the same exposure time (400 ms) of the light images. The average of these dark frames was subtracted from the light images in order to remove fixed pattern noise and dark current (components b_{ij} and c_{ij} of Equation (B.12) in the appendices).

The observing conditions were not the best during that night. Occasionally some clouds would cross the sky. Also, there was significant light pollution on the site where the tests were performed. From the location used for these tests, there was no clear view of the zenith, hence images were taken from a part of the sky

at an elevation of about 30° from the horizon, leading to a path length through the atmosphere roughly twice the one would be obtained if the camera was pointed to the zenith. A longer path length in the atmosphere (larger air mass in astronomical parlance) results in more distortion and attenuation in starlight. These images were captured in College Station, TX, on December 25, 2016.

3.6.3 Star extraction and centroiding

Star extraction was performed with a simple algorithm, designed initially for a monochrome star tracker with limited memory and CPU power (FIALHO; PERONDI; MORTARI, 2016). Images taken by the Foveon camera are multispectral, consisting of three image planes, each at a different spectral band. Since the algorithm used in this preliminary test cannot handle multispectral images, the image planes at each spectral band were processed separately.

This algorithm starts by removing column bias, using a method which will be better described in Section 6.2. Once column bias has been removed, the algorithm removes row bias on the resulting image using the same method. After that, the algorithm samples 32×34 = 1088 pixels distributed in a rectangular grid with uniform spacing, covering the whole image. The sampled pixels are stored in a list. From this list, the 64 brightest pixels are removed. This step is performed to remove occasional hot pixels or illuminated pixels from the sample. The resulting 1024 pixels are then used to estimate the average level (μ_{bkg}) and standard deviation (σ_{bkg}) of the image background, used to compute the threshold that will be used for detecting stars. In our tests, the threshold was set at $\mu_{bkg} + 5\sigma_{bkg}$.

After image pre-processing, the next step is to extract stars from the image. This is done by searching for clusters of contiguous pixels having pixel values above the threshold. Following is a description of the method used[1].

[1] According to the nomenclature used in the field of image processing, the method used is an image segmentation algorithm (RANGAYYAN, 2004, Section 5.4, p. 393).

The search starts at the top left corner of the image and progresses in raster scan mode until a pixel above the threshold (a lit pixel) is found. Once a lit pixel is found, the algorithm scans all contiguous lit pixels that are adjacent both vertically, horizontally and diagonally, while at the same time computing centroiding moments and marking the pixel as used. Once all pixels in the cluster are found, a check on the number of pixels is performed. If the cluster pass this test, its centroid is computed using a simple center of mass algorithm, and saved to the list of detected stars (Figure 2.1). After processing a cluster, the algorithm resumes its raster scan operation from where it was interrupted, skipping all pixels marked as used, until finding another lit pixel, which will necessarily belong to another cluster. To avoid the inclusion of hot pixels as detected stars, a cluster is considered valid only if it has at least 3 contiguous lit pixels. To avoid extended bodies being considered as stars, if a cluster has more than 200 pixels it is rejected.

To compute the centroid, using the simple center of mass algorithm, the following moments are computed while pixels belonging to a cluster are scanned:

$$B = \sum_{i=1}^{n} b_i - b_R \tag{3.3}$$

$$S_x = \sum_{i=1}^{n} x_i \cdot (b_i - b_R) \tag{3.4}$$

$$S_y = \sum_{i=1}^{n} y_i \cdot (b_i - b_R) \tag{3.5}$$

where B is the cluster brightness, b_i is the value of the *i*-th pixel in the cluster, n is the number of pixels in the cluster, b_R is the average background level of the image, (x_i, y_i) are the coordinates of the center of pixel *i* and S_x and S_y are the first order moments along a row and a column, respectively. From the cluster brightness and first order moments, the pixel centroid (x_c, y_c) is computed using the following equations:

$$x_c = S_x/B \tag{3.6}$$

$$y_c = S_y/B \tag{3.7}$$

These equations assume that the imager response is linear. If the image sensor response departs significantly from linearity, then the pixel value b_i used in these equations must be corrected.

3.6.4 Centroiding noise

Table 3.3 gives the differences in centroid positions for seven selected stars, computed from the eight images analyzed.

Table 3.3 – Night sky test results – centroiding noise

star*		number of pixels in the cluster						differences in centroid column coordinates in pixel units					
name	m_V	blue		green		red		$x_{c,b} - x_{c,g}$		$x_{c,b} - x_{c,r}$		$x_{c,g} - x_{c,r}$	
		$\overline{n}$	s_n	$\overline{n}$	s_n	$\overline{n}$	s_n	$\overline{\delta x_c}$	$s_{\delta x_c}$	$\overline{\delta x_c}$	$s_{\delta x_c}$	$\overline{\delta x_c}$	$s_{\delta x_c}$
Deneb	1.25	81.8	11.6	92.1	13.3	105.5	9.2	0.01	0.03	-0.07	0.05	-0.08	0.05
Sadr	2.23	34.9	6.2	52.4	7.4	71.8	9.9	0.03	0.07	0.15	0.07	0.12	0.06
ε Cyg	2.48	35.4	5.3	44.0	3.0	54.0	4.8	0.07	0.07	0.24	0.05	0.18	0.05
δ Cyg	2.87	20.4	4.2	23.2	3.9	28.0	3.0	-0.01	0.09	0.04	0.13	0.06	0.15
ν Cyg	3.94	11.8	2.1	13.0	2.8	10.5	1.4	0.02	0.11	0.17	0.21	0.15	0.18
32 Cyg	3.98	8.6	1.1	15.5	3.1	25.5	5.1	-0.14	0.22	-0.26	0.18	-0.12	0.17
54 Cyg	4.54	6.1	1.1	7.4	2.6	5.3	1.3	-0.04	0.16	0.30	0.28	0.34	0.27

* Sources: First two columns: data from the SIMBAD Astronomical Database (WENGER *et al.*, 2000)[2], remaining columns: data obtained by the author from images.

The first column gives the star name and their apparent magnitudes in the Johnson's V band. The second set of columns gives the average (indicated by $\overline{n}$) and sample standard deviation (indicated by s_n) of the number of pixels in the clusters from where the stars were extracted, for each spectral band. The third

[2] http://simbad.u-strasbg.fr/simbad/

set of columns gives centroid coordinates differences along the x direction between different bands, being $x_{c,b}$ the centroid coordinate in the blue band, $x_{c,g}$ the centroid coordinate computed in the green band and $x_{c,r}$ the centroid coordinate computed in the red band. $\overline{\delta x_c}$ is the mean and $s_{\delta x_c}$ is the sample standard deviation of the centroid coordinate differences for the same star computed using two different spectral bands. For conciseness, only centroiding differences along the *x* coordinate are shown in the table.

From these measurements, perhaps the most interesting are the $s_{\delta x_c}$ which give an idea of the noise equivalent angle (NEA) of the Foveon camera. It should be noted that $s_{\delta x_c}$ also depends on the centroiding and image segmentation algorithms used.

3.6.5 Measured magnitudes and color indexes

From the raw cluster brightness, computed from Equation (3.3), the magnitudes of clusters of pixels (hereafter, detected stars) were computed using the following equation:

$$m_{obs} = -2.5 * \log_{10}(B/B_{ref}) \tag{3.8}$$

where B_{ref} is the reference brightness that define the zero point of the magnitude scale. Since the Foveon camera provides data in three spectral bands, three different magnitude scales can be defined, each for each spectral band. The reference brightness that define the zero points of the measured magnitude scales were set to 179,013 digital units for the blue channel, 202,580 digital units for the green channel and 166,114 digital units for the red channel, after scaling the images to 16 bits per pixel per channel, during preprocessing. These values were chosen so that the measured magnitudes of Vega, if it were observed by the camera, would be close to the adopted conventional value of 0.03 for Vega in all bands, making comparisons easier with standard photometric systems used in Astronomy, as will be explained later in Section 3.6.6. A “digital unit” is a

quantization step in the preprocessed images. Since during preprocessing the pixel values were scaled by a factor of 16 (to 16 bits per pixel per channel), each "digital unit" in the preprocessed image corresponds to 1/16 digitization units of the original 12 bits per pixel per channel image.

The differences between magnitudes of the same object taken at different spectral bands is termed *color index* (plural: *color indexes* or *color indices*). For each one of the eight images analyzed, the magnitudes in each band and the associated color indexes were computed for seven selected stars. Table 3.4 presents the results.

Table 3.4 – Night sky test results – photometric measurements

star	standard magnitudes*			measured instrumental magnitudes			uncertainties in measured magnitudes			uncertainties in measured color indexes		
	B	*V*	*I*	*b*	*g*	*r*	σ_b	σ_g	σ_r	σ_{b-r}	σ_{b-g}	σ_{g-r}
Deneb	1.34	1.25	1.04	1.25	1.25	1.12	0.12	0.11	0.10	0.08	0.05	0.04
Sadr	2.90	2.23	1.40	2.50	2.25	1.96	0.13	0.14	0.15	0.07	0.04	0.06
ε Cyg	3.52	2.48	1.19	2.76	2.48	2.12	0.15	0.12	0.12	0.07	0.06	0.04
δ Cyg	2.85	2.87	2.90	3.47	3.49	3.49	0.10	0.08	0.10	0.11	0.10	0.08
ν Cyg	3.96	3.94	3.89	4.50	4.52	4.70	0.17	0.18	0.17	0.12	0.13	0.16
32 Cyg	5.50	3.98	1.86	4.91	4.36	3.86	0.12	0.16	0.21	0.23	0.17	0.08
54 Cyg	4.43	4.54	4.69	5.43	5.43	5.74	0.20	0.27	0.27	0.17	0.23	0.18

* Sources: First four columns: data from the SIMBAD Astronomical Database (WENGER et al., 2000), remaining columns: data obtained by the author from images.

For comparison, this table also presents the magnitudes of these stars in the standard Johnson-Cousins photometric system on the first set of columns, showing magnitudes in the *B* (blue), *V* (visual) and *I* (near infrared) standard bands. The second set of columns present the average of the measured magnitudes in the natural photometric system of the camera, with *b* indicating

magnitudes obtained from the blue channel[3], *g* magnitudes from the green channel and *r* magnitudes from the red channel. The third set of columns presents an estimate of the standard deviation of the magnitude measurements. The last set of columns presents an estimate of the standard deviation of the color index measurements.

To enable a comparison of the results obtained in the natural photometric system of the camera with a standard photometric system, it must be characterized. This is done in the next section.

3.6.6 A photometric system for the Foveon camera

To make comparisons easier with the UBVRI standard photometric system, we have decided to set the zero point of the red, green and blue magnitude scales of the Foveon camera such that the synthetic magnitudes of Vega (alpha Lyr.) are also 0.03 in these scales (0.03 is the magnitude of Vega in the V passband as reported by the Hipparcos catalog), thus making the non-standard photometric system we are creating for the Foveon camera also a VEGAMAG-type system (BESSELL; MURPHY, 2012, Section 7). To compute synthetic magnitudes of a star in this photometric system from its spectrum, the procedure described in Section C.3 of the appendixes can be followed. The photometric system defined here is also called a natural (or instrumental) photometric system for the Foveon camera, since magnitude measurements performed by this camera will be in that system, unless a transformation is applied to these magnitudes to transform them to another photometric system.

To obtain the camera response in the red, green and blue channels, we need to consider both the detector response and optics transmission. Figure 3.9 presents the quantum efficiencies in each band, plus the combined quantum efficiency of the image sensor of the Foveon camera.

[3] Our *b* magnitudes should not be confused with the *b* magnitudes of the Strömgren *uvby* system, which are defined with a much narrower spectral band.

Unfortunately, the transmission spectrum of the optics used in the test was unknown to the author and data provided for the image sensor used in the camera spanned only the 400nm-1000nm range. Not having the means to measure the transmittance of the optics in the range 350nm-1000nm and image sensor response in the near UV in time, the author of this thesis considered a flat transmission of the optics in the 400nm-1000nm range and no transmission outside this range. The spectral response and computed color indexes for black-bodies will not be exactly equal to those of the true photometric system of the camera used in the tests, but will be close enough for a preliminary analysis. In a series of computer simulations performed by the author, considering the transmission spectra of similar lenses to that used in the test (NAGASAWA et al., 2016) and assuming a set of probable values of image sensor response in the near-UV (obtained by extrapolation), he found that the computed color indexes for black-bodies would typically stay within 20% of the values derived here.

Figure 3.9 – Quantum efficiency of the Foveon X3 F13 image sensor.

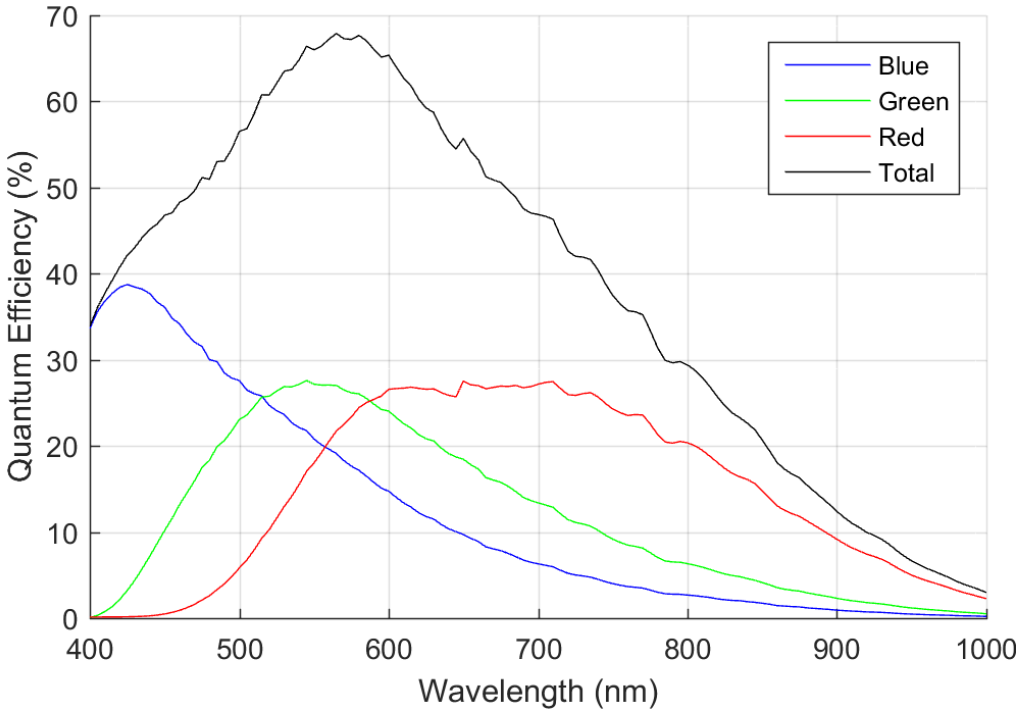

Source: Drawn by the author using data provided by Gilblom (2017, personal communication).

Multiplying the quantum efficiencies by the assumed optics transmission (flat in the 400nm-1000nm range and none outside this range) and by the wavelength (to convert from photon units to responsivity in energy units), somewhat rough approximations to the response functions of the Foveon camera were found and have been adopted in this work. These are plotted in Figure 3.10 as solid lines, together with the response functions of the standard *B*, *V* and *I* bands of the Johnson-Cousins system (BESSELL; MURPHY, 2012) plotted as dashed lines.

Figure 3.10 – Energy response functions adopted in this work

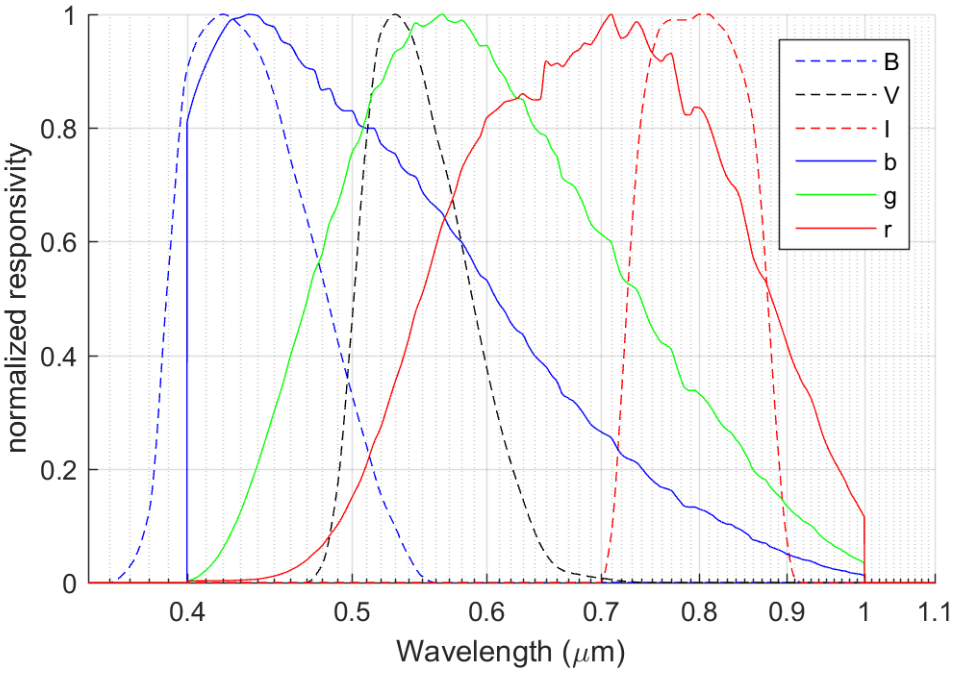

Source: Drawn by the author.

The author of this thesis could have adopted, instead, response functions that extends into the near UV (wavelengths shorter than 400 nm) and deeper in the IR (for wavelengths longer than 1000 nm) following a smooth extrapolation curve. This would give curves closer to reality. However not having enough data to accurately predict how the detector response functions would extend into the near UV and considering that there might be significant differences in the transmission curve even among similar optics, it was considered to be safer to adopt an optics transmission that is zero outside the 400nm-1000nm range and flat within this

range. At least this makes it very evident the limitations in the data used to derive the adopted response functions, since no real optical system presents abrupt, stepwise changes in their spectral response functions as the ones we have adopted. The unphysical assumption that there is no response for wavelengths shorter than 400 nm should affect mostly computations in the blue band for bluer (hotter) stars. The assumption of no response for wavelengths longer than 1000 nm is not so severe, as the response in all three bands is already very low at 1000 nm. The assumption of no response for wavelengths longer than 1000 nm also partially compensates the small drop in the infrared transmittance which was observed by Nagawasa et al. (2016) for some similar optics.

Using a procedure that will be described in more detail in Section 7.2.5, the relations between black-body temperatures with magnitudes and color indexes were found, as shown in Figure 3.11. In this figure, the horizontal axis gives the multiplicative inverse of the temperature, considering black-body temperatures in the range of 250,000 K (left edge of the plots) to 3000 K (right edges).

From Figure 3.11.a we can see that for black-bodies, the *b* magnitudes in the Foveon camera system are similar to the Johnson's *V* magnitude, while the *g* and *r* magnitudes are intermediate between the *V* and *I* standard magnitudes. The magnitudes given are the apparent magnitudes of black-bodies for a hypothetical observer situated on its surface. Figure 3.11.b gives the relation between reciprocal of temperature and the color indexes. The higher the slope of these curves, the more sensitive is the color index to changes in the temperature (or more accurately, the reciprocal of the temperature) of the black-body. This can be seen better in Figure 3.12 which gives the derivative of the color indexes with the reciprocal of the temperature.

Figure 3.11 – Magnitudes and color indexes for black-bodies versus reciprocal of the temperature

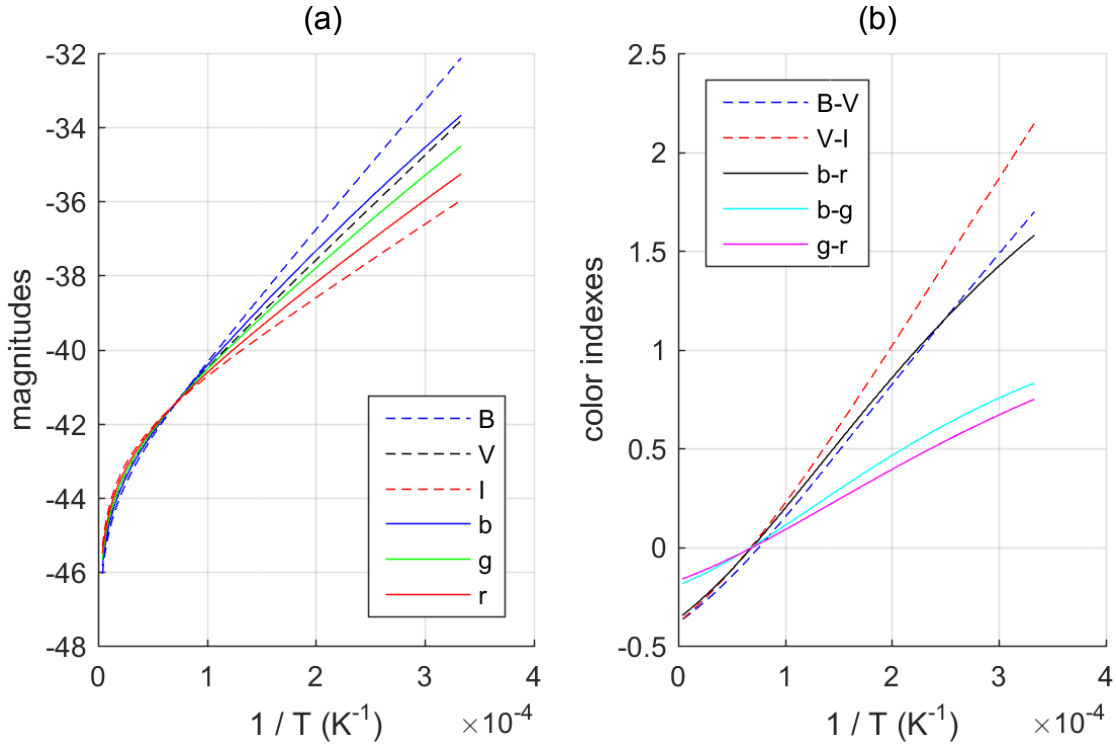

Source: Drawn by the author.

A color index that varies little with temperature or other relevant physical characteristic of stars is not very useful for stellar identification, unless measurements in that color index can be made with a very low uncertainty. Assuming that stars can be approximated as black-bodies, from Figure 3.12 we can see that the best color index for identifying different stars among those studied would probably be the *V*−*I* color index. In the photometric system of the Foveon camera, the best color index for stellar identification seems to be the *b*-*r* color index, which has about the same discrimination power of the standard *B*−*V* color index, except for cooler stars with temperature lower than 5000 K ($1/T > 2 \cdot 10^{-4}$ K^{-1}), where it is lower. Overall, for making comparisons between these two color indexes possible, we could say that the discrimination power of the *b*-*r* color index is roughly 0.9 times the discrimination power of the *B*−*V* color index.

Figure 3.12 – Variation of color indexes for black-bodies with the reciprocal of the temperature

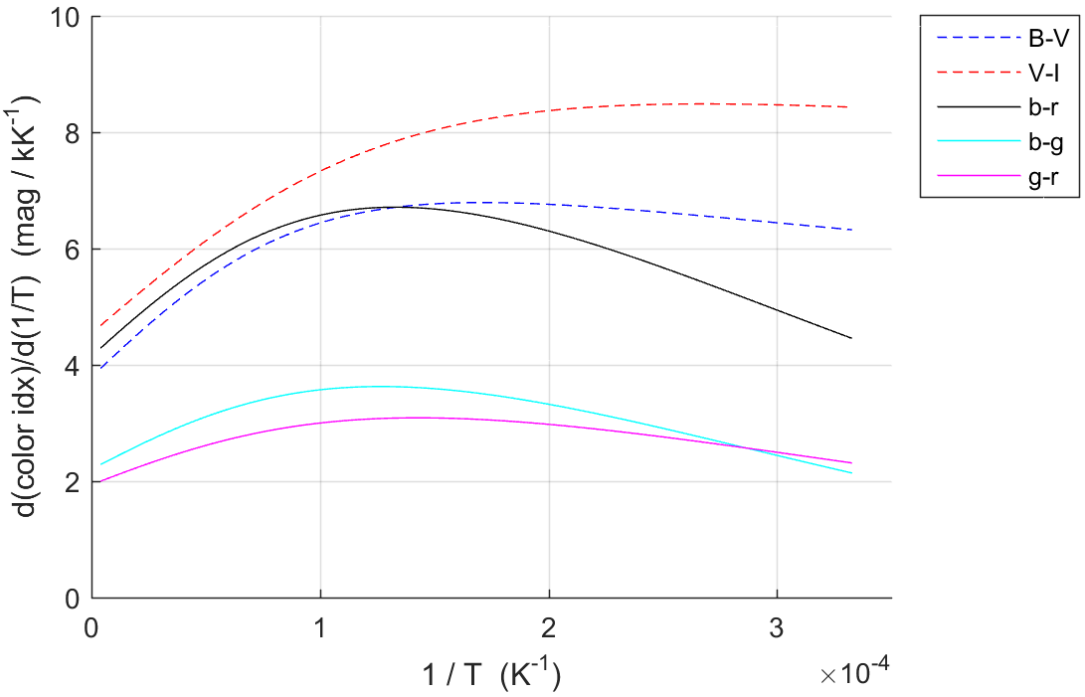

Source: Drawn by the author.

If we approximate stellar spectra with the spectra of black-bodies, only one color index is needed, since from one color index, the temperature of the black-body and any other color index can be obtained, as will be explained in Chapter 7. Table 3.4 shows that the measurement error in the *b-g* and *g-r* color indexes tend to be smaller than the measurement error in the *b-r* color index. However, analyzing this data together with Figure 3.12 it can be seen that the *b-r* color index would be still a better choice for stellar identification than the *b-g* and *g-r* color indexes. The reason is that the *b-r* color index is twice as much sensitive for temperature variations among black-bodies than the *b-g* and *g-r* color indexes. For the *b-g* and *g-r* color indexes to outperform the *b-r* color index, their measurement uncertainties should be less than half the measurement uncertainty of the *b-r* color index.

It is true that the spectra of stars are not exactly equal to black-bodies spectra, as exemplified in Section 7.3.2. However, the spectra of many stars can be

approximated by the spectra of black-bodies to a good precision (HOLLOW, 2006), making the black-body model suitable for a preliminary analysis.

3.6.7 Discussion

The dataset of eight images used in this preliminary analysis is too small to draw solid conclusions. Nevertheless, some trends can be observed. Referring to Table 3.3 and Table 3.4, we can see that the centroiding noise and uncertainties in the measured magnitudes and measured color indexes are lower for bright stars (e.g., Deneb with V magnitude of 1.25 (m_v = 1.25)) and higher for dim stars (e.g., 54 Cyg with m_v = 4.54), as would be expected, considering that dimmer stars have a lower signal to noise ratio.

From Table 3.4, we can see that the measurement uncertainty in the *b-r* color index is roughly 0.07 magnitudes for the brightest stars (at m_v = 1.2 to 2.5) and 0.17 for the dimmest star analyzed (at m_v = 4.5). Assuming that the *b-r* color index discrimination power is roughly 0.9 times that of the *B−V* color index, these measurement uncertainties are equivalent to 0.08 and 0.19 magnitudes in the *B−V* color index, respectively. Ignoring differences in exposure time and optics aperture, the measured uncertainties in the *b-g* and *g-r* color indexes, for stars of similar magnitudes, are comparable[4] to those obtained by McVittie (2013) for the Colour Filter Array STR, despite the unfavorable observing conditions of our test. This is certainly an encouraging result. However, to perform a fair comparison, we should have taken into consideration the exposure time used, the optics aperture and the precise spectral response of the system he used in his tests.

---

[4] comparable within a multiplicative error factor of 2 or 3.
Color ratios (Λ_{ab}) can be converted to color indices ($a - b$) via the equation: $a - b = -2.5 \log_{10}(\Lambda_{ab})$. From this equation, the following relation can be found between standard deviations, when they are sufficiently small: $\sigma_{a-b} = \frac{2.5}{\ln(10)} \cdot \frac{\sigma_{\Lambda_{ab}}}{\mathrm{E}\{\Lambda_{ab}\}}$, with $\mathrm{E}\{\Lambda_{ab}\}$ representing the expected value of Λ_{ab}, a and b representing two different spectral bands.
The *r*, *g* and *b* bands in McVittie's work are certainly not identical to ours, but we are ignoring these differences in this rough comparison.

Regarding magnitude errors, the standard deviation of magnitude measurements was higher than expected, particularly for bright stars. From the definition of color indexes as the difference between two magnitudes, we would expect that the rms errors in color indexes would be roughly $\sqrt{2}$ times larger than the rms error in magnitudes. A possible explanation for this unexpected high standard deviation of magnitude errors lies in the probable presence of cirrus clouds and contrails during the night sky test and the apparent positions of stars from the viewpoint of the camera moving to regions of different cloud density as the Earth rotated during measurements. Clouds attenuate star light, but, since they affect all wavelengths in the optical regime equally, they do not affect color.

From the curves shown in Figure 3.11.a, it is possible to establish relations linking the standard *BVI* magnitudes to the custom *bgr* magnitudes we have developed for the Foveon camera. These relations are valid for stars which do not depart too much from the spectra of black-bodies. Using these relations, it is possible to estimate the *b*, *g* and *r* magnitudes from the cataloged *B*, *V* and *I* magnitudes for the seven stars shown in Table 3.4. Comparing these estimated magnitudes with the measured magnitudes shown in that table, a significant bias (of roughly one magnitude) is observed for the dimmest stars (32 Cyg and 54 Cyg), whereas a much smaller bias is observed for the brightest stars (Deneb and Sadr). The explanation for this bias lies in how the image segmentation algorithm described in Section 3.6.3 works and on the poor focusing that could be achieved manually. For the brightest stars, most pixels illuminated by the star will be above the segmentation threshold, so a large fraction (~ 70%) of their luminous signal will be summed when computing the cluster brightness (Equation (3.3)), whereas for dim stars, only the most illuminated central pixels will be above the segmentation threshold, so only a small fraction (~ 30%) of their luminous signal will be summed. This points to the need of using better algorithms for computing the observed magnitudes, or calibrating the bias introduced by this algorithm.

To summarize, we could say that this preliminary test had many limitations: the observation conditions were not the best; there were some issues with focus

adjustment, there were problems with the method used to compute magnitudes and the dataset gathered was too small. To overcome these limitations, additional night sky tests will be needed. Ideally, hundreds or thousands of images should be analyzed for each setting used in the camera (exposure time and optics aperture used) to get statistically sound results. For the future, we plan to perform additional night sky tests with better observing conditions (camera pointing to the zenith, in a clear night with no clouds, and in a site with less light pollution), and use better algorithms for centroiding and magnitude estimation.

3.7 Concluding remarks

Despite all the limitations in the experimental work performed, preliminary results were encouraging. We believe that significantly better results will be obtained in future experimental works. This means that the technology of stacked pixels for color star tracker is very promising and should be investigated more deeply in the future.

An interesting subject for future research would be to investigate how image sensors with stacked pixels would behave in space environments. The main concern being the effects of ionizing radiation on the image sensor.

4 SIMULATION ENVIRONMENT

The simulation environment used in this thesis is an improved version of the simulation environment, named PTASE, used in previous works by the author (FIALHO, 2003, 2007). This simulation environment has been used in the Monte Carlo simulations that will be described in Chapter 5, Section 5.4.

4.1 Simulation model for Monte Carlo simulations

Figure 4.1 illustrates how star ID algorithms are tested in PTASE.

Figure 4.1 – Flowchart for testing star-ID algorithms under PTASE.

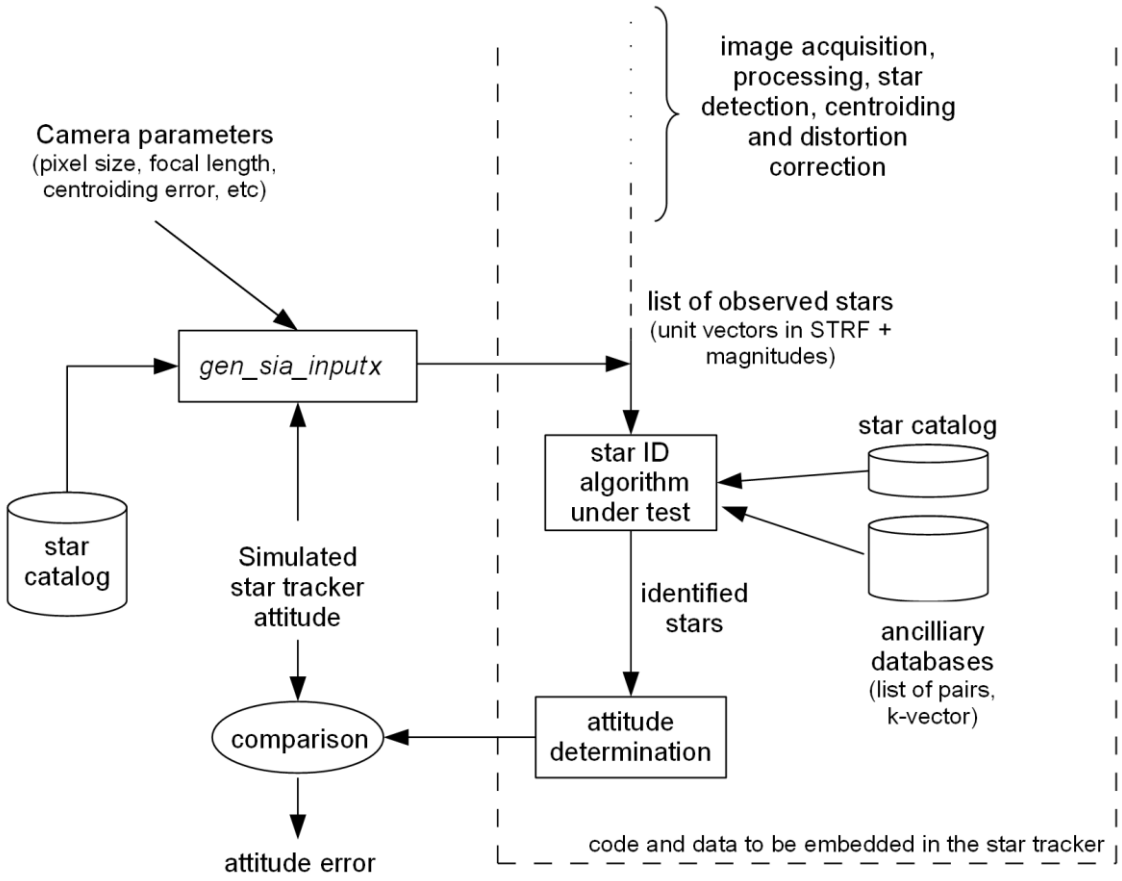

Source: Adapted from (FIALHO, 2007, page 122)

Observe that the output normally fed by a centroiding processing algorithm (see Figure 2.1) is replaced by an algorithm (*gen_sia_inputx*) that simulates the list of

observed stars from a star catalog, after corrupting observed star unit vectors and observed magnitudes with a random noise.

The catalog used by the simulated star tracker (inside the dashed box) can be derived from the main catalog loaded in the program (to the left) or from a second catalog loaded in the program for the purposes of star identification. When the catalog used for the simulated star tracker is derived from the main catalog loaded in the program, it contains all stars in that catalog up to a limiting magnitude configured by the user.

4.2 Catalog preparation

The star catalogs used in the simulations have been prepared from the Hipparcos Catalog (ESA, 1997) with the programs READCAT and PROC_CAT, as described in the author's master thesis (FIALHO; 2007), and shown in Figure 4.2. A detailed description of the processing steps is given in the following sections.

Figure 4.2 – Catalog generation for simulations in PTASE.

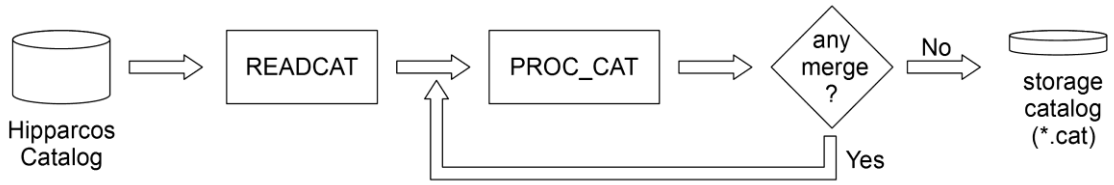

Source: Drawn by the author for this work.

The star catalogs prepared by READCAT and PROC_CAT are generated in a very compact format that is most suitable for storage in systems with limited non-volatile storage, like the Brazilian star tracker (FIALHO; PERONDI; MORTARI, 2016). When the catalog is loaded by PTASE, it is converted to another format, suitable for storage in the working memory (usually a RAM memory). This format uses twice as much memory, but is typically 10 to 100 times faster to use. This conversion has also to be performed by the star tracker, but since it is performed very occasionally (only in initialization, or to update corrections for stellar

aberration), it has little impact in its performance. Section 4.2.3 describes in more detail this conversion and the format used in these catalogs.

4.2.1 Processing by READCAT

The program READCAT takes as input the Hipparcos star catalog and user defined parameters passed to the program, generating a star catalog in a very compact format that is suitable to be used in the constrained environment of a star tracker (low memory and limited processing power).

The user can specify a maximum magnitude during processing. All stars in the catalog with visual magnitude in the Johnson-Morgan UBV photometric system (JOHNSON; MORGAN, 1953) greater than the specified magnitude (stars dimmer than the specified magnitude) are ignored.

The program also reads the *B*−*V* and *V*−*I* color indices in the Hipparcos catalog, retaining them in the color version of the star catalog. For the monochrome star catalog, these color indices can be used to compute estimates of the instrumental magnitudes of stars (magnitudes in the instrument spectral band), according to this expression:

$$m_i = m_v + k_{bv}(B - V) + k_{vi}(V - I) \tag{4.1}$$

where:

m_i = instrumental magnitude, written to the target catalog;

m_v= visual magnitude in the Johnson-Morgan UBV photometric system, read from field H5 in the Hipparcos Catalog;

$(B - V)$ = blue minus visual color index in the Johnson UBV system, read from field H37 in the Hipparcos Catalog;

$(V - I)$ = Visual minus near infrared color index in the Cousins UBVRI photometric system (itself an extension to the Johnson UBV system), read from field H40 in the Hipparcos Catalog;

k_{bv}, k_{vi} = multiplication factors.

Since the exact spectral response of a star tracker changes from one design to the other, leading to different k_{bv}, k_{vi} factors for each star tracker model, for simplicity we have considered these factors to be zero, effectively taking the cataloged visual magnitudes as instrumental magnitudes for the simulations. In other words, we have assumed that the simulated star tracker spectral response matches the *V* spectral band.

For generating a star catalog for a colored star tracker like the Foveon camera discussed in Section 3.6, it would probably be better to store the instrumental magnitudes (for the Foveon camera, these are m_b, m_g and m_r) or the color indexes in the natural photometric system of the camera (e.g.: $m_b - m_r$ and $m_g - m_r$) instead of storing the standard $B - V$ and $V - I$ color indices, thus saving the STR the work of converting observed magnitudes and color indexes to the *UBVRI* standard system. The ability to compute these color indices in the photometric system of the instrument is planned for future releases of the program.

The program also has some options for controlling the handling of star entries flagged as binary/multiple in the Hipparcos Catalog. The user may use these options to include or exclude these entries from the destination catalog.

Another useful feature of the program is the possibility to propagate star positions from the mean epoch used in the Hipparcos Catalog (J1991.25 ≈ April 2nd, 1991) to the mission epoch, e.g. J2020.0 (January 1st, 2020)[5], by using the stellar proper motions given in the source catalog. It should be noticed, however, that READCAT does not perform any transformation of coordinates between different reference frames, nor any corrections due to Earth's nutation and precession movements which are not needed for the reference frame used in Hipparcos. The reference frame used in READCAT is the same used in the Hipparcos Catalog, which is completely decoupled from the complex orbital and rotational motions

[5] Dates converted from Julian epoch to Gregorian Calendar using the IAU SOFA (Standards of Fundamental Astronomy) library (IAU, 2017). Julian epoch is a method of specifying the date/time (JULIAN EPOCH, 2012).

performed by Earth, as described in Section 2.5.1 and in Section A.2 in the appendices.

When generating the mission star catalog, it is better that the merging step be performed with all stars in the Hipparcos star catalog, and only when the merging process has been completed the mission catalog should be trimmed to the desired limiting magnitude. The reason for this recommendation is that very dim stars that would normally be trimmed from the mission catalog can influence the position of the photometric center of an observed brighter star if it is close enough to that brighter star to be merged with it.

4.2.2 Processing by PROC_CAT

The program PROC_CAT reads star catalogs generated by READCAT and outputs a star catalog in the same file format as those generated by READCAT. It's main task is to merge stars that are very close to each other to the point of not being distinguishable by the star tracker as different stars – stars closer than the resolving power of the star sensor. Another task performed by PROC_CAT is to sort stars by magnitude. Many algorithms implemented in PTASE require that the star catalog to be sorted by increasing magnitude (decreasing brightness) order.

In the star catalogs used in PTASE, the merge radius used in PROC_CAT was set to 0.05° = 3'. This is the typical resolving power of a wide field of view star tracker, such as the one being developed at INPE (FIALHO; PERONDI; MORTARI, 2016).

Two or more stars within a merge radius of r are merged into a single photometrically equivalent star. The position of this photometrically equivalent star is computed by using the brightness of individual stars as weights. This can be expressed mathematically as:

$$\boldsymbol{R}_{eq} = \frac{\sum B_i \boldsymbol{R}_i}{\|\sum B_i \boldsymbol{R}_i\|} \tag{4.2}$$

where:

$\boldsymbol{R}_{eq}$ = unit vector representing the equivalent star;

B_i = brightness of an individual star *i* being merged;

$\boldsymbol{R}_i$ = unit vector representing the star *i* before merging.

The brightness of the combined resulting star will be the sum of the individual brightness ($B_{eq} = \sum B_i$).

The brightness used in the equation above are obtained from cataloged stellar magnitudes, using the equation:

$$B_i = 10^{-0.4\, m_i} \tag{4.3}$$

where m_i indicates the instrumental magnitude for the star *i*. The number $10^{+0.4}$ ≈ 2.512 is known as Pogson's ratio, being the brightness ratio between two stars that differ in magnitude by 1 (see Appendix C for a detailed explanation about stellar magnitudes). The minus sign in the exponent in equation (4.3) is due to the fact that the magnitude scale is an inverted logarithmic scale, with dimmer stars having higher magnitudes than brighter stars.

PROC_CAT also gives some statistics, like the number of stars in the input catalog, the number of stars merged and equivalent stars created, and the total number of entries (single stars or equivalent photometric center of multiple star systems / groups) written to the target catalog.

Since PROC_CAT does not check if the resulting merged stars fall within the merge radius of other existing catalog stars or resulting merged stars, it must be executed multiple times with the same merging radius to assure that all stars within a merging radius of *r* have been properly merged. To do this, the output of the last execution of PROC_CAT must be supplied as the input to PROC_CAT until no further merge occurs. Figure 4.3 explains the reason why PROC_CAT

must be executed multiple times. The left pane (a) shows the input for the first run of PROC_CAT. The middle pane (b) shows the output of the first run of PROC_CAT which is also feed to PROC_CAT in the second run. The right pane (c) shows the output of the second run.

Figure 4.3 – A group of stars needing multiple passes to complete merging.

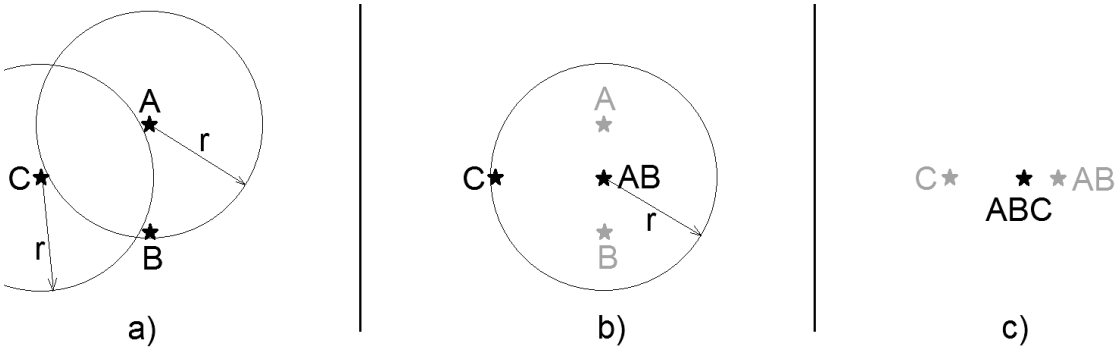

Source: Drawn by the author for this work.

In this example, there are three stars labeled A, B and C nearing each other with a distance close to the merging radius *r*. During the first pass, PROC_CAT first finds star C, selecting it as a pivot star. Since there's no star within an angular separation *r* from C, PROC_CAT keeps star C in the database and searches for another pivot star. After a while, still during the first pass, it selects star A as a pivot star. However, for star A it finds star B within the merging radius *r* (Figure 4.3.a). When multiple stars are found within a radius *r* of the pivot star, PROC_CAT computes their photometric center using Equation (4.2) and replace them with their photometric center. For stars A and B their photometric center is labeled AB in Figure 4.3.b. The results of this first pass are saved to the output catalog. Notice that for this particular example, now star C falls within a merging radius *r* of the equivalent star AB written to the catalog. However, PROC_CAT does not catch this. It's the user responsibility to perform as many passes as needed to completely merge all stars in the database separated by an angular distance smaller than *r*. This is done by running PROC_CAT multiple times, each time using the output of the last execution as the input for the next. The user

knows that no further merges are possible when PROC_CAT informs the user that no merging has occurred.

4.2.3 Storage catalog and working catalog

This section briefly describes the catalog formats used for monochrome and color star trackers in PTASE and how the conversion between one format to the other is performed (FIALHO, 2003).

4.2.3.1 Storage Catalog

The catalogs generated by READCAT and PROC_CAT are in a storage catalog format, as described in Appendix D. This format was created with the goals of minimizing the amount of storage memory required and at the same time avoiding the need of complex decompression algorithms. The reason for this is that many star trackers of the early 2000's (the period when PTASE was conceived) had very limited amount of non-volatile memory and low processing power. There are two variants of this star catalog format: one for monochrome star trackers and another for color star trackers with two spectral bands. The detailed specification of these formats is given in Appendix D.

Note that we do not store the distance to the stars in the catalog, since this information is not needed for most star trackers, except for very accurate star cameras working in the sub-arcsecond range or for deep space missions, much beyond the orbit of Jupiter. Stars are so far away from each other, that even from the closest star to our Sun (Proxima Centauri), and imagining that the dwarf planet Pluto (which lies around 40 times farther from the Sun than Earth) were as bright as the Sun, a human observer located near Proxima Centauri would not be capable of resolving the Sun from Pluto at its greatest angular separation from the Sun (around 30 arc-seconds). From Proxima Centauri, Pluto (if it were a star) would become discernible from the Sun only with the aid of a binoculars or a small telescope. The distances used in this computation can be obtained from

any good textbook in Astronomy, e.g., the book by Zeilik and Gregory (1998), and the typical human visual acuity from works discussing eye physiology, e.g. the work by Hartridge (1922) and the course webpage created by Stokes (2014).

4.2.3.2 Working Catalog

By using only two numbers (right ascension and declination) to specify the coordinates of every star in the celestial sphere, the storage catalog is very compact, which makes it suitable for storage in systems with limited amount of non-volatile memory. However, the representation of star coordinates in terms of spherical coordinates (e.g., right ascension and declination) in the storage catalog leads to the need of complicated and slow trigonometric functions during stellar identification and attitude determination, which makes the direct use of the storage catalog format unfeasible.

Hence, during the initialization phase, a STR typically converts the storage catalog to another format when loading the catalog in volatile memory (RAM). This format, which exists solely in volatile memory and is used for stellar identification and attitude determination, is termed in this work as *working catalog*. In this format, the stars (or more appropriately, the directions to each star) are represented by unit vectors pointing to points in the celestial sphere. This format has the disadvantage that each unit vector has three components, versus two components for the right ascension - declination representation, with one of them being redundant. However, the extra memory needed for this redundant component is more than compensated by the much faster manipulation with unit vectors and the avoidance of singularities at the poles of the spherical coordinate system used in the storage catalog.

The unit vector components can be calculated from the spherical coordinates by the following equations, derived from Figure 4.4:

$$P_x = \cos\alpha \cos\delta \quad (4.4)$$

$$P_y = \sin\alpha \cos\delta \quad (4.5)$$

$$P_z = \sin\delta \quad (4.6)$$

where:

P_x , P_y, P_z = components of the unit vector $\boldsymbol{P}$ representing a star

α = right ascension of the star

δ = declination of the star

Figure 4.4 – Conversion between a spherical coordinate system and a Cartesian coordinate system.

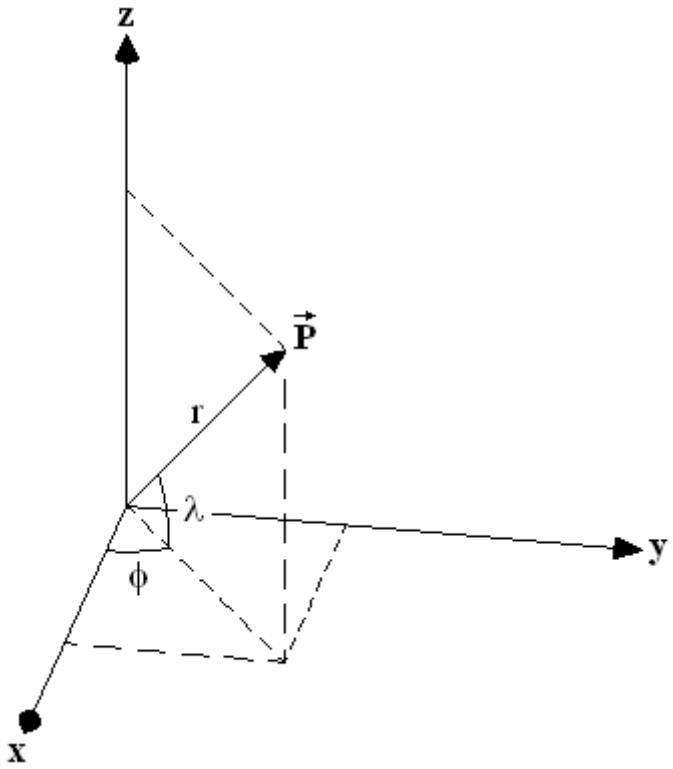

Source: Fialho (2007).

In PTASE and in the Brazilian star tracker, the components of the unit vector $\boldsymbol{P}$ representing a star are computed in double precision floating-point values (IEEE 754 binary64 format (IEEE, 2008)) since the shorter single precision

floating-point value (IEEE 754 binary32 format) with only 24 bits of mantissa might not provide enough accuracy for some computations during attitude determination[6]. By representing unit vectors components with double precision floating-point values (52 bits of mantissa), the maximum rounding error is on the order of $1.1 \cdot 10^{-16}$ rad ≈ $2.3 \cdot 10^{-11}$ arcsec.

In PTASE, stellar magnitudes are represented in the working catalog also as double floating-point values, also taking 8 bytes each. However, as this format has much more precision than required, in future releases the datatype used for stellar magnitudes may change. Currently, each entry in the working catalog takes 32-bytes, this is twice the memory requirements for the storage catalog.

4.3 Catalog preparation for color star trackers

The catalog preparation for color star trackers is met with new challenges not found for monochrome star trackers. One of these is introduced by the existence of double and multiple stars where the angular separation between individual stars is so small to the point of making them not resolvable by the star tracker, so that the star sensor will observe the whole group as a single equivalent star with a brightness equal to the sum of the brightness of individual stars and located at the photometric center of the group.

If the individual stars that compose this group have different colors, as usually happens, the position of the photometric center of that group will depend on the spectral band used by the star tracker. This effect is illustrated in Figure 4.5. The existence of binary or multiple systems is very common, about 58% of the entries listed in the Hipparcos catalog (ESA, 1997) brighter than visual magnitude 5 are flagged in Hipparcos as being components of binary or multiple systems or the photometric center of a binary/multiple star system.

[6] Even though with a 24-bit mantissa the least significant bit represents an angle of about 0.049 arc-seconds for angles approaching π, which should suffice for a wide field of view star tracker, a detailed numerical analysis would have to be performed to ensure that no unacceptable loss of precision would occur with single precision floating point format due to cancellation errors.

Figure 4.5 shows a simulated binary system composed of stars A and B where each component has a different color in two spectral bands: band 1 (blue) and band 2 (red). They are closer to each other than the resolving power of the star tracker, so they are seen by it as a single star, but the exact position of this equivalent star depends on the spectral band used. The left pane shows the system in color, at high magnification, with the center positions of stars A and B indicated. A scale at the bottom of this pane gives the size of one pixel. The middle pane shows the same figure in band 1, where star A is stronger, whereas the pane to the right shows the system in band 2, where star B is stronger. Notice how the photometric center changes with spectral band – it is indicated by letter C in band 1 and letter D in band 2.

Figure 4.5 – Photometric centers in different spectral bands for a binary system. Detailed view in the image plane at a great magnification. Left: composite color image from the middle and right images. Middle: simulated image in spectral band 1. Right: simulated image in spectral band 2. The letters A and B indicate the true positions of stars A and B. The photometric center in band 1 is indicated by letter C. Letter D indicates the photometric center in band 2.

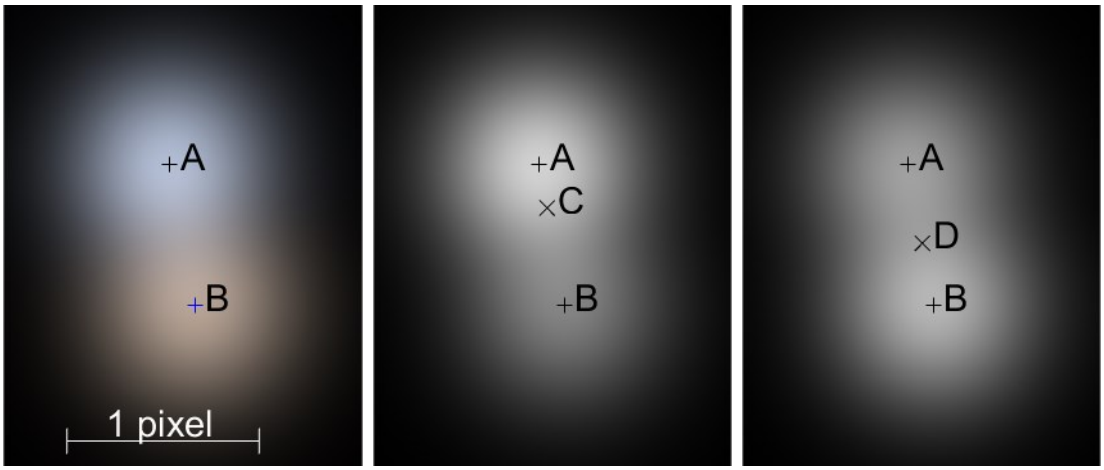

Source: Drawn by the author for this work.

There are three ways of coping with this:

a) adding together data from different spectral bands before doing centroiding, in effect, computing the star centroid in a new spectral band

that is the result of the merge of all spectral bands of the star tracker, and compute the photometric center in this spectral band.

b) creating a different star catalog for each spectral band, or, alternatively, creating a catalog that stores all the positions of the photometric center of group of stars in different spectral bands.

c) neglecting this effect, by computing the centroid using only one spectral band.

Option a) has the advantage of providing a simple solution, with no significant changes in the star catalog format. If this option is chosen, the only modification in the star catalog is the addition of additional magnitude or color index fields, each for additional spectral band.

Option b) has the advantage of providing more information about the stars, at the expense of a greater complexity of the star tracker on-board software. Option b), for example, allows to better measure chromatic distortions introduced by the optics.

Option c) is the simplest approach, but is also the least accurate. Our current implementation in `proc_cat.exe` uses this option when generating a star catalog containing *B−V* color indices, but we plan to replace this approach with a better solution (either a or b) in a future release of the program.

4.4 List of observed stars

During Monte Carlo simulations, the list of observed stars that is fed to the star-ID algorithm under test is generated in the program PTASE (FIALHO; SAOTOME, 2005) by the algorithms *gen_sia_input5*, *gen_sia_input6*, *gen_sia_input7* or *gen_sia_input8.* These algorithms generate a simulated list of observed stars from a star catalog that can be the same catalog from where the catalog used by the star-ID algorithms is derived or a different one, depending if only one or two star catalogs are provided to PTASE when loading the program.

The name *gen_sia_input* comes from an abbreviation of the expression "generate star identification algorithm input." The last number (5, 6, 7 and 8) is a version number distinguishing older from more recent implementations of this algorithm. *gen_sia_input5* is the original algorithm used by Fialho (2007), whereas the remaining algorithms are improvements over *gen_sia_input5* created for this work.

The list of observed stars is generated by scanning all stars that can be within the field of view of the star tracker. Those that are inside the simulated field of view have their coordinates converted from the star catalog reference frame to the STR reference frame. Then star coordinates and magnitudes are corrupted by adding a Gaussian noise, whose standard deviation depends on cataloged magnitude. This is modeled in *gen_sia_inputx* (with x being either 5, 6, 7 or 8), as can be seen in the continuous blue curves in Figure 4.6 and in Figure 4.7 (FIALHO, 2007). This is done so more representative values are used, as it would be on a real star sensor. The model also includes a parameter named $\mathrm{m}_{\mathrm{offset}}$ which is used in to shift the whole curves to the right or to the left, simulating the effect of an increase or decrease in star tracker sensitivity, e.g., due to a change in the exposure time in the acquisition of the images.

These curves were obtained by running a centroiding algorithm multiple times and performing a best fit on the results (FIALHO, 2007). For magnitudes (Figure 4.7), an additional uncertainty of 0.25 magnitude has been quadratically added (FIALHO, 2007) to the magnitude standard deviation used in the model. This is to account for miscalibration, change in optics transmittance with aging and variability intrinsic to some stars. Likewise, for the centroid position (Figure 4.6), an additional uncertainty of 0.05 pixel per axis has been quadratically added to the per axis position standard deviation (FIALHO, 2007). This is to account for uncertainties introduced by miscalibration, thermo-elastic deformations, etc.

Figure 4.6 – Variation of centroid standard deviation versus magnitude for *gen_sia_inputx*.

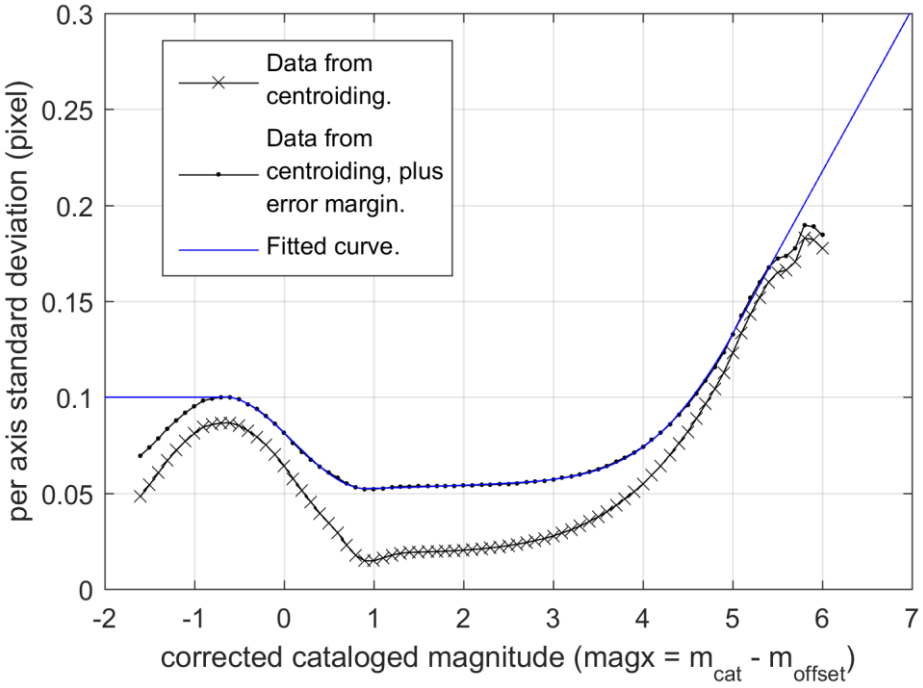

Source: Fialho (2007)

Figure 4.7 – Variation of observed magnitude standard deviation versus cataloged magnitude for *gen_sia_inputx*.

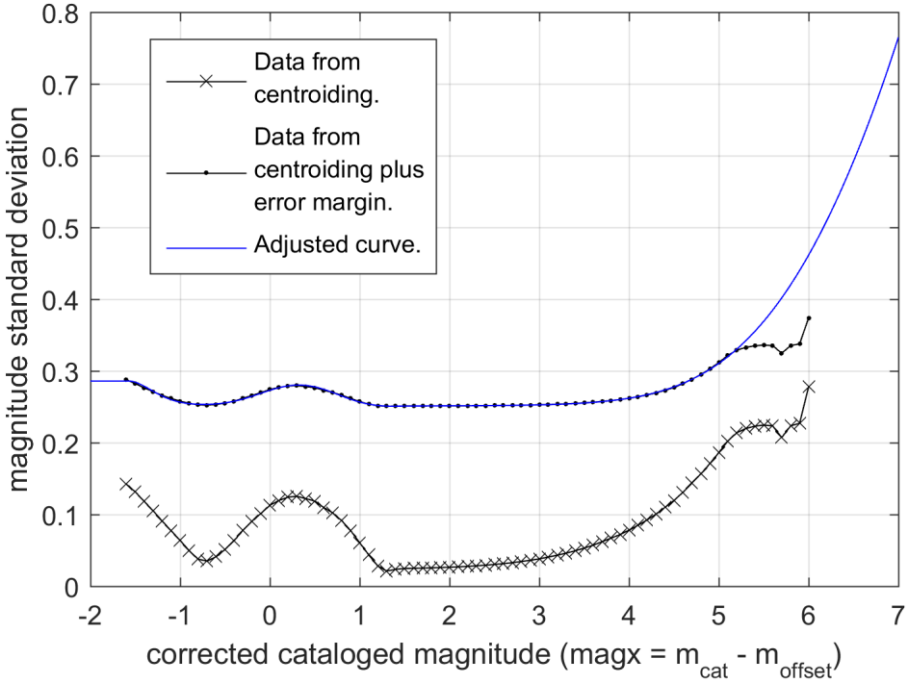

Source: Fialho (2007)

These values of 0.25 magnitude and 0.05 pixel which were quadratically added to the model (FIALHO, 2007) were chosen based on the expected errors in magnitude and position due to miscalibration, stellar variability and thermo-elastic deformations for the Brazilian star tracker (FIALHO; PERONDI; MORTARI, 2016). However, these values should be reviewed once a better characterization of this star tracker is performed. Considering the preliminary results obtained in Section 3.6, this additional magnitude error of 0.25 magnitude could, perhaps, be revised downwards.

As expected, the standard deviations in magnitude and position increase with magnitude, since dimmer stars (higher magnitudes) have worse signal to noise ratio. For very bright stars, with $magx = m_{cat} - m_{offset} < 1$, we can see the effects of image sensor saturation, causing an increase in the magnitude and position errors as their brightness increase (*magx* decreasing from 1 to 0). For stars brighter than magnitude 0, which cause a very strong saturation in the detector, we observe oscillations of the position and magnitude standard deviations with increasing star brightness. These are caused by complex interactions between the adopted PSF (point spread function), saturation in the detector distorting the observed PSF and the centroid algorithm used. In any event, the exact behavior of these curves for $magx < 0$ is of little importance for the simulations (which will be presented in Chapter 5), since there are very few stars brighter than a visual magnitude of zero in the sky, as can be seen by the exponential relation between the number of stars and limiting magnitude described by Equation (3.1) in Section 3.2.

Note that for magnitudes we have to consider the existence of a bias that is dependent on magnitude for very bright and very dim stars, even for a perfectly calibrated star tracker, as can be seen in Figure 4.8. The algorithms *gen_sia_inputx* also models the probability of detection of stars in function of cataloged magnitude, as can be seen in Figure 4.9.

Figure 4.8 – Variation of observed magnitude versus cataloged magnitude for *gen_sia_inputx*.

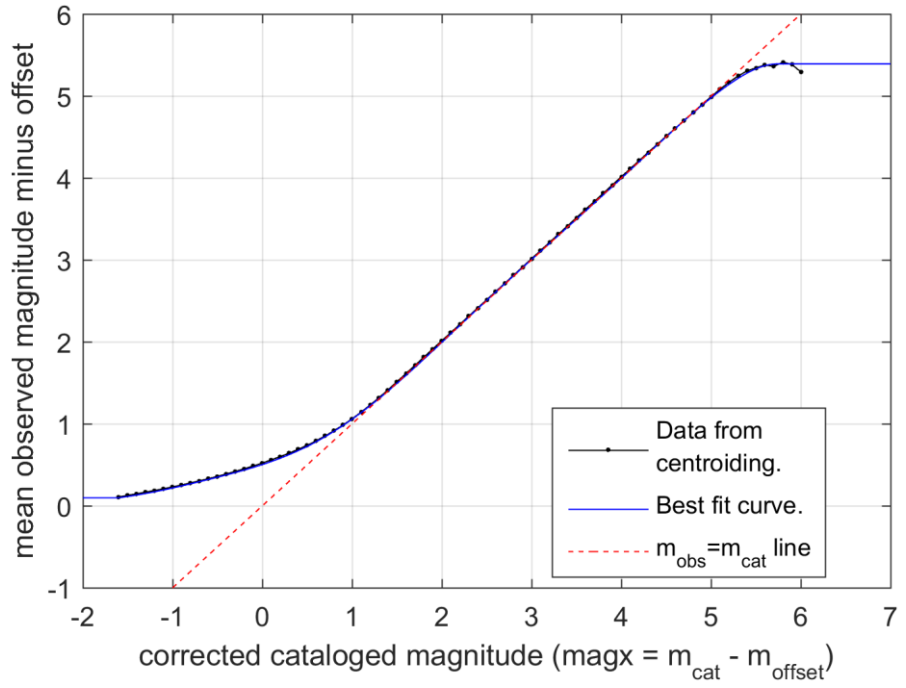

Source: Fialho (2007)

Figure 4.9 – Probability for detection modeled in *gen_sia_inputx*.

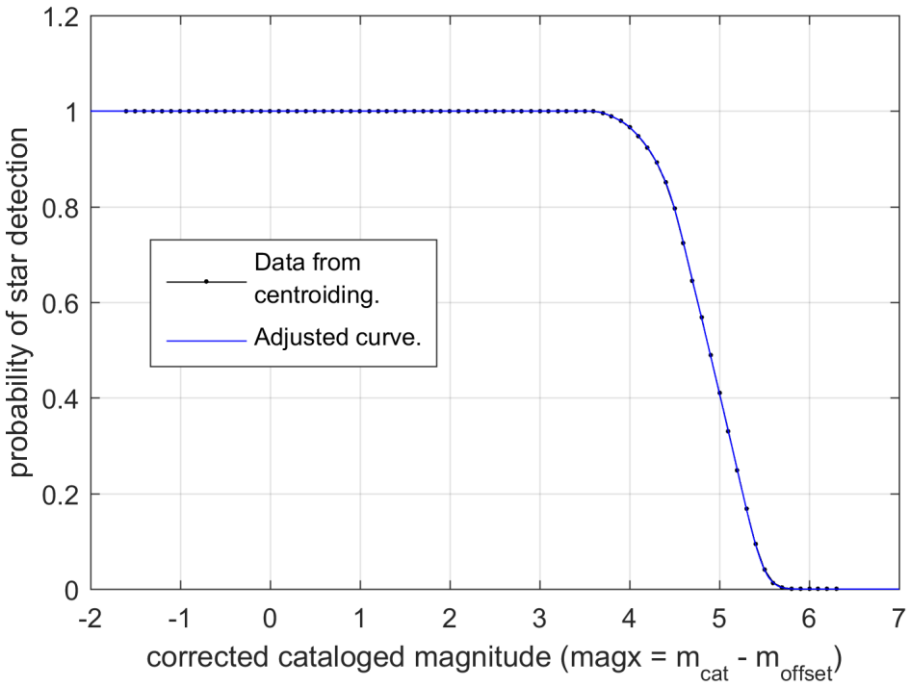

Source: Fialho (2007)

The origin of the magnitude bias for low magnitude stars (bright stars) is the saturation of the detector array, which makes the observed brightness being lower than the actual brightness (observed magnitude higher than the cataloged instrumental magnitude). On the other hand, for dim stars which are on the limit of detection, these will normally be detected only if the random noise in the system contributes to the gray level of the pixels illuminated by the star, pushing them above the threshold used for star detection during image processing. This causes a skew in the sampling space, such that the dimmest stars that had been detected will have a brightness almost always higher than their actual brightness (observed magnitudes smaller than their true magnitudes). This effect was captured by the simulations used to derive these curves, being first observed by us in 2005 (FIALHO; LOPES; SAOTOME, 2005).

Note that the centroiding algorithm used in the simulations performed to derive the curves adopted in this model is not the same algorithm described in Section 3.6.3. The main difference being that the centroiding algorithm used in these simulations utilizes all pixels of a 3x3 matrix centered on the true position of the star when computing its centroid, whereas the algorithm described in Section 3.6.3 considers only pixels above the detection threshold, causing a very different behavior in magnitude estimation. In a real application where the true position of the star is unknown, the algorithm used here would center the 3x3 matrix on the brightest pixel of the star image.

In the model used to derive the curves presented in this section, the point spread function (PSF) is considered to follow a Gaussian distribution with standard deviation for the vertical and horizontal axes of 0.4065 pixel (MATOS, 2005, personal communication). Even though this representation is not very accurate it has been adopted due to its simplicity. Also for simplicity, this model disregards spectral content of stars, assuming all stars having the same spectra as of the Sun. Due to lack of accurate pixel geometry information, this model assumes that the sensitive area of each pixel in the STAR-1000 image sensor is a square covering 70% of the total area of the pixel. Further details of the model used are

given in Fialho (2007). Even though this model has many limitations, it better represents the behavior of real star trackers than simple models commonly used in the literature (ZHANG, 2017) that do not take into account the dependence of centroiding error and magnitude error with stellar brightness.

The curves used in *gen_sia_inputx* (with $x \geq 5$) have been derived from a camera with the following specification (FIALHO, 2007):

- image sensor: STAR-1000
- imager resolution (pixels): 1024 x 1024;
- pixel size: 15 μm x 15 μm;
- STAR-1000 analog gain factor = 1
- A/D converter input range = 2 volts
- A/D converter resolution: 10 bits
- A/D converter non-linearity: 1.4 ADU (1σ)
- A/D converter bias (dark level) = 20.6 ADU
- conversion factor in the A/D converter per photoelectron collected = 11.4 $\mu V/e^-$
- dark current per pixel: 3135 e^-
- PRNU: 1.34% (1σ)
- readout noise: 50 e^- (1 σ)
- FPN: 300 e^- (1 σ)
- fill-factor: 70%
- optics aperture area: 4.6 cm^2
- optics transparency (transmittance) : 80%
- image sensor quantum efficiency: 14.38%
- exposure time (integration time) : 350 ms.

4.4.1 Versions of *gen_sia_inputx*

gen_sia_input5 was the original algorithm developed by the author for his master thesis defended in 2007. *gen_sia_input6, gen_sia_input7* and *gen_sia_input8* are improvements to *gen_sia_input5* done for this doctorate thesis. The following features were introduced with each new version:

- *gen_sia_input6* introduces a new parameter which specifies the resolution of the image sensor. For the same field of view, the higher is the resolution of the image sensor, the smaller is the angular width and height subtended by central pixels in the imager, and lower is the standard deviation of the noise added to observed stars' unit vectors. Hence, this new parameter can be used as a scaling factor for the position noise added to observed stars.

- *gen_sia_input7* introduces support for $B-V$ color index in star catalogs with color information. To simulate in a more realistic way the noise behavior in the $B-V$ color index, instead of using a fixed standard deviation we have used a standard deviation in the $B-V$ color index that changes with cataloged magnitude, following the same curve used for magnitude standard deviation (Figure 4.7).

- *gen_sia_input8* introduces support for $V-I$ color index in star catalogs derived from Hipparcos. The simulated noise behavior in $V-I$ color index also follows the same curve used for magnitude standard deviation.

4.4.2 False stars

A limitation of *gen_sia_inputx* (with $x \leq 8$) is that they are not capable of inserting false stars (spikes) in the list of observed stars. However, to properly evaluate the reliability of star identification algorithms it is very important that these algorithms be tested with scenes containing false stars. The inclusion of false stars in the list of stars generated by *gen_sia_inputx* is a planned improvement for future

releases of PTASE. With current versions of *gen_sia_inputx* the only way to include false stars in the simulation is to use a star catalog containing false stars.

An imperfect way to simulate the effects of false stars with current versions of *gen_sia_inputx* is to limit the star catalog used for star identification to a magnitude that is smaller (brighter) than the dimmest cataloged stars used by *gen_sia_inputx*. With this method, observed stars generated by *gen_sia_inputx* from stars beyond the magnitude limit of the catalog used for star identification would be seen by the star-ID algorithm as false stars.

4.5 Computation of attitude errors in PTASE

One way to define the attitude error is as the angle in which the axes of the estimated body frame have to be rotated around the Euler axis (of the Euler axis/angle representation of the corrective attitude matrix $C_T C_E^t$) to coincide with the axes of the true body frame (MORTARI, 2002). Using this definition, which was adopted in this work, the attitude error is given by the equation:

$$\theta = \operatorname{acos}\left(\frac{\operatorname{tr}(C_T C_E^T) - 1}{2}\right) \tag{4.7}$$

With C_T being the true attitude matrix and C_E^T the transpose of the estimated attitude matrix C_E, determined from the stars that were identified by a star ID algorithm. $\operatorname{tr}(M)$ indicates the trace of a square matrix M. However, when the attitude error is small (small θ), a first order approximation can be employed, leading to the following approximate equation:

$$\theta \approx \frac{1}{\sqrt{2}}\|C_E - C_T\| = \sqrt{\frac{1}{2}\sum_{i=1}^{3}\sum_{j=1}^{3}\left(c_{E,ij} - c_{T,ij}\right)^2} \tag{4.8}$$

For very small attitude errors, the numerical computation of the approximate equation becomes more accurate than the computation of the exact equation, because the arc-cosine is numerically not stable for arguments close to 1 or −1

(its derivative exhibit a singularity at +1 and −1). Also, the approximate equation is faster, since it does not require the computation of an inverse trigonometric function. Hence, in PTASE attitude errors are computed using the approximate Equation (4.8).

5 IMPROVEMENTS TO THE PYRAMID STAR-ID ALGORITHM

This chapter presents many improvements that were made to the Pyramid star identification algorithm by the author, plus the result of Monte Carlo simulations used to assess these improvements.

5.1 Why Pyramid

According to Spratling and Mortari (2009), the Pyramid star-ID algorithm was one of the fastest star identification algorithms which was still suitable for being embedded in a star tracker, this being one of the reason Pyramid was chosen for this work. Faster algorithms do exist, such as the algorithm proposed by Hong in 2000 using neural networks, however these algorithms require the use of massively parallel processing which is not available in space hardware (SPRATLING and MORTARI, 2009). Another factor in favor of Pyramid is its flight heritage aboard the HETE spacecraft and high success rate even in the presence of many false stars (MORTARI et al., 2004).

The name Pyramid comes from the fact that the algorithm initially identifies a set of three stars from the list of observed stars and confirms this identification with a fourth observed star forming a pyramid (a set of four stars) with those three initially identified stars.

5.2 Introduction to the Pyramid star-ID algorithm

Before presenting the improvements made by the author in Pyramid, a brief introduction to the Pyramid star-ID is made in this section. A flowchart of the original version of the Pyramid star identification algorithm is shown in Figure 5.1.

When less than 3 stars are observed, Pyramid fails, since its original version uses only positional information from the stars for identification. In that case, the absolute minimum number of stars needed for star identification is three, as explained in Section 2.6.

Figure 5.1 – Flowchart of the original version of Pyramid

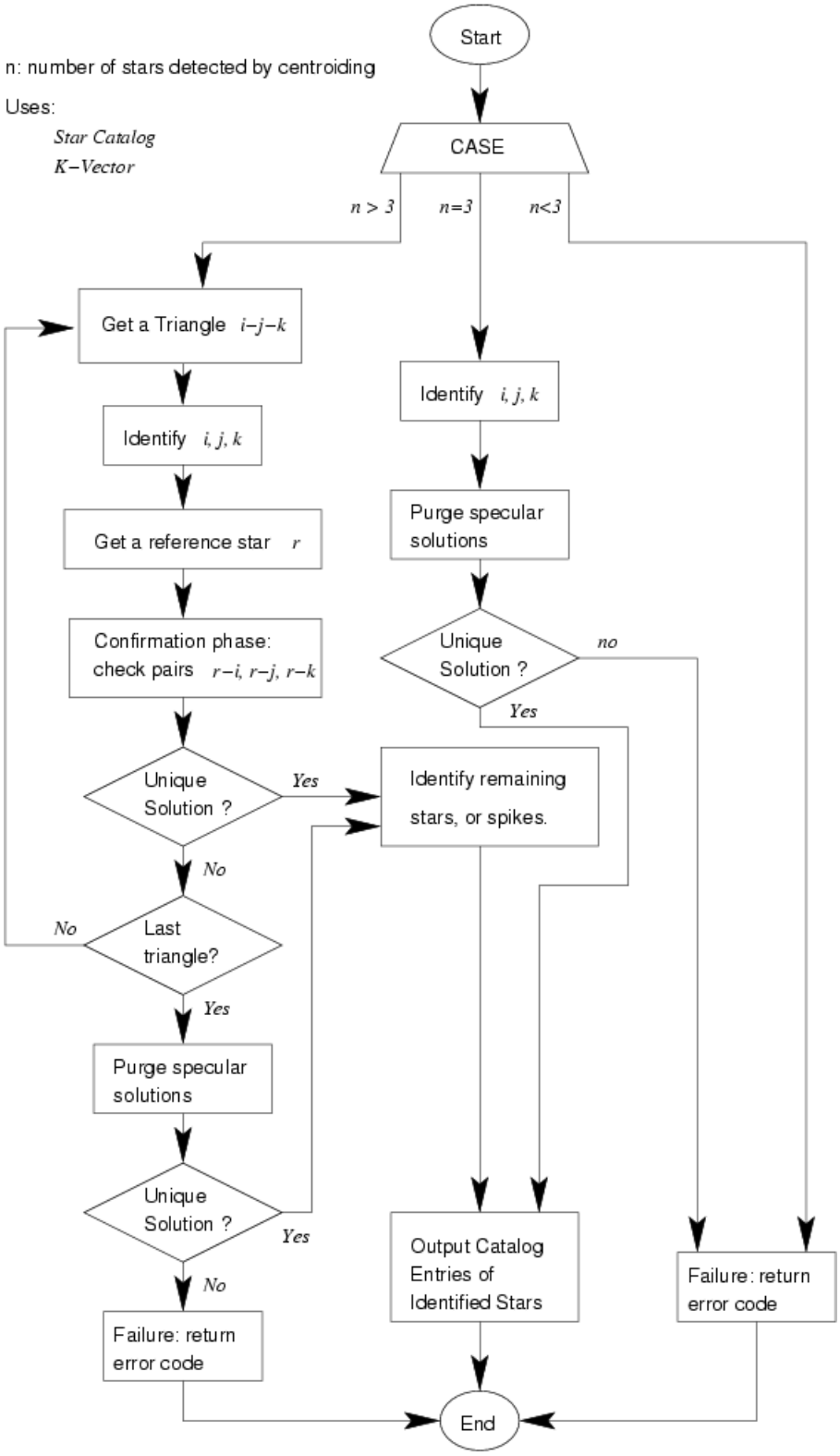

Source: adapted from Mortari et al. (2004)

5.2.1 Identification with three stars

When only three stars are observed, Pyramid attempts to identify the only triangle that can be formed. This process is depicted by the "Identify *i, j, k*" boxes of Figure 5.1, being described in detail in Section 5.2.5. The output of this step is a list of candidate triangles from the star catalog that match the observed triangle within measurement tolerance. If this list is empty, the algorithm returns with an error code (not shown in the diagram), otherwise it proceeds to the next step, which is to purge specular (mirror) solutions from this list. This is done to to reduce the probability of a misidentification or ambiguous identification happening. This second step is explained better in Section 5.2.7. In cases where more than one candidate triangle remains after the purging operation, there exists an ambiguity which cannot be solved, so Pyramid returns an error code.

5.2.2 Identification with four or more stars

When at least four stars have been observed (indicated by $n > 3$ in the flowchart), the first step in Pyramid is to select a subset of three observed stars (a *kernel*), and to attempt to identify it before identifying the remaining stars. This kernel is composed initially of the first three stars in the list of observed stars fed to Pyramid. If Pyramid does not succeed in finding a set of three cataloged stars matching these observed stars, another set of observed stars is selected as a new kernel and the process is repeated. Section 5.3.2 discusses the improvements performed in kernel selection.

5.2.3 Databases used in Pyramid

To speed up star identification, Pyramid uses two additional databases besides the star catalog, as shown in Figure 5.2. These databases are the list of pairs of stars and the *k*-vector, explained in Section 5.2.4. They are used by Pyramid to quickly find all pairs of cataloged stars used for identification that are equivalent to the observed star pairs that form the kernel within measurement tolerance.

Figure 5.2 – Databases used in Pyramid.

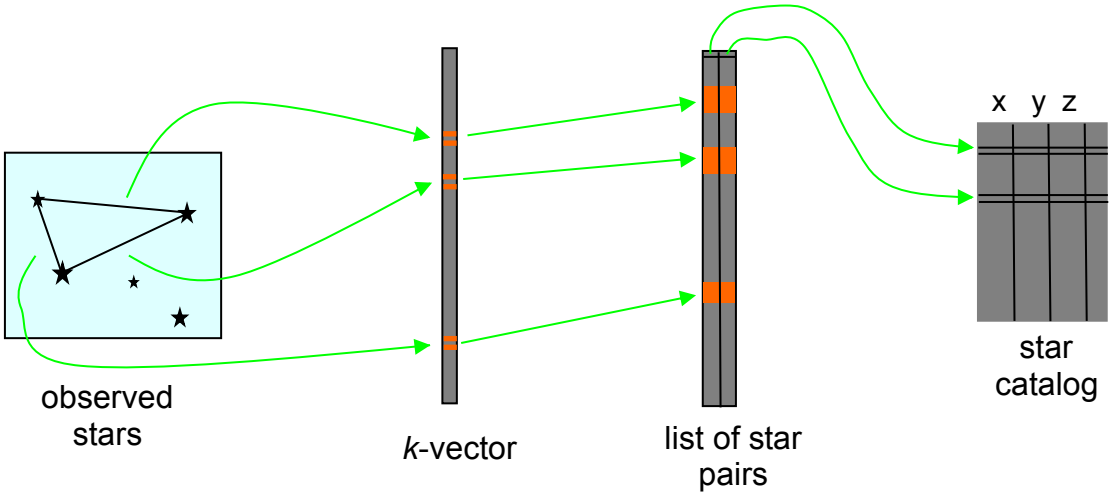

Source: Fialho (2007).

The list of star pairs (or catalog of star pairs) is a table where each entry (a star pair) contains two fields. Each field is an index with the position of the corresponding star in the star catalog. For example, the star pair (32, 144) is composed of stars at position 32 and position 144 in the star catalog. The *k*-vector (explained in the next section) is a helper table which allows the algorithm to quickly find all star pairs in the catalog of star pairs with the same angular separation of an observed pair of stars, within measurement tolerance. Section 5.2.5 gives a description of how stars are identified from the list of star pairs.

The list of pairs contains all pairs of stars used for identification that fit inside the FOV. This list is sorted by the length of the star pairs – the angular separation between the stars that compose the pair. It should be noted that it is not required to store the pair length, nor the coordinates of each star in the list of stars, since these pieces of information can easily be obtained by accessing the star catalog, using the two star indices stored in the pair.

The original version of Pyramid does not use the star catalog in the star identification phase, since it is possible to identify stars using solely the list of star

pairs and the *k*-vector, as will become clear later. When using the original version of Pyramid, the star catalog is needed only for attitude determination.

5.2.4 The *k*-vector

The *k*-vector is a lookup table that permits to quickly find elements in an ordered database, being originally developed by Mortari (1996) for the star-ID problem, but later finding applications in many other areas (MORTARI; NETA, 2000). Basically, each element of the *k*-vector indicates how many elements in the ordered database are below a value computed using a strictly increasing monotonic function of the *k*-vector element index, this function later being named *mapping function* (FIALHO; MORTARI, 2017a, 2017b) or *k-vector support function* (this work).

For the linear (affine transformation case) *k*-vector, the *j*-th element of the *k*-vector counts how many elements of the ordered database are below $z(j) = a*j + b$, where *a* and *b* are coefficients chosen in such a way that for the first element of the *k*-vector, $a*j + b$ is slightly below the lowest value of the ordered database; and for the last element of the *k*-vector, $a*j + b$ is slightly above the largest value of the ordered database. So, the first element of the *k*-vector will always have the value zero, and the last element of the *k*-vector will always have a value equal to the size of the ordered database. This choice of *a* and *b* coefficients simplifies the use of the *k*-vector by avoiding the need of special logic to search for database elements that would otherwise be outside the range addressed by it.

Pyramid uses a linear *k*-vector where each element of the *k*-vector counts the number of star pairs whose cosine of the inter-star angle (the dot product between the unit vectors representing cataloged stars) is smaller than $z(j) = a*j + b$. Thus, with the *k*-vector, it is very easy to find all pairs of stars in the catalog of star pairs whose cosine of inter-star angle lies between y_{min} and y_{max}.

An extension of the *k*-vector search method for strongly non-linear databases, using a non-linear support function, was proposed by Fialho and Mortari (2017b).

5.2.5 Triangle identification

Let's name the three observed stars that compose the kernel selected by Pyramid as *alpha*, *beta* and *gamma*, with corresponding indices *i*, *j* and *k* in the list of observed stars. Pyramid starts with the pair made by *alpha* and *beta*, computing its length ($\theta_{\alpha\beta}$). Then, with the help of the *k*-vector, it quickly finds in the list of pairs all the cataloged star pairs with lengths between ($\theta_{\alpha\beta} - \delta_\theta$) and ($\theta_{\alpha\beta} + \delta_\theta$), where δ_θ is the tolerance used by the algorithm for star pair lengths. All the catalog stars present in these star pairs are candidates to be both *alpha* and *beta*.

After working with the pair formed by *alpha* and *beta*, Pyramid repeats the same process with the pair formed by *alpha* and *gamma*. If a cataloged star appears both in the pairs matching *alpha-beta* and in the pairs matching *alpha-gamma*, that star is a candidate for *alpha*. The other stars in the same star pairs where *alpha* was found are candidates for *beta* and *gamma*. Then the catalog candidates for observed stars beta and gamma are searched in the list of star pairs matching the observed pair beta-gamma to confirm the match. This process is graphically depicted in Figure 5.3. In this example, star 86 in the star catalog is a candidate for *alpha*, star 64 in the star catalog is a candidate for *beta* and star 142 from the star catalog is a candidate for *gamma*.

Figure 5.3 – Finding a candidate for *alpha* and confirming it.

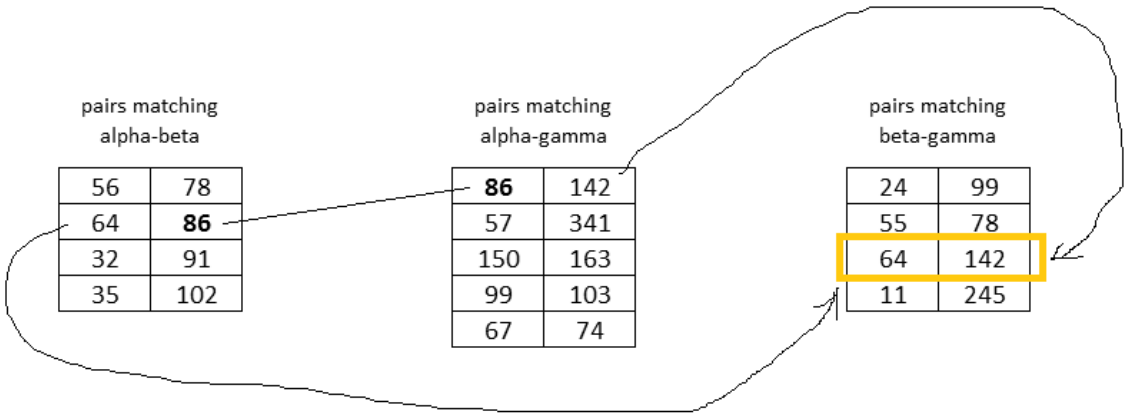

Source: Drawn by the author.

The indexes *i*, *j*, *k* indicate the position of *alpha*, *beta* and *gamma* in the list of observed stars (these indexes are known from kernel selection). For example, if *i*=0, *j*=1 and *k*=2 in the example shown in Figure 5.3, then the observed star at position 0 has been matched with cataloged star at position 86, observed star at position 1 has been matched with cataloged star at position 64 and observed star at position 2 has been matched with cataloged star at position 142.

5.2.6 Kernel selection

If a triangle of observed stars was not identified, the cause can be that one of the observed stars selected for that kernel was a false star (e.g., a planet, or a debris in the field of view, noise in the image sensor, etc.). Hence, ideally a complete new set of observed stars should be selected for a new kernel. The original Pyramid algorithm had a very simple kernel generator that avoided persisting on the same observed star for many consecutive kernels. One of the original contributions of the author of this thesis is proposing an improved version of this simple kernel generator that generates better sequences of kernels but still retain much of the simplicity of the original kernel generator in Pyramid. Algorithms that generate better kernel sequences do exist, but many of these are unsuitable for an embedded environment due to low speed, large memory requirements or code complexity.

Pseudo-codes of the original kernel generator and the improved kernel generator are presented in Section 5.3.2 together with a more detailed explanation.

5.2.7 Purging mirror solutions

Considering only angular separations, a triangle of observed stars could also match a candidate triangle which is a mirror image of the observed triangle. This would obviously result in a misidentification (see Figure 5.4 for an illustration of two identical triangles except for their differing handedness). Therefore, Pyramid

performs an additional test to purge mirror solutions. This test is done inside the two boxes labeled “purge specular solutions” in Figure 5.1.

Figure 5.4 – Mirror triangles: these two triangles are identical except for their differing handedness.

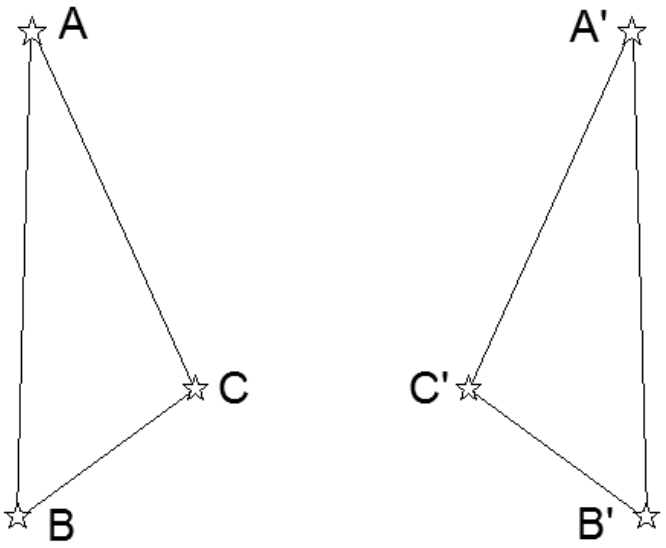

Source: Drawn by the author.

To purge mirror candidate triangles, Pyramid computes the mixed product between the unit vectors representing the stars of the observed triangle and do the same for the cataloged stars of the candidate triangle. If the signs of their mixed product differs, then these triangles are the mirror image of each other, therefore the candidate triangle must be discarded. In mathematical terms, this can be expressed as follows:

Let $\mathbf{b}_i$, $\mathbf{b}_j$ and $\mathbf{b}_k$ be the unit vectors of the stars of the observed triangle i-j-k, and $\mathbf{r}_I$, $\mathbf{r}_J$ and $\mathbf{r}_K$ be the unit vectors of the stars of the candidate triangle I-J-K that is a potential match. The candidate triangle I-J-K is rejected if the following relation is not met (MORTARI et al., 2004):

$$\text{sign}\big(\mathbf{b}_i \cdot (\mathbf{b}_j \times \mathbf{b}_k)\big) = \text{sign}\big(\mathbf{r}_I \cdot (\mathbf{r}_J \times \mathbf{r}_K)\big) \tag{5.1}$$

In Pyramid, $\mathbf{b}_i$, $\mathbf{b}_j$ and $\mathbf{b}_k$ are given in the star tracker reference frame (described in Section 2.5.3) whereas $\mathbf{r}_I$, $\mathbf{r}_J$ and $\mathbf{r}_K$ are given in the star catalog reference

frame (this is the NRRF described in Section 2.5.2 if the star tracker is compensating stellar aberration).

5.3 Description of the improvements

This section describes the improvements performed by the author to the Pyramid star-ID algorithm.

5.3.1 Use of the memory adaptive *k*-vector

5.3.1.1 Introduction

In the original Pyramid algorithm (MORTARI; JUNKINS; SAMAAN, 2001; MORTARI *et al.*, 2004) the *k*-vector has the same length (number of elements) as the list of pairs of stars that fit inside the star tracker's FOV. However, the size of the *k*-vector does not need to be the same as the list of pairs. As pointed out by Mortari (2014), the *k*-vector may be made smaller for applications constrained in memory, or be made larger in order to speed up database queries in systems with abundant memory. So, basically, it is possible to perform a trade-off between speed and memory requirements by changing the *k*-vector size. The possibility of freely selecting the size of the *k*-vector during its construction is one of the reasons for the name "memory adaptive *k*-vector" of the paper that introduced the idea, as the *k*-vector size may be freely adjusted to available memory in the target system.

The creation of a memory adjusted *k*-vector follows the same basic procedure as outlined in Section 5.2.4, the only difference being in the angular constant factor *a*, which is steeper for a shorter *k*-vector. As described in that section, each element K(*j*) of the *k*-vector just counts the number of elements in the database (for Pyramid, the database is the list of star pairs) whose value is smaller than $z(j) = a*j + b$.

Figure 5.5 illustrates how a “memory adaptive” *k*-vector can be built for a database S containing 10 elements. The left side of this figure shows the ordered database S with 10 elements, while the right side shows the mapping function *z*(*x*) used to build the *k*-vector. The *k*-vector is shown in blue under the horizontal axis in the right plot. In this example, the *k*-vector is K = {0, 2, 4, 6, 7, 9, 10}, having 7 elements, hence the size ratio between the *k*-vector and the database is 7 / 10 = 0.7. The constant ξ shown in the figure is a very small number used just to make sure that K(1) = 0 and K(7) = n = 10. This simplifies the *k*-vector use. In this example, it was assumed that the first index in vectors is 1. However, in many programming languages, such as the C language and derivatives, the first index in a vector is 0, hence some adaptations in the mapping function *z*(*x*) and in the way the *k*-vector is built must be performed when porting the code from one programming language to the other. These and other issues are discussed in a paper written by the author of this thesis about the *k*-vector (FIALHO; MORTARI, 2017b).

Figure 5.5 – Building a 7 element *k*-vector for a database S with 10 elements.

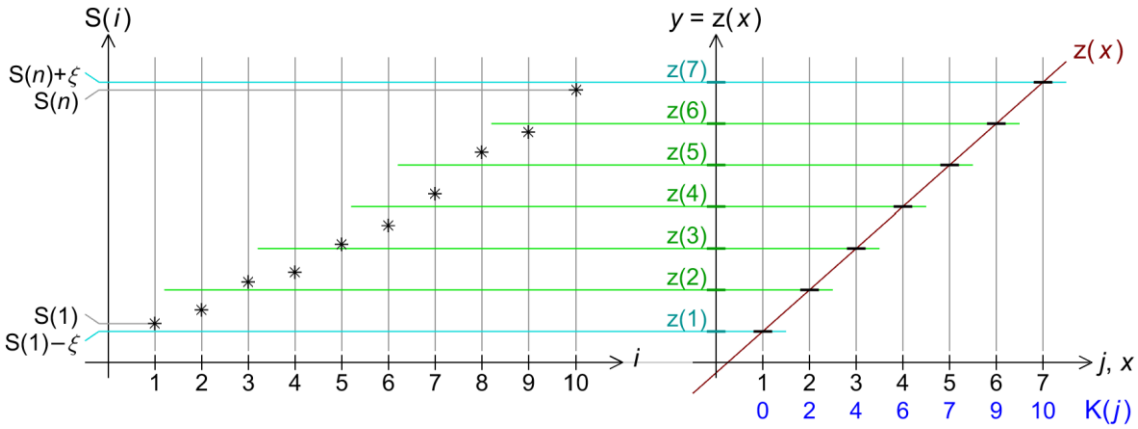

Source: Drawn by the author, used in (FIALHO; MORTARI, 2017a, 2017b).

Figure 5.6 shows how the *k*-vector can be used to locate elements in the database S inside the range given by $(y_{bot}, y_{top}] = \{y \in \mathbb{R} \mid y_{bot} < y \leq y_{top}\}$. Note that sometimes a *k*-vector search can return elements outside the requested range, but very close to its limits (outliers). Whether these outliers are acceptable

or not depends on the application. A detailed mathematical description on how the *k*-vector is built and used can be found on the references (FIALHO; MORTARI, 2017a, 2017b). The *k*-vector can also be extended to non-linear functions (quadratic, transcendental, etc.), as long as the mapping function is monotonic (FIALHO; MORTARI, 2017b).

Figure 5.6 – Using the k-vector to find elements in S between y_{bot} and y_{top}.

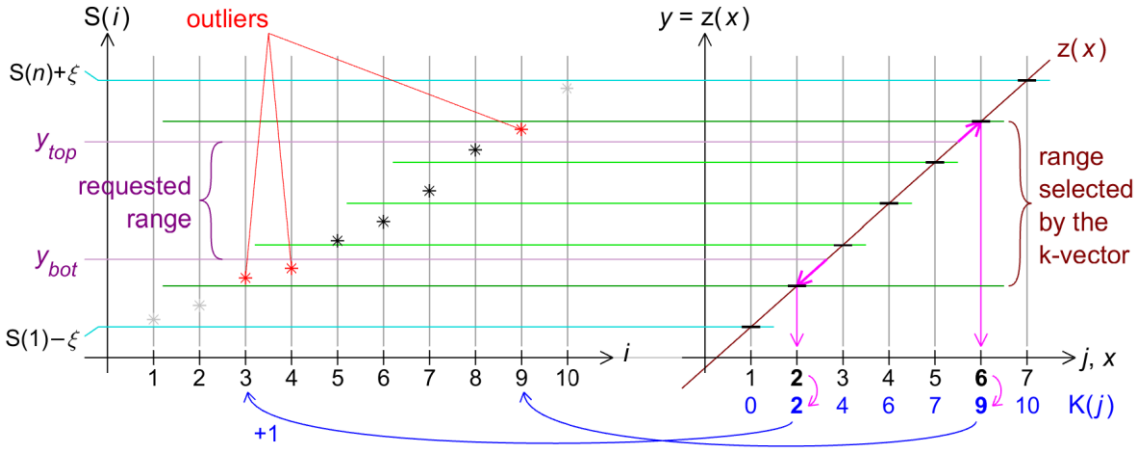

Source: Drawn by the author, used in (FIALHO; MORTARI, 2017a, 2017b).

5.3.1.2 Results

Following the suggestion of Dr. Mortari (personal communication, 2016), some tests were performed with Pyramid using *k*-vectors of different sizes. These tests were performed in an IBM-PC notebook with 8GB of system RAM and a processor at 1.6GHz running Windows 7, by varying the size of the *k*-vector from about 0.004 to 1024 times the size of the list of pairs. For this test, the list of pairs had 129,678 pairs, which resulted in the *k*-vector size ranging from 507 to about 132.8 million elements. The list of observed stars was generated from a subset of the Hipparcos catalog limited at magnitude 7.0, and then corrupted by adding a Gaussian noise dependent on stellar magnitude to both stellar positions and observed stellar magnitudes, according to the algorithm *gen_sia_input_5* (FIALHO; 2007, Section 6.5.4) with $m_{offset} = -0.3$. The *k*-vector was derived from the same catalog, limited to magnitude 5.0. The simulated star tracker field of

view was a square 25.457° x 25.457° covering 1.545873% of the celestial sphere. Results are shown in Figure 5.7.

Figure 5.7 – Pyramid mean run time versus size of the *k*-vector.

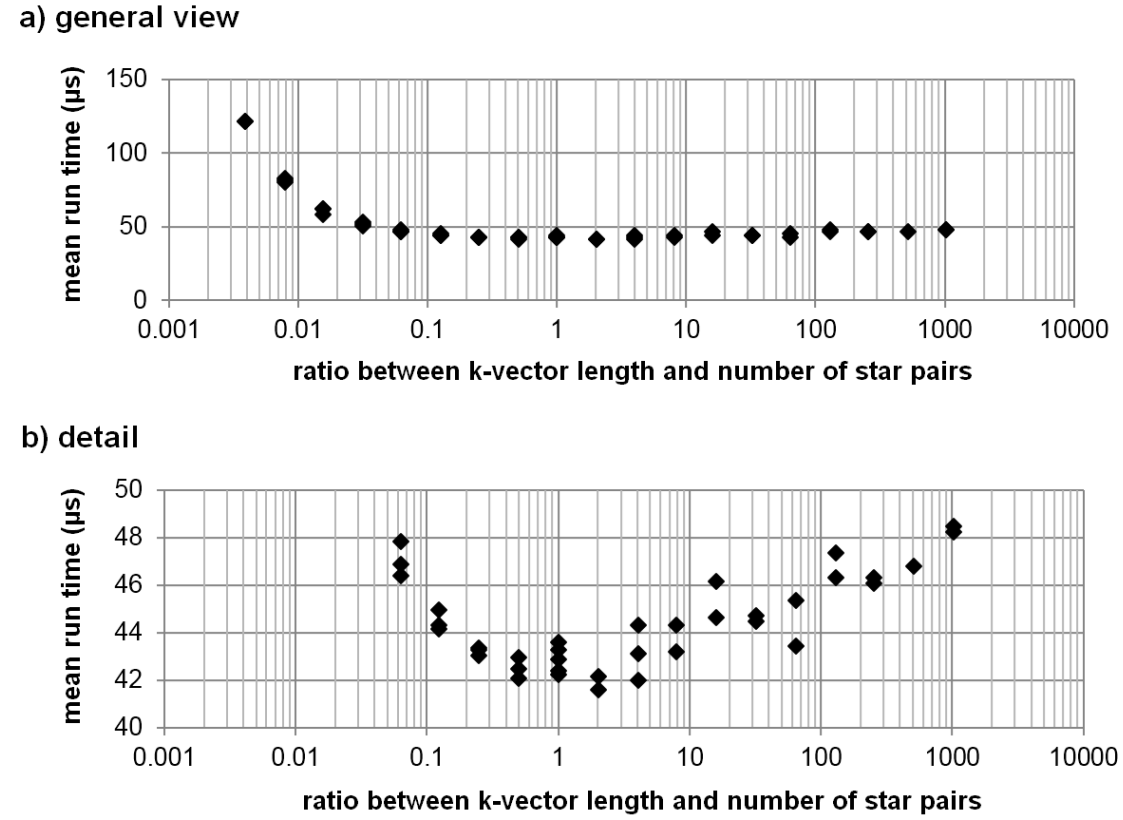

Source: Drawn by the author.

The Pyramid implementation used in this simulation purged all outliers returned by a *k*-vector access. In principle, for Pyramid, outliers could be kept, since they are very close to the requested angular separation range, being outside that range by a very small amount. For us it was not clear whether keeping or purging outliers would be faster. By one hand, not purging outliers saves time in the purging process, but increases the time spent on the triangle identification step (Section 5.2.5). A side effect of not purging outliers is that the effective tolerance for measured angular separation increases. Since we wanted to have this

parameter stable to perform other measurements during simulations, we have opted to purge outliers in our Pyramid implementation.

From Figure 5.7, it can be seen that as the size of the *k*-vector becomes smaller than about ¼ of the size of the list of pairs, Pyramid starts to run slower, as would be expected. However, for *k*-vectors larger than about four times the size of the list of pairs we can observe an increase in run-time with increasing *k*-vector size, which is counter-intuitive considering that a larger *k*-vector leads to less outliers being selected. This increase in run-time for larger *k*-vectors can be explained by the architecture of the machine used in the tests, where a larger *k*-vector leads to a higher rate of cache misses. For simple processors that do not include cache memories, such as the one used in the Brazilian star tracker (FIALHO; PERONDI; MORTARI, 2016), it is expected that larger *k*-vectors will not lead to a degradation in performance. More details about this experiment are given in a conference paper presented by the author (FIALHO; MORTARI, 2017a).

5.3.2 An improved kernel generator for Pyramid

Pyramid, like many other star-ID algorithms, first selects a small number of observed stars and attempts identification of this small group before advancing to the identification of the remaining stars. This small initial group of stars is named a *kernel* (ARNAS; FIALHO; MORTARI, 2017). If one or more stars in a kernel is a *spike* (a false star), the identification of that kernel fails, and Pyramid has to select another kernel from the list of observed stars. Hence the performance of Pyramid, especially in scenes with a large number of spikes, depends on how well the kernels are replaced. Ideally, the observed stars selected for the kernels should change as much as possible between successive kernels. A kernel of two stars is a *pair*, a kernel of three stars is a *triad*, and a kernel of four stars is termed a *quad* or a *pyramid*. Unfortunately, for the current accuracy achieved by star trackers, the number of pairs that match a given pair of observed stars is typically in the order of tens or hundreds. In order to reduce the number of spurious matches, at least three (and in some cases even four)

stars must be selected, that's basically the reason why Pyramid works with kernels of three stars (triads).

The original version of Pyramid (MORTARI et al., 2004) employs a simple sequence generator for triads which avoids persisting on a single reference star for too long. However, in a series of experiments performed by the author of this thesis, it was noted that this simple sequence generator could be improved with the inclusion of an additional inner loop which in most cases avoid the repetition of the same stars in successive triads. The original triad generator algorithm was named Pattern Shifting – PS in a journal paper co-authored by the thesis author (ARNAS, FIALHO, MORTARI, 2017). The new triad generator was named Enhanced Pattern Shifting (EPS). Listings in pseudo-code for both PS and EPS are present in the aforementioned paper. For the convenience of the reader, these listings are also presented here, in Figure 5.8 and Figure 5.9.

Improvements using the new algorithm become evident when the number of observed stars is equal to or larger than twice the size of kernels. For triads (kernels of size 3), when the number of observed stars is 6, we have the following sequences: For PS: 1-2-3, 2-3-4, 3-4-5, 4-5-6, 1-2-4, ... whereas for EPS: 1-2-3, 4-5-6, 2-3-4, 3-4-5, 1-2-4, ... If star 3 were a false star, the first three kernels generated by PS would fail, while in EPS only the first generated kernel would contain that false star. This simple example shows that EPS provides better variation of selected stars than PS.

Table 5.1 presents a comparison of the EPS versus PS kernel generators in terms of the *expected time to discovery* metric (MUELLER et al., 2016), being *n* the number of observed stars. The *expected time to discovery* metric gives the average number of kernels that must be tested until a kernel composed only of actual (cataloged) stars is found, under the simplifying assumption that the $\sum_{t=\kappa}^{n}\binom{n}{t}$ possible scenes of n observed stars having at least κ cataloged stars are equally probable. We consider a scene to be a particular combination of actual and false stars. κ is the number of stars in a kernel, being 3 for triads.

Figure 5.8 – Listing for the PS triad generator

```
for dj from 1 to (n-2) do
   for dk from 1 to (n-dj-1) do
      for i from 1 to (n-dj-dk) do
         j = i + dj;
         k = j + dk;
         next combination is (i, j, k);
      end
   end
end
```

Source: Mortari et al. (2004)

Figure 5.9 – Listing for the EPS triad generator

```
for dj from 1 to (n-2) do
   for dk from 1 to (n-dj-1) do
      for ii from 1 to 3 do
         for i from ii to (n-dj-dk) in steps of 3 do
            j = i + dj;
            k = j + dk;
            next combination is (i, j, k);
         end
      end
   end
end
```

Source: author

Table 5.1 – Expected time to discovery for PS and EPS for triads

n	PS	EPS	*n*	PS	EPS	*n*	PS	EPS
3	1.00	1.00	9	15.91	15.62	15	22.42	21.67
4	2.20	2.20	10	18.37	18.03	16	22.04	21.24
5	4.19	4.19	11	20.26	19.91	17	21.48	20.68
6	6.86	6.74	12	21.55	21.04	18	20.81	19.80
7	9.89	9.74	13	22.28	21.72	19	20.10	19.05
8	13.01	12.85	14	22.54	21.98	20	19.38	18.33

Source: Arnas, Fialho and Mortari (2017).

Table 5.2 compares EPS with PS using the *worst-case failure count sum* metric introduced by the author in Arnas, Fialho and Mortari (2017).

Table 5.2 – Worst-case failure count sum for PS and EPS for triads

n	PS	EPS	*n*	PS	EPS	*n*	PS	EPS
3	0	0	9	198	192	15	1564	1546
4	3	3	10	321	311	16	1999	1975
5	12	12	11	464	454	17	2520	2494
6	34	32	12	670	660	18	3192	3156
7	66	65	13	878	867	19	3781	3755
8	128	123	14	1239	1219	20	4695	4642

Source: Arnas, Fialho and Mortari (2017).

The *worst-case failure count sum* is the sum of the *worst-case failure count* metric (introduced by Arnas and Mortari) for the number of false stars varying from 0 to $n - \kappa$. For a given sequence generated by a kernel generator and a given number of false stars *f*, the *worst-case failure count* is the number of kernels that have to be tested before the first kernel composed solely of cataloged stars is found for the *worst* possible scene for that sequence having *n* observed stars and *f* false stars. The lower the value of the *worst-case failure count* and *worst-case failure count sum*, the better.

PS and EPS can be easily generalized for kernels of different sizes ($\kappa \neq 3$). Future work will compare the differences between PS, EPS and other proposed fast kernel generators (ARNAS, FIALHO, MORTARI, 2017) in Pyramid when typical configuration parameters that would be found in a real star tracker are used.

5.3.3 Optimized storage of star pairs

An optimization in the way star pairs are stored was performed. Instead of storing the *i* and *j* star indexes in different lists, they were stored in a single list, with the *i* star index of a star pair stored at an even position (2**k*) and corresponding *j* star

index stored at the consecutive odd position (2*k + 1). This change enabled some interesting optimizations in the C/C++ code, especially in the triangle identification step described in Section 5.2.5. With it, a sequence of eight different cases could be merged into a single test case, significantly reducing the size and complexity of the algorithm (in our implementation, from 108 lines to 36 lines of code in the part responsible for that task.

5.3.4 Mirror condition check for all triads

In the original version of Pyramid, the mirror condition check (described in Section 5.2.7) is not performed if a unique solution is found for a selected triad of observed stars when four or more stars are observed. Also, in that version, all triangles of candidate stars that match the observed triad within measurement tolerances, including mirror solutions, are saved to a list. The mirror solutions are purged from this list in a later step.

One of the changes introduced by the author of this thesis is to perform the mirror condition test inside the routine responsible for finding candidate triangles (Section 5.2.5), so mirror solutions are discarded before being stored in the output list of this routine. This change had the benefits of reducing the amount of memory needed by the star-ID algorithm and improving its robustness. Simulation results are shown in Section 5.4.5.

5.3.5 Limit to the number of kernels to be tested

If a large number of stars is observed, the number of different triangles (kernels) that can be assembled from these is very large. For example, for n = 50 observed stars, the total number of triangles that can be formed is $\binom{50}{3} = \frac{50!}{47!\ 3!} = 19{,}600$. If the STR is unfortunate enough that all the stars in that scene being identified are false stars, Pyramid could spend a large amount of time attempting identification on that scene before exhausting all possible combinations, whereas the STR could probably return a valid attitude faster if it gave up on that difficult

scene and started over, acquiring a new image. Plus, a successful identification obtained after many attempts on a difficult scene containing many false stars (spikes) has a higher probability of being incorrect. Besides that, the presence of spikes on an image is sometimes a transient phenomenon, disappearing in the following image frame. Spikes could originate, for example, due to stray light entering the star tracker optics while the spacecraft is maneuvering. Another cause for spikes is ionizing radiation, as discussed in Section B.2.12 of the appendices. Therefore, a mechanism to abort identification on difficult or impossible to solve scenes is required and beneficial in terms of identification reliability. In an embedded hardware, this could be implemented with a timeout mechanism. In our implementations of Pyramid, we have opted to limit execution time with a limit to the number of kernels to be tested, as this mechanism is simpler to implement.

5.3.6 Augmenting Pyramid with stellar magnitudes

Even though the basic version of Pyramid presents an impressive performance and a very good robustness, with a misidentification rate less than 10^{-6} for typical star tracker parameters, its robustness can be further enhanced if it is augmented with a magnitude check, since any additional information about stars is useful in confirming their identity. This is especially true for the cases where there are few observed stars (three or four stars).

A magnitude check was added for all triads found by the triangle identification step (Section 5.2.5). Being m_{obs} the observed magnitude of star alpha, beta or gamma and *tol_mag* the magnitude tolerance, a triad of cataloged stars is rejected if for any of alpha, beta or gamma the corresponding cataloged star magnitude is outside the open interval given by (m_{obs} – *tol_mag*, m_{obs} + *tol_mag*). Only triads of cataloged stars that pass this magnitude test are saved, hence, this magnitude test reduces the amount of memory needed for storing possible solutions.

The same magnitude check was also added for the confirmation star *r* and for the identification of the remaining stars. Simulation results are shown in Section 5.4.8.

5.3.7 Augmenting Pyramid with color indices

Likewise to what happen with the inclusion of magnitude information, the use of color information can further improve star identification robustness. This color information is usually expressed as color indices, each color index being the difference of star magnitudes in two spectral bands, as explained in Appendix C, Section C.2. Optional color index checks have been added for the three stars belonging to a candidate triad returned by the triangle identification step. Considering that the majority of star trackers are monochrome and would not be able to observe the color indexes of stars, these optional checks can be ignored during compilation simply by setting a compilation directive. Simulation results when using Johnson's $B-V$ and $V-I$ color indexes as given in the Hipparcos catalog are shown in Section 5.4.9 and in Section 5.4.10.

With the addition of magnitude and color index checks, in theory, it would be possible to determine attitude with only two observed stars. However, the probability of an ambiguous identification or a misidentification happening with only two observations is very high, even with the additional checks of magnitude and color indexes. Therefore, the author has decided to keep $n = 3$ as the bare minimum number of observed stars required for identification in the modified versions of Pyramid.

5.4 Monte Carlo simulations

This section describes results of the improvements in the Pyramid star-ID algorithm, described in the previous section, using the simulation environment described in Chapter 4.

5.4.1 Versions of the algorithm

To distinguish the C++ implementations used in the Monte Carlo simulations from the original description of Pyramid, the prefix “mf” will be added to the name of the various versions of the algorithm tested here. This prefix was created from the first letters of the first and last name of the author of this thesis. Many versions of the algorithm were created during development. From these, the most important for this work are:

a) *mfPyramid v01* – This is the version which was chosen as the baseline for the Monte Carlo simulations. This version implements the changes described in Section 5.3.1, Section 5.3.2 and Section 5.3.3. This version will be described in more detail in Section 5.4.4.

b) *mfPyramid v02* – This version includes all modifications introduced by the author in *mfPyramid v01* plus the following modifications:

   - added a limit to the number of kernels to test (Section 5.3.5);
   - included the magnitude filter (Section 5.3.6);

   This version was not used in the simulation results shown in the following sections.

c) *mfPyramid v03* – This version includes all modifications introduced by the author in *mfPyramid v01* and *mfPyramid v02* plus the following:

   - mirror condition test for all candidate triangles of cataloged stars (Section 5.3.4);
   - inclusion of $B-V$ and $V-I$ color index filters (Section 5.3.7).

5.4.2 Configuration used for Monte Carlo simulations

This section presents the configuration which was used for the Monte Carlo simulations described in the following sections.

Since one of the goals of the Monte Carlo simulations was to measure the misidentification rate, and this misidentification rate is typically very small, to make it measurable without having to run the star-ID algorithm hundreds of million times, which would take a prohibitively long time, we have considered in our simulations a very coarse hypothetical star tracker, with standard deviation in centroid position in the order of minutes of arc. To do that, we modified a parameter in *gen_sia_inputx* (described in Chapter 4) that defines the imager width and height in pixels, from the default value of 1024 pixels to 128 pixels, while still keeping the simulated star tracker field of view at 25.457° × 25.457°. This had the effect of increasing the angular width and height of the central pixel in the imager from 91 arc-seconds to 728 arc-seconds. Since the standard deviation in position in *gen_sia_inputx* (for $x \geq 6$) are scaled by the pixel size, increasing the pixel size has the effect of increasing position noise in the simulated observed stars. With this noise level, the tolerance δ_θ used for selecting star pair candidates from the catalog of star pairs has to be increased proportionally to keep the success rate at acceptable levels.

Algorithms *gen_sia_inputx* (with x = 5,...,8 being the version number) have a configuration parameter m_{offset} that can be used to simulate the star tracker sensitivity to light, as explained in Section 4.4. Positive values of m_{offset} mean increased sensitivity to dim stars, whereas negative values of m_{offset} mean decreased sensitivity. In an actual star tracker, this change in sensitivity is usually accomplished through a change in exposure time, since many other parameters that also affect sensitivity such as optics aperture and image sensor quality are usually set to their best design values and cannot be easily changed.

In an actual application, there's always the desire to work with the shortest exposure time (or more precisely, integration time) that will enable detection of

the minimum number of stars required for a reliable identification. This is justified by the fact that long exposure times lead to blurring in star images if the spacecraft is slowly rotating. Another strong reason is related to the time needed for attitude acquisition and to the rate of attitude update in attitude tracking mode. In modern wide field of view star trackers, the limiting factor for attitude acquisition and update rate is no longer the processing power, but the minimum exposure time required to detect stars[7]. However, a too low exposure time will decrease the star tracker availability, since in that case there will be many scenes without sufficient stars for stellar identification and attitude determination. To select the value of m_{offset} to be used in the simulations, it was assumed that the simulated star tracker had a requirement of an attitude acquisition probability from its first acquired image of at least 99%, in other words, provided that its field of view is not obstructed or blinded by bright sources (Sun, Moon or Earth), it should be able to acquire an attitude in more than 99% of the cases without having to acquire a new image, assuming a random and uniformly distributed initial attitude.

After many tests, the minimum value of m_{offset} that was found to give an availability of at least 99% was $m_{offset} = -0.42$. This was taken as the baseline configuration for our tests.

With this configuration, the value of the angular separation tolerance δ_θ in star pairs that provided the best star tracker availability (or success rate) was $\delta_\theta = 170$ arc-seconds. This value was selected for our baseline.

In the simulations presented here, the effects of stellar aberration (Section 2.5) were not included. Considering that the angular separation tolerance of 170 arc-seconds adopted here is much wider than the maximum, worst-case, apparent displacement in star positions of 28 arc-seconds due to stellar aberration for an

[7] In a wide FOV star tracker employing an old generation processor running at 12 MHz, star identification takes, on average, less than 0.6 s using a slow star-ID algorithm and less than 40 ms using a fast star-ID algorithm (FIALHO, 2007). These are comparable to 400 ms of minimum exposure time needed to detect enough stars in all sky configurations in the same STR design.

Earth orbiting spacecraft[8], not including this effect in the simulations will have little or negligible impact in the results obtained. However, simulations using much tighter tolerances should include this effect.

Following is the configuration used in all tests, except where noted otherwise:

- Global parameters:
  - Simulated star tracker FOV: square FOV of 25.4570° × 25.4570°
  - Catalog used by *gen_sia_input6* and *gen_sia_input8* for generating the list of observed stars: limited at visual magnitude 7.0 with 15,513 stars (files: `cat_m7g.cat` or `cat_m7gc2.cat`)
  - Catalog used for star identification: subset of catalog used by *gen_sia_input6* and *gen_sia_input8* containing the brightest 1612 stars (limited to visual magnitude 5.0)
- Default parameters used by *gen_sia_input6* / *gen_sia_input8*:
  - m_{offset} = −0.42 ==> 99% probability of star detection at m_v = 3.37; 50% probability of star detection at m_v = 4.466 and 1% probability of star detection at m_v = 5.20.
  - imager resolution (width and height): 128 pixels ==> pixels near the center of the array have an angular size of 728".
  - maximum number of stars in the output: unlimited.
- Default parameters for *mfPyramid v01* and *mfPyramid v03*:
  - angular separation tolerance (δ_θ): 170"
  - min_sep: 0.03 * $FOV_{diagonal}$ = 1.06295°
  - max_tries: 15 (maximum number of kernels to use before giving up, introduced in *mfPyramid v02*)
  - number of stars used for identification: 1612 ==> catalog of star pairs with 129,678 star pairs.
  - $k_{vector\_size\_ratio}$ = 1.5 => k-vector with 194,517 elements.

[8] Assuming that the master catalog has its origin at the Solar System's barycenter.

All tests were performed on a machine with the following configuration:

- processor: Intel® Core™ i7-4500U @ 1.80 GHz / 2.40GHz;
- memory: 8GB;
- operating system: Windows10 64-bit.

5.4.3 Presentation of results

Simulation results are presented in the following sections, being summarized in Table 5.3 to Table 5.9. Each row in these tables represents the results of a Monte Carlo simulation where *mfPyramid v01* or *mfPyramid v03* was run 10^6 times, except for the last row, that gives the averages of the five Monte Carlo simulations with a given configuration, for a total of 5,000,000 star-ID runs.

The first column gives the Monte Carlo simulation test number. This is a number that identifies a Monte Carlo simulation in PTASE log files, it starts at 1 when the program is loaded and is incremented at every test. The log files from where the data presented in the tables was extracted is indicated. These log files have been made available on-line[9] as supplementary material to this thesis.

The second and third columns present the rate in which attitudes computed from the stars identified by the algorithm had significant errors, greater than 1 degree and 30 degrees, respectively.

The fourth column provides the rate in which the attitude was successfully computed with an error less than 1°.

The current version of PTASE is not able to check if stellar identification was correct or incorrect by comparing cataloged star indexes obtained from the star-ID algorithm with the actual cataloged star indexes used to generate the lists of observed stars fed to it, being this a planned modification for the future. The

[9] Stored in a zip archive available in the following URLs:
http://urlib.net/8JMKD3MGP3W34P/3PN626S and
https://figshare.com/articles/MarcioFialho_PTASE_results_2017_zip/5455480
Archive uploaded to two different URLs for redundancy.

reason for this limitation is that in PTASE the attitude determination algorithms are called as subroutines of the star-ID algorithm and the final result of a star-ID algorithm under test is the estimated STR attitude. Since in the current implementation the individual star identities are not returned by the star-ID algorithm to the routine that controls simulation, it has no means of checking if the stars were correctly identified. The rationale for the design decision of implementing first the verification of the final estimated attitude and letting for the future the codification of the verification of the identities of individual stars when writing PTASE is that the true identity of identified stars is of little or no importance to the attitude and orbit control subsystem (AOCS) that consumes the data generated by a star tracker. For the AOCS what really matters is how close the estimated attitude is to the actual attitude.

The maximum acceptable attitude error given by a star tracker depends on the mission requirements, being typically much smaller than 1°. Given that we have used a very coarse hypothetical star tracker to make the misidentification rate observable (as explained in Section 5.4.2), the threshold between valid attitudes and invalid attitudes had to be increased accordingly. In our analysis, we regard attitude errors between 1° and 30° as severe, and attitude errors larger than 30° as very severe. These limits have been set arbitrarily for this work. The reason for a separate class of attitude errors larger than 30° is that, for the coarse star tracker used in the simulations, a tail was observed in the main mode of the distribution of the attitude errors extending beyond 1°. This main mode (with its peak close to 2 arc-minutes) contains the valid star identifications, implying that some cases counted in the severe attitude error class might have resulted from valid star identifications where “measurements” were unluckily severely affected by noise. On the other hand, we can confidently state that all cases where attitude errors were larger than 30° (very severe attitude errors) resulted from misidentifications, since an attitude error larger than 30° is too large to be explained solely by “measurement noise” even when considering the very coarse hypothetical star tracker used in the Monte Carlo simulations. Therefore, the

count of attitude errors larger than 30° can be used as a proxy for the number of misidentifications. A crude histogram of the attitude errors can be seen in the log files generated by PTASE.

The values provided in column 2 are the sum of both severe and very severe attitude error cases. These errors in attitude estimation were computed using the approximate Equation (4.8) from Section 4.5, instead of the exact Equation (4.7). Therefore, the values quoted in the tables, especially for the very severe attitude error rate (>30° attitude error), should be regarded as approximate instead of exact.

The fifth column gives the star-ID failure rate: the percentage of cases were the star-ID was unable to identify a scene. Some of these are results of scenes impossible to be identified – scenes having less than 3 observed stars. Others might be a result of the limit used of a maximum 15 kernels to be tested before giving up.

The sixth column gives the averages of the attitude error for each Monte Carlo simulation, computed using the first order approximation given by Equation (4.8), considering only those cases were the attitude error was less than 1°.

The seventh and last column gives the duration of each Monte Carlo simulation in seconds.

5.4.4 Tests with a baseline version

The first sequence of Monte Carlo simulations presented here were performed with *mfPyramid v01*, which was chosen as the baseline for further modifications. This version was implemented in C++ by the author, being based on Matlab and C codes of Pyramid provided by Mortari and Bruccoleri (2016, personal communication). This version differs from the original Pyramid algorithm implemented in Matlab in several points. The most important differences are the following:

a) the inclusion of the memory adaptive *k*-vector described in Section 5.3.1;

b) the inclusion of the new kernel generator described in Section 5.3.2;

c) the inclusion of the optimization in storage of star pairs described in Section 5.3.3;

d) the analytical frequency test that a spurious match could be made between the observed star polygon and a polygon built with cataloged stars (MORTARI et al., 2004, p. 177) was not included in this implementation;

e) the cache mechanism used to avoid identical information requests to the list of star pairs and *k*-vector (MORTARI et al., 2004, p. 176) was not implemented;

f) the mirror condition check was not being performed for the most common case of $n > 3$. Later this was found to be caused by an implementation error, fixed in *mfPyramid v03*.

The justification for these implementation differences are the following:

- Regarding item d), the spurious match frequency filter was not implemented because one of the goals of the Monte Carlo tests was to measure the base rate of stellar misidentification in the very unfavorable conditions of the test.

- Regarding item e), it was initially not implemented due to the fact that it was not essential for having a working version of Pyramid on PTASE. Later, after profiling the code with the `gprof` tool, it was found that the C++ implementation of Pyramid in PTASE (mfPyramid) was spending on the development machine less than 5% of its CPU time on accesses to the *k*-vector and to the database of star pairs, meaning that implementation of this cache mechanism would probably bring little performance improvements in the test machine. Another factor against its

implementation is the large memory requirements of the table necessary for storing it, whose size is proportional to $n^2 \cdot N^2 \cdot \varepsilon$, being n the number of observed stars, N the number of catalog stars used for identification and ε the tolerances used in angular separations. Nevertheless, its implementation and testing on an embedded platform could be done in the future, with the goal of performing speed-space tradeoff studies.

These tests were performed using a monochromatic star catalog (`cat_m7g.cat`), with the list of observed stars generated by *gen_sia_input6* sorted by their position in the field of view, mimicking the typical order that would be returned by an image processing algorithm in an actual star tracker if a sorting subroutine is not implemented. Results are presented in Table 5.3.

Table 5.3 – Results obtained with *mfPyramid v01* for 10^6 Monte Carlo runs per row, with observed stars sorted by position in the FOV

test nbr.	rate of incorrect attitude determination with error: > 1°	> 30°	success rate with att. error less than 1°	failure rate	mean attitude error[(c)]	raw measured run time[(d)]
2[a]	0.4115%	0.3445%	98.718%	0.871%	128.795”	418.90 s
4[a]	0.4044%	0.3397%	98.705%	0.891%	128.684”	401.15 s
8[b]	0.4044%	0.3392%	98.739%	0.856%	128.759”	400.72 s
9[b]	0.4129%	0.3545%	98.696%	0.892%	128.774”	402.70 s
11[b]	0.4210%	0.3553%	98.725%	0.854%	128.659”	401.50 s
mean	0.4108%	0.3466%	98.717%	0.873%	128.734”	401.52 s

data from files: a = ptase_20170814_v01.log; b = ptase_20170814_v02.log.
For downloading these files, see footnote on Section 5.4.3.
[(c)] considering only attitude determinations with errors less than 1 degree.
[(d)] The value in red is suspected to have been affected by background processes running on the test machine, being excluded from the computation of the mean run time.
Source: created by the author.

The measured misidentification rate of around 0.4% is in good agreement with the theoretical estimates given by (MORTARI et al., 2004) and Fialho (2007) when the mirror condition for triads is not checked. Later, it was found that this

baseline algorithm was not checking mirror condition when n ≥ 4. It should be noted that these theoretical estimates are not very accurate, since they assume that the stars are distributed on the sky following a uniform distribution, which is not true, stars tend to accumulate in the galactic plane.

Interpretation of speed measurements: Values shown in Table 5.3 also include the time spent in *gen_sia_input6* generating the list of observed stars. Performing tests with a dummy star-ID algorithm that returned immediately, just to measure the time overhead imposed by *gen_sia_input6* and PTASE has shown that this time overhead was 38.67 ± 0.07 seconds for 10^6 runs. Subtracting this overhead from the raw measured run time average, we conclude that *mfPyramid v01* took on average 362.8 μs to perform star identification on the test machine with the settings used – tests have shown that with the tolerances used in a typical star tracker, *mfPyramid* can be more than 10 times faster. As a final remark, it should be noted that speed measurements performed on the test machine are not very reliable (see Section 5.4.11.2).

5.4.5 Checking for mirror condition in all triads

Adding a verification for mirror condition for all triangles of candidate stars from the catalog reduces the incorrect attitude determination rate by half, as can be seen in Table 5.4. This modification also led to improvements in the success rate, mean attitude error, in the speed of the algorithm and a decrease in the failure rate.

These tests were performed using *mfPyramid v03* with all new features described in Section 5.3 “disabled”, except for the mirror condition test, now performed for every candidate triangle.

In the new version of PTASE, running *gen_sia_input8* and *mfPyramid v03*, the time overhead of *gen_sia_input8* and PTASE, included in the results shown in this section and following sections, was measured as 40.81 ± 0.04 s for 10^6 Monte Carlo runs.

Table 5.4 – Raw results obtained with *mfPyramid v03* for 10^6 Monte Carlo runs, with observed stars sorted by position in the FOV and no limit to the number of kernels

test nbr.	rate of incorrect attitude determination with error: > 1°	> 30°	success rate with att. error less than 1°	failure rate	mean attitude error	raw measured run time*
7	0.1954%	0.1695%	99.013%	0.792%	126.983”	308.31 s
9	0.1993%	0.1725%	98.998%	0.803%	127.118”	309.78 s
10	0.1967%	0.1705%	98.985%	0.818%	127.220”	309.81 s
11	0.1901%	0.1658%	99.012%	0.798%	127.214”	308.19 s
13	0.1996%	0.1723%	99.017%	0.784%	127.174”	309.49 s
mean	0.1962%	0.1701%	99.005%	0.799%	127.142”	309.11 s

data from file: ptase_20170926_v01.log
*see important remark at the end of this section when interpreting data from this column.
Source: created by the author.

A remark about speed measurements: Since speed measurements performed on a PC running MS-Windows are not very reliable (see Section 5.4.11.2) and considering that the expected computational cost of the additional comparisons present in the new filters and limit added in *mfPyramid v03* is negligible in comparison to other steps in the algorithm, it was considered not worth the effort of building, managing and running different versions of PTASE solely for taking speed measurements accurately. Therefore, to remove the effects of filters and limit added in *mfPyramid v03* which were not being used in the tests (in this section and following sections), the approach adopted here was to set very large tolerances/values for them that will never be reached in practice, effectively disabling them. The values used to “disable” these filters and limit were: tolerances of 10,000.0 mag. for magnitude, $B-V$ and $V-I$ color indexes filters and a limit of 1,000,000,000 kernels to be tested. With this approach, the sole effect of these filters and limit should be a very small increase in the execution time of the algorithm, an increase which was not quantified in this study.

5.4.6 Limiting the number of kernels to be tested

Table 5.5 presents the results obtained with *mfPyramid v03* when the limit of the number of kernels to be tested was set to 15.

Table 5.5 – Raw results obtained with *mfPyramid v03* for 10^6 Monte Carlo runs, with observed stars sorted by position in the FOV and a maximum of 15 kernels tested

test nbr.	rate of incorrect attitude determination with error: > 1°	> 30°	success rate with att. error less than 1°	failure rate	mean attitude error	raw measured run time*
1	0.1963%	0.1687%	98.591%	1.213%	126.886”	303.094 s
2	0.1931%	0.1674%	98.594%	1.213%	127.081”	302.916 s
3	0.1935%	0.1697%	98.599%	1.208%	126.942”	302.518 s
4	0.1926%	0.1667%	98.573%	1.234%	127.225”	303.635 s
5	0.1931%	0.1638%	98.587%	1.220%	126.924”	303.394 s
mean	0.1937%	0.1673%	98.589%	1.217%	127.012”	303.111 s

data from file: ptase_20170731_v04.log
*see important remark at the end of Section 5.4.5 when interpreting data from this column.
Source: created by the author.

The inclusion of this limit led to an increase in the speed of the algorithm and a very slight, almost unnoticeable, improvement in the misidentification rate. However, the success rate decreased and the failure rate (proportion of scenes where the algorithm was unable to identify stars) increased. It should be noted, nonetheless, that the simulations presented in this chapter did not include false stars. In a real application, where false stars might be present, the inclusion of a limit to the number of kernels to be tested is beneficial due to the reasons presented in Section 5.3.5. Also, the value chosen for this limit of maximum 15 kernels tested was not optimal for the Monte Carlo simulations performed in this work.

5.4.7 Pre-sorting observed stars by magnitude

Using exactly the same *mfPyramid* code, with exactly the same parameters as used in the previous section, a series of five Monte Carlo simulations was performed, with the only difference being that the list of observed stars was sorted in *gen_sia_input8* by observed magnitude. Results are shown in Table 5.6.

Table 5.6 – Raw results obtained with *mfPyramid v03* for 10^6 Monte Carlo runs, with observed stars sorted by magnitude.

test nbr.	rate of incorrect attitude determination with error: > 1°	> 30°	success rate with att. error less than 1°	failure rate	mean attitude error	raw measured run time*
2[b]	471 ppm	451 ppm	99.042%	0.911%	112.744”	453.458 s
1[a]	452 ppm	431 ppm	99.057%	0.898%	112.643”	454.397 s
3[b]	489 ppm	474 ppm	99.042%	0.909%	112.566”	453.336 s
4[b]	455 ppm	440 ppm	99.062%	0.893%	112.671”	453.278 s
7[b]	455 ppm	439 ppm	99.056%	0.898%	112.640”	455.367 s
mean	464 ppm	447 ppm	99.052%	0.902%	112.653”	453.967 s

data from files: a = ptase_20170727_06.log; b = ptase_20170801_01.log.
*see important remark at the end of Section 5.4.5 when interpreting data from this column.
Source: created by the author.

It is interesting to note that even though nothing had changed, simply by sorting observed stars by magnitude a major reduction in the misidentification rate was observed. This can be explained by a quirk in the simulation. Since *gen_sia_input8* does not generate random false stars (all observed stars were taken from the larger star catalog limited at magnitude 7), bright observed stars will surely be present in the shorter star catalog (limited at magnitude 5) used by the star-ID algorithm, whereas for dim observed stars, there is some probability that some of them will be generated from cataloged stars with a magnitude greater than the magnitude limit of the shorter star catalog used for identification, thus behaving in the simulation as if they were false stars (spikes). If a spike is

matched with a cataloged star, this matching will surely be a misidentification. Hence, the identification of dimmer stars has a higher probability of being incorrect. This explains the abrupt reduction in the misidentification rate observed in this test. In a real star tracker, the effect of sorting observed stars by magnitude in reducing misidentification rate is probably not as large as in this simulation, since in a real scenario, bright false stars can occasionally occur. Nevertheless, this simulation shows the importance of using first observed stars having the least probability of being false stars in the process of star identification. Most likely, these are the brightest ones. A more detailed investigation about this effect, including the injection of false stars, should be performed in the future.

A significant increase in the run time was also observed. Multiple simulations performed at different times and using different machines confirmed that this increase was a real phenomenon, not an effect of background processes running in the test machine. A possible explanation for this seemingly strange behavior is the following: The image processing algorithm usually process the raw image starting from the top lines and progressing to the bottom. As clumps of pixels above a certain threshold are found, they are assumed to belong to a potential observed star, thus having their centroid computed and stored in an output list (list of detected stars in Figure 2.1). The algorithm *gen_sia_input8* was used in Section 5.4.6 with a setting that mimics this behavior of the image processing / centroid extraction algorithm by sorting the generated list of observed stars by their position in the FOV. When stars are sorted by position, the mean length (angular separation) of the star pairs alpha-beta, alpha-gamma and beta-gamma will be smaller than the case when observed stars are sorted by magnitude (as in this test). Assuming a uniform distribution of catalog stars on the celestial sphere, a smaller angular separation between the observed stars forming a pair means less star pairs from the catalog matching that observed star pair, according to Equation (7) in Mortari et al. (2004).

5.4.8 Using magnitude as a filter

Simulations performed in the previous sections were done with a magnitude filter tolerance of ± 10000.0, effectively disabling it, since stars have much shorter magnitude range. For example, considering all stars in the Hipparcos catalog (ESA, 1997), the magnitude range in the V band goes from −1.44 (for the brightest star) to about +13.6 (for the dimmest). Reducing the tolerance in magnitude, there is a slight increase in the success rate until a certain point. Tightening the magnitude tolerance even further causes a reduction in the success rate with a significant decrease in the rate of attitude misidentifications. The turning point seems to be around a magnitude tolerance of ± 1.5. Similar behavior was observed with the tolerances used for $B-V$ and $V-I$ color indexes. After some experimentation, it was decided to use the same value of 0.9 for these tolerances as these filters were "enabled" in this and following sections. This value was chosen because it is the tightest value that did not result in a reduction in the success rate as new filters were enabled. Table 5.7 shows results after setting only the magnitude tolerance to ± 0.9 (color indexes tolerances remaining at ± 10,000.0).

Using magnitude as a filter, a reduction in the incorrect attitude determination rate by a factor of roughly 6 was observed. Even though the reduction in the number of candidate stars for each observed star is not that large (with a tolerance of 0.9, it could typically lead to elimination of 35% to 50% of the candidate stars), their combined effect becomes appreciable. In fact, if we assume that this magnitude tolerance leads on average to a reduction of 45% in the number of candidate stars, the expected frequency of spurious catalog matches would reduce by a factor of $1/(0.55)^3 \approx 6$ if it is applied to three stars. This happens because the frequency of spurious star pattern matching is proportional to the product $N_1 \cdot N_2 \cdot \ldots \cdot N_k$, being N_i the number of candidate stars from the catalog for star i in a pattern with k stars.

Table 5.7 – Raw results obtained with *mfPyramid v03* for 10^6 Monte Carlo runs, with observed stars sorted by magnitude, and *V* magnitude tolerance of ± 0.9

test nbr.	rate of incorrect attitude determination with error: > 1°	> 30°	success rate with att. error less than 1°	failure rate	mean attitude error	raw measured run time*
1[a]	87 ppm	82 ppm	99.216%	0.775%	108.570”	299.788 s
6[a]	66 ppm	58 ppm	99.221%	0.772%	108.602”	301.037 s
7[a]	71 ppm	67 ppm	99.227%	0.766%	108.699”	301.773 s
8[b]	71 ppm	68 ppm	99.220%	0.773%	108.721”	302.170 s
9[b]	87 ppm	85 ppm	99.223%	0.769%	108.793”	300.352 s
mean	76 ppm	72 ppm	99.221%	0.771%	108.677”	301.024 s

data from files: a = ptase_20170727_05.log; b = ptase_20170801_01.log
*see important remark at the end of Section 5.4.5 when interpreting data from this column.
Source: created by the author.

With the inclusion of the magnitude filter, a significant reduction of the processing time was observed. This can be attributed to a reduction of ambiguous identifications in the triangle matching phase, resulting in less kernels being rejected in *mfPyramid*. We also observed a decrease in the failure rate and in the mean attitude error (from 112.7” to 108.7”).

5.4.9 Using the *B*−*V* color index as an additional filter

Enabling the filter based on the Johnson’s *B*−*V* color index (ESA, 1997) with a tolerance of ± 0.9 on top the magnitude filter enabled in the previous section, gave a further reduction in the misidentification rate.

Considering values of the attitude error > 30°, the misidentification rate reduced by a factor of about 3.8, a significant reduction. A slight improvement in star identification speed was also observed. This can be attributed to a reduction in ambiguous and incorrect identification of triangles. The mean attitude error and success rate remained practically the same.

Table 5.8 – Raw results obtained with *mfPyramid v03* for 10^6 Monte Carlo runs, with observed stars sorted by magnitude, using magnitude filter and *B*−*V* color index filter

test nbr.	rate of incorrect attitude determination with error: > 1°	> 30°	success rate with att. error less than 1°	failure rate	mean attitude error	raw measured run time[(c)]
2[a]	28 ppm	21 ppm	99.226%	0.771%	108.523”	296.457 s
5[a]	20 ppm	15 ppm	99.233%	0.765%	108.617”	296.265 s
8[a]	31 ppm	24 ppm	99.232%	0.765%	108.508”	296.437 s
12[b]	19 ppm	14 ppm	99.239%	0.759%	108.542”	295.898 s
15[b]	29 ppm	22 ppm	99.223%	0.774%	108.602”	294.820 s
mean	25 ppm	19 ppm	99.231%	0.767%	108.558”	295.975 s

data from files: a = ptase_20170727_05.log; b = ptase_20170801_01.log
[(c)]see important remark at the end of Section 5.4.5 when interpreting data from this column.
Source: created by the author.

5.4.10 Using the *V*−*I* color index as an additional filter

Enabling the filter based on the Johnson’s *V*−*I* color index (ESA, 1997) with a tolerance of ± 0.9 on top the magnitude filter and *B*−*V* filters enabled in the previous sections lead to the results shown on Table 5.9.

The inclusion of the *V*−*I* color index filter in the selection of stars resulted in a reduction of the misidentification rate by a factor of roughly 2, however this come at a cost of a slight increase in the failure rate. No changes in the mean attitude error nor in the execution time of statistical significance were observed.

Table 5.9 – Raw results obtained with *mfPyramid v03* for 10^6 Monte Carlo runs, with observed stars sorted by magnitude, using magnitude filter plus $B-V$ and $V-I$ color index filters

test nbr.	rate of incorrect attitude determination with error: > 1°	> 30°	success rate with att. error less than 1°	failure rate	mean attitude error	raw measured run time[(c)]
3[a]	10 ppm	5 ppm	99.228%	0.771%	108.537”	296.248 s
4[a]	22 ppm	14 ppm	99.211%	0.787%	108.637”	295.288 s
9[a]	17 ppm	9 ppm	99.195%	0.803%	108.489”	295.279 s
14[b]	13 ppm	7 ppm	99.209%	0.790%	108.631”	295.885 s
17[b]	20 ppm	10 ppm	99.200%	0.798%	108.738”	294.587 s
mean	16 ppm	9 ppm	99.209%	0.790%	108.606”	295.457 s

data from files: a = ptase_20170727_05.log; b = ptase_20170801_01.log.
[(c)]see important remark at the end of Section 5.4.5 when interpreting data from this column.
Source: created by the author.

5.4.11 Discussion

Given the specifications of the coarse star tracker used in the simulations, we can confidently state that all cases of very severe attitude errors (errors larger than 30°) result from misidentifications, whereas in the severe class (errors between 1° and 30°), some of these could be the result of a partial misidentification (where some stars are correctly identified and others are incorrectly identified) or a correct identification where each star had an extremely large measurement error in their position, since many cases of attitude errors between 1° a 5° seem to be at the tail of attitude error distribution. Further analysis will be needed to understand exactly what is happening in these cases.

Figure 5.10 summarizes the reduction in the frequency of severely incorrect attitude determinations versus the modifications tested in this section. This frequency of incorrect attitude determinations serves as a proxy for the misidentification rate of the algorithm.

Figure 5.10 – Reduction of the rate of incorrect attitude determination versus each new added feature.

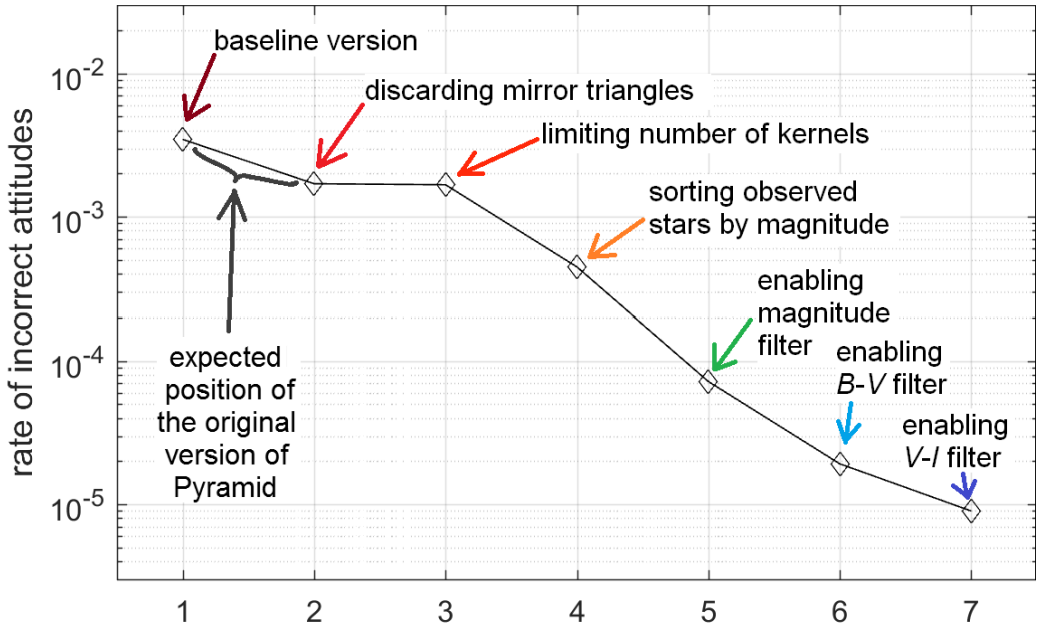

Source: Drawn by the author.

It can be seen that, proportionally, the most significant reduction of the mis-ID rate was obtained with the inclusion of the magnitude filter (reduction by a factor of 6.2 in the rate of incorrect attitudes), followed by the inclusion of the first color index filter (reduction by a factor of 3.8 in the rate of mis-ID) and pre-sorting the list of observed stars by magnitude (reduction by a factor of 3.7 in the rate of misidentifications). Removing all mirror triangles in the triangle identification step (Section 5.3.4) reduced the misidentification rate by 2. Addition of a secondary color index reduced the misidentification rate by 2, at a cost of a slight decrease in the success rate. The effect of adding a limit of maximum 15 kernels to be tested was very small in the misidentification rate. The original version of Pyramid was not tested, since to test it in PTASE would demand many modifications in the original code to make it compatible with the program. But judging from its code and from the fact that it checks mirror condition for most triangles, but not in every case, it is expected that its misidentification rate would be intermediate between the “baseline version” and the test configuration labeled “discarding all mirror triangles” (numbers 1 and 2 in Figure 5.10).

Taken in isolation, each of these new features don't seem to provide a significant increase in the star identification reliability, but when all these modifications are taken into account, they lead to a reduction of more than 2 orders of magnitude in the misidentification rate.

5.4.11.1 Use of additional bands

As shown by the simulations, the verification of additional spectral bands can give further gains for stellar identification, but with diminishing returns for each new spectral band included, since each new spectral band introduced becomes more and more correlated with the previous ones. This becomes clear in the color-color diagram shown in Figure 5.11. From this diagram, it is evident that there is a significant correlation between the $V-I$ and $B-V$ color indexes. Therefore, when designing a color star tracker, a balance on the number of spectral bands added must be made considering the benefits of additional color information and the drawbacks of increased system complexity and cost. These considerations would probably favor monochrome star trackers. However, when we consider that color information enables to diagnose optics degradation caused by ionizing radiation (usually manifested as a reddening in the lenses), and enables a better correction of chromatic aberration, the possibility of measuring color becomes more interesting. Another consideration in support for using a hardware capable of color discrimination is that with the need to reduce mass, volume and power consumption, instruments aboard future spacecraft will tend to accumulate more functions. Thus, the same hardware used for star tracking might also be used for target recognition, optical navigation, and other uses in other phases of the mission. Some of these uses may require color information.

Figure 5.11 – *B*−*V* and *V*−*I* plot for the 5000 brightest stars in the Hipparcos catalog.

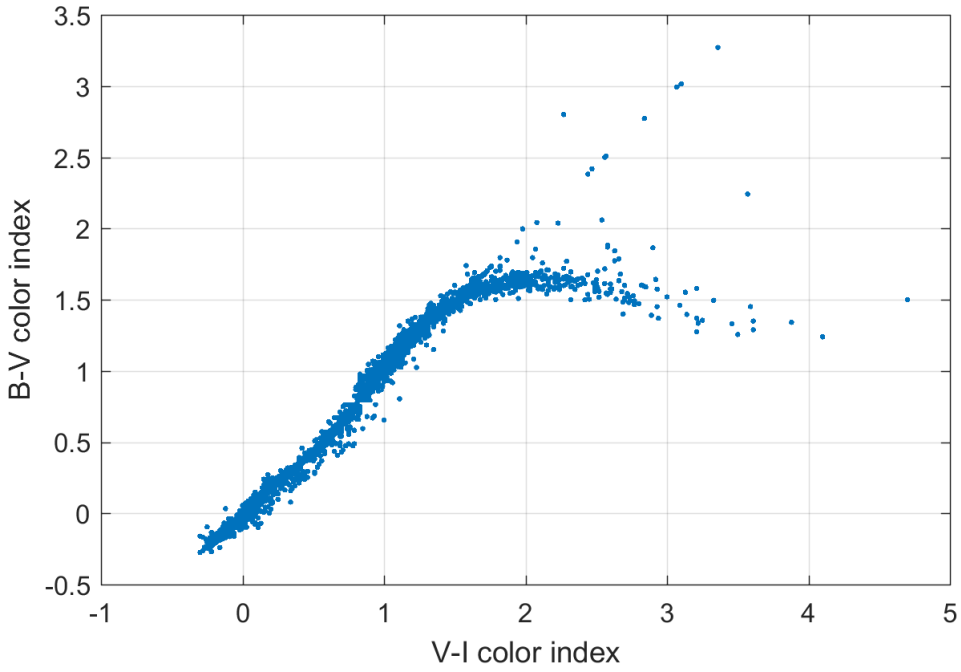

Source: Drawn by the author.

5.4.11.2 Timing measurements

Timing measurements were the most difficult ones, also being the least reliable type of measurement presented in this work. In modern computers, running modern operating systems, many times it is not possible to disable all background processes, such as antivirus, system processes, etc. Hence, it is not possible to predict when a background process will request CPU resources, robbing CPU time from the algorithm under test. To work around this limitation, we have adopted a number of tactics, besides performing multiple Monte Carlo simulations using the same configuration.

As the tests were performed in a Windows machine, the first measure taken was to close all network connections to avoid unwanted downloads and update processes running concurrently with our tests. This was done by allowing all updates to complete and disconnecting the test machine from the Internet before performing the tests.

Another tactic that was used was to interleave test configurations, as can be inferred from the first column shown in Table 5.7, Table 5.8 and Table 5.9. For example, in one of PTASE runs (log file ptase_20170727_05.log), the results from the first Monte Carlo simulation were used in Table 5.7, the results from the second simulation were used in Table 5.8, the results from the third in Table 5.9, and so on. By interleaving test configurations, we can reduce the probability that a background process, running for a relatively large amount of time, would go unnoticed, affecting all measurements with a given configuration and biasing conclusions.

Unfortunately, all the measures adopted here are not failproof. The best solution to this problem would be to run the Monte Carlo simulations in an environment where the user has complete control over all the processes (including interrupt service routines) running on the test machine, such as a dedicated hardware or an emulator simulating a target processor. In cases this is not possible, an alternative would be to perform Monte Carlo simulations using an operating system where the user has better control of background tasks, such as Linux.

A final remark to this section is that the fastest algorithm or implementation in a given machine (e.g., the test computer used to evaluate them) might not be the fastest on a different machine (e.g., in the STR hardware). Hence when selecting algorithms based on speed, decisions should be made preferably on tests conducted in the target hardware.

5.4.11.3 Conclusion

Simulations have shown that magnitude and color indexes can be successfully used to reduce the misidentification rate, improve success rate and in many cases to speed up star identification. Even with the relatively large errors in magnitude and color index measurement considered in this simulation, we have obtained a significant reduction in misidentification rate by including magnitude and color indexes as additional filters in the star identification process. Had we

used the values obtained by the preliminary experimental work described in Section 3.6 in our simulations, results would be even better.

Monte Carlo simulations have shown that even for monochrome star trackers, the use of magnitude information as an additional check for star identification leads to a significant reduction in misidentification rate, therefore improving attitude determination reliability without the need of additional hardware. If color information is available, it should be used to further reduce the probability of a misidentification occurring.

An important evaluation which was not performed in this work is to verify how the tested star-ID algorithms behave in the presence of false stars (spikes). This verification is very important in real applications. Future work should evaluate how star-ID algorithms behave with the presence of false stars, using a model that attempts to mimic in a realistic way the distribution of false stars with magnitude and color indices.

6 A TECHNIQUE TO IMPROVE STAR DETECTION

6.1 Introduction

Before launching optical equipment into space, these instruments are calibrated in the laboratory. Unfortunately, some calibration parameters, such as FPN coefficients, can change with time due to a variety of reasons, including radiation damage and equipment aging. Ideally, to keep a camera calibrated, one would characterize the three components of the FPN presented in Equation (B.12) at regular intervals (e.g., once a year). The standard procedure to characterize FPN coefficients is to take a series of dark fields, flat fields and bias fields as outlined in Section B.2.7 in the appendices, average these images and from their average extract the FPN calibration coefficients.

Unfortunately, this procedure is not as simple when the camera to be calibrated is in space. Many times, the communication channels between the spacecraft and the ground do not have enough bandwidth to allow to download a series of images to be used for calibration; the instrument to be calibrated does not have enough memory and processing power to compute the FPN calibration coefficients; or the instrument does not have a physical shutter to enable acquisition of dark frames.

A space qualified star tracker could suffer from all these limitations. Hence to guarantee that it will provide accurate attitude measurements even after many years in space, and after its image sensor FPN coefficients have changed due to aging and radiation damage, innovative methods must be developed that permit to obtain crude estimates for some of the FPN coefficients from single images.

With this in mind, a simple technique that permits to estimate the bias coefficients for columns in an image sensor from a single image has been devised. This technique was specially designed for a star tracker prototype based on a CMOS APS image sensor not having enough memory to store all calibration coefficients

for correcting the FPN noise. The following section gives a brief description of the method.

6.2 Estimating column bias by sampling pixels in a column

For each column *j* in a raw image of $N_r \times N_c$ rows and columns, this algorithm samples N_{sample} pixels at regular intervals along the column. From this sample, the N_{reject} ($N_{reject} < N_{sample}$) brightest pixels are rejected, and the average value of the $N_{sample} - N_{reject}$ pixels is computed and used as a rough estimate of the column *j* bias. This bias estimate is then subtracted from the column. The N_{reject} brightest pixels are rejected because during the sample process, some samples might be hot pixels or pixels illuminated by stars. By rejecting the brightest N_{reject} pixels the likelihood that a illuminated or a hot pixel would affect the results is reduced, providing a better estimate of the column background level. This estimate of the column bias is then subtracted from every pixel in that column. This process is repeated for every column in the image. The end result is an image with corrected column FPN, presenting less non-uniformity due to column amplifier bias.

6.3 Test example

This correction method was tested with night sky images taken with an 1024 by 1024 pixel CMOS APS image sensor, using $N_{sample} = 136$ and $N_{reject} = 8$. Results are shown in Figure 6.1. To the left, is shown a section of 25 by 25 pixels of the original image. To the right is shown the same 25 by 25 pixel region after the column bias computed with the method presented here was removed. In the original image, some lighter and darker vertical stripes are visible, this is due to column amplifier bias non-uniformity in the CMOS APS imager. These vertical stripes disappear after this proposed correction is applied. To make visualization easier, the contrast in the images has been enhanced. The same contrast enhancement factor has been used in both images, to allow for a fair comparison.

Figure 6.1 – A sample region of 25×25 pixels from an image of 1024×1024 pixels
a) before and b) after FPN correction

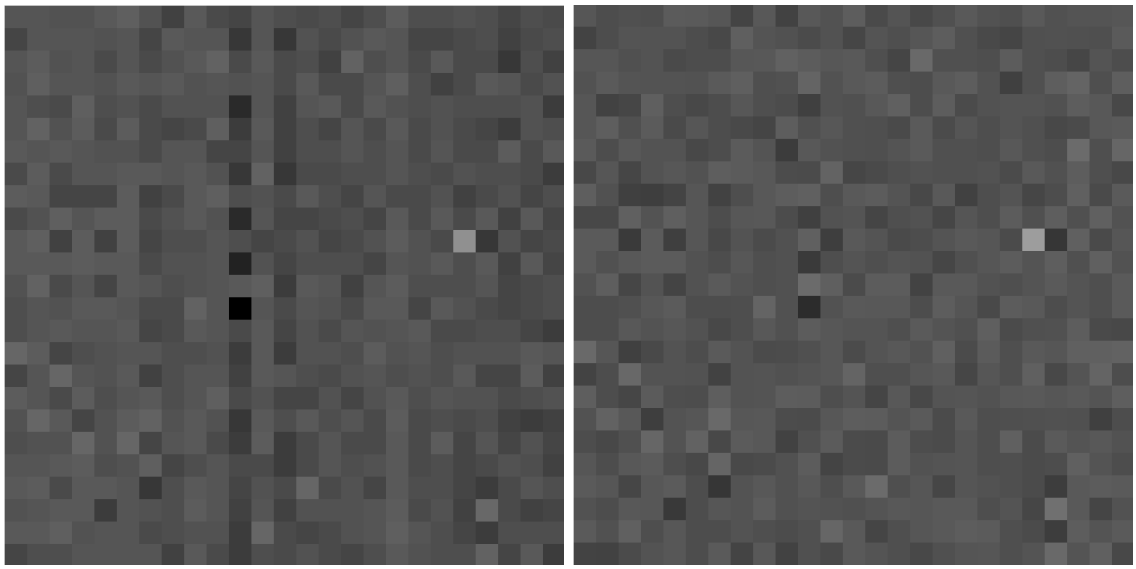

a) before FPN correction b) after FPN correction

Source: Created by the author.

The standard deviation of the original 25×25 pixels region shown in in Figure 6.1 was 2.234050 ADU, when considering only the 600 darkest pixels out of 625 in total. After applying this noise reduction method, the standard deviation of that same region (computed using the 600 darkest pixels out of the 625 pixels in the region) reduced to 1.738915 ADU. The ratio between these two values is 0.778. If the ADC response is assumed to be linear and the star detection threshold is also assumed to be proportional to the noise floor level, this means that by using this method an improvement in sensitivity of 1/0.778 = 1.285 was achieved for this small region, this gain equates to a gain in magnitude sensitivity of 0.272 magnitude. ($0.272 = 2.5 * \log_{10} (1.285)$). When computing the standard deviation of this 25×25 pixels region, the 25 brightest pixels were excluded because among them there might exist some hot pixels (pixels with abnormally high dark current) and these are normally removed by image processing before centroid computation.

6.4 Discussion

Even though the method described here is not as accurate as traditional methods proposed in the literature, it has the advantage of having a much lower computational cost than more accurate methods. Another advantage of this method is that it can provide a fairly good column FPN correction even when knowledge of column bias coefficients does not exist. These features make it a good candidate to be used in an embedded hardware with low computational power. This method is being tested with a star camera prototype being developed at INPE (FIALHO; PERONDI and MORTARI, 2016).

It should be noted that this method does not work if the image is derived from a scene with large illuminated areas, working only if very few pixels are illuminated. The method works fine for star field images, where usually much less than 1% of the pixels in the image are illuminated by stars.

For the future, an evaluation on how the column non-uniformity bias affect centroiding accuracy should be performed. Another interesting research topic is how the proposed method impacts centroiding accuracy using many different algorithms, from the simple center of mass centroiding to the more sophisticated point spread function (PSF) curve fitting techniques.

7 LOWER BOUND ON STAR TRACKER ACCURACY IN THE SOLAR SYSTEM NEIGHBORHOOD

This chapter presents an estimate of the theoretical lower bound on star tracker accuracy, for star trackers located in the Solar System's neighborhood.

7.1 Introduction

Many progresses in a variety of fields in science and technology could be accomplished thanks to the miniaturization obtained in microelectronics in the recent decades. One of the most remarkable examples is the prediction by Gordon Moore that the computational power would increase exponentially, an empirical observation that became known as Moore's law (MOORE, 1965; BALL, 2005; CHARLES JR., 2005; BEIGEL, 2013). Yet, this rate of improvement is not expected to last forever. Eventually a fundamental limit will be reached when the size of transistors reaches atomic dimensions. Likewise, in other fields of science and technology, fundamental limits to miniaturization and performance improvements are often found. For instance, in the field of telecommunications, there's a theoretical minimum amount of energy that must be spent to transmit a bit in a digital message from one point to another within a given time interval, being this quantity closely related to Planck's constant (BEKENSTEIN, 1981). Hence, it is natural to ponder whether there is a fundamental limit to the accuracy attainable by star trackers, given constraints such as the *volume* in space it occupies, the length of *time* available for observations and the distribution and brightness of stars around it.

The main goal of this chapter is to present initial estimates for the ultimate limits of traditional, camera type, single head star trackers (single head STRs), imposed by fundamental laws of Physics, i.e., limits that cannot be overcome by technology improvements. The limits derived here do not depend on STR technology used, being applicate to both refractive and reflective optics STRs. These estimates are useful as a basis for assessing real STRs as to their

potential for improvements through technology advancements. This chapter does not discuss practical limitations (such as readout noise, non-ideal point spread function (PSF) in centroiding and distortions introduced by the optics) faced by existing, real world star trackers, since this subject has already been well covered by existing literature (ENRIGHT; SINCLAIR; DZAMBA, 2010; SUN; XING; YOU, 2013; ZAKHAROV et al., 2013).

This chapter is organized as follows: Section 7.2 describes the methodology used, Section 7.3 presents and discusses the results, Section 7.4 describes how the model used here could be improved and Section 7.5 concludes this chapter.

7.2 Methodology and model description

The model used in this work is that of an equivalent ideal *spherical star tracker*, capable of measuring the direction and energy of every photon incident on its surface. This ideal STR would be able to observe stars in the whole celestial sphere simultaneously, that is, it would have a field of view of 4π sr. The knowledge on the incoming direction of photons in this model is limited only by diffraction at the star tracker aperture, assumed to be circular with the same radius of the STR itself. In other words, it is assumed that the STR aperture is given by the projection of the STR body on a plane perpendicular to the direction of incoming photons. In this ideal model, the Universe is assumed to be composed only of stars, each star being a polychromatic point source of light, with the same brightness and position in the celestial sphere of stars given in star catalogs. Figure 7.1 provides a pictorial description of the STR model used in this work. In this model, the accuracy of the centroids of each star is limited only by diffraction and shot noise. These effects depend only on the STR aperture, stellar spectra and integration time.

Figure 7.1 – Ideal star tracker (STR) model.
Ideal star tracker (STR) model (gray sphere at the center) with stars on the background. An ideal STR would be completely black, as it would absorb every photon impinging on it. However, a realistic illustration would make it harder to visualize the concept.

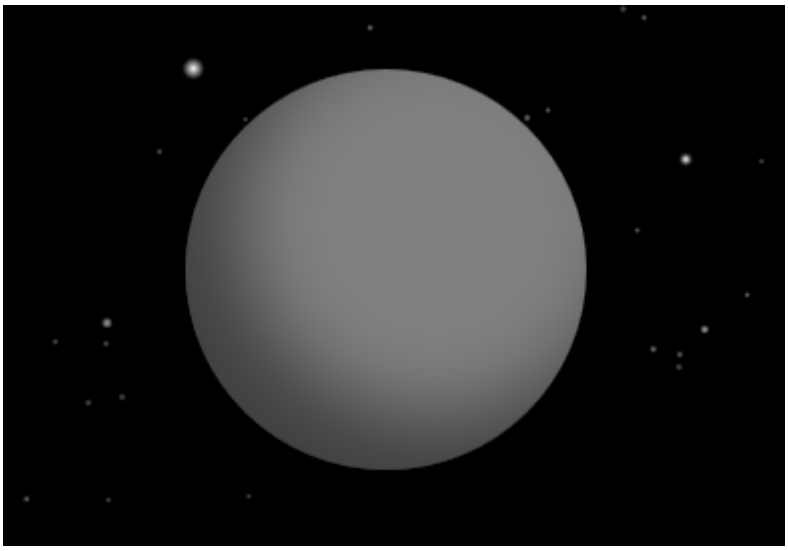

Source: Drawn by the author.

For simplicity, the spectra of stars will be approximated by the spectra of equivalent black-bodies. Ideally, the actual spectra of stars should be used, at least for the brightest stars. However, this would make this study much more complex. Therefore, this improvement will be left for the future. Section 7.3.2 discusses the adequacy of this approximation.

Also for simplicity, our computations disregard the use of the Sun and other Solar System objects as references for attitude determination. An attitude sensor in a distant future that is able to use and model very accurately the Sun and a neighboring planetary body as additional attitude references, could, perhaps, overcome the estimates on the lower bound of attitude accuracy computed in this work.

7.2.1 Basic assumptions

The following basic assumptions are made in this model:

a) the star tracker has a spherical shape with a diameter *D*, being able to detect and use for attitude determination *every* photon of stellar origin impinging on its surface[10];

b) it is capable of registering the incoming direction and energy of every detected photon with an accuracy limited only by Heisenberg's Uncertainty Principle;

c) only photons detected during a period of length *t* – the exposure or integration time – are considered for attitude determination;

d) this ideal star sensor is at absolute zero temperature, hence, there is no noise of thermal origin within this star tracker;

e) the coordinates of the stars in a non-rotating reference frame with origin in the star tracker are known with absolute precision;

f) an unbiased optimal estimator is used to determine the star sensor attitude, and computations are performed with infinite precision;

g) measurements obtained with this ideal star tracker are not merged with external measurements;

Item a) implies that this star sensor has a field of view of 4π sr, i.e., it is capable of observing the whole celestial sphere simultaneously, a fact that, coupled with its spherical shape, leads to the advantage that the accuracy of this ideal STR *does not depend on its attitude*, in contrast to real STRs, where the attitude accuracy depends on the particular set of stars that are within its limited field of view. The spherical shape was also chosen for this model due to its symmetry, which simplifies greatly the mathematical treatment. Only star trackers capable of simultaneously observing the whole celestial sphere (4π sr) are able to use all the information on star position that is provided by natural means in a given time

[10] except for stars at a *very* close range, such as the Sun when the STR is in the Solar System.

interval to the volume it occupies in space, information that is used to determine its attitude. With artificial means, it would be possible to overcome this limitation, e.g., by determining the star tracker attitude externally (with a much more accurate attitude sensor) and relaying this information to the star tracker, however this would be a violation of assumption g) of our model.

Item b) and the fact that every photon is detected, means that the optics, if any, is ideal: 100% transmission, with *no defocusing and blurring*, except for the blurring dictated by diffraction;

Items c) and g) limit the number of photons that will be observed by the ideal STR. If exposure time were not constrained, it would be possible to get attitude measurement uncertainty as low as desired, by increasing the exposure time. Item c) also means that this model does not consider the possibility of combining current observations with previous observations to improve accuracy. Item g) implies that only photons impinging on the STR surface will be used for attitude determination. Item c) also excludes from consideration the possibility of using other particles emitted from stars for attitude determination. This means that, for example, a star tracker in a very distant future that is able to observe neutrinos[11] in addition to photons (assuming that one could ever be built) or use other means of observing stars (e.g., by detecting another type of particle still unknown to science) could potentially overcome the limits established in this work.

Item e) means that the star catalog used for star identification is perfect and that all corrections needed to bring the coordinates, brightness and colors from the star catalog reference frame origin to the STR location (corrections for stellar aberration, parallax and redshift/blueshift) are performed with no errors.

Item g) expresses the goal of obtaining a lower bound on attitude error for a single star tracker used in isolation. If measurements from multiple sensors were

[11] Neutrinos interact so weakly with ordinary matter that the vast majority of neutrinos arriving at Earth pass through our planet unimpeded (JAYAWARDHANA, 2015). Therefore, detection of neutrinos emitted by stars in star trackers with current technology is virtually impossible.

permitted to be merged, a significant improvement in attitude measurement accuracy could be achieved. For example, by interferometrically combining measurements from a small number of STRs mounted in a rigid structure and separated by a distance much greater than their diameters, it would be possible to improve attitude determination by many orders of magnitude in comparison to the theoretical estimate presented in this work, with attitude uncertainty being roughly inversely proportional to the distance between them (BALDWIN; HANIFF, 2002; MOLINDER, 1978).

7.2.2 Simplifying assumptions

In order to make this study feasible, the following simplifying assumptions were made:

a) stellar spectra are approximated by the spectra of black bodies that best match the catalogued star intensity and color given by the star catalogs adopted in this work;

b) stars are considered as point sources of light;

c) Solar System objects, including the Sun, are disregarded in this model;

d) stellar proper motion is disregarded;

e) the star tracker is not rotating;

f) it is assumed that each detected photon can be univocally associated with the star from where it originated.

7.2.3 Model description

Figure 7.2 presents a flowchart for the model used in this work. Basically, for each star in the adopted star catalogs, an estimate for the lower bound on centroiding accuracy is computed, and these estimates are used together with the unit

vectors that represent the stars in the star catalog reference frame to determine the lower bound on attitude error (box at the lower right corner).

Unfortunately, no star catalog is complete. Therefore, any estimate obtained from an existing star catalog will be incomplete, since the missing stars in that star catalog still can contribute to attitude knowledge if they are observed by the star tracker, no matter how far or dim they are. To work around this limitation, we plot the relation of attitude knowledge upper bound with star catalog size for a number of publicly available star catalogs and extrapolate that to the estimated number of stars in our galaxy, plus some margin, to account for stars in other galaxies, as described in Section 7.3.3.

Figure 7.2 - Model for estimating the theoretical lower bound on attitude errors for star trackers.

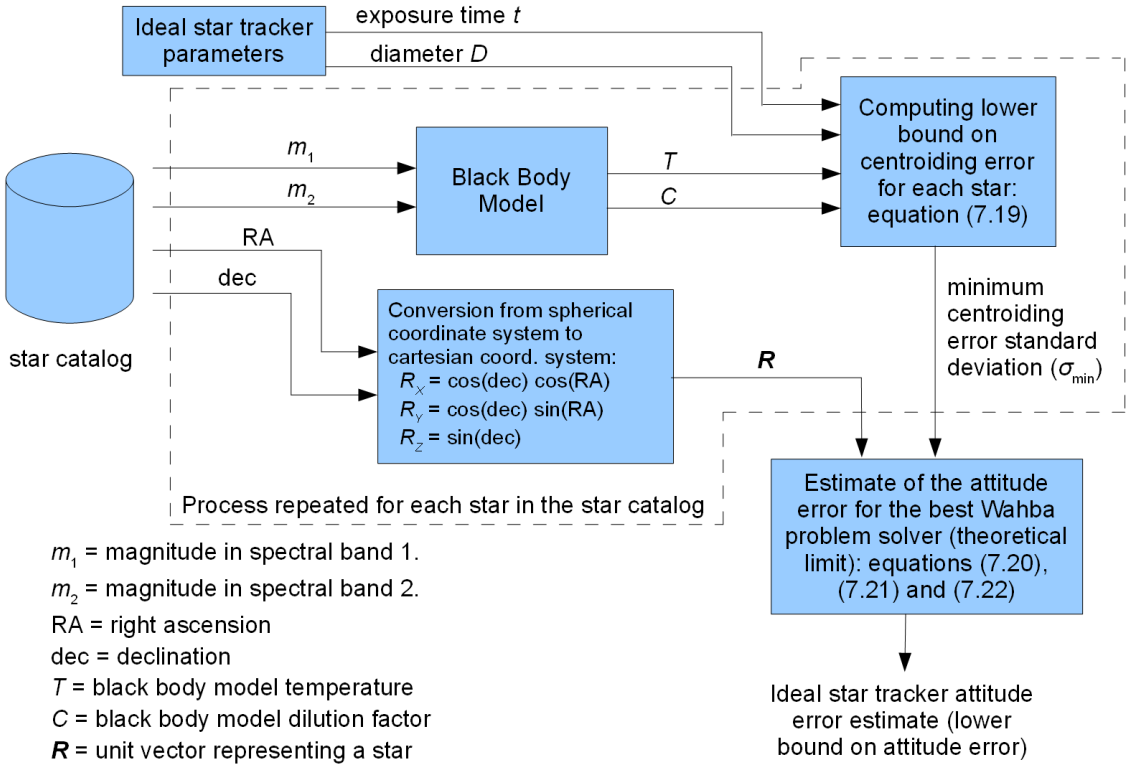

Source: Drawn by the author.

In the following sections, a more detailed description of the model used is given.

7.2.4 Black body model for stars

In the simplified model adopted in this work, the spectrum of each star is considered to be the spectrum of a black body at a temperature *T* diluted by a geometric factor *C*. This geometric factor arises from the fact that the idealized STR is at a (very long) distance from that star, instead of being placed on the surface of a spherical black body that represents that star. Hence, the radiant energy flux (irradiance) received by a surface perpendicular to the rays coming from that star, at the location of this idealized STR, will be much smaller than the radiant energy flux (radiant exitance) emitted by the surface of the equivalent black body that represents that star. As the radiant exitance of a black body is uniquely determined by its temperature, only two parameters are needed to uniquely determine the spectral distribution and intensity received by the STR from that star in this model, the temperature *T* and the dilution factor *C*. Mathematically:

$$E_{e,\lambda,i}(\lambda) = C_i \cdot M_{e,\lambda}(T_i, \lambda) \tag{7.1}$$

where:

- $E_{e,\lambda,i}(\lambda)$ is the spectral irradiance in unit of power per unit of area and per unit of wavelength (e.g: W/m^2/nm) received from star *i* by a surface, located at the same place of the star tracker, that is perpendicular to incoming rays, at a wavelength λ;
- C_i = geometric dilution factor for star *i*;
- T_i = temperature of the black body that represents star *i*;
- $M_{e,\lambda}(T_i, \lambda)$ is the spectral exitance in unit of power per unit of area per unit of wavelength (e.g.: W/m^2/nm) of the surface of the black body that represents star *i*, evaluated at wavelength λ.

In order to uniquely determine these two parameters (*T* and *C*) for each star, at least two samples of their flux taken at different wavelengths or at different spectral bands are needed. The following sections describe how *T* and *C* are derived for each star from Hipparcos catalog data, using the cataloged m_V magnitude and *B*−*V* color index. A similar procedure is performed with data from Hipparcos using the *V*−*I* color index and data from other star catalogs.

7.2.5 Black body temperatures from *B*−*V* color indexes

Taking as an example data from the Hipparcos catalog using the *B*−*V* color index information, the spectra of stars is taken as the spectra of black bodies with intensities adjusted so that the integrated spectra over the Johnson's *B* band and *V* band (BESSELL, 2005; BESSEL; MURPHY, 2012) match simultaneously the flux at these bands derived from magnitudes and color indexes given by the Hipparcos Catalog.

In order to determine equivalent black bodies temperatures for stars in the Hipparcos catalog, an empirical relation had to be established linking the *B*−*V* color indexes given in the Hipparcos catalog with black body temperatures. This section describes how this empirical relation was derived.

The spectral exitance at wavelength λ of a black body at a temperature *T* can be computed as follows (BUDDING; DEMIRCAN, 2007):

$$M_{e,\lambda}(T,\lambda) = \frac{2\pi hc^2}{\lambda^5}\frac{1}{\exp\left(\frac{hc}{\lambda kT}\right)-1} \tag{7.2}$$

where h is the Planck constant ≈ $6.62607 \cdot 10^{-34}$ J·s, c is the speed of light in vacuum (c = 299,792,458 m/s exactly, by the definition of the meter (MOHR; NEWELL; TAYLOR, 2016)) and k is the Boltzmann constant ≈ $1.38065 \cdot 10^{-23}$ J/K. The spectral exitance will have units of power per unit area per unit wavelength ([$W \cdot m^{-2} \cdot m^{-1}$] in SI units).

By integrating the product of the spectral exitance of a black body with the Johnson's *B* and *V* passbands energy responses it is possible to obtain the black-body fluxes in the *B* and *V* bands at its surface. This procedure is described in detail by Bessell (2005) in Section 1.6 – Synthetic Photometry (Section C.3 in the appendices of this thesis also gives an introduction to this subject):

$$\varphi_{BB,B}(T) = \int_{\lambda=0}^{\infty} M_{e,\lambda}(T,\lambda) R_B(\lambda) \mathrm{d}\lambda \tag{7.3}$$

$$\varphi_{BB,V}(T) = \int_{\lambda=0}^{\infty} M_{e,\lambda}(T,\lambda) R_V(\lambda) \mathrm{d}\lambda \tag{7.4}$$

where:

- $\varphi_{BB,B}(T)$ = flux at the surface of a black-body at temperature *T* in the Johnson's *B* photometric passband; and
- $R_B(\lambda)$ = spectral energy response function of the Johnson's *B* photometric passband.

Analogously, $\varphi_{BB,V}(T)$ and $R_V(\lambda)$ are quantities related to the Johnson's *V* photometric passband.

The $R_B(\lambda)$ and $R_V(\lambda)$ response functions were obtained by converting the tabulated values recommended by Bessell and Murphy (2012, Table 1 on page 146) from normalized photonic responses to normalized energy responses and interpolating the resulting values. The energy response functions adopted in this work are shown in Figure 7.3.

The conversion from normalized photonic response to normalized energy response was done by multiplying the photonic response by the wavelength and renormalizing the results (Equation A9 in Bessell and Murphy (2012)). The explanation for this procedure is given in Section A2 in the appendix of Bessell and Murphy (2012), on page 153. The method of interpolation used was a "shape-preserving piecewise cubic interpolation," provided by the MATLAB function

`interp1` with method "`pchip`". Computations were performed with MATLAB R2015b.

Figure 7.3 – Spectral energy response of the *B* (blue) and *V* (visual) passbands. The *B* band is the blue dashed curve to the left.

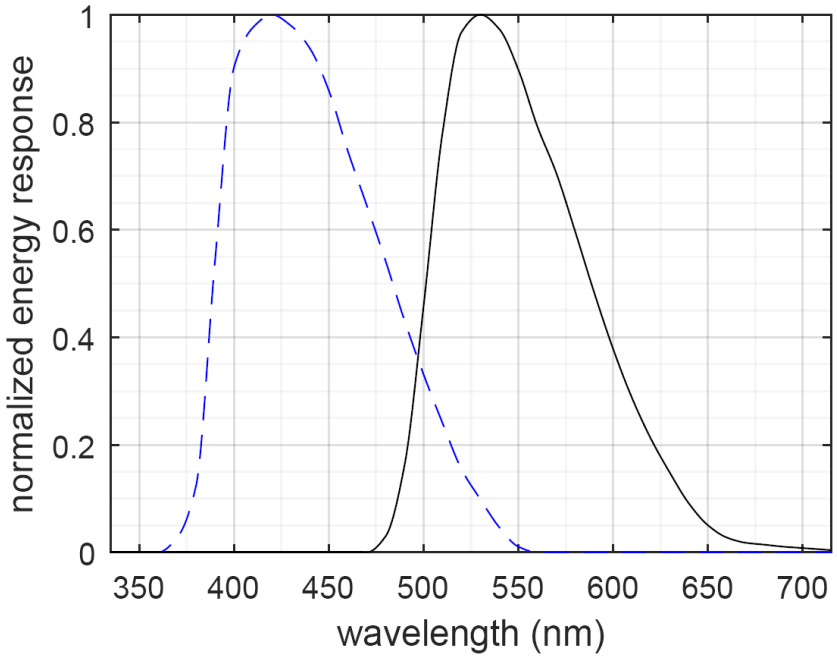

Source: Drawn by the author.

From the fluxes in the *B* and *V* bands, the magnitudes in these bands can be computed:

$$m_{BB,B}(T) = -2.5\log_{10}\left(\varphi_{BB,B}(T)/\varphi_{REF,B}\right) \tag{7.5}$$

$$m_{BB,V}(T) = -2.5\log_{10}\left(\varphi_{BB,V}(T)/\varphi_{REF,V}\right) \tag{7.6}$$

These equations give the apparent magnitudes in the *B* and *V* spectral bands of a spherical black body for an observer situated just above its surface looking down towards its center. $\varphi_{REF,B}$ and $\varphi_{REF,V}$ are the reference fluxes that define the zero point of the magnitude scales in these bands, having being obtained by numerically integrating the spectrum of Vega (α-Lyr) multiplied by the passband responses, and adjusting their values such that the computed *B* and *V*

magnitudes of Vega matches those in the star catalog ($m_{Vega,B} = 0.029$ and $m_{Vega,V} = 0.030$ in Hipparcos). Mathematically:

$$\varphi_{REF,B} = 10^{0.4 m_{Vega,B}} \int_{\lambda=0}^{\infty} E_{Vega}(\lambda) R_B(\lambda) \mathrm{d}\lambda \tag{7.7}$$

$$\varphi_{REF,V} = 10^{0.4 m_{Vega,V}} \int_{\lambda=0}^{\infty} E_{Vega}(\lambda) R_V(\lambda) \mathrm{d}\lambda \tag{7.8}$$

where $E_{Vega}(\lambda)$ is the spectral irradiance from Vega measured at the top of Earth's atmosphere. The spectrum of Vega used in equations (7.7) and (7.8) was obtained from file `alpha_lyr_stis_008.fits` (STSCI, 2017).

Figure 7.4 shows the apparent magnitudes of black bodies versus temperature in the Johnson's *B* and *V* bands for an observer located at the surface of said black bodies. In this plot, brighter sources (more negative magnitudes) are at the top. Note that the magnitude scale used in astronomy is reversed, with smaller magnitudes meaning brighter sources. The magnitudes are said to be apparent because they depend on the observer location, contrasting to stellar absolute magnitudes that are the magnitudes of a star seen from a standard distance of 10 parsecs (ZEILIK; GREGORY, 1998).

The *B* magnitude minus the *V* magnitude of a celestial body is its *B*−*V* color index. Figure 7.5 presents the relation between the *B*−*V* color index and temperature for black-bodies. The plot to the right relates the *B*−*V* color index with the multiplicative inverse of the black body temperature. Note that this curve is much more linear than the direct relation between temperature and *B*−*V* color index. Therefore, to get equivalent black-body temperatures for stars in the catalog, we interpolate using the 1/*T* versus *B*−*V* curve. To avoid temperature estimates with large errors from appearing, the *B*−*V* color indexes in the Hipparcos catalog are clamped into the interval [−0.2357, +2.7028] before conversion. These limits correspond to black-body temperatures of 30,000 K and 2000 K, respectively. Most stars have effective temperatures in that range.

Figure 7.4 – Apparent magnitudes of a black body for an observer lying on its surface and looking down towards its center versus black body temperature, in the Johnson-Morgan *B* and *V* passbands.

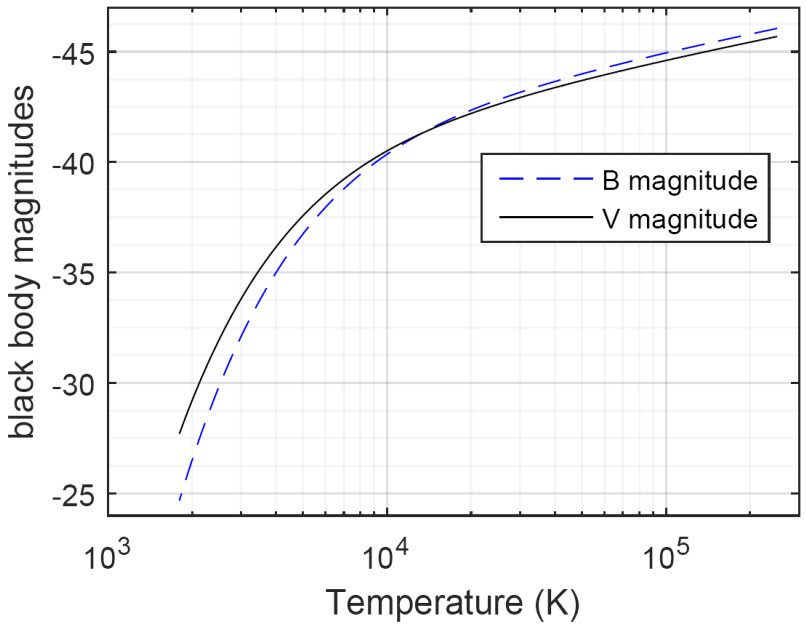

Source: Drawn by the author.

Figure 7.5 – Relation between temperature (or its reciprocal) and *B*−*V* color index for black bodies.

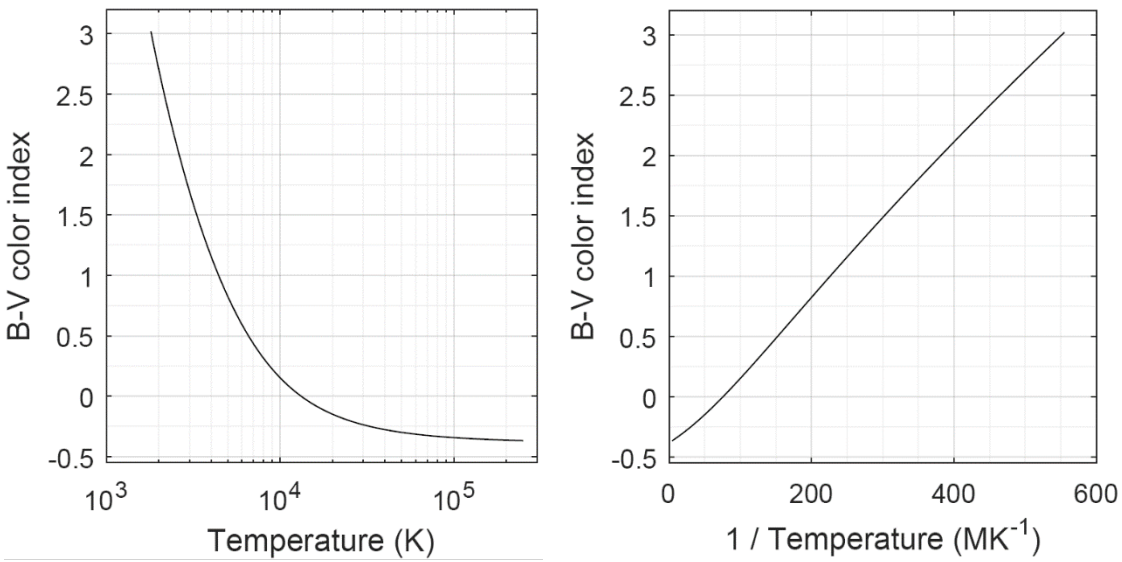

Source: Drawn by the author.

It should be noted that for many stars, the temperature *T* used in our model will not be equal to the effective temperature of the star – the temperature that a black body with the same physical size of that star should have to irradiate the same amount of electromagnetic radiation as the star – but will usually be smaller. The reason for that is the reddening caused by selective absorption by dust in the intervening light path from that star to the observer. Likewise, the constant *C* will have a different value than the one it would have in the absence of interstellar dust and clouds. In the absence of interstellar absorption, the constant *C* would be equal to $(r_{star}/d_{star})^2$ if the stars were also assumed to be spherical black bodies, being r_{star} the stellar radius and d_{star} the distance from the center of the star to the star tracker.

7.2.6 Determination of the geometric dilution factor *C* from Hipparcos data

From the temperature *T*, the apparent visual magnitude of that black body at its surface ($m_{BB,V,surface}$) was determined by interpolating the solid black curve in Figure 7.4. The dilution factor *C* can be computed by comparing this magnitude with the cataloged visual magnitude (m_V) in the Hipparcos catalog, and considering the definition of magnitude scale:

$$C_i = 10^{0.4\cdot(m_{BB,V,surface} - m_{V,i})} \tag{7.9}$$

The geometric dilution factor *C* will be typically between 10^{-20} and 10^{-14} for stars in the Hipparcos catalog. In this equation, the subscript i indicates that the values refer to star i.

7.2.7 Number of photons detected per unit wavelength

This section derives equations for the number of photons that will be detected, per wavelength, by the idealized star tracker used in this model, for a given exposure time *t* and a given STR diameter *D*, also assumed to be equal to its aperture diameter.

The energy of each photon is related to its frequency ν by the following equation:

$$E_{ph} = h\nu = \frac{hc}{\lambda} \tag{7.10}$$

Dividing the spectral irradiance at the location of the star tracker due to the black-body equivalent of star i (equations (7.1) and (7.2)) by the energy of a photon of wavelength λ, the following expression for the spectral photon flux density received by the STR from the equivalent of star i is obtained:

$$\varphi_{ph,\lambda,i} = C\frac{2\pi c}{\lambda^4}\frac{1}{\exp\left(\frac{hc}{\lambda k T_i}\right) - 1} \tag{7.11}$$

This flux density has units of photons per unit of time per unit of area per unit of wavelength. Multiplying this by the star tracker's cross section area $A = \pi D^2/4$ and by the integration time t we obtain:

$$n_{ph,\lambda,i} = C_i \cdot t \cdot \frac{\pi^2 D^2 c}{2 \cdot \lambda^4}\frac{1}{\exp\left(\frac{hc}{\lambda k T_i}\right) - 1} \tag{7.12}$$

which is the number of photons from star i equivalent being collected by the STR, per unit wavelength.

7.2.8 Diffraction and shot noise

Diffraction and optics blurring set the format of the point spread function (PSF) of stellar image. In an ideal star tracker, there's no optical blurring, except for that set by diffraction. Therefore, for the STR model adopted in this work, the PSF function will be the diffraction pattern given by a circular aperture of diameter *D* contained in a plane perpendicular to the incoming direction of photons. This diffraction pattern consists of a disk (Airy disk) with a series of concentric rings, being first derived by Airy in 1835.

If the description of Nature given by Classical Mechanics were correct, it would be possible, at least in theory, to measure the intensity of the electromagnetic

field at the detector plane with no error, from where the true, error free, direction of the incoming light rays would be obtained. However, the fact that light is discretized in photons leads to the situation where the number of detected photons will be finite, even with an ideal detector. Therefore, instead of defining precisely the intensity of the electromagnetic fields at each point in the detector (as thought by 19th century physicists), the PSF will define the probability density function that a photon coming from a point source at infinity will be detected on a particular location at the detector. Since the number of photons detected will be finite, even for the case of an ideal star tracker, and these photons are detected at random positions, with probabilities given by the PSF, the centroid estimate for each observed star will have a noise. The lower bound for this noise was determined by Lindegren (2013), being discussed in the next subsection.

7.2.9 Lower bound on centroiding error for single stars

According to Lindegren (2013), Heisenberg's uncertainty principle sets a fundamental limit for centroiding, and this limit assumes the following form for monochromatic light of wavelength λ:

$$\sigma_{xc} \geq \frac{\lambda}{4\pi\Delta x\sqrt{N}} \tag{7.13}$$

where:

- σ_{xc} = angular centroid uncertainty along an axis *x* perpendicular to the direction of incoming photons, in radians;
- $\Delta x = \sqrt{\int x^2 \mathrm{d}S / \int \mathrm{d}S}$ = root mean square extension of the star tracker aperture (entrance pupil) in the *x* direction;
- N = number of photons detected.

For circular apertures of diameter *D*, Δx = *D*/4. Substituting this into Equation (7.13) the following expression for the reciprocal of the lower bound of variance

of centroiding error (the Fisher information F) over a circular aperture of diameter *D*, for monochromatic sources of light is obtained:

$$\frac{1}{\sigma_{xc}^2} \leq \frac{1}{\sigma_{min}^2} = F_{N,mono} = \frac{\pi^2 D^2 N}{\lambda^2} \tag{7.14}$$

Since stars are incoherent sources of light, the detection of a given photon is not correlated with the detection of another photon from the same star. This means that the number of detected photons from a given star will follow a Poisson distribution with parameter ι, being ι the expected number of detected photons. (We are using the Greek letter ι instead of the more common λ for the Poisson distribution parameter to avoid confusion with λ for wavelength.) This parameter can be obtained by integrating Equation (7.12). For large values of ι, the Poisson distribution narrows down in comparison to the value of ι. This means that when the expected number of detected photons is significantly large, the true value of the lower bound of centroiding accuracy will be very close to the value predicted by Equation (7.14) if we substitute N by ι. Numerical tests have shown, assuming that the centroiding error for exactly N detected photons follows a Gaussian distribution with a standard deviation given by Equation (7.12), that the error between the actual centroiding error and the value estimated by Equation (7.14) using ι in place of N will be smaller than 23% for $N \geq 1$, 6.4% for $N \geq 10$ and 0.51% for $N \geq 100$. It is true that the actual probability density function for centroiding error along one axis will not be exactly Gaussian, especially for a low number of detected photons, but a Gaussian distribution provides a good approximation, even when only one photon is detected.

Another consequence of the fact that the detection of a given photon is not correlated with the detection of another photon from the same star is that the centroiding error of a centroid computed using photons in the wavelength interval $[\lambda_1, \lambda_2]$ is independent on the centroiding error using photons in the wavelength interval $[\lambda_3, \lambda_4]$ when these intervals do not overlap ($\lambda_2 < \lambda_3$ or $\lambda_4 < \lambda_1$). Therefore,

we can consider each wavelength interval individually and then merge the centroid estimates from each wavelength.

For the discrete case of having n independent unbiased estimates of the same physical variable (e.g., the *x* coordinate of a star centroid), each having an actual variance σ_i^2, the best estimate for that variable is obtained by summing these estimates using the reciprocal of their variances as weights (a procedure sometimes known as inverse variance weighting) (HARTUNG; KNAPP; SINHA, 2008; YEN, 2002). In that case, the variance of this optimal estimate will be given by:

$$\sigma_T^2 = \left(\sum_{i=1}^{n} \frac{1}{\sigma_i^2} \right)^{-1} \tag{7.15}$$

where:

- σ_T^2 = total variance in the estimate of a scalar physical variable obtained by merging n independent measurements;
- σ_i^2= variance of each individual measurement i.

Since the spectra of black bodies is continuous, the following adaptation of Equation (7.15) is used to compute centroid estimates for black bodies:

$$\frac{1}{\sigma_{xc}^2} = \int_{\lambda=0}^{\infty} \frac{\mathrm{d}\left(\frac{1}{\sigma^2}\right)}{\mathrm{d}\lambda} \mathrm{d}\lambda \tag{7.16}$$

The contribution from each wavelength to the centroid Fisher information can be obtained from Equation (7.14) by replacing N with $n_{ph,\lambda,i}$, where $n_{ph,\lambda,i} = \mathrm{d}N_{ph,i}/\mathrm{d}\lambda$ is the derivative with wavelength of the number of photons from star i entering the star tracker aperture within an integration time of t, as given by Equation (7.12) from Section 7.2.7. Hence, for each star i, the derivative of the centroiding Fisher information (the integrand of Equation (7.16)) is given by:

$$\frac{\mathrm{d}F}{\mathrm{d}\lambda} = \frac{\mathrm{d}\left(\frac{1}{\sigma_{min}^2}\right)}{\mathrm{d}\lambda} = \frac{\pi^2 D^2}{\lambda^2} n_{ph,\lambda,i} \tag{7.17}$$

Here we have dropped the subscript i to simplify notation. Plugging Equation (7.12) into Equation (7.17) yields:

$$\frac{\mathrm{d}F}{\mathrm{d}\lambda} = C \cdot t \cdot \frac{\pi^4 D^4 c}{2 \cdot \lambda^6} \frac{1}{\exp\left(\frac{hc}{\lambda k T}\right) - 1} \tag{7.18}$$

Integrating this equation for $\lambda = 0$ to ∞ gives the Fisher information for stellar centroid i (F_i) and its reciprocal, the minimum variance for the centroid position error in *x* direction, being *x* an axis perpendicular to the incoming light rays:

$$\frac{1}{\sigma_{min}^2} = F_i = \int_{\lambda=0}^{\infty} \frac{\mathrm{d}F_i}{\mathrm{d}\lambda} \mathrm{d}\lambda = 12\zeta(5)\pi^4 \cdot \frac{k^5}{h^5 c^4} \cdot D^4 t \cdot C_i T_i^5 \tag{7.19}$$

where $\zeta(5)$ = 1.0369277551... is the Riemann zeta function evaluated at 5.

Since the aperture is symmetrical, Equation (7.19) gives the minimum centroiding variance for star i ($\sigma_{min,i}^2$) along any axis perpendicular to the direction of incoming light rays. From this equation, it can be noted that the lower bound of the standard deviation on centroiding error along any axis perpendicular to the true direction of the star is proportional to D^{-2} and $t^{-1/2}$, when the number of detected photons is sufficiently large. This means that the star tracker diameter has a much larger effect in the ultimate centroid accuracy and precision than the exposure time.

7.2.10 Estimating the lower bound of attitude error from many stars

This section follows the formulation given by Markley and Crassidis (2014, Section 5.5). This formulation is valid when measurement errors are small, uncorrelated and axially symmetric around the true direction of stars, conditions fulfilled by our model, except for ideal star trackers with very small diameters, much less than 1 mm.

According to equations 5.113 and 5.114 in Markley and Crassidis (2014), the covariance matrix ($\mathbf{P}_{\vartheta\vartheta}$) of the rotation vector error ($\boldsymbol{\delta\vartheta}$) for an optimal attitude estimator is the inverse of the Fisher information matrix $\mathbf{F}$:

$$\mathbf{P}_{\vartheta\vartheta} = \mathbf{F}^{-1} \tag{7.20}$$

with:

$$\mathbf{F} = \sum_{\mathrm{i}=1}^{\mathrm{N}} \frac{1}{\sigma_i^2} [\mathbf{I}_3 - \mathbf{r}_i^{\mathrm{true}} (\mathbf{r}_i^{\mathrm{true}})^T] \tag{7.21}$$

where σ_i^2 is the measurement variance associated with star *i*, as defined by Markley and Crassidis, $\mathbf{I}_3$ is a 3x3 identity matrix and $\mathbf{r}_i^{\mathrm{true}}$ is the true direction of star *i*, represented by a unit vector expressed as a 3x1 column matrix. $\mathbf{r}_i^{\mathrm{true}}$ is given in some reference frame R and N is the number of identified stars used in attitude computation.

In the ideal STR model adopted in this work, the measurement variance σ_i^2 is identical to the lower bound of centroiding error variance $\sigma_{min,i}^2$ given by Equation (7.19). A proof of this statement is given in Appendix E.

7.2.11 A compact metric for the attitude error

Even though the covariance matrix $\mathbf{P}_{\vartheta\vartheta}$ provides detailed information about the attitude uncertainty, as it has six independent parameters, it has the disadvantage of being hard to visualize. Therefore, to perform comparisons, we use a more compact metric derived from the covariance matrix:

$$(\bar{\vartheta}_{rms})^2 = E\{\vartheta^2\} = \mathrm{tr}(\mathbf{P}_{\vartheta\vartheta}) \tag{7.22}$$

The trace of the covariance matrix $\mathbf{P}_{\vartheta\vartheta}$ gives the variance of the overall attitude error, that is, the sum of the variances of the attitude error around the three defining axes of the reference frame. It is also equal to the square of the limiting value of the root mean square (rms) of the angle theta (ϑ) of the Euler axis/angle

parameterization of the attitude error when the number of attitude determinations tends to infinity.

When the STR diameter and exposure time are large enough so that most stars contributing to the Fisher information matrix $\mathbf{F}$ have many detected photons, the lower bound of the expected rms value of theta ($\bar{\vartheta}_{rms,min}$) can be computed by the equations (7.19) - (7.22). These equations can also be rearranged in the following manner, which makes more explicit the dependence of $\bar{\vartheta}_{rms,min}$ with *D* and *t*:

$$\bar{\vartheta}_{rms,min} = G \cdot D^{-2} \cdot t^{-1/2} \tag{7.23}$$

with

$$G = \sqrt{\frac{h^5 c^4}{12\zeta(5)\pi^4 k^5} \cdot \mathrm{tr}\left(\left(\sum_{\mathrm{i}=1}^{\mathrm{N}} C_i T_i^5 \left[\mathbf{I}_3 - \mathbf{r}_i^{\mathrm{true}}(\mathbf{r}_i^{\mathrm{true}})^T\right]\right)^{-1}\right)} \tag{7.24}$$

G is a constant which depends only on stellar distribution around the star tracker, stellar brightness and on attenuation of stellar light by the intervening medium.

7.3 Discussion and results

7.3.1 Star catalogs used

The Hipparcos star catalog (ESA, 1997) was initially selected because it was until very recently one of the most accurate star catalogs available for precise attitude work. Therefore, we had already all the tools needed to process it. Unfortunately, the Hipparcos star catalog having less than 120,000 stars is too short to give an adequate basis for extrapolation. Therefore, it was decided to include data from two larger catalogs, the Tycho-2 (HOG et al., 2000; TURON, 2009) with around 2.5 million stars and 2MASS (SKRUTSKIE et al., 2006) with about 470 million objects.

The Hipparcos and Tycho-2 star catalogs give magnitudes in the optical regime (near-UV, visible and near-infrared), whereas the 2MASS star catalog gives magnitudes in the near-IR / shortwave infrared bands *J* (1.25 μm), *H* (1.65 μm) and K_s (2.16 μm).

7.3.2 Adequacy of the black-body approximation

In order to check the adequacy of the black-body approximation used in section 7.2.4, we have performed a numerical integration in wavelength of Equation (7.17) for some selected stars, using their actual spectra. It was observed that, given the color index used, the black-body approximation provides a good fit for some stars, but the fitting is not so good for some other stars. Figure 7.6 compares the actual spectra of two stars with the spectra of their black-body equivalents, derived using the methods described in sections 7.2.5 and 7.2.6 and their *B*−*V* color index given in Table 7.1.

Figure 7.6 – Comparison between the actual spectra for the Sun and Vega (α-Lyr) with the spectra of their black-body equivalents derived from their *B*−*V* color index and *V* magnitudes with the methodology explained in sections 7.2.5 and 7.2.6. Actual spectra represented by continuous line. Dashed lines represent the spectra of equivalent black-bodies.

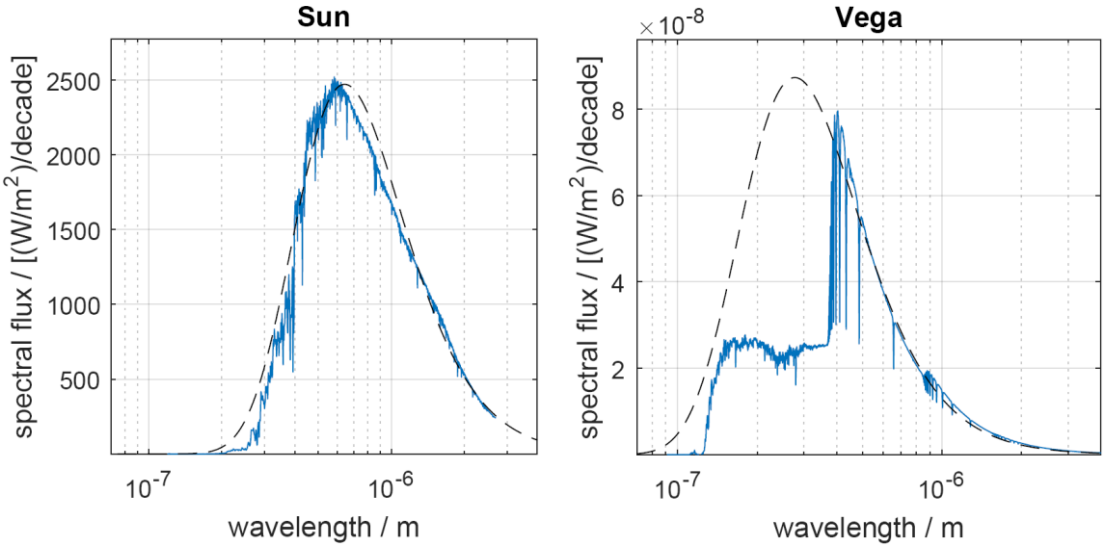

Source: Drawn by the author.

Table 7.1 presents a comparison between the lower bound of centroiding error obtained by numerical integration $\sigma_{min,num}$ (last row) and the lower bound of centroiding error $\sigma_{min,BB}$ obtained from the black-body approximation. To show how $\sigma_{min,BB}$ can vary depending on the spectral bands used for estimating the equivalent black-bodies, results are presented for two photometric systems: Johnson's UBV and 2MASS JHK$_s$, with the derived black-body parameters (*T* and *C*) also shown. As can be seen, the error in $\sigma_{min,BB}$ is typically less than a factor of 2, but sometimes it can be much larger (see for example star VB8).

The magnitudes and color indexes listed in Table 7.1 were computed from spectra downloaded from the CALSPEC library (STSCI, 2017) assuming some fixed values for the magnitudes of Vega, obtained from the Hipparcos and 2MASS star catalogs.

Table 7.1 – Comparison for some selected stars when *D* = 1 m and *t* = 1 s

parameter		star				
name/symbol	unit	Vega	1757132	Sun	KF06T2	VB8
spectral type	-	A0V	A3V	G2V	K1.5III	M7V
m_V	1	0.030	11.81	-26.75	13.97	16.8
$B-V$	1	-0.001	0.26	0.65	1.18	2.0
T	K	13,231	8580	5711	3951	2613
C	1	2.97e-17	1.87e-21	2.42e-5	9.59e-21	2.0e-20
$\sigma_{min,BB}$	rad	3.76e-13	1.40e-10	3.40e-18	4.29e-10	8.3e-10
m_H	1	-0.029	11.20	-28.15	11.23	9.1
$H-K_s$	1	-0.158	-0.14	-0.12	-0.05	0.2
T	K	10,417	8961	8058	6050	3282
C	1	4.80e-17	1.94e-21	1.41e-5	3.72e-21	1.0e-19
$\sigma_{min,BB}$	rad	5.37e-13	1.23e-10	1.88e-18	2.37e-10	2.0e-10
$\sigma_{min,num}$	rad	5.50e-13	1.75e-10	3.61e-18	4.67e-10	2.9e-10

Source: created by the author.

7.3.2.1 Color index limiting values

As explained in Section 7.2.5, the color indexes were limited to the interval that corresponds to a temperature range of 2000 K to 30,000 K. It was observed when the upper temperature limit was raised to more than 100,000 K, the Fisher information matrix $\mathbf{F}$ would be dominated by a few very blue, hot stars where the interpolation from the color index curve versus temperature would give a very high temperature, much higher than their actual temperatures, leading to a significant underestimate of $\bar{\vartheta}_{rms,min}$. In fact, even the 30,000 kelvins upper limit adopted in this work might be too high, resulting that the $\bar{\vartheta}_{rms,min}$ estimated here is probably lower than the actual lower bound of attitude error attainable by star trackers.

The lower limiting temperature of 2000 K could perhaps be set to a lower value (e.g.: 500 K) to better accommodate interstellar absorption and the existence of brown dwarfs. However, it was noted that this lower temperature limit has very little effect in the estimated value of $\bar{\vartheta}_{rms,min}$.

The optimal selection of temperature limits to be adopted for the black-body model will be a subject of a future work, if this model is not abandoned in favor of a more accurate stellar spectra model.

7.3.3 Results from catalogs and extrapolation

Some scripts were written to numerically evaluate the lower bound on star tracker attitude error, using the equations described in the previous section. We have used stars from the following star catalogs: Hipparcos, Tycho-2 and 2MASS, as described in Section 7.3.1. Figure 7.7 shows the results obtained using these catalogs versus the number of brightest stars (horizontal axis), for D = 1 m and t = 1 s. The letter codes J-H, J-K, H-K, B-V, V-I and B_T-V_T indicate the spectral bands used in each curve. In total, the procedure outlined in the previous section was performed for six different combinations of star catalogs and spectral bands.

Figure 7.7 – Inverse of the trace of the attitude error covariance matrix error for D = 1 m and t = 1 s, computed from the following star catalogs and their subsets: Hipparcos, Tycho-2 and 2MASS.

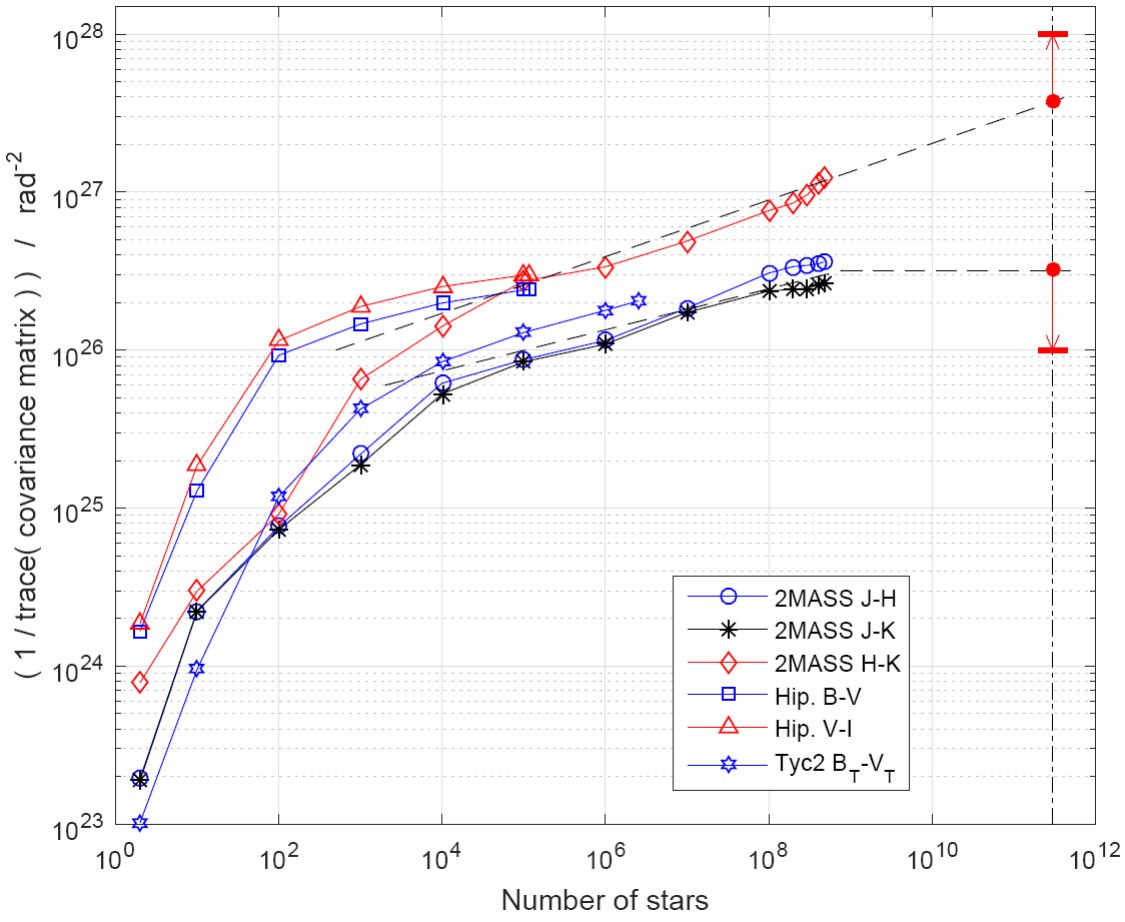

Source: Drawn by the author.

Many sources give a number between 10^{11} and $4{\cdot}10^{11}$ stars in our galaxy, with Guo, Zhang and Chen (2009) considering that our galaxy has about $3{\cdot}10^{11}$ stars (300 billion in the short scale[12]). Performing a rough extrapolation, we obtain for N = 300 billion stars, $1/\mathrm{tr}(\mathbf{P}_{\vartheta\vartheta})_{,min} \approx 4 \cdot 10^{27}\ \mathrm{rad}^{-2}$ for the upper curve and $3.2 \cdot 10^{26}\ \mathrm{rad}^{-2}$ for the lower curve. However, there were many approximations made in the model, mainly the assumption of black-body spectra for stars, hence the $1/\mathrm{tr}(\mathbf{P}_{\vartheta\vartheta})_{,min}$ estimate for D = 1 m and t = 1 s might still be wrong by a factor of

[12] unfortunately, the word *billion* is ambiguous, meaning 10^9 in the short scale and 10^{12} in the long scale. See for example, https://en.wikipedia.org/wiki/Billion and https://en.oxforddictionaries.com/explore/how-many-is-a-billion

2 or 3. Therefore, $1/\mathrm{tr}(\mathbf{P}_{\vartheta\vartheta})_{,min}$ is probably between 10^{26} rad^{-2} and 10^{28} rad^{-2}. From this we obtain that the G constant of Equation (7.23) is bounded by 10^{-14} rad·m^2·s$^{1/2}$ < G < 10^{-13} rad·m^2·s$^{1/2}$, with the upper bound of 10^{-13} rad·m^2·s$^{1/2}$ not being surpassed when D > 0.1 m and t > 0.01 s, as explained in the following paragraph.

For D = 0.1 m and t = 0.01 s (which gives a value of 0.001 m^2·s$^{1/2}$ for the combined $D^2t^{1/2}$ metric used in Figure 7.8), it was found that the expected number of detected photons, using values derived from $J-H$ color index in the 2MASS catalog, is larger than 1 for the $8\cdot10^8$ brightest stars. Since the accurate determination of the contribution to the Fisher information of stars for which the expected number of detected photons ι is less than 1 is difficult to determine, in this work, for simplicity, we have ignored all stars for which ι is less than 1. That is the reason why our extrapolation curve for the lower curve in Figure 7.7 becomes flat at $8\cdot10^8$ stars, making the estimated $\bar{\vartheta}_{rms,min}$ obtained from that curve being slightly overestimated. Note that we do not apply this approximation to the upper curve, as we want the $\bar{\vartheta}_{rms,min}$ estimate obtained from it to be somewhat underestimated, so that the true value of $\bar{\vartheta}_{rms,min}$ will lie in between.

7.3.3.1 Contributions from extragalactic sources

The contribution of all existing extragalactic sources in the known Universe for the attitude accuracy is probably very small (probably less than 10% of the overall Fisher information). The reason for that is the vast distances between galaxies in comparison to their dimensions. For example, the nearest galaxy about the same size or larger than our galaxy is the Andromeda Galaxy. Its center lies about at a distance of 780 kpc from us (RIBAS et al., 2005), which is about 10-20 times the diameter of their disks.

Our galaxy, the Milky Way Galaxy, is orbited by many dwarf galaxies, such as the Small and Large Magellanic Clouds, but the total number of stars in these dwarf

galaxies is less than 10% of the number of stars in our galaxy, therefore their contribution is also negligible.

Considering that the light intensity (and number of detected photons per unit time) falls off with the square of the distance from the source and that the Fisher information contributed by a star is proportional to the number of detected photons from that source, it is easy to see that the contribution from extragalactic sources will be small.

7.3.3.2 Need to consider some stars as extended sources

The lower bound on attitude uncertainty is so low that future star trackers would probably need to consider some stars as extended bodies and correct the effects of stellar spots (akin to sun spots, but in other stars) in their atmospheres to be able to come close to this theoretical lower bound, something that is unthinkable for current generation star trackers. For example, the star R Doradus, the star with largest apparent diameter after the Sun has an apparent diameter of 57 ± 5 milli-arc-seconds (ESO, 1997), with one milli-arc-second being 1/1000 of an arc-second.

7.3.4 Comparison with commercial star trackers

To give a feeling on how much room for improvement there is for future technology developments, Figure 7.8 compares the reported accuracy of some commercially available star trackers (JENA-OPTRONIK, 2015; TERMA A/S SPACE, 2012; SODERN, 2013; LEONARDO, 2017; VECTRONIC AEROSPACE, 2017a, 2017b; SINCLAIR INTERPLANETARY, 2016; BALL AEROSPACE, [1998 or 2005]; SPACE MICRO, 2015) with the theoretical lower bounds of an equivalent spherical star tracker having approximately the same

volume of a sphere that circumscribes the optical head of the star tracker[13], excluding its baffle[14].

Figure 7.8 – Comparison by reported attitude errors of some star trackers with the lower bound on attitude accuracy estimated in this work.

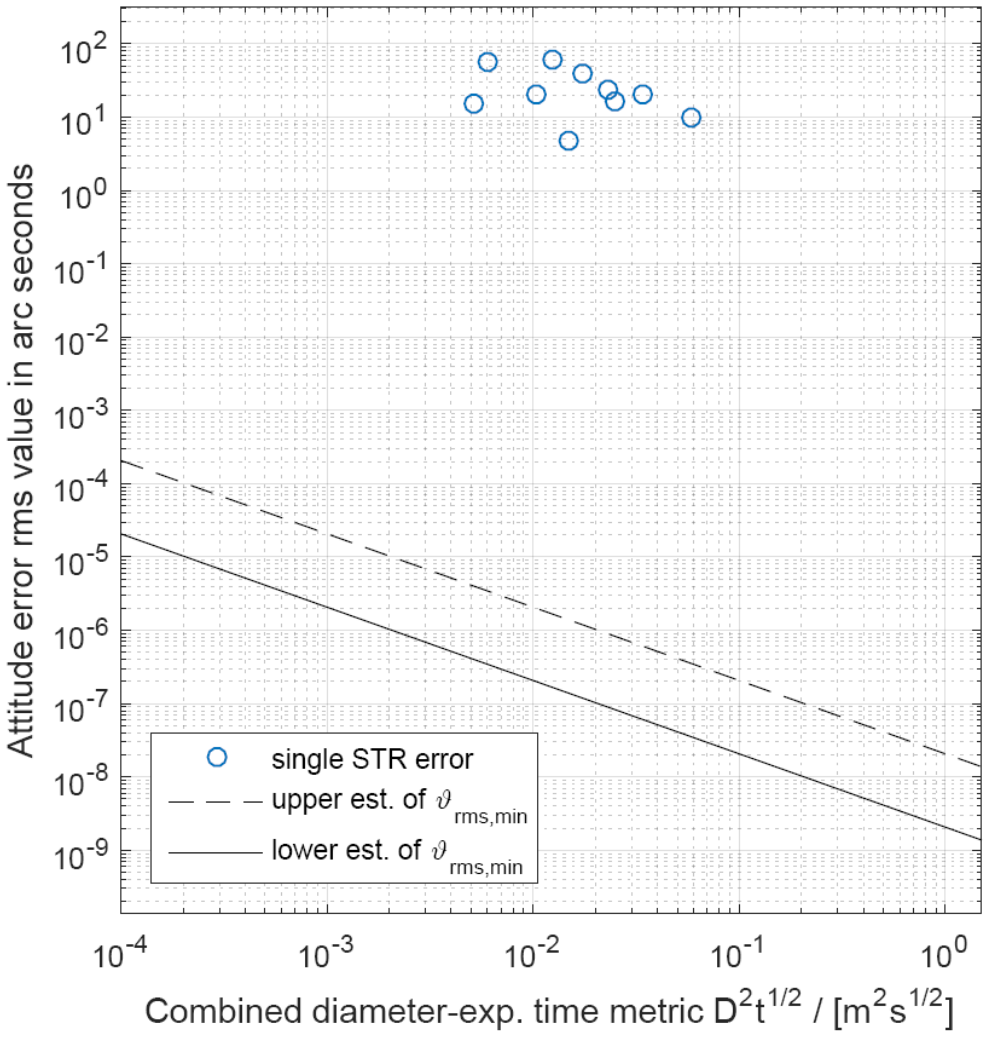

Source: Drawn by the author.

The comparison is performed in terms of the combined metric $D^2\,t^{1/2}$, according to Equation (7.23), which makes it possible to compare many different star

[13] the optical head is the box that houses the optics and image sensor. In some models, it includes the whole star tracker with the exception of its baffle. In other models, the processing electronics is in a separate box.
[14] A baffle is a protective light shade used in star trackers to prevent blinding by the Sun or other bright sources.

trackers in a single plot. The solid line at the bottom left of this plot denotes the lower estimate of the lower bound of the attitude error $\bar{\vartheta}_{rms,min}$, derived from the upper curve in Figure 7.7. The dashed line immediately above this solid line is the upper estimate of the lower bound of the attitude error $\bar{\vartheta}_{rms,min}$, derived from the lower curve in Figure 7.7. For D > 0.1 m and t > 0.01 s the true lower bound of attitude error ($\bar{\vartheta}_{rms,min,true}$) that can be obtained using electromagnetic radiation emitted from bodies (mostly stars) outside the Solar System should lie between these two curves. No star tracker that satisfies the constraints c) and g) stated in Section 7.2.1 should be able to surpass $\bar{\vartheta}_{rms,min,true}$ without making use of additional attitude reference sources, such as the Sun and other Solar System objects (excluded from analysis by the simplifying hypothesis c) in Section 7.2.2) or artificial attitude references.

We have opted to exclude the baffle in the estimate of D, because the sole reason for including them in star trackers is to protect star trackers from being temporarily blinded by stray light coming from the Sun and other bright sources (Earth, Moon and other spacecraft parts), something that would not happen in the absence of Solar System objects. Also, including the baffle would greatly inflate the diameter D of the circumscribing sphere. Unfortunately, star tracker product briefs and other publicly available information only provide their total dimension, including their baffle. Therefore, we had to estimate what would be their sizes without the baffle, by measuring lengths in photos included in the product briefs, from which D could be estimated with an uncertainty probably around 25%. It would be interesting as well to compute the $D^2\,t^{1/2}$ metric considering only the optical head aperture, typically much smaller than its dimensions. Unfortunately, this information is almost never provided in product briefs. The accuracy used in this plot was derived from the reported (1-σ) noise equivalent angle or attitude accuracy, using the equation $\vartheta_{rms}^2 = \sigma_x^2 + \sigma_y^2 + \sigma_z^2$, being $\sigma_x = \sigma_y$ the uncertainties in the rotation angles around the cross-boresight axes (pitch and yaw angles) and σ_z the uncertainty in the rotation angle around the boresight axis

(roll angle). For single head star trackers, the uncertainty in the roll angle is usually much larger than those in the yaw and pitch angles.

It should be noted that the positions of the commercial star trackers listed in this plot have large errors, being probably wrong by a factor of 2 or 3 in the combined $D^2\ t^{1/2}$ metric (horizontal axis) and also by a factor of 2 or 3 in the overall attitude error (vertical axis). The reason for that is the scarcity of information that is available in product briefs and websites. In many cases to obtain accurate information about star tracker dimensions, exposure time and accuracy it would be necessary to perform lengthy negotiations with star tracker manufacturers.

As can be seen, there's still a lot of room for improvement in star sensors. The theoretical lower bound is around 6 or 7 orders of magnitude lower than what is currently attained by most star trackers.

7.4 Future work

Here are some ideas for future works that could improve the accuracy of the lower bound of attitude error estimated in this work:

a) Use more complete star catalogs:

   A more accurate estimate on the Cramér-Rao bound on attitude accuracy obtainable from stars could be computed using a more complete star catalog, such as the USNO-B star catalog[15] with over one billion objects (MONET et al., 2003), or the forthcoming complete star catalog from the Gaia astrometric mission (PRUSTI et al., 2016)[16].

b) Use a better model for stellar spectra:

   Using a more accurate model for the stellar spectra, that takes into account the peculiarities of stellar spectral types and interstellar absorption is

[15] http://www.usno.navy.mil/USNO/astrometry/optical-IR-prod/usno-b1.0.
[16] http://sci.esa.int/gaia/

something that could be done in the future to improve the accuracy of the results obtained in this work.

c) Use magnitudes and color index uncertainties provided in star catalogs: Due to operational limitations we have ignored the uncertainties in magnitude and color indexes provided in star catalogs. An overhaul of the software used to determine the estimate of the lower bound of attitude error is planned for the future. With it we will include the propagation of uncertainties provided in star catalogs.

d) Use a more rigorous statistical treatment:
We plan in the future to reevaluate this estimate, using a more rigorous statistical treatment, taking into consideration of what happens when the expected number of detected photons is small, less than one. In this scenario, there exist a high probability that no photon from that star will be detected.

e) Include the Sun and other Solar System bodies in the lower bound estimate:
It would be interesting to know how much the lower bound attitude estimate could be improved if the Sun and other bodies in the Solar System could be used to improve attitude determination accuracy.

f) Compute estimates for other parts of the galaxy:
The estimates derived in this work are valid only in the Solar System neighborhood, since they are based on star coordinates, color indexes and magnitudes as seen from the Solar System. It would be interesting in the future to expand this work for other regions of our galaxy. For example, in star dense regions, the ultimate accuracy attainable by star trackers should be better than the ultimate accuracy attainable in our part of the galaxy.

7.5 Summary

To our best knowledge, this is the first work that attempts to obtain an estimate of the lower bound of attitude accuracy attainable by star trackers in the Solar System's stellar neighborhood. Being the first work to attempt to derive this estimate we did not aim to obtain an accurate estimate. The estimate obtained in our work might be wrong by a factor of 3 or 4, but it suffices for the purpose of obtaining an order of magnitude evaluation on how much room for improvement there exists for current state-of-the-art star trackers. Our work shows that the accuracy of current star trackers can still improve by about 6 or 7 orders of magnitude before reaching the ultimate limits imposed by laws of Physics and stellar distribution in our stellar neighborhood.

8 CONCLUSION

This work demonstrated that the use of magnitude and color information can improve star identification reliability and speed, even in algorithms that were initially developed to use star position information only, such as Pyramid, if it is assumed that the noise associated with star direction information remains at the same level. For Pyramid, the addition of magnitude filtering, color index filtering and pre-sorting the list of observed stars by magnitude resulted in a reduction of over two orders of magnitude in the rate of stellar misidentification. Even though the rate of stellar misidentification is typically very low for Pyramid in modern star trackers (less than 10^{-6}), in the presence of many spikes (false stars) this rate can become significant. Other modifications to the algorithm were performed, such as the realization of the mirror condition test for all kernels tested and the inclusion of a limit to the number of kernels to be tested. These modifications helped to reduce the misidentification rate even further.

Even though this was not the first work to propose the use of color information for star identification, as far as the author of this thesis is aware, it is the first work that uses color indices for star identification. Star identification using color information was previously proposed by McVittie in his PhD dissertation (2013). However, he used as a parameter for color information the color ratio, which is defined as the ratio between the fluxes of the same object measured in two different spectral bands. The main disadvantage of using color ratios directly is that their standard deviation is proportional to the value of the color ratio, being small for color ratios close to zero and large for color ratios much larger than a unit. By using color indexes (or color indices), which are basically the logarithm of the color ratios, this dependence of the standard deviation with the value of the variable representing color does not exist. Another advantage of using color indexes is that this is a more usual parameterization of star color in Astronomy, being easily found in star catalogs. There exists a vast literature in the field of stellar photometry that can be consulted providing methods to convert cataloged

magnitudes and color indexes from a standard photometric system to a custom photometric system devised for the color star tracker at hand.

In systems having more than two spectral bands, many different color indices can be defined. To aid in the selection of which color indexes to use, the author presented a method which can be used to estimate the sensitivity of the color indices to differences in temperature (and interstellar reddening) of stars. This method is described in Section 3.6.6.

The author of this thesis also investigated the use of color image sensors with stacked pixels for star tracking. Preliminary results obtained with this type of sensor were encouraging. This type of image sensors should provide many benefits for star identification and optical navigation compared to current alternatives, once this technology matures. More tests are needed with current generation of stacked pixel sensors and competing technologies to determine their relative performances for centroiding and star identification.

Considering that current generation color image sensors tend to be noisier than their monochrome counterparts for the purpose of star tracking, more detailed studies are needed to determine if color star trackers can compete with monochrome star trackers in terms of attitude accuracy and identification reliability. However, even if it is proved that color star trackers cannot compete with monochrome star trackers, it is worth investigating star-ID algorithms that make use of color information, as these could be used in color cameras aboard the spacecraft when these cameras are reconfigured as backup star trackers when the primary star trackers have failed.

Another interesting contribution of the author is the development of a better kernel generator for star-identification algorithms than the one originally proposed with Pyramid (Section 5.2.6). This contribution resulted in a journal paper co-authored with D. Arnas and D. Mortari (2016).

On the field of image processing, an algorithm to remove column fixed pattern noise has been proposed. This algorithm does not depend on calibration parameters and has a very low computational cost, making it a good candidate for compensating the column component of FPN in star trackers with low computational power based on CMOS APS image sensors, even if the FPN changes over time due to degradation caused by aging and exposure to ionizing radiation.

Concluding this thesis, an estimate of the Cramér-Rao lower bound for attitude determination error by star trackers operating in the vicinity of the Solar System was derived. This lower bound sets a fundamental limit which cannot be exceeded by star trackers operating in isolation, being this limit determined solely by the star tracker diameter, exposure time and stellar distribution around it. Our work shows that the accuracy of star trackers operating in the vicinity of the Solar System can still improve by 6 or 7 orders of magnitude before reaching this lower bound. This limit is also valid for star trackers operating inside the Solar System if they do not use the Sun and other Solar System bodies as additional references for attitude determination, as is the case of virtually every star tracker currently in use. The importance of estimating or computing fundamental limits cannot be overstated, since it is physically impossible to overcome these limits. Therefore, knowledge of fundamental limits enables us to rule out impossible designs during feasibility studies. Also, these limits are useful as benchmarks for comparing different designs. To the best knowledge of the author of this thesis, this contribution is novel, representing an original contribution to the field.

8.1 Future work

To properly set magnitude and color index tolerances in a color star tracker, it would be important to perform a census on stellar variability for the brightest stars used in star tracker catalogs. This is especially important for future star trackers using very tight magnitude tolerances (less than ± 0.05 magnitudes). The same can be said for color indices.

A natural evolution of this thesis would be to build a star tracker prototype based on the same image sensor used on the Foveon camera, and compare its performance with traditional star trackers based on monochrome image sensors.

An interesting topic for research would be to investigate how Pyramid behaves if the geometric pattern of observed stars is significantly distorted by stellar aberration (this happens when the spacecraft has very large heliocentric speed) and the catalog of star pairs is not updated to compensate this distortion.

Another interesting experiment would be to evaluate the behavior of Pyramid if a star catalog excluding all stars flagged as binary or multiple in the Hipparcos catalog were used. A previous test performed with a different star-ID algorithm gave disappointing results when all stars flagged as binary/multiple were removed from the star catalog (FIALHO; 2007).

Future work should also investigate how the use of magnitude and color indexes improve the reliability of star identification in the presence of false stars (spikes).

8.2 Acknowledgements

I would like to thank all my colleagues, friends and family that have in one way or other helped me during this long journey. Special thanks for my advisors, Dr. Leonel Perondi and Dr. Daniele Mortari.

I also thank CNPq and AEB for the scholarship grant that allowed me to stay for a year in Dr. Mortari's research group, performing theoretical and experimental work.

REFERENCES

AIRY, G. B., On the diffraction of an object-glass with circular aperture. **Transactions of the Cambridge Philosophical Society**, v. 5, p. 283-291, 1835.

ALBERT. **How to measure:** fixed-pattern noise in light or PRNU (1). 2012. Available at: <http://harvestimaging.com/blog/?p=916>. Accessed on: 04 Nov. 2014.

ALBUQUERQUE, B. F. C. **Estudo dos erros sistemáticos inerentes a um sensor de estrelas de cabeça fixa, quanto à localização relativa de estrelas**. 2005. 194 p. (INPE-14401-TDI/1127). Master Dissertation in Spatial Mechanics and Control - Instituto Nacional de Pesquisas Espaciais, São José dos Campos, 2005. Available at (in Portuguese): <http://urlib.net/sid.inpe.br/jeferson/2005/06.01.18.06 >. Accessed on: 14 Nov. 2014.

ALBUQUERQUE, B. F. C; FIALHO, M. A. A. **Estudo das fontes de erro existentes no sensor de estrelas autônomo em desenvolvimento no INPE**. São José dos Campos: INPE, 2005. (Internal publication of the Aerospace Electronics Division: DEA-EO-005/05, in Portuguese).

ARNAS, D.; FIALHO, M. A. A.; MORTARI. D. Fast and robust kernel generators for star trackers. **Acta Astronautica**, v. 134. p. 291-302, 2017. doi: 10.1016/j.actaastro.2017.02.016.

ANZAGIRA, L.; FOSSUM, E. R. Enhancing low light color imaging with pixel concept utilizing two vertically stacked detector layers. In: ANNUAL CONNECTICUT SYMPOSIUM ON MICROELECTRONICS AND OPTOELECTRONICS, 24., 2015, Bridgeport, CT. **Proceedings...** Bridgeport: University of Bridgeport, 2015.

BAER, R. L. A model for dark current characterization and simulation. **Proc. SPIE** 6068, Sensors, Cameras, and Systems for Scientific/Industrial Applications VII, 606805 (February 06, 2006); doi:10.1117/12.639844.

BALDWIN, J. E.; HANIFF, C. A. The application of interferometry to optical astronomical imaging. **Phil. Trans. R. Soc. Lond. A**, v. 360, p. 969-986, 2002. doi: 10.1098/rsta.2001.0977.

BALL, P. Moore for less. **Nature**, 21 Apr. 2005. doi:10.1038/news050418-14. Available at: < http://www.nature.com/news/2005/050418/full/news050418-14.html > Accessed on: 21 July 2017.

BALL AEROSPACE & Technologies Corp. **CT-633 stellar attitude sensor**. Boulder, CO, USA. [1998 or 2005]. Datasheet.

BEIGEL, J. It's a small world and getting smaller. **Sensors Online**. Dec. 20, 2013. Available at: <http://www.sensorsmag.com/components/it-s-a-small-world-and-getting-smaller> Accessed on: 21 July 2017.

BEKENSTEIN, J. D. Energy cost of information transfer. **Phys. Rev. Letters,** v. 46, n. 10, p. 623-626. 9 Mar. 1981. doi: 10.1103/PhysRevLett.46.623.

BESSELL, M. S. Standard photometric systems. **Annu. Rev. Astron. Astrophys.,** 2005. 43:293-336. doi:10.1146/annurev.astro.41.082801.100251.

BESSEL, M. S.; MURPHY, S. Spectrophotometric libraries, revised photonic passbands, and zero points for UBVRI, Hipparcos, and Tycho photometry. **Publications of the Astronomical Society of the Pacific,** v. 124, p. 140-157, Feb. 2012.

BRÄTT, S. P. **Analysis of star identification algorithms due to uncompensated spatial distortion.** Thesis (Master of Science in Mechanical Engineering). Utah State University, 2013.

BRUM, A. G. V.; FIALHO, M. A. A.; SELINGARDI, M. L.; BORREGO, N. D.; LOURENÇO, J. L. The Brazilian Autonomous Star Tracker – AST. **WSEAS Transactions on Systems,** Issue 10, v. 12, p. 459-470, Oct. 2013. E-ISSN: 2224-2678.

BUDDING, E., DERMICAN, O. **Introduction to Astronomical Photometry**. 2nd ed. Cambridge: Cambridge University Press, 2007. 450p. ISBN 978-0-521-84711-7.

CARVALHO, G. B. **Levantamento de técnicas de identificação de estrelas e desenvolvimento de um ambiente de simulação e testes para análise de seus desempenhos em aplicações espaciais.** 2001. 290p. Master's Dissertation (Mestrado em Engenharia e Tecnologia Espaciais/Mecânica Espacial e Controle) – Instituto Nacional de Pesquisas Espaciais, São José dos Campos.

CHARLES Jr., H. L. Miniaturized Electronics. **Johns Hopkins APL Technical Digest**, Laurel, MD, USA, v. 26, n. 4, p. 402-413, 2005.

CROSSLINK – The Aerospace Corporation magazine of advances in aerospace technology: Radiation in the Space Environment. Los Angeles: Aerospace Corporation. v. 4, n.2, Summer 2003. Available at: < http://www.aerospace.org/publications/crosslink-magazine/previous-issues/ > Accessed on: 10 Aug. 2017.

ENRIGHT, J.; SINCLAIR D.; DZAMBA, T. The things you can't ignore: evolving a sub-arcsecond star tracker. In: AIAA/USU CONFERENCE ON SMALL SATELLITES, ADVANCED TECHNOLOGIES III, 26., 2012. **Proceedings...** AIAA/USU, 2012. Paper SSC12-X-7. Available at: < http://digitalcommons.usu.edu/smallsat/2012/all2012/79/ > Accessed on: 21 July 2017.

ENRIGHT, J.; SINCLAIR D.; GRANT, C; MCVITTIE, G.; DZAMBA, T. Towards star tracker only attitude estimation. In: ANNUAL AIAA/USU CONFERENCE ON SMALL SATELLITES, 24., 2010, Logan, Utah. **Proceedings...** AIAA/USU , 2010. Paper SSC10-X-3.

EUROPEAN SPACE AGENCY (ESA). **The Hipparcos and Tycho catalogues**: astrometric and photometric star catalogues derived from the ESA Hipparcos Space Astrometry Mission. Noordwijk, Netherlands: ESA Publications Division, Series: ESA SP Series v. 1200, 1997. ISBN: 9290923997.

EUROPEAN SOUTHERN OBSERVATORY (ESO). **The biggest star in the sky**. 11 Mar. 1997. Available at: <http://www.eso.org/public/news/eso9706/> Accessed on: 2 Oct. 2017.

FALLON III, L. Star sensors. In: WERTZ, J. R. (editor) **Spacecraft attitude determination and control.** Dordrecht: D. Reidel, 1978. Section 6.4. p. 184-195.

FIALHO, M. A. A. **Ambiente de simulações e testes de algoritmos para sensores de estrelas autônomos**. 2003. 120f. Undegraduate Thesis – Instituto Tecnológico de Aeronáutica, São José dos Campos, 2003. (in Portuguese).

FIALHO, M. A. A. **Estudo comparativo entre dois algoritmos de identificação de estrelas para um sensor de estrelas autônomo de campo largo**. 2007. Master Thesis (Mestrado em Engenharia Eletrônica e Computação. Área de Dispositivos e Sistemas Eletrônicos) – Instituto Tecnológico de Aeronáutica, São José dos Campos, 2007. (in Portuguese)

FIALHO, M. A. A.; LOPES, R. V. F.; SAOTOME, O. Um método de calibração automática em magnitude para sensores de estrelas. In: CONGRESSO TEMÁTICO DE DINÂMICA, CONTROLE E APLICAÇÕES, 4., Bauru, 2005. **Anais...** Bauru: UNESP, p 526-535, 2005.

FIALHO, M. A. A.; MORTARI, D. Performance tests of Pyramid star-ID algorithm with memory adaptive k-vector. In: AAS/AIAA SPACE FLIGHT MECHANICS MEETING, 27., 2017, San Antonio, TX. **Proceedings...** San Diego, CA: Univelt, Feb. 2017a. Paper AAS 17-311.

FIALHO, M. A. A.; MORTARI, D. Non linear k-vector. In: AAS/AIAA SPACE FLIGHT MECHANICS MEETING, 27., 2017, San Antonio, TX. **Proceedings...** San Diego, CA: Univelt, 2017b. Paper AAS 17-485.

FIALHO, M. A. A.; MORTARI, D.; PERONDI, L. F. Ideas for multispectral cameras with stacked pixels for star tracking and optical navigation. In: AAS/AIAA SPACE FLIGHT MECHANICS MEETING, 26., 2016, Napa, CA. **Proceedings...** San Diego, CA: Univelt, 2016. Paper AAS 16-321.

FIALHO, M. A. A.; PERONDI, L. F.; MORTARI, D. The Brazilian autonomous star tracker development. In: AAS/AIAA SPACE FLIGHT MECHANICS MEETING, 26., 2016., Napa, CA. **Proceedings...** San Diego, CA: Univelt, 2016. Paper AAS 16-322.

FIALHO, M. A. A.; SAOTOME, O. An environment for testing and simulating algorithms for autonomous star sensors. In: INTERNATIONAL CONGRESS OF MECHANICAL ENGINEERING, 18., 2005, Ouro Preto. **Proceedings...** Ouro Preto: ABCM, 8p., 2005. Paper COBEM2005-1228.

FOVEON, Inc. **Foveon X3 F13 direct image sensor** 14.1 megapixels in a 1.7x FLM optical format. Santa Clara, CA, USA, 2006. (Product Brief) Document DS109-01 05/2006 Rev B.

FOSSUM, E.; HONDONGWA, D. B. A Review of the pinned photodiode for CCD and CMOS image sensors. **IEEE Journal of the Electron Devices Society**, v. 2, n. 2, p. 33-43, May 2014.

GAMAL, A. E.; FOWLER, B.; MIN, H.; LIU, X. Modeling and estimation of FPN components in CMOS image sensors, **Proc. SPIE** 3301, Solid State Sensor Arrays: Development and Applications II, 168 (April 1, 1998); doi:10.1117/12.304560

GHAEMI, F. T. Design and fabrication of lenses for the color science cameras aboard the Mars Science Laboratory rover. **Optical Engineering**, v. 48(10), 103002. October 2009.

GILBLOM, D.; YOO, S.; VENTURA, P. Operation and performance of a color image sensor with layered photodiodes. **Proc. SPIE**, v. 5074, p. 318-331, 2003.

GOTTLIEB, D. M. Star Identification Techniques. In: WERTZ, J. R. **Spacecraft Attitude Determination and Control**. Dordrecht: D. Reidel, 1978. p. 259-266.

GREEN, M. A. Self-consistent optical parameters of intrinsic silicon at 300K including temperature coefficients. **Solar Energy Materials & Solar Cells.** v. 92, p. 1305-1310, 2008.

HAHN, G. J.; SHAPIRO, S. S. **Statistical models in engineering.** New York: John Wiley & Sons, 1967. 355p.

HARTRIDGE, H. Visual Acuity and the Resolving Power of the Eye. **The Journal of Physiology**, v. 57, issue 1-2. p. 52-67. 1922.

HARTUNG, J.; KNAPP, G.; SINHA, B. K. **Statistical meta-analysis with applications**. Hoboken, NJ, USA: Wiley, 2008. 256 p. ISBN 978-0-470-29089-7.

HOG, E. et al. The Tycho-2 Catalogue of the 2.5 Million Brightest Stars. **Astronomy & Astrophysics**. 355: L27. 2000.

HOLLOW, R. Spectroscopy: unlocking the secrets of star light. **Science Teachers' Workshop** 2006. [s.l.]: CSIRO Australia Telescope National Facility. 2006. Available at: <www.atnf.csiro.au/outreach/education/teachers/resources/spectroscopystw2006.pdf> Access date: 07 Aug. 2017.

HOLST, G. C.; LOMHEIM, T. S. **CMOS/CCD sensors and camera systems**. 2nd ed. Bellingham, WA, USA: SPIE Press, 2011. 388p. ISBN:9780819486530.

HORNSEY, R. I. **Noise in Image Sensors**. 2003. 86 p. Class notes. Available at <https://ece.uwaterloo.ca/~ece434/Winter2008/Noise.pdf>. Accessed on 08 Oct. 2017.

INNOCENT, M. General Introduction to CMOS Image sensors. In: INTERNATIONAL SYMPOSIUM ON RELIABILITY OF OPTOELECTRONICS FOR SYSTEMS (ISROS 2009), 2009, Tolouse, France. **Proceedings...** Tolouse: International Society on Reliability of Optoelectronics for Systems (ISROS), p. 78-98, 2009. Available at: <http://cct.cnes.fr/system/files/cnes_cct/459-mce/public/3_Tutorial.pdf>. Access on 12 Nov. 2014.

INSTITUTE OF ELECTRICAL AND ELECTRONICS ENGINEERS (IEEE). **IEEE standard for floating-point arithmetic**. New York, 29 Aug. 2008. 70 p. IEEE Std 754-2008.

INTERNATIONAL ASTRONOMICAL UNION (IAU). **Standards of Fundamental Astronomy**. Tauton, UK. 2017. Available at: <http://www.iausofa.org/index.html>. Accessed on 19 September 2017.

INTERNATIONAL EARTH ROTATION AND REFERENCE SYSTEMS SERVICE (IERS). **The International Celestial Reference System (ICRS)**. 2013. Available at: <https://www.iers.org/IERS/EN/Science/ICRS/ICRS.html>. Accessed on 29 July 2017.

JAYAWARDHANA, R. **The neutrino hunters:** the chase for the ghost particle and the secrets of the universe. London: Oneworld Publications. 256 p., 2015. ISBN: 1-780-74647-4.

JENA-OPTRONIK GmbH. **Autonomous star sensor ASTRO 15**. Jena, Germany, 2015. Datasheet. Available at: <http://www.jena-optronik.de/en/aocs/astro15.html> Accessed on 23 May 2017.

JOHNSON, H. L.; MORGAN, W. W. Fundamental stellar photometry for standards of spectral type on the revised system of the Yerkes spectral atlas. **The Astrophysical Journal**, v. 117 n. 3, p. 313-352, May 1953.

JULIAN EPOCH. In: RIDPATH, I. **A Dictionary of Astronomy**. 2 rev. ed. Oxford: Oxford University Press, 2012. 534 p. Available at: < http://www.oxfordreference.com/view/10.1093/oi/authority.20110803100026731 > Accessed on 30 Sep. 2017.

KORDAS, J. F. et al. Star tracker stellar compass for the Clementine mission. **Proc. SPIE**, v. 2466, p. 70-83, 1995.

LEONARDO – Società per azioni. **A-STR and AA-STR autonomous star trackers**. Campi Bisenzio (FI), Italy. 2017. Datasheet. Available for download at: <http://www.leonardocompany.com/en/-/aastr>. Accessed on 24 May 2017.

LIEBE, C. C. Star trackers for attitude determination. **IEEE Aerospace and Electronic Systems Magazine**, v. 10, issue 6, p. 10-16, June 1995. DOI 10.1109/62.387971.

LIEBE, C. C. Accuracy performance of star trackers: a tutorial. **IEEE Transactions on Aerospace and Electronic Systems**, v. 38, n. 2, p. 587-599, Apr. 2002.

LINDEGREN, L. High-accuracy positioning: astrometry. In: **Observing photons in space**. v. 9 of the series ISSI Scientific Report Series, p. 299-311. Oct. 2013. ISBN 978-1-4614-7804-1 DOI 10.1007/978-1-4614-7804-1_16.

MACKAY, D. J. C. **Information theory, inference, and learning algorithms.** Cambridge: Cambridge University Press, 2005. 640p. Available online at: <http://www.inference.org.uk/mackay/itila/book.html>. Accessed on 03 July 2017.

MARKLEY, F. L.; CRASSIDIS, J. L. **Fundamentals of spacecraft attitude determination and control**. New York: Springer, 2014. 486 p. ISBN 978-1-4939-0801-1.

MANSOORIAN et al. **Stacked photodiodes for extended dynamic range and low light discrimination.** US Patent Application US2015/0090863. Apr. 2015.

MARTIN, E. **Etude physique de la dégradation et modèles pour l'assurance durcissement des capteurs d'image en environnement spatial**. 214p. Phd Thesis (Doctorat en ED GEET: Photonique et systèmes optoélectroniques) - Université de Toulouse / Institut Supérieur de l'Aéronautique et de l'Espace (ISAE), Tolouse, 2012. Available at: <http://depozit.isae.fr/theses/2012/2012_Martin_Emma.pdf>. Access on 12 Nov. 2014.

McCLUNEY, W. R.. **Introduction to radiometry and photometry**. Artech House. 1994. ISBN 0-89006-678-7.

McVITTIE, G. **Development and performance characterization of colour star trackers**. PhD Dissertation. Ryerson University, Toronto, Canada. 2013.

MERRILL, R. B. **Vertical color filter detector group and array**. US Patent 6632701 B2. 2003.

MICROCHIP TECHNOLOGY Inc. **Understanding A/D converter performance specifications.** 2000. Application note AN693. Available on-line at: <http://ww1.microchip.com/downloads/en/appnotes/00693a.pdf>. Access on 22 May 2014.

MOHR, P. J.; NEWELL, D. B.; TAYLOR, B. N. CODATA recommended values of the fundamental physical constants: 2014. **Reviews of Modern Physics**, v. 88, July-Sep. 2016. 73 p. doi: 10.1103/RevModPhys.88.035009.

MOLINDER, J. I. A tutorial introduction to very long baseline interferometry (VLBI) using bandwidth synthesis. **DSN Progress Report 42-46**, p. 16-28. May-June 1978.

MONET, D. G. et al. The USNO-B catalog. **The Astronomical Journal**, v. 125 p. 984-993, 2003.

MOORE, G. E. Cramming more components onto integrated circuits. **Electronics**, v. 38, n. 8, p. 114-117, 1965. Republished in IEEE Solid-State Circuits Society Newsletter, v. 20, issue 3, Sept. 2006.

MORTARI, D. A fast on-board autonomous attitude determination system based on a new star-ID technique for a wide FOV star tracker. In: AAS/AIAA SPACE FLIGHT MECHANICS MEETING, 1996, Austin, TX. **Proceedings...** San Diego, CA: Univelt, 1996. Paper AAS 96-158.

MORTARI, D. The Attitude Error Estimator. In: INTERNATIONAL CONFERENCE ON DYNAMICS AND CONTROL OF SYSTEMS AND STRUCTURES IN SPACE, 2002, King's College, Cambridge, UK. **Proceedings...** 2002.

MORTARI, D. Memory Adaptive k-vector. In: AAS/AIAA SPACE FLIGHT MECHANICS MEETING, 24., 2014, Santa Fe, NM. **Proceedings...** San Diego, CA: Univelt, 2014. Paper AAS 14-207.

MORTARI, D.; JUNKINS, J. L.; SAMAAN, M. A. Lost-in-space Pyramid algorithm for robust star pattern recognition. In: ANNUAL AAS ROCKY MOUNTAIN GUIDANCE AND CONTROL CONFERENCE, 24., 2001, Breckenridge, CO. **Proceedings...** San Diego, CA: Univelt, 2001. Paper AAS 01-004.

MORTARI, D; NETA, B. k-vector range searching techniques. In: AAS/AIAA SPACE FLIGHT MECHANICS MEETING, 2000, Clearwater, FL. **Proceedings...** San Diego, CA: Univelt, 2000. Paper AAS 00-128.

MORTARI, D.; SAMAAN, M. A.; BRUCCOLERI, C.; JUNKINS, J. L. The Pyramid Star Identification Technique. **Navigation**, v. 51, n. 3, p. 171-183, Fall 2004.

MUELLER, J. H.; SÁNCHEZ-SÁNCHEZ, C.; SIMÕES, L. F.; IZZO, D. Optimal orderings of k-subsets for star identification. **2016 IEEE Symposium Series on Computational Intelligence (SSCI)**. Athens, Greece, 2016. doi: 10.1109/SSCI.2016.7850106.

NAGASAWA, D. Q. et al. Throughput of commercial photographic camera lenses for use in astronomical systems. In: PROC. SPIE, GROUND-BASED AND AIRBONE INSTRUMENTATION FOR ASTRONOMY VI, 9908, 99085C, 2016. **Proceedings...** Edinburgh, UK: SPIE, 2016. doi 10.1117/12.2233723.

NATIONAL AERONAUTICS AND SPACE ADMINISTRATION (NASA), **Instrument information**. June 2017. Available at: < https://pds.nasa.gov/ds-view/pds/viewInstrumentProfile.jsp?INSTRUMENT_ID=NAVCAM&INSTRUMENT_HOST_ID=RO>. Access date: 28 July 2017.

ON SEMICONDUCTOR. **STAR-1000 frequently asked questions.** Application note (document AND9113/D rev. 1 dated November 2012). 3 p.

ON SEMICONDUCTOR. **STAR1000: 1 megapixel radiation hard CMOS image sensor.** datasheet. (document NOIS1SM1000A-D.PDF dated 04/Feb./2014) Available at: <http://www.onsemi.com/PowerSolutions/product.do?id=STAR1000>. Accessed on 04 Nov. 2014.

PALMER, J. M.; GRANT, B. G. **The art of radiometry**. Bellingham: SPIE Press, 2010. 370p. ISBN 9780819472458.

PORCO, C. C. et al. Cassini imaging science: instrument characteristics and anticipated scientific investigations at Saturn. **Space Science Reviews**. v. 115 p. 363-497, Nov. 2004.

PORTER, W. C. et al. Dark current measurements in a CMOS imager. **Proc. SPIE** 6816, Sensors, Cameras, and Systems for Industrial/Scientific Applications IX, 68160C, 29 Feb. 2008. doi:10.1117/12.769079.

PRUSTI, T. et al. The Gaia Mission. **Astronomy & Astrophysics**. v. 595, 36 p., 2016. doi: 10.1051/0004-6361/201629272.

QUEST INNOVATIONS. **The Condor Foveon**. Middenmeer, Netherlands. 5 p. [2015?]. Datasheet.

RANGAYYAN, R. M. **Biomedical Image Analysis**. Boca Raton, FL: CRC Press. 2004. 1312p. ISBN 0-8493-9695-6.

RAO, G. N.; BHAT, M. S.; ALEX, T. K. Star Pattern Identification Using Discrete Attitude Variation Technique. **Journal of Guidance, Control, and Dynamics.** v. 28, n. 6, 2005. p. 1140-1149.

RIBAS, I. et al. First determination of the distance and fundamental properties of an eclipsing binary in the Andromeda Galaxy. **The Astrophysical Journal**. v. 635, L37-L40. 10 Dec. 2005. doi: 10.1086/499161.

RINDLER, W. **Essential relativity:** special, general and cosmological. New York: Springer-Verlag, 1977. 284p. ISBN: 0-387-07970-x.

ROBINSON, M. S.; MALARET, E.; WHITE, T. A radiometric calibration for the Clementine HIRES camera. **Journal of Geophysical Research**, v. 108, n. E4, 5028. 2003. doi: 10.1029/2000JE001241.

ROSSER, W. G. V. **Introductory relativity**. London: Butterworks, 1967. 347p.

SAMUS N. N. et al. General catalogue of variable stars: version GCVS 5.1. **Astronomy Reports**, 2017, v. 61, n. 1, p. 80-88.

SINCLAIR INTERPLANETARY. **Second generation star tracker (ST-16RT2)**. [s.l.], 2016. Datasheet. Available for download from: <http://www.sinclairinterplanetary.com/startrackers> Accessed on 24 May 2017.

SHANNON, C. E. A Mathematical theory of communication. **Bell System Technical Journal**, v. 27, n. 3, p. 379-423, July 1948.

SHUSTER, M. D. Stellar aberration and parallax: a tutorial. **The Journal of the Astronautical Sciences**, v. 51, n. 4, October-December 2003, p. 477-494.

SKRUTSKIE, M. F. et al. The Two Micron All Sky Survey (2MASS). **The Astronomical Journal**, v. 131, p. 1163-1183. Feb. 2006.

SMITH, P. H. et. al. The imager for Mars Pathfinder experiment. **Journal of Geophysical Research**, v. 102, n. E2. p. 4003-4025, 25 Feb. 1997.

SMITH, R. M.; RAHMER, G. Pixel area variation in CCDs and implications for precision photometry. **Proc. SPIE** 7021, High Energy, Optical, and Infrared Detectors for Astronomy III, 70212A (22 July 2008); doi: 10.1117/12.789665.

SODERN. **SED26 Star Tracker**. Limeil-Brevanes, France, 2013. Datasheet. Available at: <http://www.sodern.com/sites/en/ref/SED26_45.html>. Access date 23 May 2017.

SPACE MICRO. **μSTAR Tracker**. San Diego, CA, USA. 2015. Datasheet. Available for download at: <http://www.spacemicro.com/products/guidance-and-navigation.html>. Accessed on 24 May 2017.

SPACE TELESCOPE SCIENCE INSTITUTE (STSCI). **CALSPEC Calibration database.** 2017. Available at: <http://www.stsci.edu/hst/observatory/crds/calspec.html> Access date: 19 June 2017.

SPACE TELESCOPE SCIENCE INSTITUTE (STSCI). **Hubble Space Telescope WFC3 Filters**. [2015?]. File irfiltwheel.jpg. Available at: <http://www.stsci.edu/hst/wfc3/ins_performance/filters/>. Accessed on 8 Sept. 2017.

SPRATLING, B.B. and MORTARI, D. A survey on star identification algorithms, **Algorithms**, Special Issue: Sensor Algorithms, v. 2, n. 1, p. 93-107, Jan. 2009.

STRAIŽYS, V. The method of synthetic photometry, **Baltic Astronomy**, v. 5, p. 459-476. 1996.

SUN, T.; XING, F.; YOU, Z. System error analysis and calibration method of high-accuracy star trackers. **Sensors**, Basel, Switzerland, v. 13, p. 4598-4623, 2013. doi:10.3390/s130404598

STOKES, H. T. **Resolving power of the eye**. Last modified on September 2014 (from webpage metadata). Available at:
< http://stokes.byu.edu/teaching_resources/resolve.html >.
Access date: 4 July 2017.

TERMA A/S SPACE. **Star Tracker HE-5AS**. [s.l.], 2012. Datasheet. Available at: <https://www.terma.com/media/101677/star_tracker_he-5as.pdf> Accessed on 23 May 2017.

TIAN, H. **Noise analysis in CMOS image sensors**. A Dissertation of Stanford University, 2000. (PhD Dissertation).

TURCHIN, M. et al. On Random and Systematic Errors of a Star Tracker. In: ANNUAL AIAA/USU CONFERENCE ON SMALL SATELLITES, 27., 2013, Logan, UT, USA. **Proceedings**... Logan: Utah State University, 2013. Paper SSC13-I-10. Available at:
<http://digitalcommons.usu.edu/smallsat/2013/all2013/>. Accessed on: 12 Nov. 2014.

TURON, C. The Tycho-2 Catalogue: a reference for astrometry and photometry. Combining the most modern and the oldest astrometric data. **Astronomy & Astrophysics**. v.500, p. 587-588, 2009.

VARINTELLIGENT (BVI) LIMITED. Hoi Sing Kwok; Xu Liu. **Optical assembly for reflective light valves**. 1999. European Patent EP 1 145 565 B1, 22 Dec. 1999, 20 Oct. 2004.

VECTRONIC AEROSPACE GmbH. **Star Tracker VST-41M**. Berlin, 2017a. Datasheet. Available at:
<http://www.vectronic-aerospace.com/space-applications/star-sensor/>
Accessed on: 24 May 2017.

VECTRONIC AEROSPACE GmbH. **Star Tracker VST-68M**. Berlin, 2017b. Datasheet. Available at:
<http://www.vectronic-aerospace.com/space-applications/star-tracker-vst-68m/>
Accessed on: 24 May 2017.

WENGER, M. et al. The SIMBAD astronomical database. **Astronomy & Astrophysics**. Suppl. Series. v. 143, p. 9-22, 2000.

WERTZ, J. R. (Editor). **Spacecraft attitude determination and control.** Dordrecht: D. Reidel, 1978. 858p. ISBN 9-0277-1204-2.

WERTZ, J. R.; LARSON, W. J. (Editors). **Space mission analysis and design**. Third Edition. New York: Springer, 1999. ISBN 978-1-881883-10-4.

WIDENHORN, R.; BLOUKE, M. M.; WEBER, A.; REST, A.; BODEGOM, E. Temperature dependence of dark current in a CCD. **Proc. SPIE** v. 4669, p. 193-201. 2002.

WOOLARD, E. W.; CLEMENCE, G. M. **Spherical astronomy**. New York: Academic Press, 1966. 469p.

YEN, J. **Combining information**. [s.l.], 2002. (Lecture notes on Statistics) Available at: <https://www.nist.gov/document-13811>. Accessed on 19 May 2017.

ZAKHAROV, A. I.; PROKHOROV, M. E.; TUCHIN, M. S.; ZHUKOV, A. O. Minimum star tracker specifications required to achieve a given attitude accuracy. **Astrophysical Bulletin** October 2013, v. 68, Issue 4, p. 481-493.

ZEILIK, M.; GREGORY, S. A. **Introductory astronomy & astrophysics**. Fourth Edition. United States of America: Thomson Learning, Inc., 1998. 672 p. ISBN: 0-03-006228-4.

ZHAI, C.; SHAO, M.; GOULLIOUND, R.; NEMATI, B. Micro-pixel accuracy centroid displacement estimation and detector calibration. **Proc. R. Soc. A** 467, 3550, 2011.

ZHANG, G. **Star identification**: methods, techniques and algorithms. Berlin: Springer / Beijing: National Defense Industry Press, 2017. 231 p. ISBN: 978-3-662-53783-1.

APPENDIX A REFERENCE FRAMES AND COORDINATE SYSTEMS

In this appendix, reference frames and coordinate systems usually adopted in star tracker work will be presented. Many of these concepts were presented in previous works by the author (FIALHO, 2003; FIALHO, 2007), but will be presented here with improvements due to its importance for the field. This appendix is a revised version of Appendix B of the master thesis presented by the author (FIALHO, 2007).

A.1 Basic concepts

A.1.1 Celestial sphere

Ancient people, when observing the night sky, had the impression that there existed a giant sphere concentric with the Earth, with fixed stars on it. This sphere, known by the name *celestial sphere* performed an east to west movement, carrying with it all celestial bodies. Nowadays, we know that such a sphere does not exist. The westward movement of this sphere is simply a consequence of the true rotational motion of our planet.

Despite it having no physical existence, the celestial sphere is a very useful concept when one wishes to express only the apparent position of celestial bodies, without worrying about the true distances of these objects to the observer. Therefore, the celestial sphere can be defined as a sphere with an infinite or indeterminate radius centered in the observer, where the celestial bodies would be projected, as depicted in Figure A.1 (WOOLARD, 1966).

Using this concept, points in the celestial sphere actually represent directions in the three-dimensional space, and distances between these points correspond to the angular separations between the directions represented by these points.

Figure A.1 – Celestial bodies projected on a celestial sphere centered in the observer.

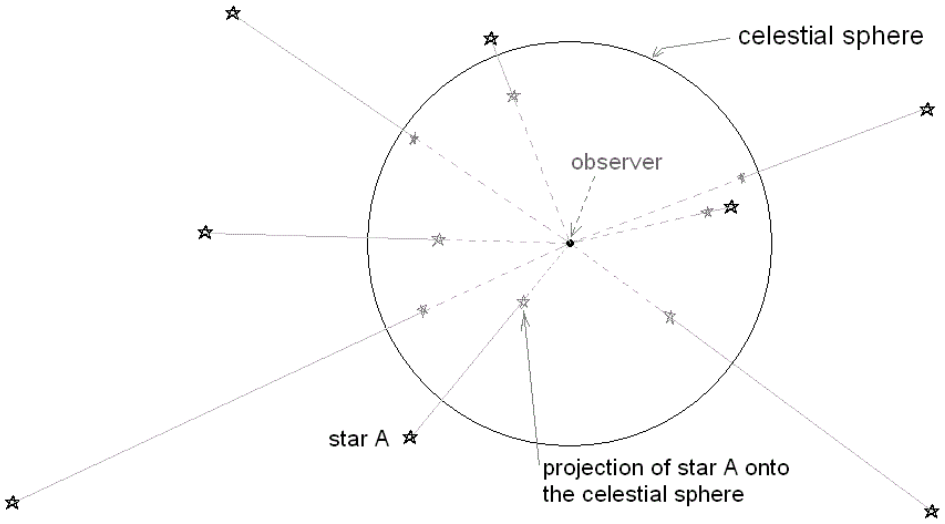

Source: Adapted from Fialho (2007).

In the same manner that a celestial sphere centered on Earth can be defined, so can be defined a celestial sphere centered on Mars, on Venus, etc. Therefore, we will adopt for this work a celestial sphere centered on the star tracker.

A.1.2 Celestial equator, ecliptic, equinoxes, solstices and poles of the celestial sphere

Since the most important reference frames and coordinate systems adopted in Astronomy were originally defined based on concepts derived from the projection of rotational and translational motions of the Earth on the celestial sphere it is important to know the definition of these concepts.

From the point of view of a hypothetical observer located at the center of the Earth we can define the following:

a) celestial equator => it is the projection of Earth's equator onto the celestial sphere;

b) north and south poles of the celestial sphere (in the equatorial coordinate system, described in Section A.2.1) => they are the projection of the Earth's North Pole and South Pole onto the celestial sphere. In other words, these are the intersection of Earth's spin axis with the celestial sphere;

c) ecliptic => is the projection of Earth's orbital plane onto the celestial sphere. It corresponds to the Sun's apparent mean annual path in the celestial sphere for an observer located at the center of the Earth;

d) equinoxes => the intersection between the celestial equator and the ecliptic. There are two equinoxes: the March equinox and the September equinox. The March equinox happens when the Sun, considering its mean apparent motion in the celestial sphere crosses the ecliptic from the Southern Hemisphere to the Northern Hemisphere, happening around March 21st every year. The March equinox, also known as vernal equinox or first point of Aries (♈) defines the origin of the angular coordinates used in the equatorial coordinate system.

e) solstices => they correspond to the maximum displacement from the celestial equator to the north or to the south of the Sun in its mean apparent motion in the sky. Following the ecliptic, they are at 90 and 270 degrees from the vernal equinox;

f) north and south poles of the ecliptic => They are at 90 degrees from the plane of the ecliptic (Earth's orbital plane).

Figure A.2 depicts some of these concepts.

Figure A.2 – Definition of the vernal equinox (♈) from Earth's rotational and orbital motions.

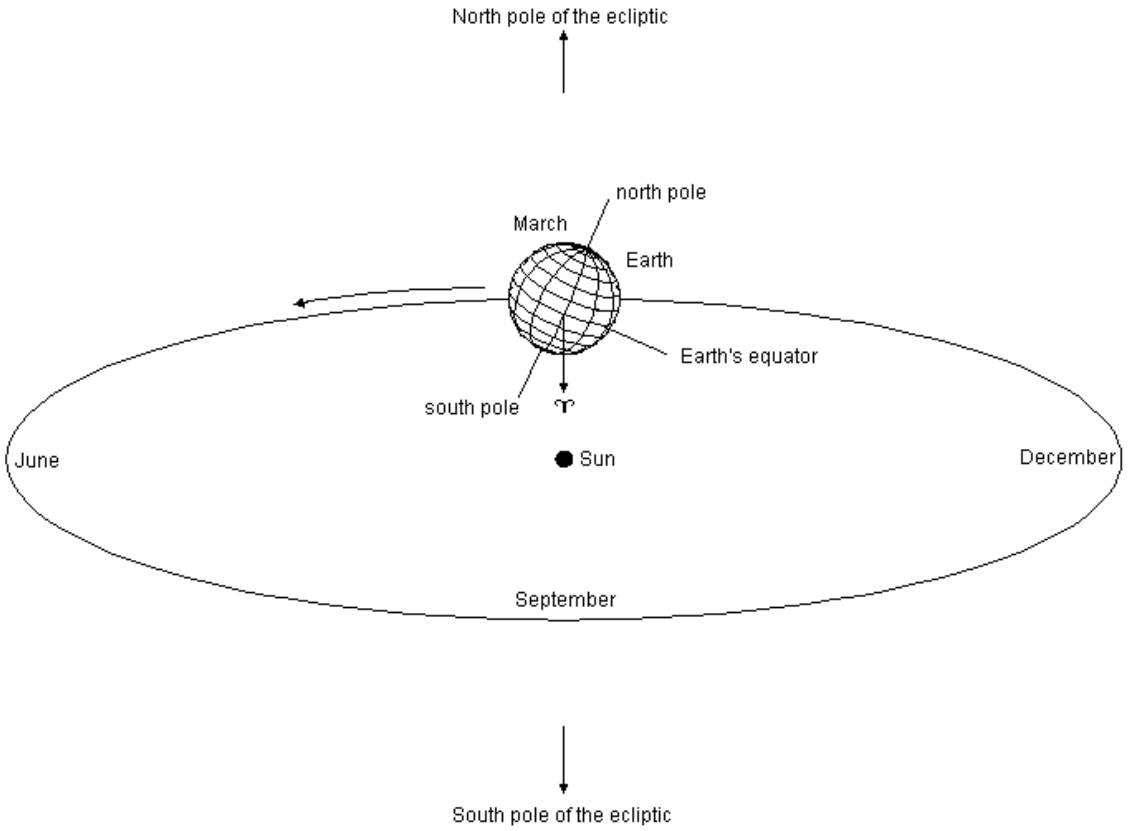

Source: Adapted from Fialho (2007).

A.1.3 Adopted definitions

It is common to find in the literature the expressions "reference frame" and "coordinate systems" with different meanings, leading many times to confusion. Therefore, to make matters clear, we will adopt the following definitions for these terms in this work:

Reference frame

A reference frame (or frame of reference) provides a basis in which the position of an object can be specified. In the three-dimensional space, it is defined by an origin point and by three orthogonal axes that meet at the origin. It is not possible

to tell the position of a point in space without referring that position to a reference frame.

Coordinate system

A coordinate system provides a method to associate a set of numbers to a point in space, enabling to locate the position of that point in relation to a reference frame in a unique way. These numbers are known as the coordinates of that point in relation to the adopted frame of reference in a given coordinate system. In a three-dimensional space, three scalars are needed to completely specify the position of a point, unless a discontinuous, fractal-like coordinate system is used.

According to this definition, more than one coordinate system can be used with a reference frame. For instance, in a given frame of reference, the position of a point can be specified using a cartesian coordinate system, or a spherical coordinate system or a cylindrical coordinate system or any other coordinate system. The following section gives a description of the most commonly used coordinate systems in spacecraft work.

A.1.4 Cartesian coordinate system

In this coordinate system, the position of a point in a given reference frame is specified by a set of three real numbers. These numbers specify how much someone, starting from the origin, should walk along the directions given by the three orthogonal axes that define the reference frame to reach that point. These three orthogonal axes are usually denoted by x, y and z. Figure A.3 illustrates this coordinate system for a point P with coordinates (p_x, p_y, p_z) in the cartesian coordinate system. This point can also be represented by a vector $\vec{\mathbf{P}}$, that connects the origin to it, as depicted in Figure A.4. The components of this vector are $p_x\mathbf{x}$, $p_y\mathbf{y}$ and $p_z\mathbf{z}$, being $\mathbf{x}$, $\mathbf{y}$, $\mathbf{z}$ unit vectors parallel to the axes x, y and z, respectively.

Figure A.3 – Cartesian coordinate system

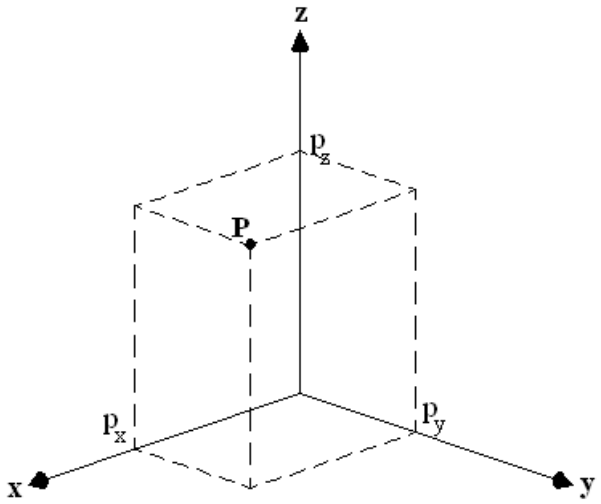

Source: Fialho (2007).

Figure A.4 – Cartesian coordinate system (vector representation)

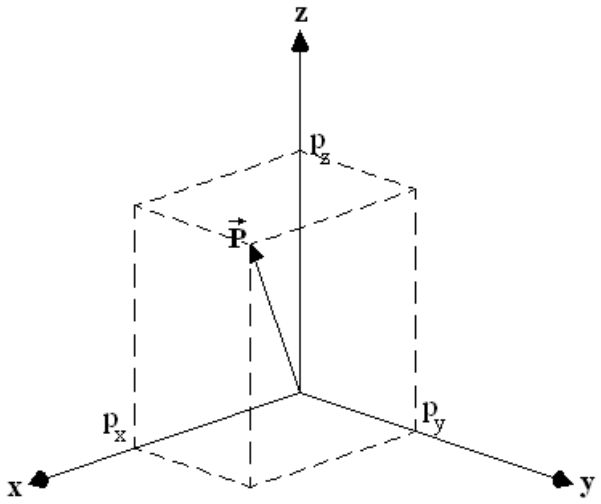

Source: Fialho (2007).

A.1.5 Spherical coordinate system

In the spherical coordinate system, the position of a point is specified by two angular coordinates and one linear coordinate. The angular coordinates (φ and λ) specify the direction of this point from the origin, as depicted in Figure A.5. The linear coordinate *r* specifies the distance from the point to the origin.

Figure A.5 – Spherical coordinate system

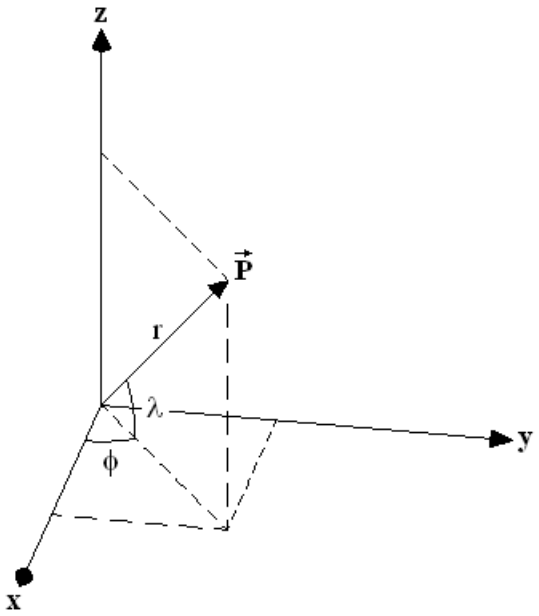

Source: Fialho (2007).

The first angular coordinate φ, usually known as azimuth or longitude, specifies the angle between the x axis and the projection of vector $\vec{\mathbf{P}}$ (connecting the origin to the point P) in the xy plane, being considered positive for rotations from x axis to y axis.

The second angular coordinate λ, usually known as elevation or latitude, is the angle between the vector $\vec{\mathbf{P}}$ and the xy plane. The reader should be aware that there exist alternate definitions of the spherical coordinate system, one common definition replaces λ by its complement, i.e., the angle between the positive z-axis and the vector $\vec{\mathbf{P}}$.

A.1.6 Transformations between the spherical and cartesian coordinate systems

The spherical coordinate system defined here is related to the cartesian coordinate system by the following equations:

$$p_x = r \cdot \cos \varphi \cos \lambda \quad \text{(A.1)}$$

$$p_y = r \cdot \sin \varphi \cos \lambda \quad \text{(A.2)}$$

$$p_z = r \cdot \sin \lambda \quad \text{(A.3)}$$

The inverse transformation can be performed with the following algorithm adapted from Fialho (2007):

Figure A.6 – Pseudo-code for the transformation from cartesian to spherical coordinate system

```
r = [x² + y² + z²]^1/2
if x > 0 :
      φ = atan (y / x)
      s = [x² + y²]^1/2
      λ = atan (z / s)
else if x < 0 :
      φ = atan (y / x) + π
      s = [x² + y²]^1/2
      λ = atan (z / s)
else if x = 0 :
      if y > 0 :
            φ = π/2
            λ = atan (z / y)
      else if y < 0 :
            φ = -π/2
            λ = atan (z / (-y))
      else if y = 0 :
            φ = 0 ;(or any other value)
            if z > 0 :
                  λ = π/2
            else if z < 0 :
                  λ = -π/2
            else: ;( z = 0 or z ≠ ±r)
                  error "Invalid coordinate "
      else:
            error "Invalid y"
else:
      error "Invalid x"
```

Source: adapted from Fialho (2007).

A.2 Reference frames and coordinate systems used in attitude work

In attitude work, there's no need to know the distances from the spacecraft to the celestial bodies that serve as references for attitude determination. All that is needed is the knowledge of the apparent position of these objects in the sky. In

other words, all one need to know is the position of these objects in a celestial sphere centered on the spacecraft. These can be expressed using two angles (components φ and λ of the spherical coordinate system). Since distances are not important, points on the celestial sphere can be conveniently represented by unit vectors. The representation of coordinates in the celestial sphere as unit vectors has many advantages for numerical computation, since it avoids the expensive computation of trigonometric functions.

The remainder of this section describes the reference frames normally used in star tracker work.

A.2.1 Equatorial coordinate system and ECI – Earth Centered Inertial reference frame

The “equatorial coordinate system” used in Astronomy can be understood as a reference frame based on rotational and orbital parameters of the Earth associated with a spherical coordinate system. It is the historical basis for defining the modern ICRS (International Celestial Reference System) used in most modern star catalogs. In the equatorial coordinate system, star coordinates are represented in terms of right ascension (RA or α) and declination (dec. or δ), being right ascension analogous to longitudes on the Earth’s surface and declination analogous to latitudes. In the equatorial coordinate system, the declination of a celestial body is the angle between the celestial equator and the line joining the center of the Earth to that celestial body. The origin of the right ascension coordinates is given by the vernal equinox (♈). Figure A.7 depicts the equatorial reference frame plus some commonly defined terms.

Figure A.7 – Equatorial coordinate system

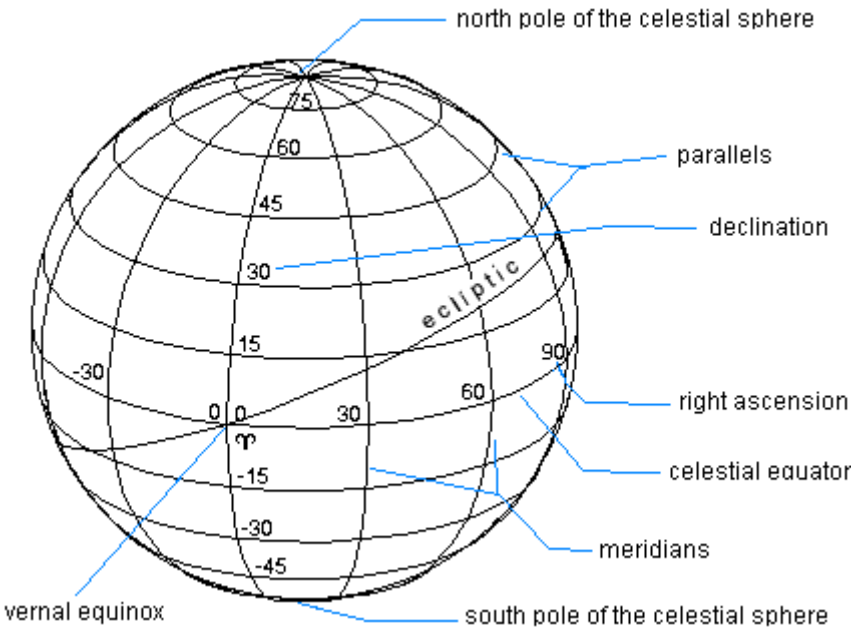

Source: Fialho (2007).

In spacecraft work, the equatorial coordinate system is also known as Earth Centered Inertial (ECI) reference frame, since it has its origin at Earth's center and its fundamental axis are defined by Earth's rotation and orbital motion. The fundamental axes defining the ECI reference frame are given by the vernal equinox (axis x), the Earth's spin axis (axis z, pointing to the north pole) and the $y = z \times x$ axis.

Unfortunately, the equatorial coordinate system (or ECI reference frame) as defined above is not truly inertial, slowly rotating due to the precession of Earth's rotation axis (precession of equinoxes), small changes in Earth's orbital plane and other minor Earth movements. This makes its use cumbersome for precise astrometric work. Hence, astronomers usually fix a particular date (epoch) for Earth's equinox and spin axis (e.g. J2000.0 = approx. 1 January 2000) when using that reference system for stating star coordinates, even when observations are performed at a different date. For instance, one could say that the coordinates

of a star observed in 1980 are being given in the equatorial coordinate system using equinoxes and poles of J2000.0.

A.2.2 The International Celestial Reference System (ICRS)

The ICRS can be thought of as being an improvement to the old equatorial celestial coordinate system with equinox and poles of J2000 used in Astronomy in the past, but using more accurate astrometric references no longer tied to the complex motions performed by the Earth. The replacement of the old equatorial coordinate system with the ICRS is akin to the replacement of the original definition of the meter based on the physical dimensions of the Earth with more accurate definitions no longer tied to the Earth. The main advantage of using the ICRS reference system is that it is much more stable than the equatorial coordinate system used in the past. The main difference is that its origin is precisely defined as being located at the center of mass of the Solar System, contrary to the equatorial coordinate system, that many times was defined as having its origin at the center of the Earth. The ICRS provides a much better approximation to a truly inertial reference frame than the equatorial coordinate system.

Being the current celestial reference system adopted by the International Astronomical Union (IAU), the ICRS is technically defined by a series of conventions, prescriptions and models necessary to define a triad of orthogonal axes that best approximate an inertial (or quasi-inertial, to be more accurate) reference frame with the origin at the Solar System's barycenter (IERS, 2013) while keeping backwards compatibility with older reference systems adopted in Astronomy, including the equatorial coordinate system described in the previous section when using the equinox and poles of the J2000 epoch (approx. 1 January 2000).

Its most recent and accurate realization is given by the ICRF2 – The second realization of the International Celestial Reference Frame[17], derived from Very-long-baseline interferometry (VLBI) observations of distant extragalactic sources (mostly quasars) in microwave. The ICRF2 uncertainty in the definition of its fundamental axes is on the order of few microseconds of arc (picoradians).

In the optical regime, for a long time, the best realization of the ICRS was given by the Hipparcos star catalog. This realization (known as HRF - Hipparcos Reference Frame) matches the older equatorial coordinate system for the mean equinox and poles of J2000.0 within a tolerance better than 80 milliseconds of arc (ESA, 1997). However, this should change soon with data releases from the Gaia astrometric mission. An overview of the Gaia mission is provided by Prusti et al. (2016).

Being defined by sources outside the Solar System, the practical realizations of the ICRS are completely independent of orbital and rotational motions of the Earth, but their fundamental axes are aligned with those of the equatorial coordinate system for the mean equinox and poles of J2000.0 within a tolerance much better than that typically found on star trackers. Hence, for most attitude work they can be considered to be the same if the fact that their origins are defined at different places can be neglected.

[17] https://www.iers.org/IERS/EN/DataProducts/ICRF/ICRF/icrf.html.

APPENDIX B SOURCES OF ERRORS THAT AFFECT ATTITUDE ACCURACY IN STAR TRACKERS

This appendix describes sources of errors and the many types of noise that ultimately affect the accuracy of the estimated attitude by a star tracker.

B.1 Sources of errors outside the STR

Unfortunately, there are many sources of errors and types of noise that prevent determination of attitude with an infinite accuracy. In Section B.2 a detailed description of sources of noise and errors that affect image generation are described. This section focuses more on other sources of errors, many of them outside the star tracker and related to spacetime geometry or stellar motion. Detailed descriptions about the sources of errors briefly presented in this section can be found in the master thesis of Fialho (2007) and in the report written by Albuquerque and Fialho (2005).

B.1.1 Stellar aberration

Stellar aberration is an apparent displacement of light sources in the celestial sphere caused by the movement of the observer and by the fact that the speed of light is finite. The direction of this apparent displacement caused by stellar aberration is the same as the movement of the observer. This effect is illustrated in Figure B.1.

This effect can be understood by making an analogy to a car standing in a rainy day without wind. In this analogy, the observer would be the car, the light source would be the cloud and the photons would be the rain droplets. When the car is still, the rain droplets are seen falling vertically. When the car is moving, the rain droplets are seen falling at a slanted angle in relation to the car. If the location of the source of the droplets could be determined only from the direction the droplets are travelling relative to the observer (as is the case if we replace water droplets with real photons), when the car is still the source of the droplets (the star in our

analogy) would seem to be directly overhead the car. When the car is moving, the source of the droplets would seem to be ahead of the car.

Figure B.1 – Stellar aberration

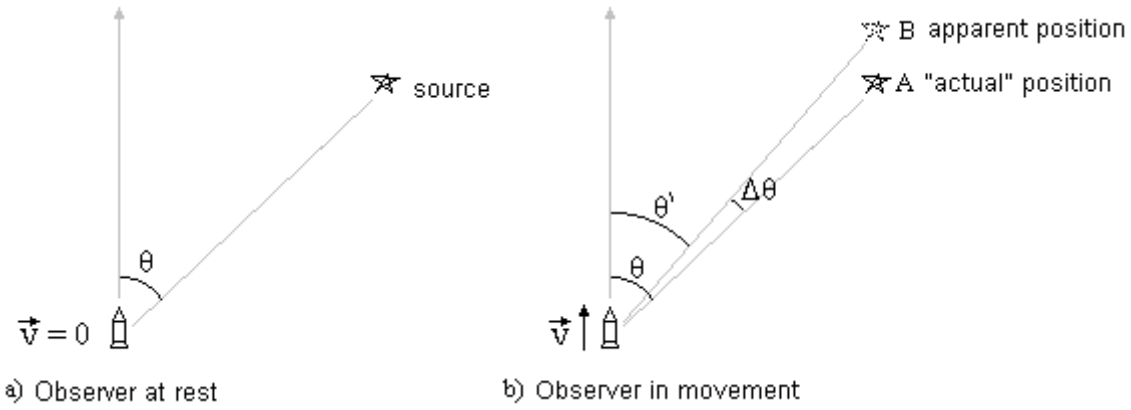

Source: Adapted from FIALHO (2007).

An approximate equation for the stellar aberration can be derived using the methods of Classical Mechanics (ALBUQUERQUE; FIALHO, 2005; WOOLARD, 1966):

$$\boldsymbol{R}' = \frac{\boldsymbol{R} + \boldsymbol{v}/c}{\|\boldsymbol{R} + \boldsymbol{v}/c\|} \tag{B.1}$$

where:

$\boldsymbol{v}$ = observer (star tracker) velocity vector relative to the light source;

c = speed of light in vacuum = 299,792,458 m/s (exact, by definition of the meter, see for example, Mohr *et al.* (2016));

$\boldsymbol{R}$ = unit vector representing star direction in the star catalog;

$\boldsymbol{R}'$ = unit vector giving the aparent position for the moving observer.

An exact formulation for the displacement caused by stellar aberration is given by Rindler (1977):

$$\tan\left(\frac{\theta'}{2}\right) = \sqrt{\frac{c - v}{c + v}} \cdot \tan\left(\frac{\theta}{2}\right) \tag{B.2}$$

where:

θ' = angle between the observer velocity vector and light source apparent position;

θ = angle between the observer velocity vector and light source actual position;

v = observer velocity.

For star trackers, the component of the stellar aberration due to the movement of the origin of the inertial reference frame used in the star catalog with respect to cataloged stars does not need to be considered, since this effect is already included in the cataloged coordinates. However, the component of the stellar aberration due to the movement of the spacecraft with respect to the star catalog origin must be considered and corrected.

Typically, the origin of the reference frames used in most star catalogs is located at the Solar System's center of mass (barycenter). For all Earth orbiting spacecraft, where the speed with respect to the Solar System's barycenter is limited to about 41 km/s (30 km/s from Earth velocity vector plus 11 km/s at the perigee for a spacecraft in a very eccentric orbit with perigee just above Earth's surface), the displacement in the apparent position of the stars in relation to their cataloged positions can reach up to 28 arc-seconds (ALBUQUERQUE; FIALHO, 2005), which is larger than the typical accuracy of most star sensors. Hence this effect must be corrected, either by the AOCS or by the star tracker, so that the full accuracy provided by the star sensor can be used. If this effect is to be corrected by the star tracker, then the AOCS must provide the spacecraft velocity vector to the star tracker at regular intervals or the star tracker must have means of computing the spacecraft velocity vector (e.g.: from ephemerides stored on board).

A very accurate way of taking stellar aberration into account is to distort the star coordinates in the star catalog using either the approximate Equation (B.1) or the exact formulation (Equation (B.2), and use this catalog with distorted star coordinates as the star catalog used for stellar identification. This star catalog

with distorted star coordinates is basically a star catalog for a non-rotating reference frame that has its origin at the spacecraft and its defining axes parallel to those of the inertial reference frame used in the star catalog.

A simpler approach to correct for stellar aberration, that works reasonably well for star trackers with only one optical head, is to initially ignore stellar aberration effects (assuming initially that the spacecraft is at rest with respect to the origin of the reference frame used in the star catalog) and perform star identification and attitude determination as usual, and then correct the determined attitude for stellar aberration. This procedure is not as accurate as the previous method because the attitude error due to the stellar aberration effect will also depend on the position of stars used for attitude determination in the field of view (if the stars are more to the left, or to the right, to the top or to the bottom of the field of view). Also, this procedure does not work if the distortions introduced by stellar aberration are large enough to make the star patterns unrecognizable by the star identification algorithm.

A third approach is to remove the effects of stellar aberration from the measurements and then perform stellar identification. However, this approach is not suitable for the *lost-in-space* condition, since, for this operation to be performed, an attitude estimate must be available.

In any case, for the star tracker to be able to perform this correction, it must have knowledge of the spacecraft velocity vector $\mathbf{v}$ with respect to the origin of the reference frame used in the star catalog. This information could be provided externally (e.g: from the AOCS main computer) or in more sophisticated designs, it could be computed by the star tracker from spacecraft ephemeris (including Earth ephemeris for an Earth orbiting spacecraft) and current time.

The work of Albuquerque and Fialho (2005) provides an interesting table with maximum residual aberration angles after applying varying levels of correction for stellar aberration in an low Earth orbit spacecraft, considering the most accurate method of correcting (distorting) star coordinates in the star catalog.

This table is reproduced here as Table B.1 due to its usefulness for spacecraft design.

Table B.1 – Residual aberration angle for a spacecraft in low Earth orbit, for each correction used*

Correction performed or ignored	maximum error in the velocity vector (km/s)	maximum residual stellar aberration (in arcsec.)	Interval between catalog corrections
No correction performed	38.06	26.18	-
Correct only the stellar aberration given by Earth's orbital motion, using Earth's velocity vector averaged in a period of 1 month.	15.7	10.80	1 month
Correct only the stellar aberration given by Earth's orbital motion, using Earth's velocity vector averaged in a period of 1 day.	7.78	5.35	1 day
Correct for Earth's orbital motion** and spacecraft motion once every 15 minutes.	4.03	2.77	15 minutes
Correct for Earth's orbital motion** and spacecraft motion once every minute.	0.27	0.19	1 minute
Error committed by neglecting that the Sun is not coincident with the Solar System center of mass due to the existence of Jupiter and Saturn.	0.016	0.011	-
Additional error if the displacement between Earth's center and Earth-Moon system barycenter is not considered.	0.013	0.0086	-
Maximum error when using the approximate equation derived from Classical Mechanics (Equation (B.1)) versus the exact formulation (Equation (B.2)).	-	0.00083	-

* Considering that in all corrections shown in this table the spacecraft velocity vector is computed for a point in time at the center of the interval. For instance, if the star catalog is corrected for stellar aberration once per minute, the velocity vector used for the correction is the one the spacecraft will have 30 seconds in the future.

** considering Earth's orbit eccentricity.

Source: Albuquerque and Fialho (2005).

As can be seen in this table, the error of using the approximate equation (Equation (B.1)) versus the exact equation (Equation (B.2)) for correcting stellar aberration is negligible for most spacecraft work, except for missions working in the miliarcsecond/microarcsecond range or in spacecraft with very high heliocentric speeds. The advantage of the approximate equation over the exact equation is that it is easier to implement.

A good tutorial containing a comprehensive discussion of methods to correct the stellar aberration effect and stellar parallax effect (to be discussed in the next section) is given by Shuster (2003).

B.1.2 Stellar parallax

Parallax is a displacement in the apparent position of an object due to a change in the location (viewpoint) of the observer, as illustrated in Figure B.2. In this example, note how the foreground tree moves in relation to the background as the photographer changes his viewpoint (from “left view” to “right view”).

Figure B.2 – Parallax

Source: Photographs taken by the author.

For Proxima Centauri, which is the closest star to our sun, the parallax angle between an observer on Earth and another observer on the Sun is just 0.77 arc-seconds (ESA, 1997; ZEILIK; GREGORY, 1998). Since all other stars are farther away from the Sun, their parallax angles are even smaller. Hence stellar parallax might be of concern only for missions with attitude knowledge requirements more stringent than 1 arc-second, or for missions to the Outer Solar System (e.g., missions to the gas giants and ice giant planets).

B.1.3 Proper motion

Proper motion is the projection of three-dimensional motion of other stars with respect to the Solar System's barycenter in the celestial sphere (ZEILIK; GREGORY, 1998).

Even though stars are moving at relative speeds of tens or even hundreds of kilometers per second, as they are very far apart from each other, their apparent motion on the sky is very small. The fastest moving star on the celestial sphere, Barnard's star, has a proper motion of only 10.3 arcseconds per year. More than 99% of stars with visual magnitudes smaller than five (stars brighter than m_v = 5.0) have proper motion smaller than 1"/yr (ALBUQUERQUE; FIALHO, 2005). Hence, stellar proper motion should not be an issue if the star catalog to be used in a mission is derived from an accurate star catalog released close to the mission launch date, such as the star catalog to be generated by the ongoing Gaia astrometric mission (http://sci.esa.int/gaia/). On the other hand, if the star tracker star catalog is derived from an older star catalog, such as the Hipparcos star catalog, whose reference epoch is J1991.25 (stellar coordinates in the Hipparcos catalog are the coordinates the star had in J1991.25 = approx. April of 1991), roughly three decades ago, then the coordinates of the stars should be propagated to the mission mean epoch (time when the star tracker will be used) during catalog preparation. To do that, a knowledge of the proper motion of each star and the time difference between the source catalog epoch and the mission

epoch must be known. Uncertainties in these values will lead to uncertainties in the mission catalog – star catalog to be used in a star tracker.

B.1.4 Binary/multiple star systems

The existence of binary/multiple star systems (ESA, 1997; ZEILIK; GREGORY, 1998) introduces some inaccuracy in attitude determination in star trackers.

In many cases, the angular separation between the components of a multiple star system is smaller than the resolving power of a star sensor. The resolving power of a large field of view star tracker is typically in the order of few arc-minutes, whereas there exist many binary stars whose components are separated by angles in the range of few arc-seconds. These systems are observed by the star tracker as a single star. However, in many cases, the individual components of these systems are listed in the source star catalog (from where the mission star catalog is derived) as separate stars.

When the star catalog to be used in the mission is being prepared, these binary/multiple systems where the components are closer to each other than the resolving power of star tracker must be merged into a single equivalent star having the combined brightness of all components and located at the photometric center of the system. Not performing this merging can result in difficulties and in loss of accuracy in the process of star identification or in the process of determining the attitude from identified stars.

This procedure must also be performed for optical double/multiple stars (stars that are physically unrelated, being many times very far apart, but which are seen to be very close to each other due to a perspective/viewpoint effect) when the angular separation between them from the star tracker vantage point in the Universe is smaller than the resolving power of that star tracker.

For a set of *n* stars, their photometric center can be computed using the following equations:

$$\widehat{\boldsymbol{R}}_{\boldsymbol{t}} = \frac{\boldsymbol{R}_{\boldsymbol{sum}}}{\|\boldsymbol{R}_{\boldsymbol{sum}}\|} \tag{B.3}$$

with

$$\boldsymbol{R}_{\boldsymbol{sum}} = \sum_{i=1}^{n} b_i \widehat{\boldsymbol{R}}_{\boldsymbol{i}} \tag{B.4}$$

where:

$\widehat{\boldsymbol{R}}_{\boldsymbol{t}}$ = unit vector giving the coordinates in the celestial sphere of the photometric center of a set of *n* stars;

b_i = brightness of star i, in the spectral band of the star tracker;

$\widehat{\boldsymbol{R}}_{\boldsymbol{i}}$ = unit vector giving the coordinates of star i.

Unfortunately, for binary and multiple star systems, the photometric center of the system usually does not follow the same path as the system barycenter, since the brightness of each component star is rarely proportional to their individual masses. The effect of this is that the apparent position of the system (given by its photometric center) will wobble around the path followed by its center of mass, instead of following a straight path. Figure B.3 illustrates this effect.

Figure B.3 – Oscillation of the photometric center of a system composed of two stars gravitationally bound (binary star) around its center of mass. T is the orbital period of the system.

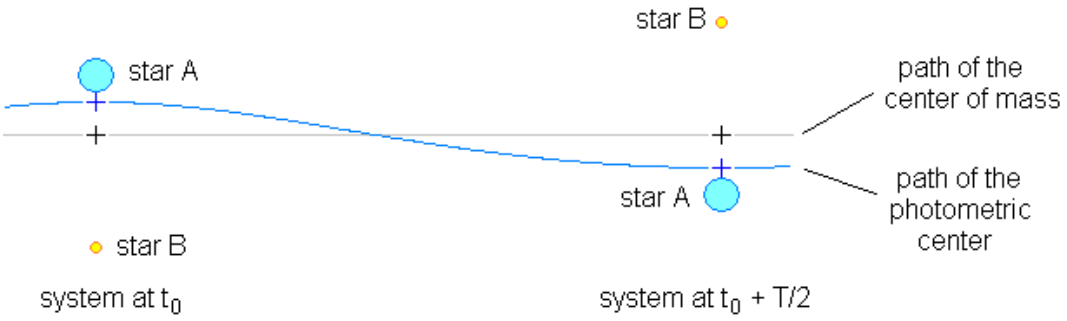

Source: Adapted from Albuquerque and Fialho (2005).

Fortunately, for all binary stars where the angular separation between the components is greater than 10″, the orbital period is of many decades or even

larger. Hence this effect should not be of great concern for wide field of view star trackers, whose accuracy is in the order of few arcseconds.

B.1.5 Gravitational deflection

This effect is described here only for completeness, since its effects are negligible for most space missions, except for those working in the milli- and micro-arcsecond ranges.

When a light ray coming from infinity passes near a massive body, it is deflected by an angle proportional to the square of the escape velocity from that body at the closest point to that body found in the path of that light ray (ALBUQUERQUE; FIALHO, 2005), as shown in Figure B.4.

Figure B.4 – Light deflection due to a massive body

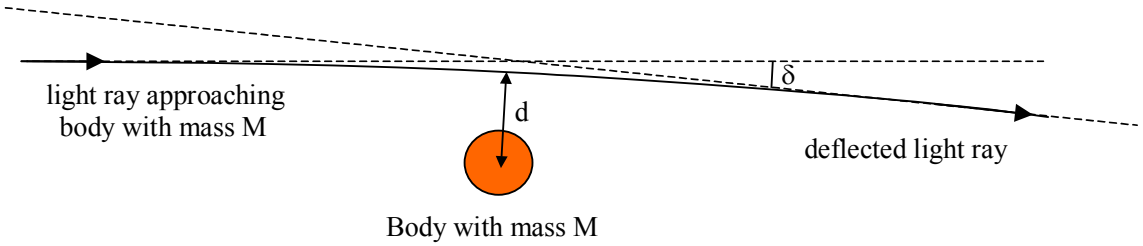

Source: Adapted from Albuquerque and Fialho (2005).

For bodies with spherical symmetry, this angle of deflection can be computed as (RINDLER, 1977; ROSSER, 1967; ALBUQUERQUE; FIALHO, 2005):

$$\delta = \frac{4GM}{c^2 d} = 2 \cdot \left(\frac{v_{esc}}{c}\right)^2 \cdot \frac{R}{d} \tag{B.5}$$

where:

G = graviational constant ≈ 6.6742×10^{-11} $N \cdot m^2 \cdot kg^{-2}$;

M = mass of the massive body;

v_{esc} = escape velocity at the surface of the massive body;

c = speed of light in vacuum;

R = radius of the massive body;

d = shortest distance from the light ray to the center of the massive body.

Since gravitational deflection effects caused by objects outside the Solar System are already included in the star coordinates given in the star catalog, just the additional gravitational effects due to bodies in the Solar System need to be considered. Fortunately, for current star sensor accuracies (in the order of few microradians = arcseconds or tenths of arcseconds), these effects are completely negligible, as shown in Table B.2.

Table B.2 – Gravitational deflection angle for a grazing ray at selected bodies in the Solar System

body	escape velocity (km/s)	deflection angle for grazing ray (arcsec)
Sun	617.54	1.75
Jupiter	59.55	0.0163
Saturn	35.49	0.0058
Neptune	23.49	0.0025
Uranus	21.30	0.0021
Earth	11.18	$5.7 \cdot 10^{-4}$
Venus	10.36	$4.9 \cdot 10^{-4}$
Mars	5.02	$1.2 \cdot 10^{-4}$
Mercury	4.25	$8.3 \cdot 10^{-5}$
...	...	...
Moon	2.376	$2.6 \cdot 10^{-5}$

Source: Albuquerque and Fialho (2005).

Only for the Sun, the gravitational deflection angle is considerable. However, a star tracker will never attempt to observe a background star so close to the Sun. It is reasonable to assume that only stars that are farther than an exclusion angle (say, of 22.5 degrees) from the Sun would be observed. For a star tracker at 1 AU from the Sun and observing a star at 22.5 degrees from the Sun, the gravitational deflection angle is just 0.02 arc-seconds (ALBUQUERQUE; FIALHO, 2005). Hence, for current wide field of view star trackers, gravitational deflection of light in the Solar System can be safely neglected.

B.2 Sources of error in image acquisition

This section briefly describes the principal sources of noise and errors that affect the quality of images generated by star trackers.

The detection of stars in images acquired by a star sensor is made difficult by the existence of noise in the image and by the non-uniform response of the photosensitive elements (pixels) used to capture that image. In an ideal world, where images acquired by star trackers would be free from noise, stellar detection would be much easier. All one needed to do would be to locate in the acquired images pixels with non-zero values, since the background would be zero in an ideal world. In practice, images generated by star trackers will always be corrupted by noise, from many sources. These sources of noise lead to the challenge of developing algorithms that are capable of accurately determining the angular position of observed stars with a computational cost low enough to be used in the star tracker hardware, much more limited than that of a personal computer or even a cell phone. In order to overcome the problems caused by the existence of noise and detector non-uniformity and be able to obtain the best possible attitude measurement from a star tracker / star sensor hardware, many techniques capable of mitigating the effects of noise and detector non-uniformity (noise reduction techniques) must be employed. The quality of a star tracker is directly related to the effectiveness and robustness of these noise reduction techniques.

In general, the main sources of noise and error that affect the generation of images by fixed head star trackers are the following:

- thermal noise;
- shot noise;
- dark current;
- amplifier noise and 1/f noise;
- fixed pattern noise;
- digitization errors;

- pixel non-uniformity;
- detector non-linearity;
- image lag;
- ionizing radiation.

These types of noise and error sources can be divided in two large classes, following the same classification proposed by Tuchin et al. (2013): systematic errors (or bias), and random noise. Systematic errors can be removed by proper calibration if their sources are very well known. On the other hand, random noise presents a stochastic behavior, only being possible to determine its statistical properties, such as mean, standard deviation, probability distribution function, etc. Random noise can be mitigated and sometimes removed by reducing the temperature or by the use of techniques such as CDS (correlated double sampling), if allowed by the image sensor architecture.

B.2.1 Thermal noise and kTC noise

Thermal noise, also known as Johnson or Nyquist noise, has its origin in the thermal motion of charge carriers in a conductor (PALMER, 2010). Thermal noise can be modeled as a Gaussian white noise up to about 10^{12} Hz for circuits at room temperature. For an RC circuit near room temperature, with time constant much larger than 10^{-12} seconds, the root mean square voltage (V_{rms}) at the capacitor will be (PALMER, 2010):

$$V_{rms} = \sqrt{\frac{kT}{C}} \tag{B.6}$$

Where:

k = $1.38065 \cdot 10^{-23}$ J/K = Boltzmann's constant

T = absolute temperature of the RC circuit

C = capacitance of the capacitor

Thermal noise in RC circuits is also known as kTC noise, an acronym derived from the terms used in Equation (B.6). The kTC noise is one of the dominant noise sources in low light conditions for image sensors that are not capable of performing a true CDS (correlated double sampling) to remove pixel reset noise, like CMOS APS image sensors with a 3T (three-transistor) pixel architecture (HOLST; LOMHEIM, 2011). The pixel reset noise is associated with the capacitance *C* of the pixel sense node.

A detailed study about the contribution of thermal noise in the quality of images generated by CMOS APS sensors has been tackled by Hiu Tian (2000). Temperature reduction leads to a modest gain, due to thermal noise originated voltage (or current) dependency with the square root of the absolute temperature. More effective ways to reduce thermal noise requires more elaborate techniques such as CDS (INNOCENT, 2009; MARTIN, 2012, Section 1.1.1.5.2.2, page 20).

B.2.2 Shot noise

Shot noise has its origin in the discrete nature of light and matter. Regarding photovoltaic image sensors, like CCD sensors and CMOS sensors, shot noise can be divided into photon shot noise and dark current shot noise, described in the following subsections.

B.2.3 Photon shot noise

Photon shot noise is an intrinsic phenomenon of nature, which does not depend on the type of detector used, being a result of the fact that light itself is discretized in photons and that the photons hit the detector in a stochastic manner. The number of photons that hit a particular pixel in the detector follows a Poisson distribution (HANH; SHAPIRO, 1976):

$$P_n = \frac{\iota^n}{n!} \cdot e^{-\iota} \tag{B.7}$$

Where:

P_n = probability that exactly *n* photons hit a particular pixel, for a given illumination condition and exposure time.

ι = mean number of photons that should hit that pixel for the same illumination condition and exposure time[18].

In lit scenes, or for long exposure times, the average number of photons (ι) that should hit the detector is high. In this condition, the Poisson distribution can be approximated by a normal distribution with standard deviation (σ) equal to the square root of the expected number of photons (PALMER, 2010):

$$\sigma = \sqrt{\iota} \tag{B.8}$$

Even though the absolute value of the photon shot noise increases with the expected number of collected photons (ι), its importance decreases in brighter scenes, since the signal (proportional to the number of photons collected) increases even faster. In fact, the signal to noise ratio improves with the square root of the expected number of collected photons:

$$SNR_{photon\_noise} = \frac{signal}{noise} = \frac{\iota}{\sqrt{\iota}} = \sqrt{\iota} \tag{B.9}$$

Being an intrinsic phenomenon of Nature, shot noise can be regarded as a noise present in the luminous signal itself, before hitting the detector. As has been shown in this section, the only way to decrease its influence is to increase the number of collected photons, which can be done by increasing the exposure time or increasing collecting area, optics transmittance and detector's quantum efficiency.

[18] Here we are using the Greek letter ι (iota) instead of the more common λ for the Poisson distribution parameter to avoid confusion with wavelength, which is also represented by λ.

B.2.3.1 Effects of quantum efficiency in shot noise

In practice, not every incident photon will be absorbed by the pixel, and not every absorbed photon will generate charge carriers that are later collected by the device, so the generated photoelectrical signal will be smaller. The ratio between the number of collected charge carriers (electrons or holes, depending on the device) and incident photons is known as quantum efficiency (η) (McCLUNEY, 1994; PALMER, 2010 (Section 5.3)). The fact of quantum efficiency being smaller than 100% results in a smaller signal, and hence in a worse signal to noise ratio. In fact, if we consider a quantum efficiency different than one, the expected number of photons (ι) in equations (B.7), (B.8) and (B.9) should be replaced by the product between the expected number of incident photons and the quantum efficiency ($\iota\eta$), before computing the probability P_n that exactly n pairs of charge carriers will be generated in the pixel (modified Equation (B.7)), the standard deviation of the number of charge carrier pairs (modified Equation (B.8)) and the signal to noise ratio (modified Equation (B.9)), this when considering only this noise source.

B.2.4 Dark current and its contribution to shot noise

Many detectors present some kind of output even when there's no external stimulus (in the case of optical detectors, that would be luminous flux incident on the detector). This response is known as dark output (McCLUNEY, 1994). In the case of quantum detectors, such as CCDs and CMOS sensors, dark output is usually known as dark current, for reasons that will become clear later.

To understand how dark current arises in quantum detectors (CCDs and CMOS sensors are included in this category), first we need to understand how these devices convert light into an electrical signal.

B.2.4.1 A brief on semiconductor physics

Quantum mechanics rules dictate that not all energy levels are allowed for electrons belonging to any system occupying a limited volume in space. In the case of solids, the allowed energy levels for electrons tend to group into energy bands. In the case of semiconductor materials, the two most important energy bands for electrical conductivity in the material are known as the valence band and the conduction band, as shown in Figure B.5. Electrons in the inner bands are tightly bound to their host atoms and do not contribute significantly to electrical conduction in the material.

Figure B.5 – Energy bands in an intrinsic semiconductor.

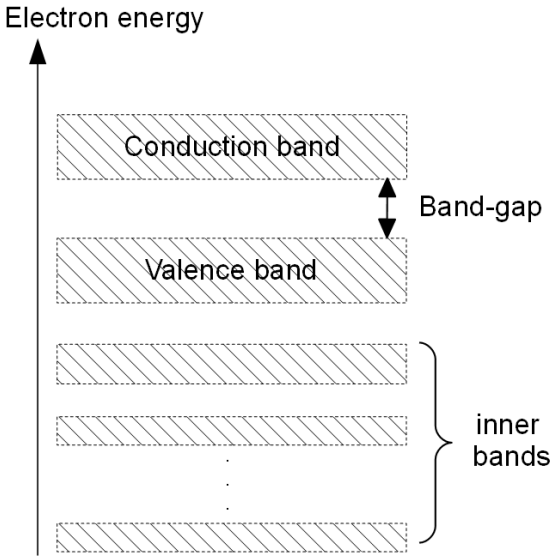

Source: Drawn by the author.

In semiconductors, electrons belonging to the valence band are not free to move, except when a neighboring atom has a vacancy on its valence shell, to where that valence electron can jump. On the other hand, the higher energy conduction band is practically empty, so electrons that are promoted to the conduction band are free to move in the semiconductor crystal lattice. When an electron from the valence band is promoted to the conduction band, it leaves behind a vacant space in the valence shell of the atom it used to belong. This vacant space can

be filled by valence electrons from adjacent atoms. Thus, vacant spaces can effectively hop from one atom to the other. In essence, these vacant spaces in the valence band behave as if they were positively charged particles, being known in solid state physics as *holes*. A vacancy in the valence band (a hole) can also be filled by an electron in the conduction band. When this occur, the electron excess energy is given off as a photon or as an increase in lattice vibration (heat), this process is known as electron-hole recombination.

In quantum detectors, when a photon with sufficient energy, larger than the bandgap of the semiconductor material that the detector is made, hits the detector, it can promote an electron from the valence band to the conduction band, being absorbed in the process. The result is the creation of two charge carriers of opposite polarities free to move in the crystal lattice, one electron in the conduction band and a hole in the valence band. If this process happens in a part of the device responsible for light capture, such as a photodiode, the device will collect the charge carriers created (usually of only one type, being the other type discarded to the VDD or VSS power supply lines). The output of the detector will be proportional to the number of charge carriers collected during the exposure time (or integration time).

B.2.4.2 Dark current mechanism

Unfortunately, a photon striking on the semiconductor material is not the only way an electron-hole pair can be created. Thermal motion can also create electron-hole pairs, and these are indistinguishable from the electron-hole pairs generated when a photon strikes the semiconductor material. This is especially important when it happens in photosensitive areas, responsible for converting light into an electric signal. The presence of impurities in the semiconductor material or surface defects can create intermediate energy levels that aid in the creation of thermally generated electron-hole pairs. The number of electron-hole pairs generated by unit time can be interpreted as a current, known as dark current:

$$I_{dark} = \frac{n}{t} \cdot q_e \quad \text{(B.10)}$$

Where:

n = number of thermally generated electron-hole pairs;

t = time interval where n electron-hole pairs have been generated;

q_e ≈ 1.6022·10^{-19} C = elementary charge = charge of a proton or charge of an electron with sign reversed.

B.2.4.3 Dark current shot noise

In the same way that photon detection is a stochastic process, so is the thermal generation of electron-hole pairs, which also follows a Poisson distribution. Since the noise generated by dark current is independent from the shot noise that originates from photon detection, these two sources can be combined in the following manner:

$$\sigma = \sqrt{\eta \cdot \bar{n} + I_{dark} \cdot t/q_e} \quad \text{(B.11)}$$

Where:

σ = standard deviation for total shot noise in number of collected charge carriers (electrons or holes);

η = pixel quantum efficiency;

$\bar{n}$ = mean or expected number of photons striking the pixel;

I_{dark} = dark current;

t = pixel integration time = time interval between last pixel reset and pixel readout;

q_e ≈ 1.6022·10^{-19} C = elementary charge.

Dark current can be modeled by the Arrhenius equation or similar equations (for example, the model presented by Wildenhorn et al. (2002) for CCD sensors), presenting an approximately exponential behavior with temperature, in such a manner that a small reduction in the detector's absolute temperature is able to

significantly reduce the dark current. This behavior makes it possible to reduce significantly the dark current and the shot noise related to it with a modest temperature reduction. For instance, using the activation energies given by Wildenhorn et al. (2002) for CCDs, it is not hard to see that a temperature reduction of just 30°C from room temperature (27°C = 300 K), which represents a reduction of only 10% in the absolute temperature, is capable of reducing the dark current by a factor typically larger than 10 and the shot noise by a factor typically larger than 3.16 (square root of 10) for silicon detectors.

B.2.5 1/f noise

This term may be used to refer to many kind of noise sources that present a spectral power density (when expressed as power per unit of frequency, e.g., V^2/Hz) that increase with the multiplicative inverse of the frequency, or with frequency raised to an exponent α, with $-3 < \alpha < -0.8$ (PALMER, 2010). This kind of noise is mostly visible at low frequencies.

In CMOS detectors, 1/f noise has many origins, being one of the leading causes charge trapping at impurities or in defects in the semiconductor crystal lattice. As these defects tend to accumulate at semiconductor interfaces (e.g., silicon to silicon dioxide interfaces), one approach that semiconductor manufacturers use is to try to avoid placing device active areas at interfaces. According to Tian (2000), 1/f noise typically is not important for CMOS APS sensors, except in low light conditions and high integration times (typically above 1 second).

B.2.6 Amplifier noise

In addition to the noise sources at pixel level studied so far, amplifiers and sampling circuits that exist along the signal path also contribute to the total noise. According to Tian (2000), in modern CMOS APS image sensors, the total contribution to noise due to amplifiers present inside the image sensor is small when compared to noise generated at pixel level.

B.2.7 Fixed pattern noise and response non-uniformity

In linear or two-dimensional image sensors, there are always some small variations in the response and in the background level from one pixel to the other. These variations are inherent to the manufacturing process or can be a result of damages that occur during use or storage or transportation. This response non-uniformity results in a fixed pattern noise (FPN), that appears practically unaltered in a succession of images captured by the same image sensor (GAMAL et al., 1998). Assuming a linear response with the luminous signal and integrated dark current, the FPN can be decomposed into three main components, that vary from pixel to pixel: a bias in the dark level, a gain, and a variation in the dark current. For two-dimensional image sensors, this can be expressed mathematically as:

$$R_{ij} = a_{ij} * f_{ij} + b_{ij} + c_{ij}(T) * t \qquad \text{(B.12)}$$

Where:

R_{ij} = response of pixel located at row i and column j;
a_{ij} = signal gain for pixel located at (i, j);
f_{ij} = number of photons incident on pixel (i, j);
b_{ij} = bias for pixel (i, j);
$c_{ij}(T)$ = dark current for pixel (i, j), function of temperature;
t = integration time (assumed to be the same for every pixel);
T = image sensor's absolute temperature.

The gain variation between pixels in a detector (coefficient a_{ij} in Equation (B.12)), also known as PRNU (photo response non-uniformity), can have many causes, from which the following may be cited:

a) small variations in pixel geometry, leading to small variations in the photosensitive area;

b) variations in the pixel quantum efficiency;

c) for two-dimensional CMOS sensors (excluding DPS sensors), variations among column amplifiers;

d) for CCD sensors: limitations in the charge transfer efficiency between pixels during image readout.

The pixel's dark level (coefficient b_{ij} in Equation (B.12)) can be adjusted for the entire image by modifying the input range of the A/D converter(s) used for image digitization or by changing the bias voltages applied to the detector. Even after making these adjustments, there still remains a variation among pixels, that can be caused by:

a) small differences in the analog path for signals generated by different pixels;

b) for CMOS image sensors: variations in the geometry and threshold voltages for each pixel MOSFET transistors;

c) for two-dimensional CMOS sensors (except DPS sensors): variation between column amplifiers.

Dark current usually varies significantly between pixels in the same detector, usually by many orders of magnitude. It is common that CMOS detectors have some pixels with dark current hundreds or even thousand times greater than average. These pixels are known as hot pixels. For CMOS APS sensors, the statistical distribution for the dark current among pixels can be modeled as a log-normal distribution (BAER, 2006; PORTER, 2008).

In CMOS detectors, usually there are a number of amplifiers for each pixel column. This becomes evident after checking the STAR-1000 datasheet (ON SEMICONDUCTOR, 2014) and datasheets from other CMOS image sensors. For these sensors, parametric variation among column amplifiers is one of the chief contributors to the image sensor FPN. Gamal *et al.* proposed in 1998 a simple mathematical model for the pixel FPN and column FPN in a CMOS

detector. Nevertheless, from Figure 4 presented in their paper and from the mathematical model description it is possible to conclude that this model is not able to represent in a realistic manner the existence of hot pixels in CMOS APS image sensors, in special, this model does not take into account the fact that the pixel dark current coefficient (parameter $c_{ij}(T)$ in Equation (B.12)) follows a log-normal distribution.

There is some variation in the nomenclature. Some authors, for instance, do not include the gain variation (PRNU) into the definition of the term FPN (fixed pattern noise) (HORNSEY, 2003), whereas others do (ALBERT, 2012).

As the FPN is fixed in the detector, not changing from image to image, fortunately it is possible to eliminate the FPN with proper calibration. A common method to remove the FPN is to acquire three kinds of images: “bias fields”, “dark fields” and “flat fields”. A “bias field” is a very short exposure (ideally with integration time of zero) taken with the image sensor in the dark. “Bias fields” are used to determine the bias coefficients b_{ij} in Equation (B.12). “Dark fields” are taken with the image sensor completely covered (in the dark) with the same exposure time used in normal imaging. The coefficients c_{ij} in Equation (B.12) can be determined from the difference between dark fields and bias fields. “Flat fields” are taken with the image sensor subject to uniform illumination and normal exposure time. “Flat fields”, after being corrected for bias and dark current, are useful to estimate the a_{ij} gain coefficient, thus correcting for photo response non-uniformity. Alternatively, “flat fields” can be taken with a complete camera subject to a uniform illumination (e.g., facing a uniformly illuminated blank sheet of paper), in this case, flat field images will also correct losses introduced by the optics. When performing calibration, “bias field”, “dark field” and “flat field” images should be taken multiple times with the same settings and averaged to remove the effects of temporal noise.

For scenarios where the pixels can be assumed to have exactly the same geometry (exactly the same size and shape), this method provides good

correction in the images for centroiding. However, for very accurate work, where pixels cannot be assumed to have exactly the same size, more elaborate calibration schemes must be used, as the ones cited in Section B.2.9.

B.2.8 Digitization errors

When an analog signal (for instance, a voltage) that can assume an infinite gamut of values is converted to the digital domain, where the number of exactly representable values is finite, it is not possible to exactly represent the original analog signal to be digitized. In the digitization process the analog signal is represented, when an ideal converter is used, by the digital value that is nearest to the analog value. The difference between the real value and the closest value that exists in the digital domain is known as truncation error, digitization error or quantization error. Figure B.6 illustrates this error.

Figure B.6 – An ideal 3 bit A/D converter.
Actual A/D response is shown in black. The cyan curve would be the A/D converter response if there were no quantization error.

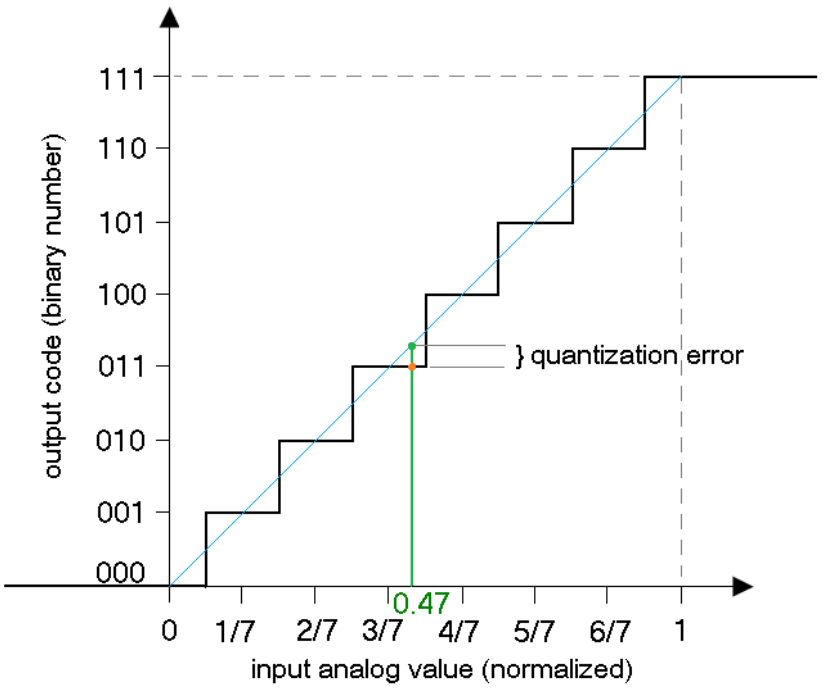

Source: Drawn by the author.

The conversion of a signal from the analog to the digital domain is performed by a device known as an A/D converter (A/D = analog to digital) or simply ADC. One way to reduce the quantization error is to add more discretization steps in the output of the A/D converter. For most A/D converters, which output their results as a binary (base-2) number, this can be accomplished by using more bits (binary digits) to represent the digitized signal. Every bit added doubles the number of representable values in the digital domain. However, the addition of more bits to the output of an A/D converter is not always advantageous due to the following reasons:

a) the A/D converter itself introduces analog noise to the signal to be digitized. To digitize a signal in a way that every or almost every bit is valid requires the use of quieter, and hence, more expensive, A/D converter;

b) increasing the number of bits usually leads to a higher computational cost to handle the data, especially if the least significant bits of the digitized value are dominated by noise present in the system. This happens because noise, by being unpredictable, has a very large information entropy. It is not possible to compress a bit stream using a lossless algorithm to a bit stream shorter than its information entropy (MACKAY, 2005; SHANNON, 1948).

When the analog signal to be digitized is not correlated to the digitization error, and assuming that the A/D converter response is linear, this error presents a rectangular probability distribution, whose standard deviation is $\sigma = h / \sqrt{12} \approx 0.289\ h$, where h is the A/D converter step. This hypothesis is true if the signal to be digitized is uniformly or almost uniformly distributed over a range of values much wider than the ADC conversion step h, as shown in Figure B.7.

Figure B.7 – Probability density function for the quantization error of an ideal ADC, when the signal is not correlated to the quantization error introduced by the ADC. *h* is the digitization step.

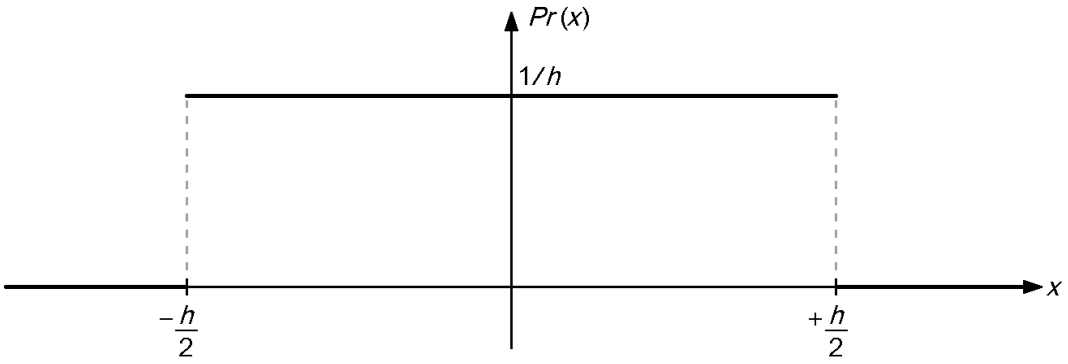

Source: Drawn by the author.

In order to avoid the quantization error becoming the dominant contributor to the overall system error, but at the same time avoiding wasting resources with an expensive A/D converter, we could say that a good rule of thumb would be to select the ADC in such a manner that the quantization error represents between 1/5 and 1/2 of the overall system noise.

Besides the quantization error, there also exists the clamping error, that happens when the signal to be digitized is outside the input range of the ADC. This error can be much larger than the quantization error. To avoid clamping error, the designer of a system must ensure that the signal to be digitized is within the ADC input range whenever possible or feasible. Hence, image sensors and ADCs are usually biased in such a way that even in the absence of a luminous signal, the analog signal obtained by the sensor will be digitized to a value slightly above the lowest possible ADC output value (usually zero), ensuring that the noise present in the system will not throw this analog signal outside the ADC's input range. This added bias in the value that represents the image sensor output when it is not illuminated can be easily removed by software during image processing.

B.2.9 Pixel non-uniformity

The model described in Section B.2.7 works well when the pixels are regularly spaced in the detector array and when all pixels have the same physical dimensions. In practice, there's always some variation in the area and center of pixels in relation to their theoretical position. These variations aren't only due to manufacturing process variations, but can be a result of damages that the sensor suffers during its life, especially in hostile environments, with high ionizing radiation dose rate. These variations are almost always neglected, but they lead to errors in star centroid computation. According to Smith and Rahmer (2008), a CCD image sensor studied by them had a random width variation of 0.34%. The fluctuation of the center position of these pixels in relation to their theoretical position was not presented by these authors, but should have about the same values. They also show that the usual consideration that PRNU is a result only of quantum efficiency variation, as is usually considered, can lead to centroiding errors when pixel values are normalized in an attempt to eliminate PRNU.

Zakharov *et al.* (2013, Section 8.4), report that irregularities in the position and geometry of pixels can in some cases exceed 1% of the size of a pixel, limiting the accuracy of centroid computation to some hundredths of a pixel size, even if all other noise and error sources are compensated.

Zhai *et al.* (2011) present a calibration procedure for two-dimensional detectors taking into account pixel response variation, pixel center variation and other parameters. With this calibration, it becomes possible to compute centroids with errors in the range of thousandths of a pixel size. Unfortunately, this procedure requires interferometric measurements performed with complex laboratory equipment, something that would not be available for star trackers in orbit.

The correction method to be used also depends on the sensor's architecture. For instance, in CCD or CMOS architectures with four or more transistors, a reduction in the pixel's area leads to a reduction in sensitivity due to a reduction in the photosensitive area. In contrast to this, in CMOS sensors with three transistor

pixel architecture (3T pixel), the reduction in sensitivity might be masked by an increase in the conversion factor from collected photoelectrons to voltage at the pixel's output (which can be interpreted as an analog gain), due to the reduction in the photodiode's capacitance when its area is reduced.

B.2.10 Detector non-linearity

Equation (B.12) presented in Section B.2.7 is strictly applicable only when the image sensor presents a linear response with the luminous signal and integrated dark current. In practice, the image sensor may present some non-linearities due to the following reasons:

a) pixel response non-linearity: when a pixel nears saturation its effective quantum efficiency decreases;

b) A/D converter non-linearities (ON SEMICONDUCTOR, 2014; MICROCHIP TECHNOLOGY Inc., 2000).

Fortunately, for most stars used for attitude determination, the pixels illuminated by them will be very far from saturation, meaning that the image sensor will be working in its linear range for most stars. For example, the STAR-1000 image sensor has a linearity better than 1% up to 70% of its full well capacity (ON SEMICONDUCTOR, 2014). Also, a good star tracker project will select an ADC with a good linearity. For example, the STAR-1000 internal ADC has a non-linearity better than 1% (ON SEMICONDUCTOR, 2014). Therefore, unless a very high accurate star tracker is being designed, these non-linearities can usually be ignored.

B.2.11 Image lag

A problem that afflicts some types of image sensors, in special CMOS APS sensors is incomplete reset, which leads to image lag. This phenomenon occurs

when the reset cycle at the start of a new image acquisition is not enough to clear completely the previous image (ON SEMICONDUCTOR, 2012).

This problem can be mitigated by software, or by hardware, by changing the sensor biasing voltages in such a way that the reset becomes complete (operation in *hard reset mode*). However, each of these alternatives has its disadvantages. Operation in hard reset mode solves the image lag problem, at a cost of an increased temporal noise in CMOS APS sensors, when employment of the CDS (correlated double sampling) technique is not feasible (TIAN, 2000). Compensation by software leads to an increase in the software complexity and to a higher computational cost.

B.2.12 Ionizing radiation

Outside the protection offered by Earth's atmosphere, spacecraft are exposed to an ionizing radiation dose rate hundreds to millions of times greater than that found on Earth's surface. Ionizing radiation causes cumulative damage (many related to the total ionizing dose or TID, for short) and also immediate effects, collectively known as SEE - single event effects. A good review and introduction to the subject is presented in the Aerospace Corporation 2003 Summer edition of the Crosslink magazine (CROSSLINK, 2003). This section attempts to summarize the key points of ionizing radiation related to image sensors used in star trackers.

Ionizing radiation found in low Earth orbit environments is composed of many kinds of particles, such as photons, electrons, atomic nuclei at relativistic velocities and hadrons (protons, neutrons, unstable baryons and mesons). These particles have many origins, including extragalactic sources, galactic sources, particles emitted by the Sun, particles trapped at Earth's magnetic field and even particles that originate from interaction of those particles with the spacecraft (secondary radiation).

B.2.12.1 Ionization effects in the detector

Electrically charged particles with energies above few keV are able to penetrate matter, leaving a trail of ionized particles along its track. If this process happens in a semiconductor material, the result will be trail of mobile charge carriers (electrons and holes). These charge carriers in this ionization trail can produce an spurious electrical signal as them are swept away by the electric fields within the device. This spurious electrical signal can produce unwanted effects, collectively known as SEEs (single event effects). In image sensors, one of these effects is the generation of temporary images very similar to images generated by true stars, leading to observed false stars. Another more serious effect lead by high energy ionizing particles occurs when they cross insulating materials in an integrated circuit (usually field and gate oxides). In these materials, the charge carriers created by the ionization process can become trapped, changing permanently the parameters of affected transistors and sometimes leading to the creation of new parasitic circuit elements. Depending on the accumulated damage, the device may work in an abnormal way or simply stop functioning.

B.2.12.2 Non ionizing effects

Besides the effects caused by ionization in the device, high energy particles can also cause other kinds of damage, not directly related to the ionization process. Among these effects, the most prominent is displacement damage. Displacement damage occurs when a high energy particle with considerable mass (e.g.: a proton, neutron, alpha particle or heavier nuclei) hits the nucleus of an atom of the irradiated material, with enough energy to knock-out that atom. The result is the appearance of defects in the crystalline structure of the material, one in the place where the atom used to be, now empty, and another in the place where that atom became lodged (interstitial defect). The colliding particle itself, if an atomic nucleus, can become lodged in the material, creating an additional interstitial defect. For CMOS APS image sensors, the main effect of displacement damage is an increase in the FPN and the appearance of new hot pixels.

B.2.12.3 Concluding remarks

Ionizing radiation, be it by the process of ionization or by non-ionizing effects cause degradation in image sensors. In the case of silicon based image sensors, one of the chief cumulative effects caused by ionizing radiation is the appearance of new hot pixels. Many times, these hot pixels are the result of damages in the detector's crystal lattice due to high energy particles, capable of dislodging atoms from their initial positions. These damages create intermediary energy levels, facilitating the thermal generation of charge carriers in the semiconductor material. Fortunately, it is possible to revert some degradation by annealing the semiconductor device. This process happens naturally, but it can be accelerated by increasing the temperature.

B.3 Other sources of errors

B.3.1 Catalog errors

Star catalogs are never perfect. There are always measurement errors associated with stellar coordinates in a star catalog. Some phenomena described in the previous sections, such as proper motion and existence of binary/multiple star systems, can pose difficulties in the preparation of accurate star catalogs for star trackers.

The Hipparcos star catalog gives stellar coordinates with uncertainties in the order of few milliarcseconds for the catalog epoch of J1991.25 (ESA, 1997) in the ICRS reference frame (equivalent to the equatorial coordinate system using poles and equinoxes of J2000.0).

B.3.2 Numerical errors during computation

It is not possible to exactly represent in a digital computer all real numbers in an exact way. Hence most measured values, intermediate values and final results

will be represented with some representation error. This representation error is smaller the higher the number of binary digits (bits) used to represent a number.

Real and rational numbers are typically represented in a computer using a binary floating point representation of 32-bits or 64-bit defined by the IEEE-754 standard (2008), as these formats are supported on most machines.

Using a 32-bit binary floating point format (IEEE binary-32 format, with 24 bits of mantissa (one bit implied), 1 sign bit and 8 bits of exponent), it is possible to represent angles in the range $[-4,4]$ rad (which includes the range $[-\pi, \pi]$) with an accuracy better than 0.049 arc-seconds. Depending on the application, this may be enough, however a detailed analysis of the code would be required to assure that truncation and rounding errors would not accumulate and lead to inaccurate results.

When using double precision (IEEE 64-bit binary floating point format with 53 bits of mantissa (one bit implied), 11 of exponent and one sign bit), it is possible to represent angles in the range $[-\pi, \pi]$ with an accuracy better than $9.16 \cdot 10^{-11}$ arc-seconds. With this format, truncation and rounding errors will be mostly negligible, unless a numerically poor algorithm is used. An example of a numerically poor algorithm is the computation of very small angles from the arccos function. This happens because there is a singularity in the derivative of the arc-cosine function when its input argument is close to one (corresponding to small angles), which means that small errors in the input argument of the arc-cosine function lead to large errors in the computed angle in this case. This situation can arise when attempting to compute the angle between two unit vectors by computing the arc-cosine of their dot product, when this angle is very small.

B.3.3 Other sources

Besides the sources of error described in this appendix, there are many other sources of error that may affect the accuracy centroids, for example:

a) distortions introduced by the optics: a large part of these distortions and techniques to compensate them have been discussed by Albuquerque in his master's thesis (2005);

b) thermal expansion of the structure that holds the detector and optics;

c) thermal expansion in the optical elements (lenses or mirrors);

d) thermal expansion in the detector (image sensor);

e) existence of thermal gradients in the optics and in the detector;

f) electromagnetic interference, adversely affecting the video signal integrity before digitization;

g) rounding and truncation errors in centroid computation.

Even if all those errors had been compensated for, and centroid determination were free of errors, the attitude generated by a star tracker could be adversely affected by sources of errors briefly discussed in Section B.1.

Even after taking into consideration all the sources of error cited in this appendix, we don't arrive at an exhaustive list of all sources of error and noise that may affect the accuracy in the determined attitude by a star tracker. The higher is the desired accuracy, the higher is the number of factors that must be taken into account, in such a way that it seems that there does not exist an upper limit to the number of noise and error sources that must be considered when one wants to attain an infinite accuracy, which would make impractical the development of a star tracker. Hence, what should be done is to prioritize the most relevant sources of error, compensating first the sources with higher impact in the accuracy of the determined attitude before compensating the remaining sources of error.

APPENDIX C MAGNITUDES AND COLOR INDICES

This appendix gives a brief description of stellar magnitudes and color indices.

C.1 Magnitudes

In Astronomy, stellar brightness is usually measured with magnitudes. The great Greek astronomer Hipparchus is usually credited as having invented the magnitude scale (it is not clear whether he actually invented it or if he got to know about magnitudes from older sources). In this scale, Hipparchus assigned an integer number for each star, being 1 for the brightest stars, 2 for the not so bright stars and so on, until stars of magnitude 6, the dimmest that could be observed by naked eye in a moonless dark night.

With the invention of the telescope, more stars become observable, so the magnitude scale was extended by including additional magnitude classes (7th magnitude, 8th magnitudes and so on). By the eighteen and nineteen centuries it became clear to the astronomers that traditional magnitudes followed roughly a logarithmic scale. Also, without a clear definition of magnitude, quantitative studies about stellar properties was difficult. Hence in 1857 Pogson devised a logarithmic magnitude scale that remained compatible with magnitudes used in old star catalogs, being largely adopted by astronomers and becoming the modern definition of the magnitude scale. According to this definition, the magnitude of a star can be computed as follows:

$$m = -2.5 \cdot \log_{10}\left(\frac{B}{B_{ref}}\right) \tag{C.1}$$

where m is the star magnitude, B is the luminous flux or stellar brightness, and B_{ref} is a reference luminous flux that sets the zero point of the magnitude scale.

Note that the magnitude scale is an inverted scale. The higher the magnitude of a star, the fainter the star is. Also notice that with current definition of magnitude,

magnitudes can be zero or even negative. Table C.1 presents magnitudes for some selected celestial bodies.

Table C.1 – Approximate magnitudes for some celestial bodies

Celestial body	visual magnitude (m_V)	brightness in comparison to Vega
the Sun, as seen from Earth	−26.86	$5.7 \cdot 10^{10}$
full Moon	−12.7	$1.2 \cdot 10^{5}$
Venus, maximum elongation	−4.4	60
Sirius, the brightest star in the night sky	−1.45	3.8
Vega, old reference for magnitude scale	+0.03[a]	1
Dimmest stars visible to naked eye	6	0.004
dwarf planet Pluto	15	10^{-6}
Dimmest objects visible to a telescope with an aperture of 8 meters	27	$1.6 \cdot 10^{-11}$

[a] Originally, Vega was used as a reference for the magnitude scale, which made its magnitude being zero, according to Equation (C.1). However, with the recognition that the brightness of Vega was not very stable, the zero point of magnitude scale was later redefined by a set of stars.
Source: Fialho (2007).

Initially, magnitudes were only defined in the visual spectral band defined by the human eye. However, with the advent of photographic plates, and more recently electronic detectors, magnitudes could also be defined for other spectral bands, not restricted to the visible. Its usual to refer to the magnitude measured in the spectral band defined by an instrument as *instrumental magnitude*.

C.2 Color indices and photometric systems

In astronomy, color indices (or color indexes) are defined as the difference between star magnitudes in two different spectral bands. For example, if the $B-V$ color index of a star is 0.65, it means that its magnitude in the B (blue) band minus its magnitude in the V (visual) band is 0.65. As this star has a higher magnitude in the B band than in the V band, with higher magnitudes meaning dimmer or weaker, it means that it is weaker in the B band than in the V band when compared to a reference star that has the same magnitude in both B and V bands. Incidentally, we have used the Sun for this example. Since the reference star for

defining the *B* and *V* bands used to be the star Vega (which originally had *B* and *V* magnitudes of 0 in the original scale devised by Johnson and Morgan (1953), this means that the Sun (with a $B-V$ color index of 0.65) emits comparatively less in the *B* band and more in the *V* band than the reference star Vega. In fact, Vega has a bluish white color, whereas the Sun appears to the human eye to be white or white with a yellowish tinge.

A photometric system is a set of different magnitude scales (one magnitude scale for each spectral band) and their associated color indexes. Some photometric system became of standard use in Astronomy, such as the Johnson's *UBV* photometric system, derived with a standard set of filters and detectors. However, whenever a new equipment is constructed, it is hard to make its spectral bands exactly match the spectral bands of a standard photometric system. Hence, each equipment will have its own natural photometric system. For the Foveon camera with stacked pixels, described in Chapter 3, it has its own natural photometric system, defined by the spectral response of its blue, green and red channels and also on how we define the zero point of the three magnitude scales associated with each one of its three spectral bands (see Section 3.6.6 for an example). A common procedure to fix the zero points of the magnitude scales is to assign for a bright star or a set of stars a conventional magnitude value in each one of these spectral bands.

C.3 Synthetic photometry

If the spectrum of a star and the spectral response functions of each spectral band of a photometric system are known, it is possible to compute the magnitudes and color indexes of that star in that photometric system by integrating, in wavelength or in frequency, the product of the stellar spectrum with the spectral response functions. This procedure is known as *Synthetic Photometry*, being explained in more detail by Straižys (1996), Bessell (2005) and Bessel and Murphy (2012). This section provides the formulation that has been used in this work.

Let $R_X(\lambda)$ be the energy response function that defines the spectral band *X* and let $f(\lambda)$ be the spectral energy distribution a star, then the flux of that star in the spectral band *X* (or passband *X*, in astronomical parlance) can be computed by the following integral:

$$\varphi_X = const \cdot \int_{\lambda=0}^{\infty} f(\lambda) R_X(\lambda) \mathrm{d}\lambda \tag{C.2}$$

where $const$ is an arbitrary constant that may be present to effect a change of units or for other reasons. Its exact value is unimportant, provided it is non-zero, as will become clear later.

Let $\varphi_{X,REF}$ be the reference flux that defines the zero point of the magnitude scale in band *X*, then, according to Equation (C.1), the synthetic magnitude of the star in band *X* is given by:

$$m_X = -2.5 \log_{10}\left(\varphi_X / \varphi_{X,REF}\right) \tag{C.3}$$

The constant $const$ of Equation (C.2) also multiplies the value of $\varphi_{X,REF}$. If this constant is changed, it will affect φ_X and $\varphi_{X,REF}$ equally, so that the value of m_X will remain unchanged. This explains why $const$ can be chosen as any non-zero value.

For the natural photometric system of a camera, the energy response function $R_X(\lambda)$ is the product of the transmittance of all optical components in the camera (including any spectral filters used to better define the spectral bands) with the detector response. For systems using photomultiplier tubes, it was usually expressed in amperes per watt [A/W].

The spectral energy distribution $f(\lambda)$ is expressed in units of power per unit of area per unit of wavelength (e.g., $W \cdot m^{-2} \cdot m^{-1}$ in SI units).

The reference flux $\varphi_{X,REF}$ that defines the zero point of the magnitude scale in band *X* can be defined in many different ways, depending on how the magnitude

scale is defined. In this work, we have used the star Vega (α-Lyr) as a reference for defining the zero point. Using Vega as a reference, $\varphi_{X,REF}$ is given by:

$$\varphi_{X,REF} = 10^{0.4 m_{Vega,X}} \int_{\lambda=0}^{\infty} f_{Vega}(\lambda) R_X(\lambda) \mathrm{d}\lambda \qquad \text{(C.4)}$$

where $m_{Vega,X}$ is the adopted (by definition) magnitude for Vega in band *X*, usually chosen to be equal or very close to 0.03 in order to make comparisons with standard photometric systems based on Vega easier. $f_{Vega}(\lambda)$ is the spectral irradiance from Vega measured at the top of Earth's atmosphere. The spectrum of Vega adopted in this work has been obtained from the CALSPEC Calibration Database, file `alpha_lyr_stis_008.fits` (STSCI, 2017).

APPENDIX D STAR CATALOG FORMATS

This appendix presents the star catalog formats used in PTASE. These were initially developed for the Brazilian star tracker (FIALHO; PERONDI; MORTARI, 2016) and then expanded to accommodate color indexes. Since that star tracker had limited availability of non-volatile memory, it was decided to create two formats of star catalogs, a compact format used solely for storage and a larger format (working catalog) used for stellar identification and attitude determination. Upon initialization, the storage catalog is converted to the working catalog format.

D.1 Storage catalog

The storage catalog is the star catalog in a format more suitable for storage in limited non-volatile memory (PROM, EPROM, EEPROM or FLASH memories). In this format, star coordinates are represented in a spherical coordinate system (right ascension and declination). This format has the advantage of being very compact, since only two scalar values (two angles) are required to completely specify the coordinates of a star. However, this format is unsuitable for stellar identification, since operations with spherical coordinates involves computation of trigonometric functions (sine, cosine) which are computationally expensive. Also, this form of representation has singularities at the poles. Hence before the star-ID process starts, the storage catalog is converted to a working catalog format which employs a format more suitable for star identification and attitude determination.

D.2 Working catalog

In the working star catalog, star coordinates are represented by unit vectors in a three-dimensional space. Even though this representation requires the use of three scalar components (with one being redundant), it has the advantage of being much faster than the representation used in the storage catalog. Working with unit vectors, the angular separation between stars, when represented by its

cosine, can be easily computed by the dot product between the unit vectors that represent the stars. Computing the dot product between two three-dimensional vectors is usually much faster than computing the angle using trigonometric and inverse trigonometric functions.

D.3 Storage catalog format for monochrome star catalogs

The following fields are stored per each star (entry in the catalog): right ascension (R.A), declination (dec.), instrumental magnitude, catalog identifier, a flag field and a checksum field, as shown in Table D.1.

The right ascension and declination give the angular coordinates of the star in the ICRS reference frame. For the purposes of autonomous attitude determination, in the stellar identification process, only right ascension, declination, and (depending on the star-ID algorithm) magnitude are needed. The catalog identifier and flags field are useful for debugging, but they are not strictly required, since to determine attitude from stars, all that is needed is to discover the coordinates in an inertial reference frame (the one used in the star catalog) of the observed stars (whose coordinates in the star tracker frame are already known from the image processing and centroiding).

Even though the format used in READCAT, PROC_CAT and PTASE introduces some rounding errors, these errors are negligible for most star sensors. Right ascension is stored with a resolution of $360°/ 78000000_{16} \approx 3.12$ nrad ($1.79 \cdot 10^{-7}$ degrees = 0.64 mas) and declination is stored with a resolution of $180°/ 78000000_{16} \approx 1.56$ nrad ($8.94 \cdot 10^{-8}$ degrees = 0.32 mas), where nrad is a nanoradian (10^{-9} radians), and mas is a milli-arc-second (1/1000 of an arc-second). The subscript 16 is used to denote numbers in hexadecimal base. Instrumental magnitudes are stored with a resolution of 0.001 magnitude (one millimagnitude), corresponding to a flux ratio of $10^{0.4 \cdot 0.001} \approx 1.00092$ between two consecutive values.

Table D.1 – Fields stored for each star in the monochrome storage catalog in PTASE

field	type*	size (bytes)	range**	description
flags	uint8	1	0 - 255	Indicates whether the entry represents a single entry in the Hipparcos Catalog, or the result of merging multiple entries in the Hipparcos Catalog by PROC_CAT.
chksum	uint8	1	0 - 255	Stores a check code for each star, in order to detect possible errors in the catalog (still not used as of October 2017)
mI	int16	2	−30000 to +30000	Instrumental milli-magnitude. −30000 means a magnitude of −30.0, +30000 means a magnitude of +30.0. Values under −30000 or greater than +30000 are reserved.
ID	uint32	4	0 to 2^{32} -1	Star and catalog identifier. Indicates the source catalog and the star identifier within the source catalog. Used for debugging only.
RA	uint32	4	0 to 78000000h	Right ascension in the range of 0° to 360°, with 0 meaning 0° and 78000000h meaning 360°. Values greater or equal to 78000000h (2,013,265,920 in decimal) are reserved for future extensions.
dec	uint32	4	0 to 78000000h	Co-declination, in the range 0 (0°) to 78000000h (180°). Value 0 means a declination of +90°, and a value of 78000000h means a declination of −90°. Values greater than 78000000h (2,013,265,920 in decimal) are reserved.

* uint8, uint16 and uint32 means 8-bit, 16-bit and 32-bit unsigned integers, respectively. int16 means signed 16-bit integer.
** hexadecimal numbers are suffixed with the letter ‘h’.
Source: created by the author.

This catalog is stored in a file with extension .cat. This file format consists of a small header of 48 bytes followed by n-entries, each entry corresponding to a star and taking 16 bytes. These values are multiple of 4 bytes, making it possible to load the storage catalog in memory in such a way that the header and the entries

are kept aligned at 4 byte boundaries. This has the advantage of simplifying and speeding up conversion from this format to the working catalog format in embedded 32-bit systems, like the Brazilian star tracker.

D.4 Storage catalog format for color star catalogs

The star catalog containing color index information is very similar to the format used in the monochrome star catalog, the largest difference being the addition of two fields containing the *B*−*V* and *V*−*I* color indexes derived from the Hipparcos catalog. Detailed specification of the fields used is shown in Table D.2.

Table D.2 – Fields stored for each star in the color storage catalog in PTASE

field	type*	size (bytes)	range**	description
flags	uint8	1	0 - 255	Indicates whether the entry represents a single entry in the Hipparcos Catalog, or the result of merging multiple entries in the Hipparcos Catalog by PROC_CAT.
chksum	uint8	1	0 - 255	Stores a check code for each star, in order to detect possible errors in the catalog (still not used as of October 2017)
mv	int16	2	−30000 to +30000	Visual milli-magnitude. −30000 means a magnitude of −30.0, +30000 means a magnitude of +30.0. Values under −30000 or greater than +30000 are reserved.
ID	uint32	4	0 to 2^{32} -1	Star and catalog identifier. Indicates the source catalog and the star identifier within the source catalog. Used for debugging only.
RA	uint32	4	0 to 78000000h	Right ascension in the range of 0° to 360°, with 0 meaning 0° and 78000000h meaning 360°. Values greater or equal to 78000000h (2,013,265,920 in decimal) are reserved for future extensions.

(continues on the next page)

Table D.2 – Fields stored for each star in the color storage catalog in PTASE
(continued from previous page)

field	type*	size (bytes)	range**	description
dec	uint32	4	0 to 78000000h	Co-declination, in the range 0 (0°) to 78000000h (180°). Value 0 means a declination of +90°, and a value of 78000000h means a declination of −90°. Values greater than 78000000h (2,013,265,920 in decimal) are reserved.
B_V	int16	2	−30000 - +30000	Johnson's *B*−*V* color index in millimagnitudes.
V_I	int16	2	−30000 - +30000	Johnson's *V*−*I* color index in millimagnitudes.

* uint8, uint16 and uint32 means 8-bit, 16-bit and 32-bit unsigned integers, respectively. int16 means signed 16-bit integer.
** hexadecimal numbers are suffixed with the letter 'h'.
Source: created by the author.

In the monochrome star catalog, each star entry occupies 16-bytes. In the color star catalog, each entry occupies 20-bytes. Since both types of storage catalog use the same filename extension (.cat), identification of which format is being loaded in PTASE is done through a field in the file header.

APPENDIX E PROOF THAT $\sigma_i^2 = \sigma_{min,i}^2$

This proof is related to Chapter 7, Section 7.2.10 of this thesis.

Being $\sigma_{min,i}^2$ the lower bound of centroiding error variance for star i along any axis perpendicular to the true direction of that star, given by Equation (7.19), and being σ_i^2 the overall measurement variance associated with that star, used in Equation (5.114) of Markley and Crassidis (2014), the goal of this appendix is to prove that they are the same.

Proof. Let $\mathbf{b}_i^{\text{true}}$ be a unit vector representing the true position of star i in the star tracker reference frame (body frame) B and $\mathbf{s}_i^{\text{true}} = [0\ 0\ 1]^T$ the same unit vector in a reference frame S_i where the line joining the star tracker to star i is the z-axis of that reference frame. Then there exists an attitude matrix $\mathbf{A}_i$ such that:

$$\mathbf{s}_i^{\text{true}} = \mathbf{A}_i \mathbf{b}_i^{\text{true}} \tag{E.1}$$

Due to measurement errors, the measured direction of star i ($\mathbf{s}_i$) will differ from its true position $\mathbf{s}_i^{\text{true}} = [0\ 0\ 1]^T$ by $\Delta\mathbf{s}_i \equiv \mathbf{s}_i - \mathbf{s}_i^{\text{true}} \equiv \left[\Delta s_{i,x}\ \ \Delta s_{i,y}\ \ \Delta s_{i,z}\right]^T$. Under the assumptions of Section 7.2 and considering that $\sigma_{min,i}^2$ gives the lower bound on centroid error <u>per axis</u>, the expected values of the variances of the *x* and *y* components (components in the S_i reference frame) of $\Delta\mathbf{s}_i$ will be equal to $\sigma_{min,i}^2$. In mathematical terms:

$$E\left\{\left(\Delta s_{i,x}\right)^2\right\} = E\left\{\left(\Delta s_{i,y}\right)^2\right\} = \sigma_{min,i}^2 \tag{E.2}$$

with $E\{x\}$ denoting the expected value of a random variable x. Since $\mathbf{s}_i$ is a unit vector very close to $\mathbf{s}_i^{\text{true}}$ and $\mathbf{s}_i^{\text{true}} = [0\ 0\ 1]^T$, the *z* component of $\Delta\mathbf{s}_i$, $\Delta s_{i,z}$, will be given by:

$$\Delta s_{i,z} = \sqrt{1 - \left(\Delta s_{i,x}\right)^2 - \left(\Delta s_{i,y}\right)^2} \approx -\frac{1}{2}\left(\left(\Delta s_{i,x}\right)^2 + \left(\Delta s_{i,y}\right)^2\right) \tag{E.3}$$

As we are retaining only first order terms, like Markley and Crassidis did (2014), $\Delta s_{i,z} \approx 0 \;\Rightarrow\; E\{\Delta s_{i,x}\,\Delta s_{i,z}\} = E\{\Delta s_{i,y}\,\Delta s_{i,z}\} = E\left\{\left(\Delta s_{i,z}\right)^2\right\} = 0$ in a first order approximation. Given that the star tracker aperture is circular and contained in a plane perpendicular to the direction of incoming rays from star i, from symmetry considerations we also have $E\{\Delta s_{i,x}\Delta s_{i,y}\} = 0$, that is, the errors are axially symmetric about the true vectors $\mathbf{s}_i^{\text{true}}$. Hence, the measurement covariance matrix for star i

$$\mathbf{S}_i \equiv E\{\Delta\mathbf{s}_i\,\Delta\mathbf{s}_i^T\} \tag{E.4}$$

will be in a first order approximation:

$$\mathbf{S}_i \approx \begin{bmatrix} \sigma_{min,i}^2 & 0 & 0 \\ 0 & \sigma_{min,i}^2 & 0 \\ 0 & 0 & 0 \end{bmatrix} \tag{E.5}$$

Its trace will be:

$$\text{tr}(\mathbf{S}_i) \approx 2\sigma_{min,i}^2 \tag{E.6}$$

———— // ————

Markley and Crassidis define the following measurement covariance matrix for the errors in the measured star direction vectors $\mathbf{b}_i$ (Equation (5.104a) in their work):

$$\mathbf{R}_{b_i} \equiv E\{\Delta\mathbf{b}_i\,\Delta\mathbf{b}_i^T\} \tag{E.7}$$

Given the assumption that the vector errors are axially symmetric about the true vectors (in our model, this arises from the consideration that the star tracker has a spherical shape) and ignoring the components along the true star directions (components along vectors $\mathbf{b}_i^{\text{true}}$ = components $\Delta s_{i,z}$), since these are of higher

order than the terms that we retain, this measurement covariance matrix can be expressed as (Equation (5.107b) in (MARKLEY; CRASSIDIS, 2014)):

$$\mathbf{R}_{b_i} = \sigma_{b_i}^2[\mathbf{I}_3 - \mathbf{b}_i^{\text{true}}(\mathbf{b}_i^{\text{true}})^T] \tag{E.8}$$

being $\sigma_{b_i}^2$ the variance in the measured vector position for star i.

Considering that the inverse of an attitude matrix is its transpose, from Equation (E.1) we have $\mathbf{b}_i^{\text{true}} = \mathbf{A}_i^T\mathbf{s}_i^{\text{true}}$, hence:

$$\mathbf{R}_{b_i} = \sigma_{b_i}^2\left[\mathbf{I}_3 - \mathbf{A}_i^T\mathbf{s}_i^{\text{true}}\,(\mathbf{s}_i^{\text{true}})^T\mathbf{A}_i\right] \tag{E.9}$$

Considering that the trace of a matrix is a linear operator:

$$\text{tr}\left(\mathbf{R}_{b_i}\right) = \sigma_{b_i}^2\left[\text{tr}(\mathbf{I}_3) - \text{tr}\left(\mathbf{A}_i^T\mathbf{s}_i^{\text{true}}\,(\mathbf{s}_i^{\text{true}})^T\mathbf{A}_i\right)\right] \tag{E.10}$$

Using the matrix trace identity $\text{tr}(\mathbf{BC}) = \text{tr}(\mathbf{CB})$ with $\mathbf{B} = \mathbf{A}_i^T\mathbf{s}_i^{\text{true}}$ and $\mathbf{C} = (\mathbf{s}_i^{\text{true}})^T\mathbf{A}_i$ and considering that the trace of a 3x3 identity matrix is 3:

$$\begin{aligned}\text{tr}\left(\mathbf{R}_{b_i}\right) &= \sigma_{b_i}^2\left[3 - \text{tr}\left(\left((\mathbf{s}_i^{\text{true}})^T\,\mathbf{A}_i\right)\left(\mathbf{A}_i^T\mathbf{s}_i^{\text{true}}\right)\right)\right] \\ &= \sigma_{b_i}^2\left[3 - \text{tr}\left((\mathbf{s}_i^{\text{true}})^T\,(\mathbf{A}_i\mathbf{A}_i^T)\mathbf{s}_i^{\text{true}}\right)\right]\end{aligned} \tag{E.11}$$

Since $\mathbf{A}_i\mathbf{A}_i^T = \mathbf{I}_3$ and $\mathbf{s}_i^{\text{true}} = [0\ 0\ 1]^T$, the trace of $\mathbf{R}_{b_i}$ reduces to:

$$\begin{aligned}\text{tr}\left(\mathbf{R}_{b_i}\right) &= \sigma_{b_i}^2\left[3 - \text{tr}\left((\mathbf{s}_i^{\text{true}})^T\,\mathbf{s}_i^{\text{true}}\right)\right] \\ &= \sigma_{b_i}^2\left[3 - \text{tr}\left([0 \quad 0 \quad 1]\begin{bmatrix}0\\0\\1\end{bmatrix}\right)\right] \\ &= \sigma_{b_i}^2\cdot(3-1) \\ &= 2\,\sigma_{b_i}^2\end{aligned} \tag{E.12}$$

Considering that both the expectation $E\{\}$ and matrix trace are linear operators and using the identity $\text{tr}(\mathbf{BC}) = \text{tr}(\mathbf{CB})$, the following result is obtained from Equation (E.7):

$$\begin{aligned}\mathrm{tr}\left(\mathbf{R}_{b_i}\right) &= \mathrm{tr}(E\{\Delta\mathbf{b}_i\,\Delta\mathbf{b}_i^T\}) = E\{\mathrm{tr}(\Delta\mathbf{b}_i\,\Delta\mathbf{b}_i^T)\} \\ &= E\{\mathrm{tr}(\Delta\mathbf{b}_i^T\,\Delta\mathbf{b}_i)\}\end{aligned} \tag{E.13}$$

In the same manner that $\mathbf{b}_i^{\mathrm{true}} = \mathbf{A}_i^T\mathbf{s}_i^{\mathrm{true}}$, we have $\Delta\mathbf{b}_i^{\mathrm{true}} = \mathbf{A}_i^T\Delta\mathbf{s}_i^{\mathrm{true}}$. Substituting this into the last equation:

$$\begin{aligned}\mathrm{tr}\left(\mathbf{R}_{b_i}\right) &= E\{\mathrm{tr}(\Delta\mathbf{s}_i^T\mathbf{A}_i\mathbf{A}_i^T\Delta\mathbf{s}_i)\} = E\{\mathrm{tr}(\Delta\mathbf{s}_i^T\mathbf{I}_3\Delta\mathbf{s}_i)\} = \\ &= E\{\mathrm{tr}(\Delta\mathbf{s}_i^T\Delta\mathbf{s}_i)\} = E\{\mathrm{tr}(\Delta\mathbf{s}_i\,\Delta\mathbf{s}_i^T)\} = \\ &= \mathrm{tr}(E\{\Delta\mathbf{s}_i\,\Delta\mathbf{s}_i^T\})\end{aligned} \tag{E.14}$$

But, from Equation (E.4), $E\{\Delta\mathbf{s}_i\,\Delta\mathbf{s}_i^T\}$ is the measurement covariance matrix $\mathbf{S}_i$ for star i, whose first order approximation is given by Equation (E.5) and trace by Equation (E.6). Therefore:

$$\mathrm{tr}\left(\mathbf{R}_{b_i}\right) = \mathrm{tr}(\mathbf{S}_i) = 2\sigma_{min,i}^2 \tag{E.15}$$

From Equations (E.12) and (E.15) the following is obtained:

$$\sigma_{min,i}^2 = \sigma_{b_i}^2 \tag{E.16}$$

Equation (5.109) in Markley and Crassidis (2014) gives σ_i^2 as:

$$\sigma_i^2 = \sigma_{b_i}^2 + \sigma_{r_i}^2 \tag{E.17}$$

where $\sigma_{r_i}^2$ is the variance in the reference vector for star i. In other words, $\sigma_{r_i}^2$ gives the uncertainty in the cataloged position of that star. Since it is being assumed that these cataloged positions are known with no errors (Item (e) in Section 7.2.1), $\sigma_{r_i}^2 = 0$, implying that $\sigma_i^2 = \sigma_{b_i}^2$. Substituting this into Equation (E.16) the following result is obtained:

$$\sigma_i^2 = \sigma_{min,i}^2 \tag{E.18}$$

completing the proof. ■